Carbon Nanotube Thin Film Electrodes and Magneto-Optical Spectroscopy of Perovskite Single Crystals and Thin Films



Markus Dollmann

University College

University of Oxford

A thesis submitted for the degree of

Doctor of Philosophy

Hilary, 2019

Carbon Nanotube Thin Film Electrodes and Magneto-Optical Spectroscopy of Perovskite Single Crystals and Thin Films

Markus Dollmann, University College, Oxford

A thesis submitted for the degree of *Doctor of Philosophy*

at the University of Oxford, Hilary 2019

Abstract

With each and every passing year, weather patterns seem to become less predictable and more chaotic due to changes to worldwide climate patterns. Greenhouse gas-free energy production is a boon to the aim of preventing further rises in global temperature increases. This thesis concerns itself with one major aspect of green energy, namely photovoltaics, and some materials with great potential for application in photovoltaics, namely single-walled carbon nanotubes (SWNT), and perovskites.

SWNT have been known for almost thirty years by now, but their intrinsic fondness of bundling up due to their $2p_z$-orbitals has to date prevented any large scale application of them. Functionalising of SWNT offers a solution to this problem, either by dispersing them with surfactants in water, or by polymer functionalisation. Here, the latter method was applied to the problem, and the efficacy of deposition from solvents more advantageous than water is shown, achieving values of transmission and sheet resistance close to the necessary values for application in solar cells.

Next, an inorganic contender for solar cell applications, $Cs_2AgBiBr_6$, is characterised by magneto-optical studies. With these, a direct and indirect gap are identified at 2.85 eV and 1.31 eV. Moreover, a strongly Stokes shift influenced Ag_{Bi} anti-site defect colour centre at 2.25 eV is shown to be part of a self-trapped exciton at low temperatures.

Thereafter, the optical properties between 1.4 K and 370 K in conjunction with room temperature x-ray diffraction measurements of $MAPbI_3$ single crystals and thin films grown/annealed at different temperatures are used to explain the double emission structure visible in photoluminescence and reflectance. A dynamic Rashba effect, likely due to spontaneous alignment of the methylammonium-ions, causes a direct and indirect gap, where the former dominates the surface and the latter dominates the bulk of the samples.

The remaining chapter is a study of the polaronic influence on the transitions observed for $MAPbBr_3$ and $MAPbI_3$. In comparison between high field, high energy, and low field, low

energy, an almost two-fold difference in exciton binding energy, and an increase in effective mass can be observed due to exciton/lattice interactions in comparison to the established high field literature values. Interestingly, for both perovskites studied, single crystals show more favourable values, indicating that device application improvements could be possible by making thin films more single crystal-like.

Publications

G. Mazzotta, M. Dollmann, S.N. Habisreutinger, M.G. Christoforo, Z. Wang, H.J. Snaith, M.K. Riede, R.J. Nicholas
"Solubilization of Carbon Nanotubes with Ethylene-Vinyl Acetate for Solution-Processed Conductive Films and Charge Extraction Layers in Perovskite Solar Cells". *ACS Applied Materials and Interfaces*, 2018.

L. Schade, A.D. Wright, R. Johnson, M. Dollmann, B. Wenger, P. Nayak, D. Prabhakaran, L. Herz, R.J. Nicholas, H.J. Snaith, P. Radaelli "Structural and Optical Properties of Cs2AgBiBr6 Double Perovskite". *ACS Energy Letters*, 2018.

S.J. Zelewski, J.M. Urban, A. Surrente, D.K. Maude, A. Kuc, L. Schade, R.D. Johnson, M. Dollmann, P.K. Nayak, H.J. Snaith, P.G. Radaelli, R. Kudrawiec, R.J. Nicholas, P. Plochocka, M. Baranowski "Revealing the Nature of Photoluminescence Emission in Metal-Halide Double Perovskites". *Journal of Physical Chemistry C*, 2019.

M. Baranowski, K. Galkowski, A. Surrente, J.M. Urban, Ł. Klopotowski, S. Mackowski, D. Maude, R. Ben Aich, K. Boujdaria, M. Chamarro, C. Testelin, P. Nayak, M. Dollmann, H.J. Snaith, R.J. Nicholas, P. Plochocka. "Giant Fine Structure Splitting of the Bright Exciton in a Bulk $MAPbBr_3$ Single Crystal". *Nano Letters*, 2019.

Manuscripts in Preparation

M. Dollmann, R.D. Johnson, J.H. Warby, P. K. Nayak, A.A. Haghighirad, H.J. Snaith, P. Plochocka, R.J. Nicholas "The In-/Direct Nature of $MAPbI_3$ Perovskite". *Manuscript in preparation.*

B. Sturdza, M. Dollmann, S.N. Habisreutinger, R.J. Nicholas "Influence of Nitric Acid Doping on Optical and Charge Transport Properties of Polymer-Functionsalised Carbon Nanotube Thin Films". *Manuscript in preparation.*

Acknowledgments

After almost four years, more Keithley K199s and 405 nm lasers left behind „perfectly working“ than I would care to admit, several magnet quenches (on the last few metres!), several thousand kilometres of carbon nanotubes, solvent fumes galore, one lost lab book, and the odd late night here or there, this is finally it. My thesis. It took some doing but it is finally done. It was a great experience to have spent these years here in Oxford, including all its ups and downs. Hopefully the last experience will be an up, leaving as Dr Dollmann.

I am so grateful to everyone who helped along the way. First and foremost, Robin, who decided to take me on as a student, and is always so generous with dealing out dollops of his enormous experience accrued over 40 years in semiconductor physics. Of course also the rest of the Nicholas group, Bernd, Giulio, Nate, Severin, and Sharkey, who spent many hours, days, and weeks debating, lunching and procrastinating together with me. I thank all of the lunch crew members from year 1-2 who willing suffered through the physics common rooms food with me, and to their successors who introduced me to the finer points of (University) college lunch cuisine.
I thank my collaborators around Paulina Plochocka at the LNCMI Toulouse for all of the complementary data, especially the stuff happening above 20 T. Quite a lot of interesting stuff to be had above that threshold. Of course, also thanks to all the Oxford people without whose samples and help a lot of the work in this thesis would not have been possible. Mainly Elisabeth, Jonny, Laura, and Pabitra for single crystals, thin films and perovskite growth tricks, and to Grey and Roger, who helped with spraying tubes, and „going for gold“ on the XRD. Of course also to the rest of the Snaith group, who welcomed me into their labs and clean room and on their many pub and club trips, and formal halls. I am very grateful everyone in the University College MCR, who were always to be had for a good time, and of course to its old members, who funded my DPhil through the Berman scholarship.

Thank you so much to all my old Heidelberg friends who also opted for a PhD on the isle. I do forgive you for going to the other place. No, really, I mean it! Also to the Sebastians in London: having old friends around you have known for years is an incredible comfort. You are always welcome for dinner at my place!
Für jeden Ruperten gilt natürlich dasselbe: Ohne euch würde alles weniger Spaß machen und Ihr seid mir immer willkommen!

Lastly, of course, thank you Yael. You make every single day better for me, and I cannot wait for many more to come together with you.

Contents

1 Introduction **1**

2 Theory and Background **3**
2.1 Single-Walled Carbon Nanotubes (SWNT) . . . 3
2.1.1 Crystal Structure . . . 3
Discursion on Lattice Vibrations and Phonons . . . 5
2.1.2 Electronic Band Structure . . . 9
Tight-Binding (TB) Approximation . . . 9
TB Approximation Applied to Carbon Allotropes . . . 11
Electronic Density of States (DOS) for SWNT . . . 14
Charge Transport in SWNT . . . 14
SWNT Networks . . . 15
2.1.3 Optical Properties . . . 16
Optical Properties of Carbon Nanotubes . . . 19
2.1.4 SWNT Processing and Functionalisation . . . 20
2.1.5 Synthesis . . . 21
2.2 Hybrid Metal Halide Perovskites . . . 22
2.2.1 Crystal Structure . . . 23
Influence of Cations/Anions on Properties . . . 25
Phase Transitions . . . 26
2.2.2 Electronic Properties . . . 27
Band Structure . . . 27
Influence of Spin Orbit Coupling (SOC) . . . 29
2.2.3 Optical Properties . . . 30
Excitons . . . 30
Phonons and Excitons combining to Polarons and other -ons . . . 32
Influence of Magnetic Fields . . . 34
2.3 Summary . . . 35

3 Materials, Methods and Experimental Techniques **39**
3.1 Materials and Methods . . . 39
3.1.1 Single-Walled Carbon Nanotubes . . . 39
SWNT Functionalisation . . . 39
Substrate Preparation . . . 41
Nanotube Deposition . . . 42
3.1.2 Perovskite Single Crystals and Thin films . . . 43
Single Crystal Growth . . . 43
Thin Films . . . 44
3.2 Experimental Techniques . . . 45
3.2.1 Surface and Structural Characterisation . . . 45
DekTak and Atomic Force Microscope(AFM) . . . 45
Scanning Electron Microscope . . . 46
X-Ray Diffraction (XRD) . . . 47

3.2.2 Conductivity Measurements . . . 47
3.2.3 Optical Characterisation . . . 48
Absorption Measurements . . . 48
Magneto-Optics Setup . . . 49

4 Electrodes of Functionalised Single-Walled Carbon Nanotubes (fSWNT) 53
4.1 Investigation of Different Deposition Methods . . . 54
4.1.1 Drop-Casted fSWNT Films . . . 54
4.1.2 Spin-Coated fSWNT Films . . . 57
4.1.3 Spray-Coated fSWNT Films . . . 59
4.1.4 Deposition Techniques Summary . . . 61
4.2 Doped fSWNT Films . . . 63
4.2.1 Stability . . . 66
4.3 Summary . . . 68

5 Magneto-Optical Properties of $Cs_2AgBiBr_6$ 71
5.1 Optical Response at Room Temperature . . . 72
5.2 $Cs_2AgBiBr_6$ Temperature Sweep . . . 74
5.2.1 Reflectivity (R) . . . 74
5.2.2 Photoluminescence (PL) . . . 76
PL Intensities and the Nature of the two PL Emissions . . . 79
Nature of the PL Emission Lines . . . 80
5.3 Magneto-Optical Response of $Cs_2AgBiBr_6$ . . . 82
5.3.1 Nature of the Higher Energy PL Emission Line Revisited . . . 83
5.4 Summary . . . 85

6 Nature v Nurture: For $MAPbI_3$ Nurture Wins 87
6.1 Experimental Considerations . . . 88
6.2 $MAPbI_3$ Temperature Sweep . . . 89
6.2.1 Sub-10K Reflectance Splitting . . . 90
6.2.2 Tetragonal Phase . . . 93
6.2.3 Heating to 100°C . . . 93
6.3 XRD Structure Analysis . . . 94
6.4 Nature of the A and B Peaks . . . 99
6.4.1 Estimate of the Rashba Parameter . . . 100
6.5 Conclusions . . . 101

7 Polarons in $MAPbI_3$ and $MAPbBr_3$ 103
7.1 Samples . . . 104
7.2 Field-Dependence of Transition Energies for $MAPbBr_3$ . . . 105
Fitting The Transition Energies . . . 107
7.2.1 Transition Energies for $MAPbBr_3$ . . . 108
The Mystery of the Asterisks . . . 109
7.3 Field-Dependence of Transition Energies for $MAPbI_3$ . . . 111
7.4 Differences Thin Film/Single Crystal . . . 115
7.5 Summary . . . 115

8 Summary and Outlook 117
8.1 Electrodes of Functionalised Single-Walled Carbon Nanotubes (fSWNT) . . . 117
8.2 Outlook on Magneto-Optical Properties of $Cs_2AgBiBr_6$ . . . 118

8.3 Nature v Nurture: For $MAPbI_3$ Nurture Wins 119
8.4 Polarons in $MAPbI_3$ and $MAPbBr_3$ 120

1 Introduction

Climate change is a fact of our times, and a large share of it is due to the consumption of energy. At the moment, too much of this energy is derived from non-renewable sources, which will have to be changed if we want to leave a planet to our children that may still be worth living on. For this, there are several major branches of research at the moment: research into fusion energy, and research into renewables based on wind, water, and solar irradiation. Of these, fusion energy has always been „only 30 years“ away, and wind and water based renewables are limited in the amount of energy they can create. In contrast, earth's insolation is practically untapped and sufficient to sustain humanities entire energy needs, under the caveat of sufficient energy storage or transport [1].

One enormously cheap contender to become the solution to efficient solar irradiation conversion into electricity are perovskites, which in less than 10 years went from single digit to over 24.2 % efficiency [2]. While there are many researchers in the area, many are working on the topic coming from an angle of material sciences and chemistry, where new compounds and higher efficiencies are the biggest concern. To date, this has left open some fairly fundamental questions about this class of materials, which this thesis is trying to illuminate by magneto-optical studies of this class of materials.

For solar cells based on these perovskites, transparent conductors are of great import, as interdigitated single junction devices to date only achieve low efficiencies [3], and tandems require transparent conductive interlayers based on orthogonal solvents or other benign deposition techniques. Polymer functionalised single-walled carbon nanotubes are a material with the potential to live up to this task, as they have a low absorption and high conductivity. Moreover, they are also very flexible, opening up the possibility for flexible smartphone screens that will never break and splinter. First devices like this have already been intro-

duced. The rise of this nascent technology was shown at the last mobile world congress in Barcelona in February 2019, featuring several foldable displays [4]. When flexible transparent conductive films (TCF) are combined with organic-light emitting diodes, they can even be highly transparent.

This thesis is organised as follows:

- Chapter two presents theory and background on physical properties of single walled carbon nanotubes (SWNT), and introduces hybrid organic/inorganic perovskites, their structure and properties.
- Chapter three describes the materials, methods and experimental setups used throughout this thesis to produce and characterise the samples and perovskite single crystals and thin films.
- In Chapter four the results of different deposition methods of polymer-functionalised nanotubes, and treatments of transparent SWNT thin films are presented.
- Chapter five contains the magneto-optical studies of $Cs_2AgBiBr_6$ single crystals and relates optical to structural changes under variation of temperature.
- In Chapter six the results of optical studies between 1.4 K up to 370 K on $MAPbI_3$ single crystals and thin films are examined analysing the nature of the direct and indirect gap.
- In Chapter seven magneto-optical studies of $MAPbBr_3$ and $MAPbI_3$ single crystals, and highly crystalline $MAPbBr_3$ and $MAPbI_3$ thin films are detailed and the observed lattice-exciton interaction are discussed.
- The last, the eighth chapter, presents a short summary of the thesis and an outlook.

2 Theory and Background

This chapter gives an introduction to elementary principles of condensed matter physics based on single walled carbon nanotubes (SWNT) and hybrid organic/inorganic metal halide perovskites. Thus, the main concepts and background on SWNT and perovskites will be detailed. As both are intended for application in solar cells, certain properties important to their functioning are mentioned.

2.1 Single-Walled Carbon Nanotubes (SWNT)

Single-walled carbon nanotubes (SWNT) are a 1D carbon allotrope distinct from other 3D (graphite/diamond), and 0D (fullerenes) modifications. They are related to 2D graphene by rolling up to form a tube. This section will detail physical properties of SWNT and review their unique electronic properties.

2.1.1 Crystal Structure

In the graphene 2D honeycomb lattice structure, the orbitals of the carbon atoms rearrange from the free $\underset{1s}{\downarrow\uparrow}\,\underset{2s}{\uparrow\downarrow}\,\underset{2p_x}{\uparrow}\,\underset{2p_y}{\uparrow}\,\underset{2p_z}{}$ carbon electron structure to the hybridised sp^2 orbitals $\underset{1s}{\downarrow\uparrow}\,\underset{sp^2}{\uparrow}\,\underset{sp^2}{\uparrow}\,\underset{sp^2}{\uparrow}\,\underset{2p_z}{\uparrow}$ with a 120° angle between the sp^2 orbitals and $2p_z$-orbitals orthogonal to the sp^2 plane. For the resulting graphene honeycomb lattice in Fig.2.1, the unit cell basis vectors $\mathbf{a}_1$ and $\mathbf{a}_2$ are shown on the left, along with the unit cell vectors $\mathbf{T}$ and $\mathbf{C}$ for a SWNT. The two graphene unit cell vectors also serve as the basis for the description of SWNT, by describing the unit cell vector $\mathbf{C}$,

$$\mathbf{C} = n\mathbf{a}_1 + m\mathbf{a}_2, \tag{2.1}$$

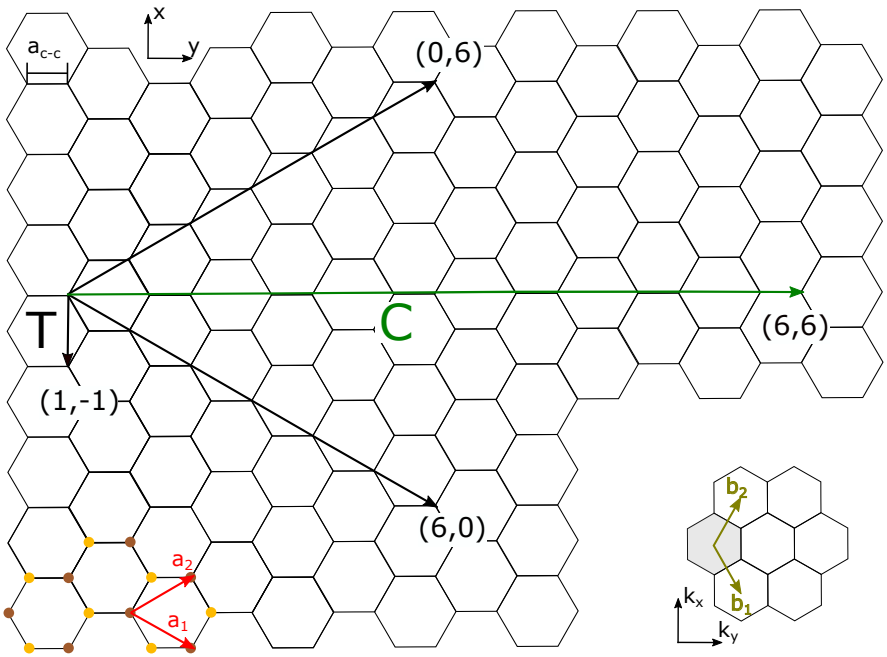


Fig. 2.1: Honeycomb lattice structure of a graphene sheet. The lattice vectors $\mathbf{a}_1$ and $\mathbf{a}_2$ of the graphene unit cell are shown on the bottom left. The yellow and brown dots give the two graphene sub-lattices. In the middle, possible roll-up axes of high symmetry are shown together with an exemplary (6,6) tube. This tube has a translational vector $\mathbf{T} = 3\mathbf{a}_1 - 3\mathbf{a}_2$ and univ cell vector $\mathbf{C} = 6\mathbf{a}_1 + 6\mathbf{a}_2$. Together, $\mathbf{T}$ and $\mathbf{C}$ describe the crystal lattice of the rolled up tube, where $\mathbf{T}$ is the axis along which the graphene sheet is cut, and is then rolled up along $\mathbf{C}$. On the lower right hand side the reciprocal lattice vectors $\mathbf{b}_1$ and $\mathbf{b}_2$ are shown.

with chiral indices n and m, that are used to uniquely characterise all tubes with (n,m). The second SWNT unit cell vector is the translational vector $\mathbf{T}$

$$\mathbf{T} = \mathbf{t}_1\mathbf{a}_1 + \mathbf{t}_2\mathbf{a}_2 = \frac{2m+n}{gcd}\mathbf{a}_1 - \frac{2n+m}{gcd}\mathbf{a}_2 \tag{2.2}$$

where gcd is the greatest common divisor of $2m+n$ and $2n+m$, which is perpendicular to $\mathbf{C}$ and fulfills $\mathbf{C}\cdot\mathbf{T} = 0$. The magnitude of circumference vector $\mathbf{C}$ then gives the diameter d_{tube} of the tube

$$d_{tube} = \frac{|\mathbf{C}|}{\pi} = \frac{a_0\sqrt{n^2+nm+m^2}}{\pi} \tag{2.3}$$

where $a_0 = 0.2461\,\text{nm} = \sqrt{3}a_{c-c}$, and a_{c-c} is the carbon-carbon bond length as shown in Fig.2.1, which for graphene is 1.42 Å [5], and in the case of SWNT ~1.44 Å, where the curvature due to the rolling up increases a_{c-c} [6].

The chiral angle ϑ describes the angle between $\mathbf{a}_2$ and $\mathbf{C}$

$$cos(\vartheta) = \frac{\mathbf{a}_2 \cdot \mathbf{C}}{|\mathbf{a}_2||\mathbf{C}|} = \frac{n + m/2}{\sqrt{n^2 + nm + m^2}}. \tag{2.4}$$

As tubes of different handedness are not distinguished, all unique tubes can be described in the range $0° < \vartheta < 30°$, implying $n \geq m \geq 0$. The resulting three cases are the zig-zag tube ($\vartheta = 0°$), the chiral tube ($0° < \vartheta < 30°$), and the armchair tube ($\vartheta = 30°$) as shown in Fig.2.2. The SWNT structure can be directly mapped using an STM, showing atomic structure and chirality [7].

In order to derive further structural properties, it is necessary to look at the reciprocal space and the Brillouin zone of the lattice. For this we need a set of reciprocal basis vectors $\mathbf{b}_i$ fulfilling $\mathbf{b}_i \cdot \mathbf{a}_i = 2\pi\delta_{ij}$. Using the Cartesian definition of the real space $\mathbf{a}_i$ of graphene

$$\mathbf{a}_1 = (\frac{\sqrt{3}}{2}, \frac{1}{2})a_0 \quad \text{and} \quad \mathbf{a}_2 = (\frac{\sqrt{3}}{2}, -\frac{1}{2})a_0, \tag{2.5}$$

the reciprocal space vectors $\mathbf{b}_i$ can be calculated to be

$$\mathbf{b}_1 = \big(\frac{1}{\sqrt{3}}, 1\big)\frac{2\pi}{a_0} \quad \text{and} \quad \mathbf{b}_2 = \big(\frac{1}{\sqrt{3}}, -1\big)\frac{2\pi}{a_0}, \tag{2.6}$$

and these reciprocal, and real space vectors are shown in Fig.2.1. For the SWNT reciprocal space vectors, the necessary criteria to fulfil are

$$\mathbf{C} \cdot \mathbf{k}_{\parallel} = \mathbf{T} \cdot \mathbf{k}_{\perp} = 2\pi \quad \text{and} \quad \mathbf{C} \cdot \mathbf{k}_{\perp} = \mathbf{T} \cdot \mathbf{k}_{\parallel} = 0, \tag{2.7}$$

where $\mathbf{k}_{\perp}$ and $\mathbf{k}_{\parallel}$ are perpendicular and parallel to the tube axis respectively. As a tube has a fixed circumference, $\mathbf{k}_{\perp}$ is quantised into distinct lines $\frac{2}{d_{tube}}j$ apart [8], where j is an integer counting over the number of hexagons $N_{hexagon}$ in the SWNT unit cell.

Discursion on Lattice Vibrations and Phonons

The lattice of a material is not static, and can undergo vibrations. An approximation thereof is a set of similar atoms in a lattice fulfilling periodic boundary conditions like $\rho(\mathbf{r} + \mathbf{R}) =$

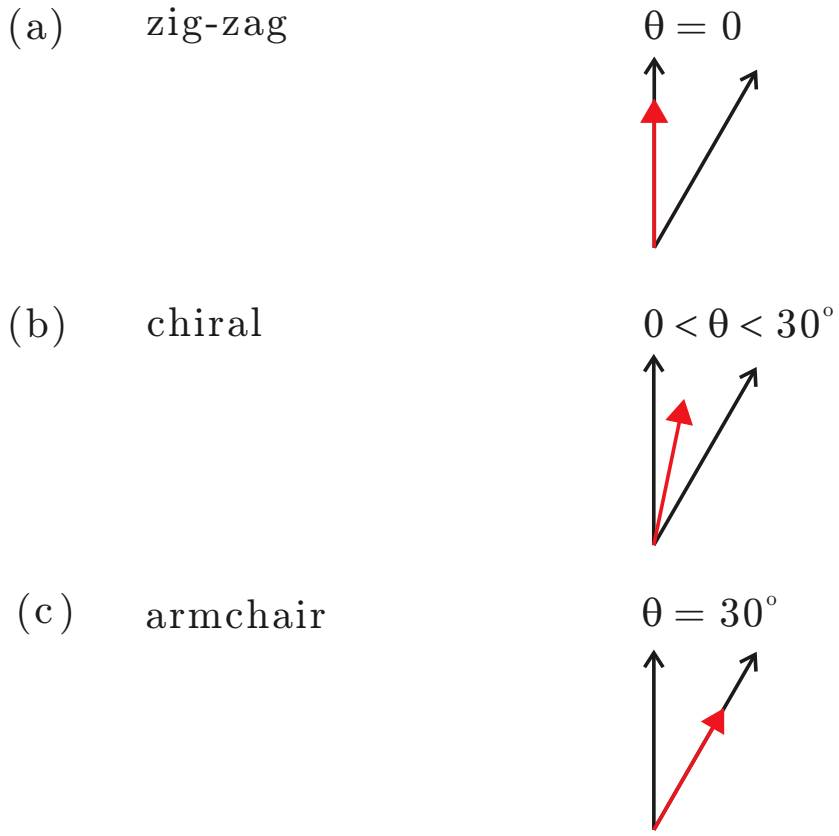


Fig. 2.2: Crystal structure of: (a) zig-zag (13,0) SWNT with $d = 1.03\,\text{nm}$, (b) chiral $(11, 3)$ tube with $d = 1.01\,\text{nm}$ and $\vartheta = 11.7°$, and (c) armchair (7,7) nanotube with $d = 0.962\,\text{nm}$.

$\rho(\mathbf{r})$. This simple $\rho(\mathbf{r})$ is an example for a single crystal, where order is given on a large scale. Such a material can be described well by assuming each atom connected to all nearest neighbours with a spring constant c following

$$m\frac{d^2u_s(\mathbf{r})}{dt^2} = \sum_n c_n(u_{s+n}(\mathbf{r}') - u_s(\mathbf{r})), \tag{2.8}$$

with atom position u_s. For the approximation of a one dimensional system, as in a SWNT, a propagating wave $u_{s+n} = Ue^{-\imath(\omega t - k(s+n)a)}$ with propagation speed ω, the distance of lattice planes a, and wavevector k, can be simplified using the symmetry of the lattice and decreasing influence of interaction over long ranges to yield

$$\omega^2 = \frac{2c_1}{m}(1 - cos(ka)) = \frac{4c_1}{m}sin^2(ka/2). \tag{2.9}$$

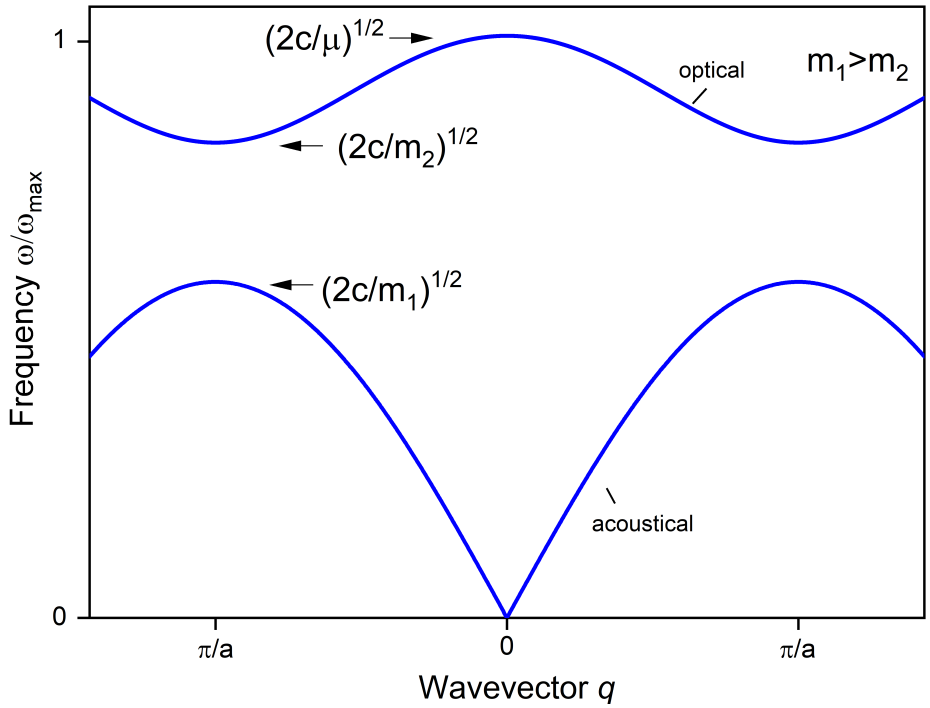


Fig. 2.3: Phonon dispersion for a two atomic crystal basis showing a split into optical and acoustical branch. Their naming refers to the frequency bands at which they occur.

These lattice vibrations ω are periodic with $2\pi/a$. The size of $2\pi/a$ gives the dimensions of the Brillouin zone, the unit cell in reciprocal space. Moving from any point to a new point by a wavevector of this length, the crystal structure will be the same as before.

For a crystal with more than one type of atoms in its basis, under the assumption of equal coupling constants c, a set of two coupled differential equations arises

$$\begin{aligned} m_1 \tfrac{d^2 u_s}{dt^2} &= c(v_s + v_{s-1} - 2u_s) \\ m_2 \tfrac{d^2 v_s}{dt^2} &= c(u_s + u_{s+1} - 2v_s) \end{aligned} \tag{2.10}$$

leading to the non-trivial lattice vibration, or phonon dispersion, solutions of

$$\omega_{a,o}^2 = \frac{c(m_1+m_2)}{m_1 m_2} \mp c\sqrt{\left(\frac{1}{m_1}+\frac{1}{m_2}\right)^2 - \frac{4}{m_1 m_2} sin^2\left(\frac{qa}{2}\right)} \tag{2.11}$$

with a and o corresponding to the negative and positive sign respectively, as displayed in Fig.2.3. Generalised for a three dimensional crystal with r atoms per unit cell, there will be three acoustic, and $3r-3$ optical branches for the phonon dispersion relations. Both branches can be excited by laser stimulation, and can give information about the system.

The acoustical branch by inelastic Brillouin scattering, the upper, optical branch by inelastic *Raman scattering*. For SWNT, Raman scattering gives a distinctive signal ω_{RBM},

$$\omega_{RBM} \propto \frac{1}{d_{tube}}, \tag{2.12}$$

the *Raman breathing mode*. The excitation of these radial vibrations allows to detect tubes of different chiral indices (n,m). There are other peaks at higher wavenumbers, where the different graphitic vibrations, G- and G'-band, and the D-band disorder vibrations can be excited.

In a more realistic model to describe lattice vibrations, the assumption of one single interaction between atoms has to be replaced with a number of valence force fields modelling stretching, bending and twisting, longer range next nearest neighbour interactions due to coulomb forces, and other influences like vacancies and defects.

Since these phonon dispersion relations describe lattice vibrations they are the basis for another interesting property, the specific heat. Summing up over all frequencies and normalising by the volume $\Theta = \left(\frac{L}{2\pi}\right)^3$, the phononic density of states $D(\omega)$ is

$$D(\omega) = \Theta \int\limits_{\omega=const} \frac{dS_q}{|\nabla_q \omega(\mathbf{q})|}, \tag{2.13}$$

integrating over the surface S_q with constant ω. For values of ω, where $\nabla_q \omega(\mathbf{q}) = 0$, there will be a so called *van Hove singularity*.

In the Debye approximation $\omega_i = v_i q$ of linear dispersion and integration over the first Brillouin zone, which in this linear case can be approximated with a sphere of volume $q_D = (6\pi^2 \frac{N}{V})^{1/3}$, the heat capacity can be approximated as

$$c_v^D = 9Nk_B\big(T/T_D\big)^3 \int\limits_0^{T_D/T} \frac{x^4 e^x dx}{(e^x - 1)^2} \tag{2.14}$$

where $x = \frac{\hbar v_s q}{k_B T}$, with the average sound velocity v_s and the Debye temperature $T_D = \frac{\hbar v_s q_D}{k_B}$. Effectively, this approximation is only valid for $T \ll T_D$, and $T \gg T_D$. Yet it does give an interesting material parameter T_D, at which all phonon modes are activated, thus describing the softness of a material.

2.1.2 Electronic Band Structure

In this section an approximation for the electronic band structure will be introduced with the tight-binding (TB) approximation, and the results thereof will be used to derive the important quantity of the electronic density of states (DOS) for SWNT.

Tight-Binding (TB) Approximation

A material's electronic properties are to a large extent dominated by its outermost electrons and orbitals. If these orbitals are almost empty, a nearly free electron description delivers a good approximation, as for metals and their delocalised electron gas. For this thesis concerned with semiconductors, the tight-binding (TB) approximation is more appropriate. In the TB approximation the electronic structure of a material is modelled under the assumption of atoms being close enough for overlapping orbitals, and electrons experiencing a strong localisation in space due to a strong, periodic potential due to the atomic cores. This ansatz works very well for semiconductors [9]. Using the periodic *Bloch-Ansatz* for the wavefunctions $\Psi(\mathbf{r})$,

$$\Psi(\mathbf{r}+\mathbf{R}) = \sum_{\mathbf{r}+\mathbf{R}} u_{\mathbf{k}} e^{\imath\mathbf{k}(\mathbf{r}+\mathbf{R})} = \Psi(\mathbf{r}) e^{\imath\mathbf{k}\mathbf{R}} \tag{2.15}$$

and as potential periodic $V(\mathbf{r})$, the sum of the screened (free) atomic potentials $V_A(\mathbf{r})$

$$V(\mathbf{r}) = V_A(\mathbf{r}-\mathbf{R}) + \sum_{\mathbf{R}'\neq\mathbf{R}} V_A(\mathbf{r}-\mathbf{R}') = V_A(\mathbf{r}-\mathbf{R}) + \widetilde{V}(\mathbf{r}-\mathbf{R}), \tag{2.16}$$

then the Hamiltonian $\mathcal{H}$ for the Schrödinger equation can be split up into a main contribution of the potential of the atom at the electrons position $\mathcal{H}_A$ and a perturbation $\widetilde{V}(\mathbf{r})$. Integration over the crystal volume with N unit cells then yields an approximated energy $E(\mathbf{k})$

$$E(\mathbf{k}) \approx \frac{1}{N} \sum_{\mathbf{R},\mathbf{R}'} e^{\imath\mathbf{k}(R-R')}(E_i - \alpha_i - \beta_i) = E_A^i - \alpha^i - \sum_{R'} \beta^i e^{\imath\mathbf{k}(\mathbf{R}-\mathbf{R}')} \tag{2.17}$$

$$\alpha^i = -\int dV \;\; u_A^{i*}(\mathbf{r}-\mathbf{R})\, \widetilde{V}(\mathbf{r})\, u_A^i(\mathbf{r}-\mathbf{R}) \tag{2.18}$$

$$\beta^i = -\int dV \;\; u_A^{i*}(\mathbf{r}-\mathbf{R}')\, \widetilde{V}(\mathbf{r}-\mathbf{R})\, u_A^i(\mathbf{r}-\mathbf{R}) \tag{2.19}$$

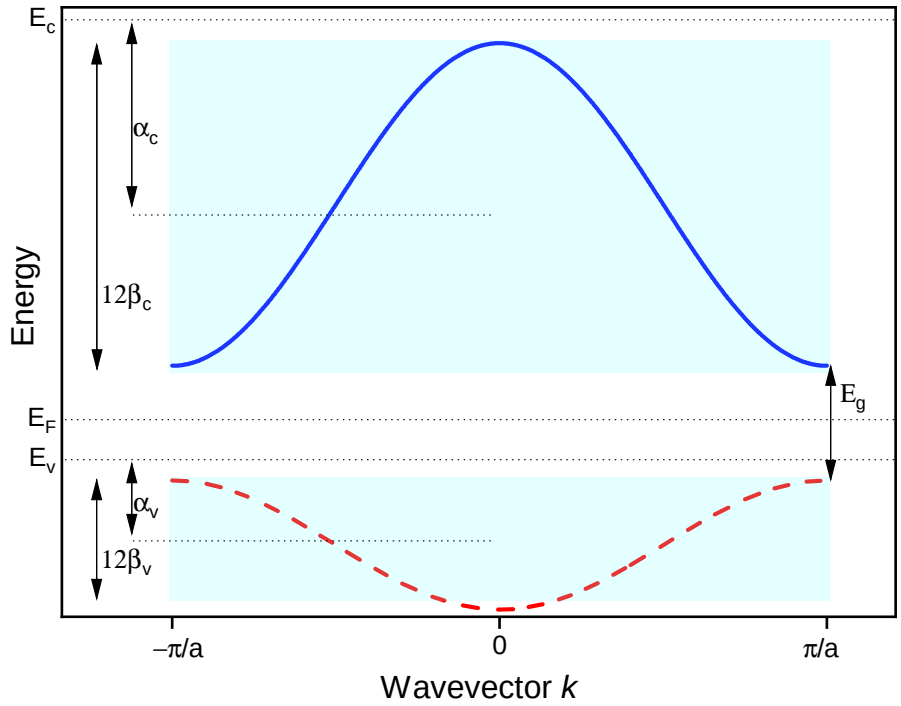


Fig. 2.4: Energy dispersion in the first Brillouin zone in a cubic crystal with 6 nearest neighbours along the $[k_x k_y k_z] = [111]$ direction, using Eq.2.17. The maximum width of the bands is $12\beta^i$, and the bandgap and Fermi energy E_F are indicated at their respective positions.

depending on the offset due to Coulomb integral α^i and free atom energy E_A^i, and the Transfer integral β^i, which measures the overlap between the orbitals of neighbouring atoms and their interaction strength. For a cubic crystal with six nearest neighbours, Eq.2.17 yields bands

$$E(\mathbf{k}) = E_i - \alpha^i - 2\beta^i \sum_i cos(\mathbf{k}_i a) \tag{2.20}$$

with a maximum width of $12\beta^i$, as displayed in Fig.2.4. The two bands shown are the valence band and conduction band, respectively the highest filled and lowest unfilled band. The indicated level of the Fermi-energy E_F gives the energy up to which bands are filled. The size of the bandgap can be influenced by implanting impurity atoms or vacancies within the crystal, causing sub-bandgap states and a resulting shift of E_F towards either conduction or valence band.

TB Approximation Applied to Carbon Allotropes

When atoms come close enough for their s- and p-orbitals to mix, they can hybridise to form mixed sp^x $(x = 1, 2, 3)$ orbitals, which lower the overall energy of the structure. Classic examples for this hybridisation are different carbon allotropes forming diamonds (sp^3) or carbon nanotubes (sp^2). The hybridised sp^2 orbitals in graphene form strongly localised

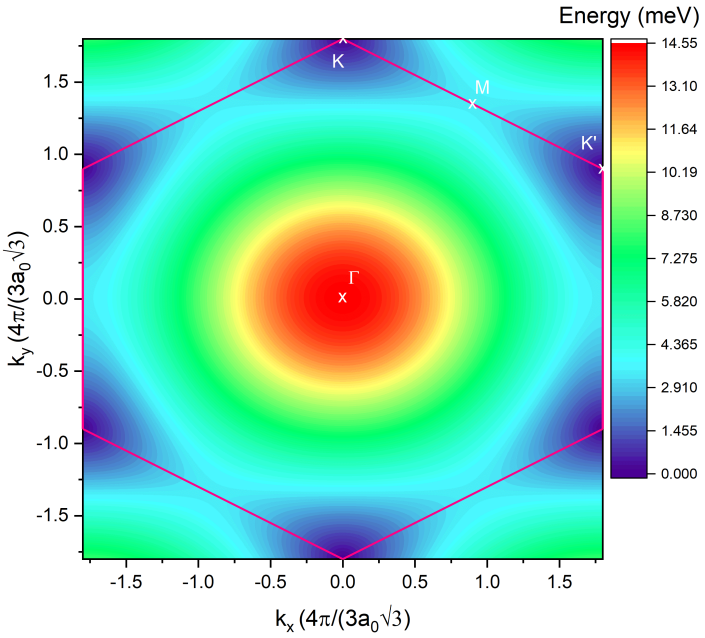


Fig. 2.5: Contour plot of the electron energy dispersion along the E^+-band in graphene using the tight binding approximation in Eq.2.21. For the parameters ϵ_{p_z}, β, and α the values 0 eV, 3 eV, and 129 meV were used respectively. Included are the Brillouin zone (magenta), and some of the special points of symmetry, denoted by white crosses. At the K and K' points, the π-bonding and π^*-anti-bonding orbitals (E_{gr}^- and E_{gr}^+ respectively) have their crossover, causing the metallic character of graphene. The energies here are given with respect to the Fermi energy E_F [10].

covalent σ-bonds between the carbon atoms. In contrast, the π (bonding) and π^* (anti-bonding) orbitals formed from the combination of the weakly bound $2p_z$-orbitals electrons are orthogonal to the graphene plane and can be treated as independent from the σ-bonds. Thus they form the electronic bands of graphene [8]. For graphene, the energy can be derived to be

$$E_{gr}^{\pm}(\mathbf{k}) = \frac{\epsilon_{p_z} \pm \beta\sqrt{f(\mathbf{k})}}{1 \mp \alpha\sqrt{f(\mathbf{k})}}, \tag{2.21}$$

with $\mathbf{k}$, and ϵ_{p_z} the wavevector and the energy of the p_z electron orbitals, and

$$f(\mathbf{k}) = 3 + 2\sum_{i=1}^{2} cos(\mathbf{k}\cdot\mathbf{a}_i) + 2cos(\mathbf{k}\cdot(\mathbf{a}_1 - \mathbf{a}_2)), \tag{2.22}$$

resulting in an energy-scape as shown in Fig.2.5. E_{gr}^{+} corresponds to the conduction- and E_{gr}^{-} to the valence-band of the crystal. Since each carbon atom contributes only one p_z electron, the valence band is full, leaving the conduction band empty. Both bands touch at the so-called Dirac points, where Eq.2.22 is equal to zero, making it a zero gap semiconductor and giving the crystal a metallic nature.

To derive the energy bands of SWNT, $E_{gr}^{\pm}(\mathbf{k})$ has to be modified with the zone-folding approximation to account for the curvature of rolling up graphene. For this, the graphene Brillouin-zone is overlaid with the discrete $\mathbf{k}_\perp$ mentioned in the last section. For an infinitely long SWNT, which is a good approximation considering the very large aspect ratio of carbon nanotubes [11], the Brillouin-zone is one dimensional and their energies are given by

$$E_{SWNT}^{\pm}(j, \mathbf{k}_\parallel) = E_{gr}^{\pm}(\mathbf{k})\big(j\mathbf{k}_\perp + k_\parallel \frac{\mathbf{k}_\parallel}{|\mathbf{k}_\parallel|}\big) \tag{2.23}$$

where

$$\mathbf{k}_\parallel + \frac{2\pi}{\mathbf{T}} = \mathbf{k}_\parallel \quad \text{and} \quad j = 0, 1, ..., (N_{hexagon} - 1). \tag{2.24}$$

The alignment of the discrete $k_\perp$ depends on the tube geometry, and all tubes where one such $k_\perp$-line crosses the K point have a metallic nature. The necessary criterion to fulfil this is that $\aleph$, the shortest distance between the line spanned by $\mathbf{k}_\perp$ and the K-point is a multiple of $\mathbf{k}_\parallel$

$$\begin{aligned} &\aleph = \tfrac{2n+m}{3}\mathbf{k}_\parallel \quad \text{or} \quad \mathbf{K}\cdot\mathbf{k}_\perp = \tfrac{2\pi}{3}(n-m) \\ &\text{implying:} \quad (n-m)\text{mod}3 = 0 \end{aligned} \tag{2.25}$$

where $\mathbf{K}$ is the vector to the K-point. Thus, the criterion for metallic SWNT behaviour can be rewritten to $(n-m)\text{mod}3 = 0$ [12, 13].

All single-walled carbon nanotubes are thus classified by their chiral indices (n,m). The three possible cases $(n-m)\text{mod}3 = q$ are all shown in Fig.2.6. The different positioning of the lines

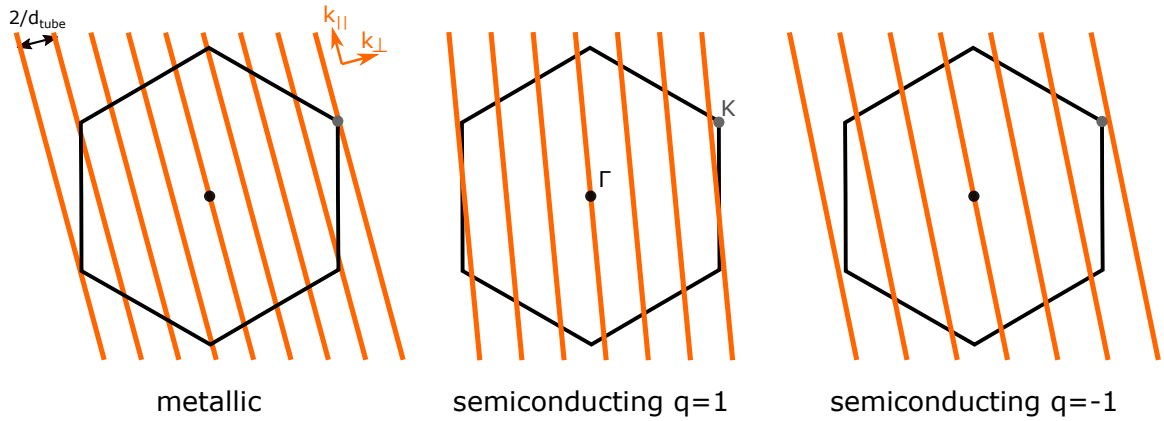


Fig. 2.6: Brillouin zone for tubes with $(n-m)\text{mod}3 = q$, where q can be 0 (metallic) or ± 1 (semiconducting), describing the three possible electronic configurations of SWNT. The orange parallels of constant $k_\perp$ are each $2/d_{tube}$ apart. Special crystal symmetry points Γ and K are indicated by black and grey dots respectively.

of constant $k_\perp$ leads to an interesting property of the tubes, where different q-tubes behave differently under strain, showing an increase ($q = -1$) or decrease ($q = 1$) of the bandgap. The size of the bandgap is determined by the two $\mathbf{k}_\perp$ lines closest to the K-point. Using the approximation of expanding to $|\mathbf{k} - \mathbf{K}|$ for the SWNT energies in Eq.2.23, the band energies close to the Fermi level for a semiconducting SWNT become

$$E^{\pm}(\mathbf{k}) \approx \pm \frac{\sqrt{3}}{2} a_0 \beta |\mathbf{k} - \mathbf{K}|. \tag{2.26}$$

For metallic tubes, as the distance from $\mathbf{k}$ to the K-point $\mathbf{K}$ is zero, the energy dispersion is linear, whereas for semiconducting tubes it will be quadratic, as

$$|\mathbf{k} - \mathbf{K}| = \sqrt{\Delta k_\perp^2 + \Delta k_\parallel^2} \tag{2.27}$$

is continuous in $k_\parallel$ and the $k_\perp$ component follows the quantisation

$$\Delta k_\perp = \frac{2}{3 d_{tube}} |3j - q|, \tag{2.28}$$

with q defined as following from Eq.2.25, and j, the band number, takes integer values. The bandgap of a semiconducting SWNT in this approximation is given by

$$E_g^{SWNT}(n,m) \approx E^+ - E^- = \frac{2 a_0 \beta}{\sqrt{3} d_{tube}}, \tag{2.29}$$

where larger tubes have a smaller bandgap as d_{tube} scales with (n,m).

Electronic Density of States (DOS) for SWNT

The universal electronic density of states (DOS) for a SWNT is given by

$$n(E) = \frac{2}{N_{hexagon}|k_\parallel|} \sum_i \int dk_\parallel \delta(k_\parallel - k_i) \left| \frac{\partial E^\pm(k_\perp, k_\parallel)}{\partial k_\parallel} \right|^{-1} \tag{2.30}$$

as derived by White *et al.* [14]. The SWNT energy approximation from Eq.2.26 can be used to derive an expression for the DOS, giving an approximation of

$$n(E) = \frac{4a_0}{\pi^2 \beta d_{tube}} \sum_{j=-\infty}^{\infty} g(E, E_j), \quad g(E, E_\nu) = \begin{cases} \frac{|E|}{\sqrt{E^2 - E_j^2}} & |E| > |E_j| \\ 0 & |E| < |E_j|. \end{cases} \tag{2.31}$$

where

$$E_j = \frac{a_0 \beta}{\sqrt{3} d_{tube}} |3j - q|. \tag{2.32}$$

For $E \to E_j$, the DOS $n(E)$ diverges in a *van Hove* singularity, which occurs at $j = 0, 3, 6, ...$ for metallic tubes, and $j = 1, 2, 4, 5...$ for semiconducting tubes. The resulting DOS for a (8,8) and (8,0) SWNT are shown in Fig.2.7, with the dominant optical transitions E_{ii} given. For a more accurate description of the energy bands and the DOS, particularly of small chiral angles, additional corrections like *trigonal warping* have to be taken into consideration, and the interested reader is referred to literature [15–18].

Charge Transport in SWNT

In regular materials, charge transport is well modelled by the *Drude model* approximation of charge carrier motion under the influence of an electric field, attenuated by collisions happening on a timescale τ

$$\frac{d}{dt}\mathbf{p} = q\mathbf{E} - \mathbf{p}/\tau, \tag{2.33}$$

with the two dominant contributions to τ being defects and phonons [11]. As SWNT are highly perfect in their crystal structure [19], scattering from defects is quite small. Correspondingly, individual tubes can achieve high conductivities [20] of up to $200\,000\,\mathrm{S\,cm^{-1}}$ with

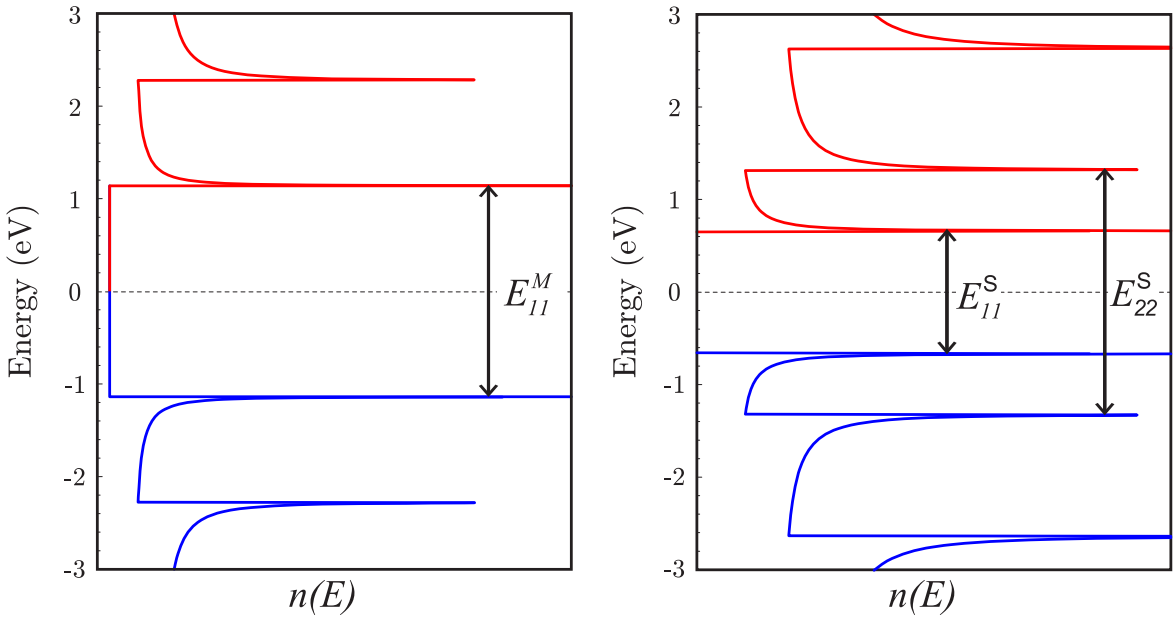


Fig. 2.7: Density of states for a metallic (8,8) tube (left) and a semiconducting (8,0) tube (right). The different states corresponding to conduction (blue) and valence bands (red) are shown along with the dominant optical transitions E_{ij}. At $E_F = 0\,\mathrm{eV}$, the metallic tube has a non-zero DOS, whereas the semiconducting tube's DOS is zero.

a mean free path approaching 4 µm in metallic tubes, and several hundred nanometres in semiconducting tubes [21–23]. As a result, field effect transistors (FET) featuring carbon nanotubes (CNT) have shown values close to the maximum quantum conductance [24] of

$$2G_0 = \frac{4e^2}{h} \approx 155\,\mu\mathrm{S}, \tag{2.34}$$

where even FETs made of an SWNT array achieved up to 0.46 G_0 per tube [20] and high mobilities around $100\,000\,\mathrm{cm^2\,V^{-1}\,s^{-1}}$ [25].

SWNT Networks

For random networks of carbon nanotubes, conductivities are much lower at about $66\,\mathrm{S\,cm^{-1}}$ [26, 27], and mobilities decreasing to around 10-20 $\mathrm{cm^2\,V^{-1}\,s^{-1}}$ [28].

There are several reasons for this drop in conductivity. CNT networks need to reach the critical percolation threshold, at which all SWNT are in contact with at least one other tube and thus with the entire network. Thereafter, the conductivity σ will roughly scale with

$$\sigma \propto (N - N_c)^{1.5} \tag{2.35}$$

with N, and N_c the tube/bundle density, and percolation threshold density [29]. For randomly oriented SWNT, the necessary surface coverage for reaching the percolation threshold can be as low as 1 % under ideal conditions [30, 31]. After contact is ensured, the type of contact between tubes matters, as the hopping conduction between tubes [30, 32–34] has a higher probability to take place for tubes with a small contact angle between them [35]. Networks with longer tubes, or longer tube bundles, are therefore highly desirable to ensure good conductivity [36, 37]. Individual, well-dispersed tubes are superior to bundles, as only the outermost tubes will contribute to the charge conduction [38]. Similarly, multi-walled carbon nanotubes are inferior to SWNT for transparent conductive thin films [38–40].

The tube diameter has an influence on the conductivity of the networks, as larger diameter tubes have smaller bandgaps following from Eq.2.29, leading to a higher amount of charge carriers that are thermally activated and can contribute as mobile carriers. The electronic nature of the tubes also matters as metallic and semiconducting tubes will form unfavourable *Schottky barriers* that charge carriers will have to overcome [41, 42]. A possibility to reduce the *Schottky barrier* is doping of the semiconducting tubes with a reducing agent like nitric acid (HNO_3) as the resulting shift of the Fermi energy towards the valence band p-type dopes the SWNT and changes the contact to an Ohmic one [43]. The resulting improvement in conductivity can be up to a factor of three [35], and also lowers the tube's absorption.

2.1.3 Optical Properties

When a photon impinges on a crystal, it will either be reflected at the surface or will be transmitted. In the latter case, the photon can be absorbed by exciting electrons from valence to conduction bands, if it has sufficient energy, or it will pass through the crystal undergoing some scattering processes. The electrons excited to the conduction band will

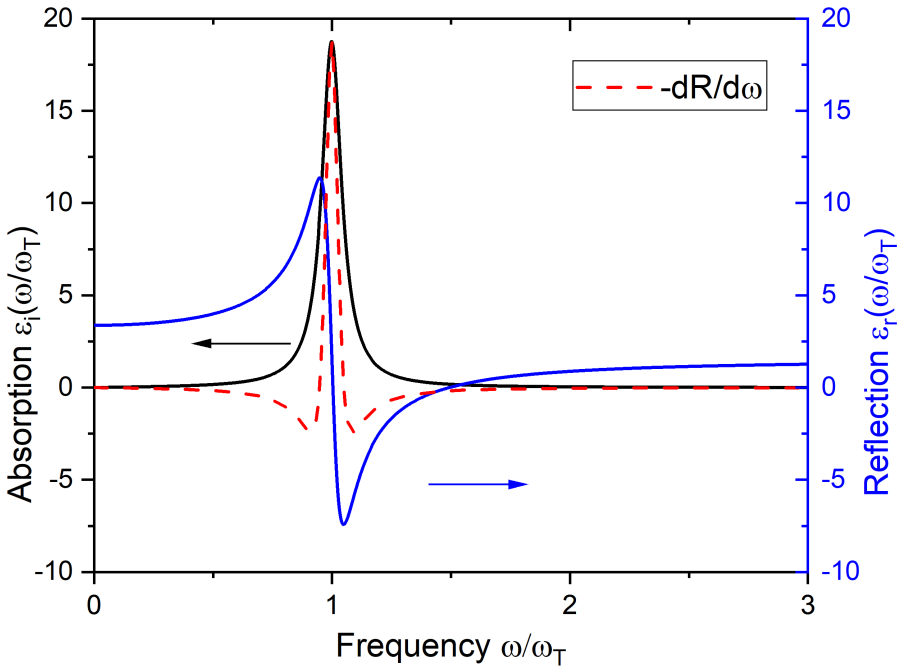


Fig. 2.8: An example of the application of the Kramers-Kronig relations from Eq.2.37, with the absorption (blue) and reflectivity (black, solid). The calculated absorption approximation (red, dashes) curve $-\frac{dR}{dE}$ showcases the validity of approximating the absorption through the energy derivative of the reflectivity.

eventually relax to their ground state in the valence band, and the timescale and photon energy of the process informs about the structure and defects of the crystal.

Absorption and reflectivity of a semiconductor single crystal are determined by the dielectric function ϵ_{ij}, which measures the response to stimulation with an external electrical field $E(\mathbf{q}, t)$.

$$D_i(\mathbf{q}, \omega) = \epsilon_0 \epsilon_{ij}(\omega) \cdot E_j(\mathbf{q}, \omega) \tag{2.36}$$

$D_i(\mathbf{q}, \omega)$ and consequently $\epsilon_i(\omega)$ are complex, with the real part corresponding to reflectivity, the imaginary component to the absorption of the crystal. Since ϵ has a real and imaginary component and describes an analytical, physical system, the Hilbert transformation or *Kramers-Kronig relations* can be used, relating two equations by using a contour integral in the upper plane

$$\begin{aligned} \chi_i &= \frac{\mathcal{P}}{\pi} \int_{-\infty}^{\infty} \frac{\chi_r(\omega')}{\omega' - \omega} d\omega' \\ \chi_r &= -\frac{\mathcal{P}}{\pi} \int_{-\infty}^{\infty} \frac{\chi_i(\omega')}{\omega' - \omega} d\omega', \end{aligned} \tag{2.37}$$

with some normalisation constant $\mathcal{P}$. Given these relations, it is sufficient to know either ϵ_r or ϵ_i to calculate the other [44].

For thick samples, where absorption and scattering are too strong to allow for transmission measurements to determine the bandgap accurately, this integral allows the determination of the absorption from the reflectivity. An example of these relations can be seen in Fig.2.8. For the case of insufficient data, where ϵ_r/ϵ_i are not known everywhere/precisely, a very good approximation for the spectral transmission can be made with the energy derivative $-\frac{dR}{dE}$ of the reflectivity R, as a local approximation of equations 2.37.

Using the Ansatz of a driven harmonic oscillator, the stationary solution can be used to describe the polarisability $\alpha(\omega)$, allowing for $\epsilon(\omega)$ to be rewritten to

$$\epsilon(\omega) = 1 + \chi(\omega) = 1 + n_V\alpha(\omega) = 1 + \frac{n_V e^2}{\epsilon_0 m}\frac{1}{(\omega_0^2 - \omega^2) - \imath\Gamma\omega} \tag{2.38}$$

with the atomic density n_V, and broadening parameter Γ. For the reflectivity, only the real part is needed, and in a real world application simplifies to

$$R(E) = r_0 + \sum_j A_j \frac{E_j^2 - E^2}{(E^2 - E_j^2)^2 + \Gamma_j^2} \tag{2.39}$$

with r_0, A_j and Γ_j the background, amplitude and broadening of the corresponding resonance j.

Photoluminescence (PL) emission is a recombination process of electrons from the conduction band and holes from the valence band under emission of a photon. At low enough temperatures, they can form the bound quasi-particle of an exciton, which has an excitation spectrum like a hydrogen atom but consists of a hole and electron and will be detailed further in section 2.2.3. Similar to reflectivity R, PL as in Fig.2.9 shows a certain broadening to a finite width following the quantum mechanical uncertainty principle [45]. Where the PL widening is directly related to the thermal energy k_BT of the crystal and charge carriers, for the reflectivity the widening is dominated by phonons, in general leading to much narrower, more well defined peaks. Effectively, this limits the possible accuracy of experiments to determine

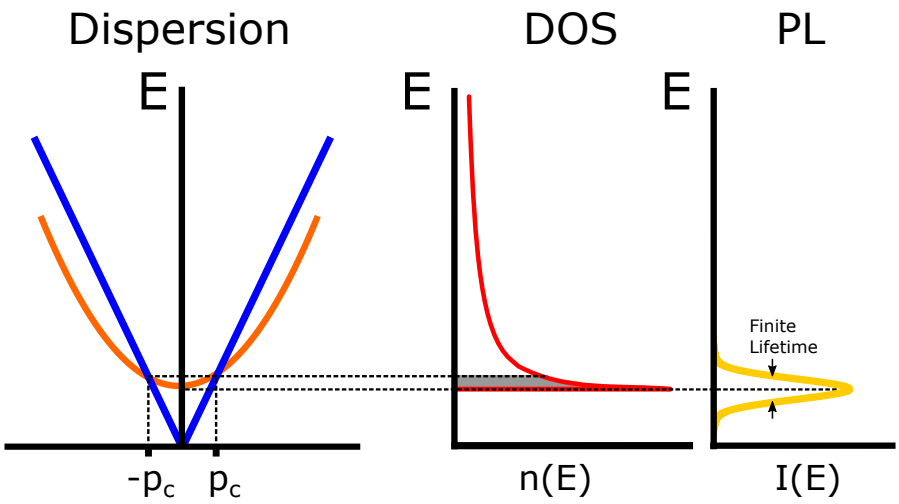


Fig. 2.9: An exciton or free carrier recombination can only take place if its energy is within the light cone (blue) in its energy dispersion (orange) due to energy conservation. The states fulfilling this criterion are marked in the DOS (red), and result in a finite lifetime ($\Delta E \Delta t \geq 1/2$) and PL width (yellow). Adapted from Christopher *et al.* [45] under the CC BY 4.0

a precise bandgap from PL (and R), especially for the case of a finite *Stokes shift* and the associated vibrational states [9, 44].

Optical Properties of Carbon Nanotubes

The optical properties of carbon nanotubes are governed by their DOS, where the main transitions E_{ii}, transitions from conduction band energy E_i to valence band E_i[1], are excited by light parallel to the tube axis. In this process, electrons hole pairs (excitons) relax to the band edges near the van Hove singularities, and then recombine under emission of a photon. This allows for a facile method for characterisation of tube species composition by identification through photoluminescence excitation (PLE) mapping as shown in Fig.2.10. Excitons excited at E_{22} energies will relax non-radiatively to smaller E_{11}, and then recombine radiatively at this energy [47]. The resulting characteristic tuple of energies allows the determination of tube chirality (n,m). For the case of large SWNT bundles containing metallic tubes, the PL is quenched almost completely, as the metallic tubes will serve as non-radiative recombination centres. Purely semiconducting bundles can also lead to non-radiative recombination through exciton energy transfer (EET) [48].

[1] In fact, a small amount of cross-polarised E_{ij} ($i \neq j$) transitions can be observed under very specific polarising conditions [46] for light perpendicular to the tube axis.

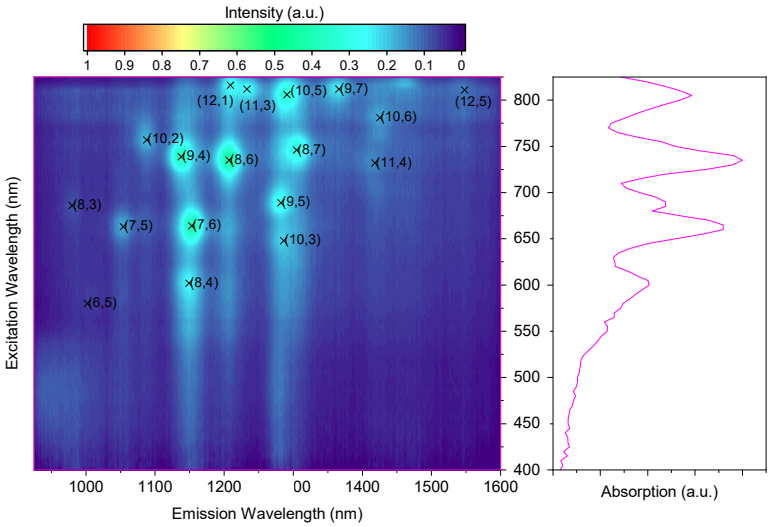


Fig. 2.10: Left: For photoluminescence excitation (PLE) maps the high energy E_{22} transitions are excited. After relaxing to the E_{11} energies, recombination processes emit photons of energies E_{11}, which tend to be in the IR wavelength range. Black crosses identify the position of the emission peak of tube species (n,m), as identified with the energies from the dataset by Weisman *et al.* [49]. Right: E_{22} absorption spectrum of the same SWNT sample.

As can be seen in Fig.2.10, many species' E_{11} and E_{22} energies are almost identical. So absorption, unless of a single chirality sample, will always show broad absorption peaks consisting of several overlapping individual tube peaks. Bundled up tubes contribute to the PL width also through EET, by allowing the exciton to relax to more favourable valence or conduction bands in tubes close by, and thereby changing the energy of eventually emitted photons.

The absolute strength of the absorption in SWNT is governed by their relation to graphene, and is limited to at maximum of $\pi\alpha = 2.3\,\%$ of the incident light [50], which has its origin in the electronic nature of graphene (and SWNT) [51].

2.1.4 SWNT Processing and Functionalisation

Carbon nanotubes experience a very large attractive force to other tubes due to their outwards-facing π orbitals, which translate into a large *van der Waals* attraction. Thus, the natural state of CNT is a large, hydrophobic bundle of tubes, strongly attached to each other. Only few solvents and liquids (among others: N-Methyl-2-pyrrolidone [8], super acids like chlorosulfonic acid [52], and o-dichlorobenzene [8]) are able to dissolve SWNT, but only in small amounts.

For a long time, research into SWNT was challenged by this inability to debundle tubes non-covalently, without changing the intrinsic properties of SWNT. Eventually, a group of surfactants [53], and DNA functionalisation [54] were discovered in 2002, allowing for some degree of separability of tubes through centrifugation. Shortly after, Nish *et al.* [55] discovered the first method able to selectively focus on semiconducting tubes and even individual species of semiconducting tubes, by functionalisation with semiconducting polymers like the polyfluorene PFO family. Additionally, polymer functionalisation of SWNT also greatly reduces the amount of amorphous carbon [56]. As the non-covalent π-π stacking between polymer and tube is quite effective, polymer functionalisation offers a good method to debundle tubes and by controlling polymer side chains also allows for control of solubility. Thus, polymer functionalisation is able to produce purely semiconducting, well dispersed, and monochiral tubes of up to 99.98 % [57, 58] purity, with only minute modifications of intrinsic tube properties by influencing their dielectric constant [59], allowing to shift the tubes towards slightly p- or n-type behaviour [60, 61].

2.1.5 Synthesis

SWNT as first described in detail by S.Iijima and T.Ichihashi [62] in 1993 were grown by the arc-discharge evaporation method, where two carbon electrodes are inserted into a helium filled chamber, and a large DC voltage induces multi-walled CNT growth on the cathode. In order to obtain mainly SWNT, a catalyst like iron or cobalt has to be added to the graphitic anode, but there will still be multi-walled nano tubes (MWNT), several concentric SWNT inside of each other [63], contamination and precipitation of fullerenes on the chamber walls [64]. The average tube length can be controlled by the growth time, where <1 min results in tubes of several hundred nm [33].

A more common method, as it produces less than 0.5 % MWNT, is the high pressure carbon monoxide (HIPco) method, capable of producing on a kilogram-per-day scale [8]. Carbon monoxide (CO) is heated up to 1000 °C and pressurised to 30 bar together with a catalyst metallocene or metal carbonyl gas. These volatile catalysts decompose, and release their metal. The metal then serves as a growth nucleus for the carbon coming from the precursor CO gas. Tubes of mainly intermediate diameters are formed [65].

The last common method for producing SWNT is the chemical vapour deposition (CVD), also called CoMoCAT (Cobalt Molybdenum oxide CATalyst) method, which allows for large scale growth of SWNT with some control of the grown diameters and species of tubes, depending on catalyst Co:MO_3 ratio [66], flow rate of precursor CO gas and temperature, where lower temperatures favour smaller diameters [67, 68]. With imaging methods, it can be shown that the evaporated Fe/Co metals serve as the nucleation core for the SWNT, which is described in detail in literature, e.g. [69]. To date, CVD is the only known scaleable method to produce purely metallic tubes, for example (6,6) tubes [70]. In the interest of high conductivity, very long high diameter tubes, as made possible by arc-discharge and CVD, are preferable as conductivity of SWNT network thin films scales roughly as $\sigma \approx L^{1.46}$ with average tube/tube bundle length [36].

After growth, SWNT still contain catalytic metal, amorphous carbon and other impurities, and need to undergo purification by thermal oxidation, oxidative acid treatments, chemical functionalisation, filtration and other methods, in order to separate SWNT from undesired by-products of growth [64, 71].

2.2 Hybrid Metal Halide Perovskites

The perovskite crystal structure has been known since 1839 [72], and is a material class of particular interest to physicists and the material sciences, as almost any material property of interest can be found in them like high T_c superconductivity [73], ferroelectricity [74], non-linearity [75], and of course favourable bandgaps for semiconductors [76].

Over the last few years, a specific subgroup of organic inorganic metal-halide perovskites has garnered wide attention after it was shown that these materials can easily surpass most other new solar cell materials in terms of efficiency [2, 77]. In this section, some of the theoretical concepts necessary for the understanding of this material class will be introduced and applied to understand some of its properties, most of them, without loss of generality, using the example of $MAPbI_3$.

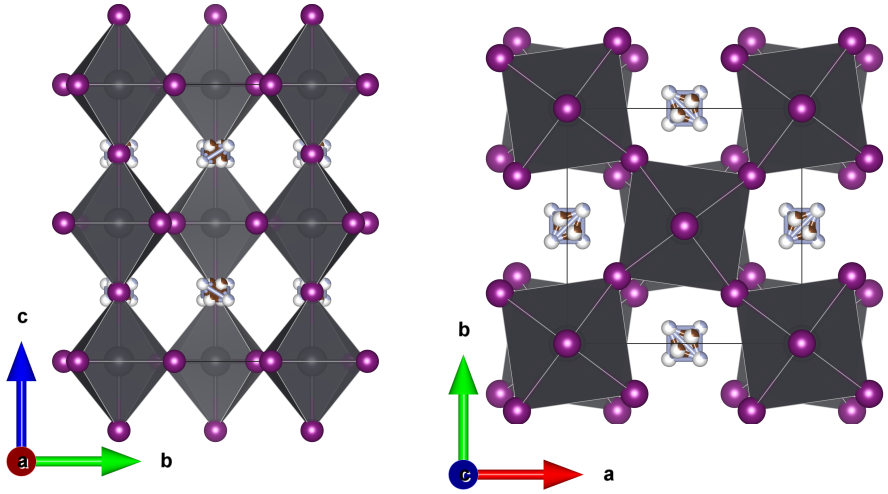


Fig. 2.11: Crystal structure of an ABX_3 perovskite compound, using the example of tetragonal $MAPbI_3$. Iodine (X) displayed in purple, lead (B) at the centre of the oxtahedra in grey, and the MA-ions with nitrogen in brown and carbon in white. The crystallographic axes are given by the tripod arrows for both orientations respectively. A double perovskite $A_2B^IB^{III}X_6$ is identical to this, but the octahedra will be filled checker board style alternating with B^I and B^{III} atoms.

2.2.1 Crystal Structure

The crystal structure of all perovskites compounds follows the ABX_3 unit cell formula with two cations A^{1+} and B^{2+}, and three anions X^{3-}. The B- and X-site moieties form BX_6 octahedra with B at its centre, and the A species fill up the remaining gaps between the octahedra as shown in Fig.2.11.

The compounds focussed on in this thesis consist of A = (caesium (Cs), methylammonium (MA, CH_3NH_3)), B = (lead (Pb), silver and bismuth (AgBi)) and a halide X=(bromine (Br), iodine (I)), with many other combinations possible consisting of A, B and X, and double perovskites $AB^IB^{III}X_6$, where B^I is 1+ and B^{III} is 3+ [76–85]. The high mass of these constituent atoms and the susceptibility to octahedral rotation and tilting lead to soft phonon modes, soft crystals and strong electron phonon coupling [86].

Despite many possible combinations of ABX_3 only those compounds fulfilling the Goldschmidt tolerance equation [87]

$$t = \frac{r_X + r_A}{\sqrt{2}(r_X + r_B)}, \tag{2.40}$$

with $t \in [0.9, 1]$ will form the cubic perovskite structure, depending on the ion radii r_i. If $t \in [0.7, 0.9]$, the perovskite will deviate from the ideal cubic structure and the symmetry will

Table 2.1: Crystal space groups for some perovskite structures as stated in literature ($Cs_2AgBiBr_6$ [78, 91], $MAPbI_3$ [92–99], $MAPbBr_3$ [100, 101]):

	Cubic	Tetragonal	Orthorhombic
$Cs_2AgBiBr_6$	$Fm\bar{3}m$	$I^4/_m$	
$MAPbI_3$	$Pm\bar{3}m$	$I^4/_mcm$ or I4cm	Pnma
$MAPbBr_3$	Pm3m	$I^4/_mcm$	Pnma

be lowered to hexagonal, tetragonal, orthorhombic, or rhombohedral [88]. For perovskites with organic moieties, this paradigm is not fully applicable, as it neglects the hydrogen bonds arising from the organic molecules [89].

For best-performing devices, it is quite common to create blends of different A-site cations and X-anions, like $(FA_{83}\ MA_{17})Pb(Br_{17}\ I_{83})_3$, which enhances stability and performance of the devices [90]. Simulations by Ghosh *et al.* predict, that the enhanced performance and stability is due to strain on the crystal locking the octahedra and A-site cations in place.

As many precursor salts like PbI already have a favourable structure very close to the perovskite octahedra, crystal formation can be induced after facile deposition from solution and solvent evaporation[2] at low temperatures.

The exact space groups for the perovskites studied here are well known, as shown in Table 2.1. Yet, for the $MAPbI_3$ tetragonal phase, this is still a debated topic, as two very similar space groups are a possibility; one of which is polar and non-centrosymmetric (I4cm), the other is non-polar and centrosymmetric ($I^4/_mcm$). These two are not discernable by XRD or neutron scattering because of the very small difference between them, and an additional parameter for the fitting model I4cm. This has often lead to contradicting reports, even from within same research groups. It has to be noted, it is likely some of the reports on the I4cm crystal structure came from groups not well versed in x-ray diffraction (XRD) and interpretation of data thereof, and the other reports of I4cm are indirect, by showing crystal properties that only a non-centrosymmetric crystal structure could show, like second harmonic generation (SHG).

Defect densities in perovskites thin films tend to be orders of magnitude larger than for solar cell grade silicon [102–104], yet can reach low levels approaching those of silicon for perovskite

[2] There are also other deposition methods like evaporation, sequential deposition from solution, and others.

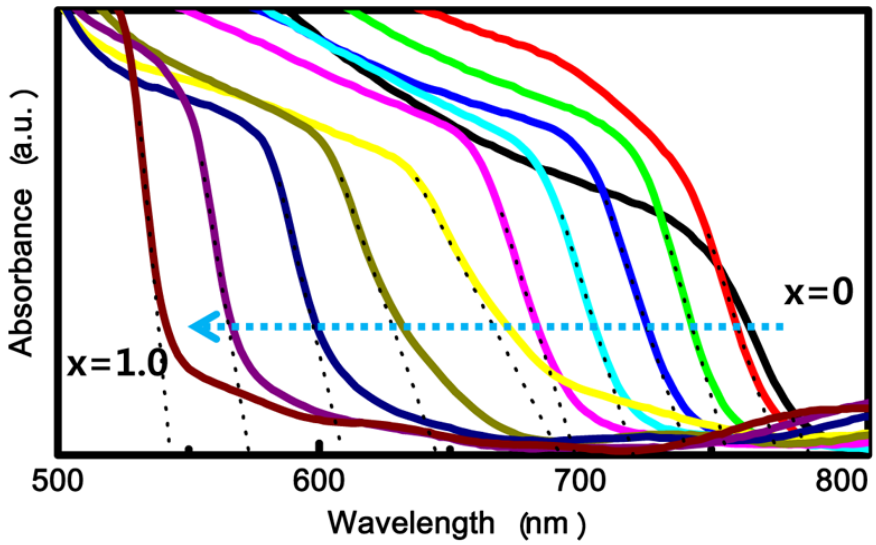


Fig. 2.12: Change of bandgap under gradual variation from $MAPbBr_3$ over $MAPb(I_xBr_{1-x})_3$ to $MAPbI_3$ as tracked by UV-vis absorption measurement using an integrating sphere. Reprinted with permission from Noh *et al.* [106], Nano Letters 2015, 13, 1764-1769. Copyright 2013 American Chemical Society.

single crystals [105]. These defects can act as colour centres and already at very low densities can reach a high luminosity[9], like for $Cs_2AgBiBr_6$ [78].

Influence of Cations/Anions on Properties

For the application as solar cell absorber or LED emitter, the size of the bandgap is crucial. The most desirable solar cell bandgap is at 1.34 eV according to the *Shockley–Queisser Limit* [107], and for the LED emitters the colours green (ca 2.3 eV), blue (ca 2.7 eV) and red (about 2 eV) are needed to cover the entire spectrum of the CIE colour space [108]. The different $MAPbX_3$ (X=I,Br,Cl) can be tuned in this range and beyond. An example of this is shown in Fig.2.12, where the bandgap increases from about from 1.55 eV for $MAPbI_3$ with an increasing share of bromine in the crystal structure to 2.3 eV for pure $MAPbBr_3$, and chloride results in even higher bandgaps of up to 3.1 eV [109]. This cation mixing is limited to a certain extent by a miscibility gap, after which separate $MAPbBr_3$ and $MAPbI_3$ phases crystallise [110, 111].

Similarly, the bandgap can be tuned by exchanging B, as the bandgap is mainly controlled by the B and X atom orbitals [112], which will be further detailed in section 2.2.2.

Table 2.2: Crystal structure phase change temperatures for different perovskite compounds. Data from literature [78, 121].

	Cubic	Tetragonal	Orthorhombic
$Cs_2AgBiBr_6$	>122 K	<122 K	
$MAPbI_3$	>327 K	327 K - 155 K	<155 K
$MAPbBr_3$	>236 K	236 K - 148 K	<148 K

The A moiety has a small, indirect influence on the bandgap, by changing the spacing and tilting of the octahedra, and by inducing deformations [113, 114]. The inorganic A site anion caesium in $CsPbI_3$ has a bandgap of 1.7 eV [115] with an tolerance factor $t = 0.85$. The large organic molecule MA has a dipole moment of about 2.3 D [116] and is capable of forming hydrogen bonds. The indirect influence on the bandgap can thus be understood as a reorientation induced fluctuation and forcing apart of the octahedra [117]. The even larger molecule formamidinium (FA, $CH(NH_2)_2$), capable of more hydrogen bonds, lowers the bandgap in comparison to $MAPbI_3$ by 150 meV by tilting the octahedra and thus increasing the influence of Pb and its spin orbit coupling on the conduction band [118].

Phase Transitions

At high temperatures the perovskites studied for this thesis are all in the cubic phase, and at lower temperatures undergo a gradual [92] rotation and tilting of the octahedra, which induces a phase change [78, 119]. As a consequence thereof, symmetry in these crystals is lowered and the bandgap changes. Depending on the crystal structure and composition, these phase changes happen at different temperatures as shown in Table 2.2, and tend to follow the order of cubic to tetragonal by a rotation of the octahedra, then octahedral rotation and tilting to orthorhombic. Eventually, at temperatures less than 100 K, the tilting and further rotation constrains the motion of MA, and its motion freezes out completely [117, 120, 121]. It is of interest to note, that $MAPbI_3$ and $MAPbBr_3$ thin films show a certain hysteresis and phase fluidity/coexistence around the transition temperatures, where for large temperature ranges phases coexist [92, 101].

Due to the nature of the band structure, which will be described in more detail later, most perovskites show a blue shift of the bandgap with increasing temperature, which is uncommon for inorganic semiconductors [122], and has its origin in the shift of the octahedra [86, 123].

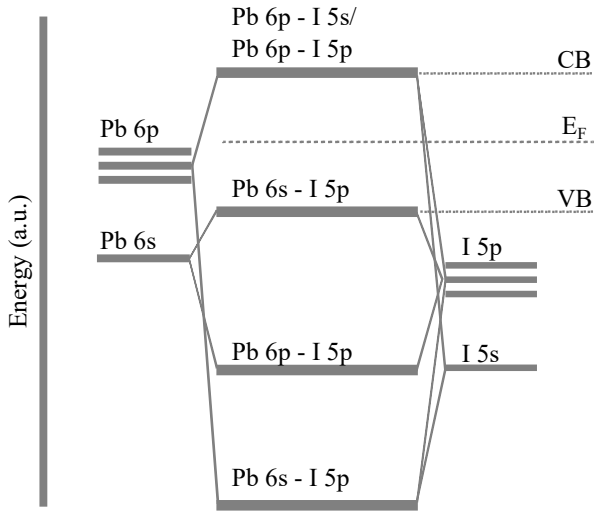


Fig. 2.13: Bonding diagram of a $[PbI_6]^{-4}$ cluster representing $MAPbI_3$. The orbitals relevant for highest valence and lowest conduction band respectively are marked with an asterisk. Adapted with permission from Umebayashi *et al.* [125], Phys. Rev. B 67, 2 (2003). Copyright 2003 American Physical Society.

2.2.2 Electronic Properties

For a semiconductor intended as a solar cell material, it is essential to have good charge transport characteristics and a high absorption. Both these properties arise from the electronic band structure.

Band Structure

Band structure in perovskites close to highest valence and lowest conduction band is dominated by combinations of s- and p-orbitals [124], as shown for $MAPbI_3$ in Fig.2.13. In the cubic and tetragonal phase, these s- and p-orbital based valence and conduction bands lead to degenerate states [126] of a mainly s-type symmetry for the top valence band, and a p-symmetry for the bottom conduction band [112, 127–129] experiencing exchange interaction and spin orbit coupling [126]. Thus, the valence band is twofold degenerate due to hole spin ($|S\rangle|\uparrow\rangle$ and $|S\rangle|\downarrow\rangle$). The conduction band is similarly twofold degenerate. Due to the strong spin orbit coupling [127] and the exchange interaction, the exciton states are a mixing of the different spatial directions $|X\rangle$, $|Y\rangle$, and $|Z\rangle$ with electron/hole spin [126]. Due to the

exchange interaction, exciton states are split into a singlet $|\mathbf{J}=0;J_z=0\rangle$ and three triplet states $|1;0,\pm1\rangle$. This system is well described by an effective-mass Hamiltonian $\mathcal{H}$ [130, 131],

$$\mathcal{H}=\begin{pmatrix} E_c+\gamma_e\frac{p^2}{2m_0} & 0 & -\frac{1}{m_0}\frac{\imath P}{\sqrt{3}}p_z & -\frac{1}{m_0}\frac{\imath P}{\sqrt{3}}p_- \\ 0 & E_c+\gamma_e\frac{p^2}{2m_0} & -\frac{1}{m_0}\frac{\imath P}{\sqrt{3}}p_+ & \frac{1}{m_0}\frac{\imath P}{\sqrt{3}}p_z \\ \frac{1}{m_0}\frac{\imath P}{\sqrt{3}}p_z & \frac{1}{m_0}\frac{\imath P}{\sqrt{3}}p_- & E_v-\gamma_h\frac{p^2}{2m_0} & 0 \\ \frac{1}{m_0}\frac{\imath P}{\sqrt{3}}p_+ & -\frac{1}{m_0}\frac{\imath P}{\sqrt{3}}p_z & 0 & E_v-\gamma_h\frac{p^2}{2m_0} \end{pmatrix} \tag{2.41}$$

with $p_\pm=p_x\pm\imath p_y$, Kane energy $P=\imath\langle S|\,p_z\,|Z\rangle$, and the valence/conduction band energies $E_{v/c}$. The resulting band structure in a DFT-LDA approximation in Fig.2.14 features the

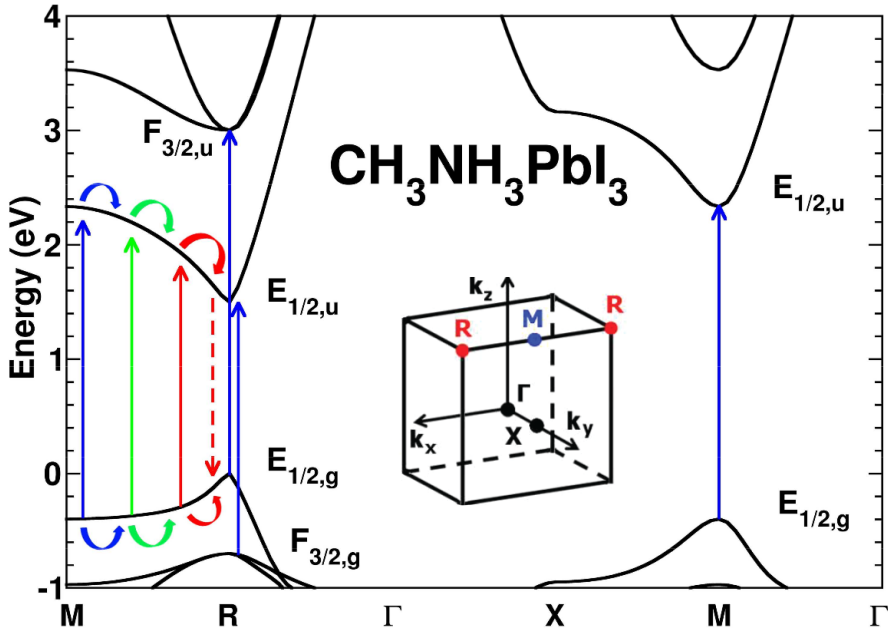


Fig. 2.14: Band structure of $MAPbI_3$ in the $Pm\bar{3}m$ cubic phase showing the bandgap at the R-point, as obtained from DFT-LDA approximation considering spin orbit coupling. To match experimental data, an upwards shift of 1.4 eV has been applied. Possible absorption and emission points are indicated by coloured arrows in the band structure. The inset shows some special symmetry points in the first Brillouin zone of the $Pm\bar{3}m$ structure. Reprinted with permission from Even *et al.* [132], Journal of Physical Chemistry C, 13, 1764-1769. Copyright 2014 American Chemical Society.

bandgap at the R point [112, 125]. A small energy-wavevector gradient band between R and M, corresponding to the Kane energy, and further dipole allowed transition locations ensure a broad band, high absorption - ideal for solar cells.

Influence of Spin Orbit Coupling (SOC)

In the special case of spin orbit coupling (SOC) for heavy atoms, the Hamiltonian $\mathcal{H}$ is modified by the additional term $\mathcal{H}_{SO} = \lambda \mathbf{L} \cdot \mathbf{S}$, which in free atoms leads to a lifting of the degeneracy, e.g., between the p-states into $p_{3/2}$ and $p_{1/2}$. For crystals with inversion symmetry, the SOC is insufficient to lift the *Kramers spin degeneracy* [133]. For crystals lacking inversion symmetry, the SOC results in the *Rashba effect* [134], locally lifting the degeneracy by splitting the spin bands, as shown in Fig.2.15. This splitting can be characterised by the Rashba parameter

$$\alpha_R = \frac{1/2 E_R}{k_R}, \tag{2.42}$$

which can be calculated from the energy splitting E_R, and wavevector splitting k_R. The splittings seen for semiconductors like, i.a., InSb, CdS, or CdSe tend to be very small, their indirect bandgap close to the direct bandgap energy [11].

For perovskites there have been many publications on this topic, most theoretical in nature, arguing for and against such a SOC induced lifting of the spin degeneracy, as it could explain the long lived excitons in perovskites [112, 120, 135–143]. So far, general experimental proof of the Rashba effect in perovskites is still elusive, as experimental works on this are either likely to be marred in their significance by surface effects and surface sensitivity [144–146], or challenged by the intrinsically large surface to volume ratio of nano crystals and thin films [95, 147–149]. Estimates of the Rashba induced splitting range from 5 meV [142] up to 120 meV [143]. It should be noted that there are two distinct possibilities for the Rashba effect in hybrid organic inorganic perovskites, static and dynamic in nature. The former can be caused by permanent disorder to the crystal structure, e.g. by displacement from the ideal atom positions for iodide or lead in $MAPbI_3$. The dynamic case, in contrast, results from the ability of the MA-ion to move and rotate in, and influence, its cage. This also opens up the possibility for both cases to co-occur.

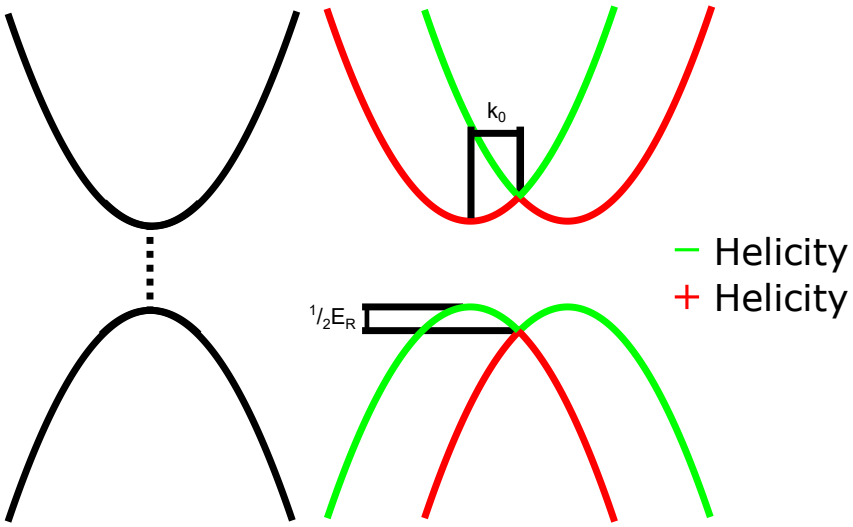


Fig. 2.15: Bands in an inversion symmetric tetragonal crystal (left) are spin degenerate. In the presence of heavy atoms and under the lack of crystal inversion symmetry, bands undergo Rashba splitting, lifting the degeneracy (right). The Rashba parameter α_R can be calculated from the parameters indicated, and can differ for valence and conduction band. The **k** values involved in the indirect transitions tend to be small, and the indirect and direct gap show a very small energy and wavevector **k** difference.

2.2.3 Optical Properties

The optical transitions of the perovskites studied for this thesis can be understood as band-to-band (free carrier) and excitonic (bound electron hole pair) transitions. These two processes and their change under magnetic fields will be discussed here.

Excitons

The excitation of an electron from the valence to conduction band leaves behind the quasi-particle of a positively charged hole in the valence band. As in a hydrogen atom, hole and electron will attract each other coulombically. In contrast to the hydrogen atom, the effective hole mass is of comparable size to the electrons and the relevant mass will be $1/\mu = 1/m_e^* + 1/m_h^*$ with a resulting energy of

$$E_X = E_g - \frac{\mu e^4}{32\pi^2\hbar^2\epsilon_r^2\epsilon_0^2}\frac{1}{n^2} + \frac{\hbar^2 k^2}{2(m_h^* + m_e^*)} \approx \frac{R_y^*}{n^2}, \tag{2.43}$$

with bandgap energy E_g, principle quantum number n, and the third term gives the translational energy of the exciton of wavevector **k** [11]. In an approximation, E_X is equal to the

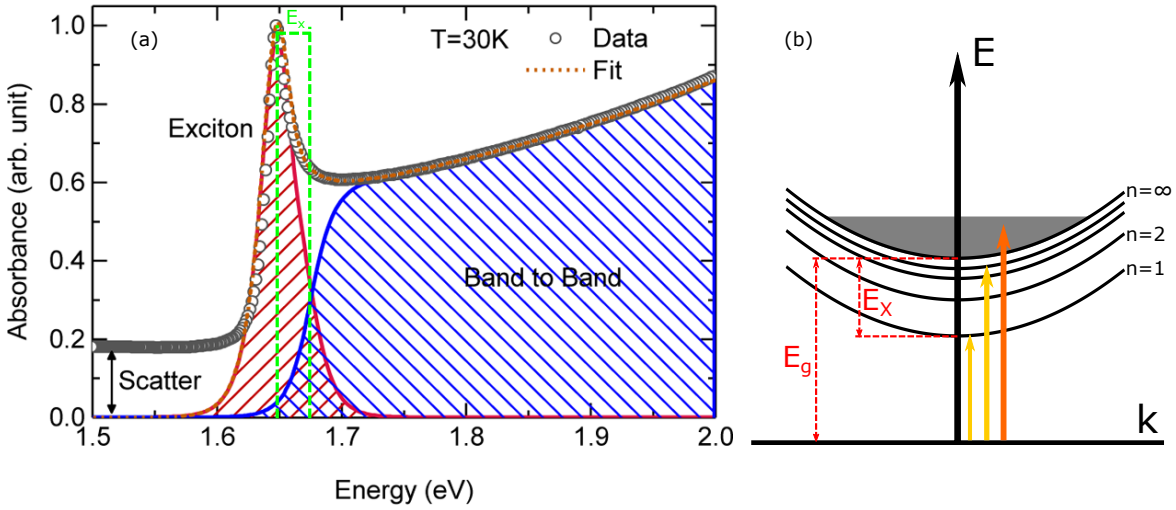


Fig. 2.16: (a) Illustration of the two main absorption processes of band-to-band and excitonic absorption in $MAPbI_3$. The *Elliott theory* [150] fit highlights the two contributions and show the large contribution of (bound) exciton absorption at low temperatures, and the bandgap E_g is indicated by the right green line. (b) Exciton energy spectrum from bound $n = 1$ up to free excitons $n = \infty$. Bandgap E_g and exciton binding energy E_x are shown, as well as some possible absorption processes into bound exciton states (yellow) and the continuum (orange / grey shaded). (a) Adapted with permission from Singh *et al.* [151], J. Phys. Chem. Lett. 2016, 7, 3014-3021. Copyright 2016 American Chemical Society.

Rydberg energy $R_y^* = R_y \frac{\mu}{m}$ modified by the reduced mass μ. For a sufficiently small excitation energy, hole and electron will enter a bound state which, depending on its binding strength, will either be a strongly bound *Frenkel* or a large, weakly bound *Mott-Wannier* exciton. The difference between these two flavours of excitons lies in the dielectric function of the host material. For many semiconductors ϵ_r is within a range that results in a *Mott-Wannier* type exciton, and these excitons tend to have a radius larger than the semiconductor's unit cell. The binding energy is of interest for solar cells, as an exciton binding energy $E_X > E_{th}$ larger than the thermal energy $k_B T$ will result in a large fraction of bound excitons at solar cell operating temperature T which do not contribute to the current[3].

As detailed in section 2.2.2, the excitons in the perovskites relevant to this thesis have one singlet and three triplet states. For the tetragonal phase with its lowered symmetry, this results in an initial lifting of the triplet degeneracy, and a completely lifted degeneracy in the orthorhombic phase, as shown in Fig.2.17, with both dark singlet state $|0;0\rangle$, bright triplet states $|1;0,\pm1\rangle$, and the allowed transitions.

[3]If the absorber semiconductor is thin and exciton diffusion strong, these bound excitons can still decay at interfaces with appropriate HOMO/LUMO values, if it is energetically favourable.

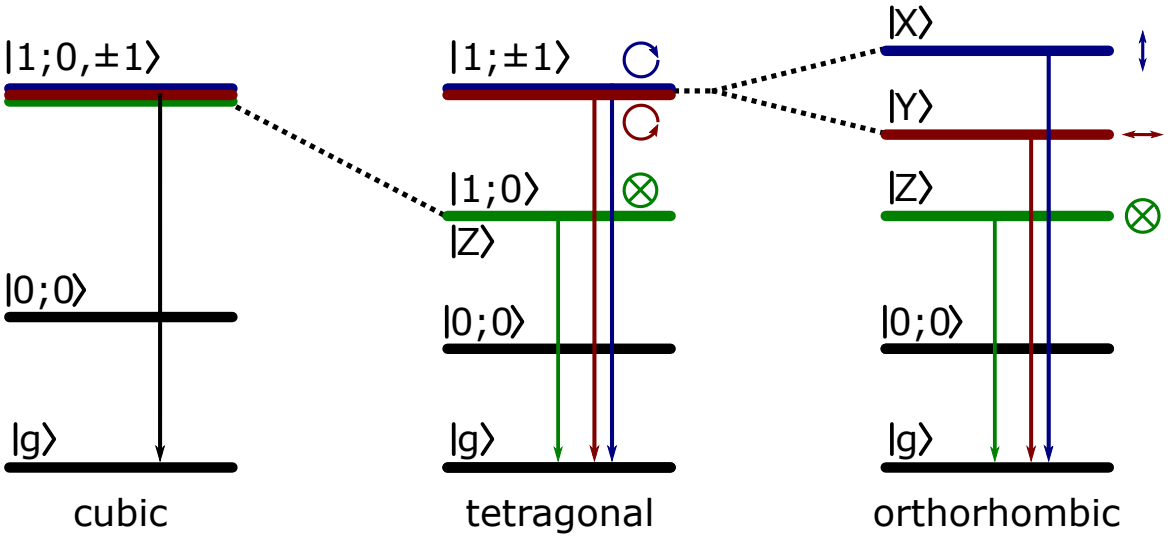


Fig. 2.17: Lifting of the degeneracy in the exciton states due to exchange interaction leads to split singlet and triplet states in the cubic phase. Following the lowering of symmetry, the triplet state's degeneracy is lifted and results in a split of the individual parts of the respective triple wavefunctions $|1;0,\pm1\rangle$ into their constituent components $|X\rangle$, $|Y\rangle$, and $|Z\rangle$. Moreover, some of the strongly allowed transitions are given together with their polarisation. The singlet, as a dark state, allows no transitions to the ground state. Rashba splitting, as reported by Becker *et al* for nanocrystals [126] would lead to further modifications of this energy-scape, lifting degeneracy already in the cubic phase. The notation used here is based on Becker *et al.* [126].

Phonons and Excitons combining to Polarons and other -ons

In the tight-binding approximation introduced in section 2.1.2, an underlying assumption is a static potential due to the nuclei moving much slower than the electrons, the *Frank-Condon approximation* [152, 153]. For materials as soft as perovskites [154], this approximation does not hold, and the corresponding electron-phonon interactions known as *Fröhlich coupling* or polarons have to be considered [44, 152, 153, 155]. For hard, inorganic semiconductors, the necessary energies are much higher, and *Fröhlich coupling* plays a secondary role [156]. The Fröhlich interaction induces an additional short range term $\mathcal{H}_{FC}$ [156]

$$\mathcal{H}_{FC} = \frac{\mathbf{p}^2}{2m} + \sum_{\mathbf{k}} \hbar\omega_{LO} a^{+}_{\mathbf{k}} a_{\mathbf{k}} + \sum_{\mathbf{k}} (V_k a_{\mathbf{k}} e^{\imath \mathbf{k}\cdot\mathbf{r}} + V^{*}_{\mathbf{k}} a^{\dagger}_{\mathbf{k}} e^{-\imath \mathbf{k}\cdot\mathbf{r}}) \tag{2.44}$$

to the Hamiltonian, where $\mathbf{p}$, $\mathbf{r}$, $\mathbf{a}^{\dagger}_{\mathbf{k}}$ and $\mathbf{a}_{\mathbf{k}}$ are electron momentum, its position, creation and annihilation operators for longitudinal optical (LO) phonons of wavevector $\mathbf{k}$, and phonon

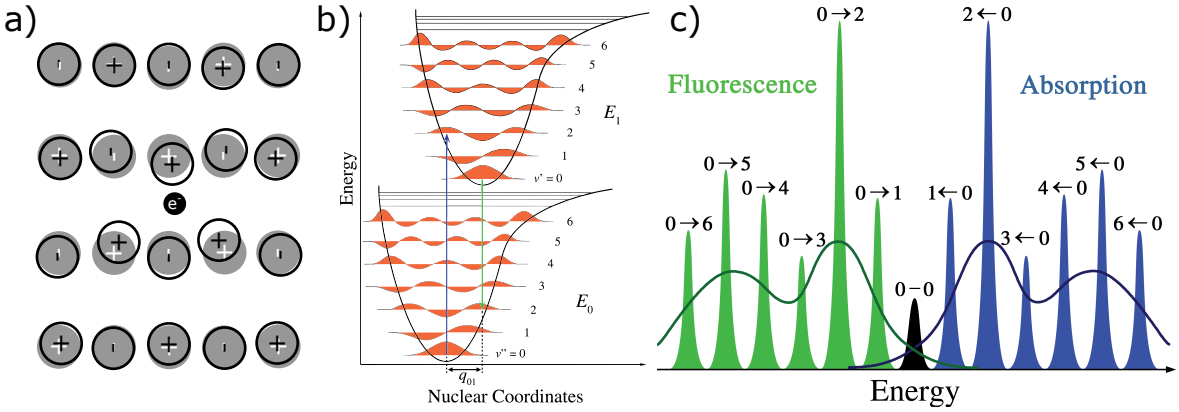


Fig. 2.18: (a) 2D rendition of the *Fröhlich coupling* between an electron and phonons. The positively/negatively charged nuclei of the lattice move towards/away from the mobile electron charge, effectively screening it. The original nuclei positions are displayed in grey, the new positions in black with no fill and the electron e^- is in the centre. (b) Frank-Condon energy diagram, with wavefunctions (orange) for the vibrational levels ν. The probability of transition from one energy $\mathrm{E}_{i,\nu}$ to another is given by the overlap between the wavefunctions. Here, this favours transitions with $\nu = 0, 2$ as shown in (c), where the transition intensities are mapped. (b) and (c) adapted from M. M. Somoza [157] under the CC BY-SA 3.0.

frequency ω_{LO} respectively. The V_k are the Fourier components of the electron-phonon interaction

$$V_k = -\imath\frac{\hbar\omega_{LO}}{k}\left(\frac{4\pi\alpha_{FC}}{V}\right)^{1/2}\left(\frac{\hbar}{2m\omega_{LO}}\right)^{1/4} \tag{2.45}$$

which are proportional to the dimensionless α_{FC}. An extreme rendition of a polaron is displayed in Fig.2.18, showing how this coupling induces an effective charge screening. As a result, the effective mass of hole and electron for exciton processes will change and can be approximated to

$$m^* = \frac{m}{1 - \frac{\alpha_{FC}}{6}}, \tag{2.46}$$

depending on the *Fröhlich coupling* constant α_{FC}. For the *Landau levels* induced by large magnetic fields, which will be introduced in the next section, the effective-mass will remain unmodified as m.

The interaction between excitons and phonons is also of influence when vibrational levels ν influence absorption and emission as shown in Fig.2.18 (b,c). Following the Frank-Condon diagram, an absorption from energy E_1 to E_2 is only likely if there is sufficient overlap between the wavefunctions for the different vibronic levels [9]. The corresponding emission pattern is thus red-shifted from the central $\nu = 0 \rightarrow \nu = 0$ transmission by the *Stokes shift*, of

which *Raman scattering* is one example. The additional energy is released as phonons. This phenomenon leads to further splitting and widening of PL peaks, in addition to the thermal PL widening introduced in section 2.1.3.

Influence of Magnetic Fields

Free charge carriers have both an associated charge and spin. Correspondingly, under the influence of a magnetic field an additional term $\mathcal{H}_B$ has to be added to the Hamiltonian, to obtain the field response

$$\mathcal{H}_B = \frac{1}{2\mu}(\mathbf{p} - q\mathbf{A})^2, \tag{2.47}$$

where $\mathbf{p}$, and q are charge carrier momentum and charge, and $\mathbf{A}$ is the magnetic vector potential [44]. This field dependent modification describes the motion of the charge carriers induced by the magnetic field, and the coupling of the spin to the field. The resulting change in energies are

$$E_\xi^{LL}(B) = (\xi + 1/2)\,\hbar\omega_c \pm 1/2 g_{\text{exc}}\mu_B B, \tag{2.48}$$

where $\omega_c = \frac{eB}{\mu}$ is the cyclotron frequency, g_{exc} is the exciton g-factor, μ_B is the Bohr magneton, and ξ gives the *Landau orbital* quantum number. The energies $(\xi + 1/2)\,\hbar\omega_c$ for $\xi = 0, 1, 2, \ldots$, give the Landau level energies, the second term the spin magnetic field interaction induced *Zeeman splitting* [11, 44]. The resulting Landau level fan is shown in Fig.2.19. For excitons, Eq.2.47 has to be modified with a term $\frac{e^2}{\epsilon_r \mathbf{r}}$, to account for the coulomb interaction of electron and hole at at distance $\mathbf{r}$ from each other, and charge screening due to the surrounding semiconductor's ϵ_r. The resulting energies can be approximated numerically by neutral hydrogen-like exciton transitions in strong fields close to the band edge with results shown in Fig.2.19 as calculated by Makado *et al.* [160]. This figure shows, that for $\hbar\omega_c > 2R_y^*$ the energy levels approach free carriers, albeit at an offset, and for $\hbar\omega_c < 2R_y^*$ follow the diamagnetic hydrogen-like field response behaviour.

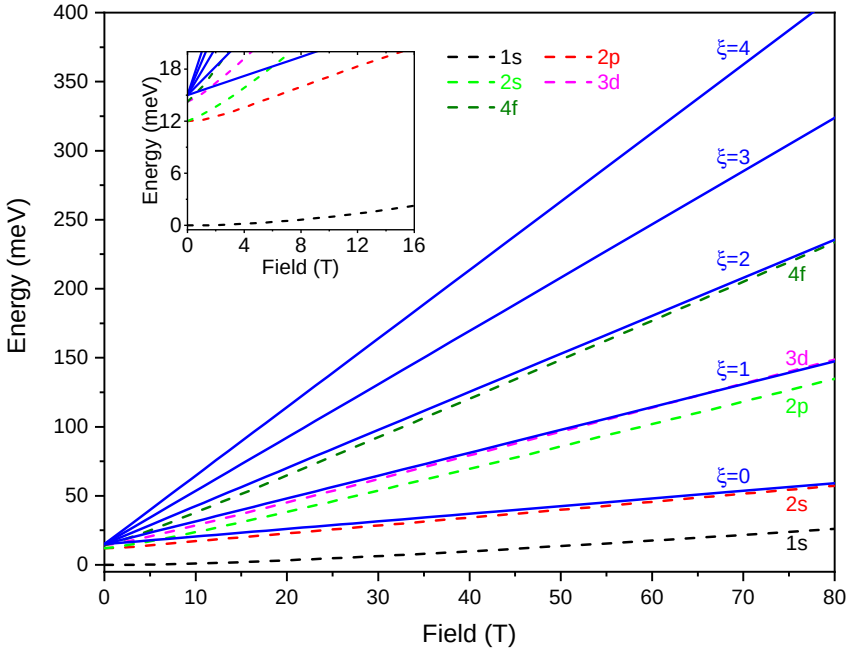


Fig. 2.19: Energies for excitonic (dashed) and free charge carrier (solid) Landau level transitions as a function of magnetic field. The inset focusses on the $\hbar\omega_c < 2R_y^*$ regime. The data displayed here uses R_y^* =16 meV and $\mu = 0.1m_0$, values close to data reported for $MAPbI_3$ [158, 159].

2.3 Summary

This chapter gave an introduction to single-walled carbon nanotubes (SWNT) and hybrid organic inorganic metal halide perovskites.

Single-Walled Carbon Nanotubes

The crystal structure of SWNT is derived from the properties inherited from the graphene honeycomb lattice. It is shown, that SWNT can be fully characterised using the chiral indices (n,m), describing the rolling up of a graphene sheet into a carbon nanotube. Depending on the relation of n and m, tubes can take on either metallic, or semiconducting properties. For a sample of uniform distribution of chiralities, this leads to a 2:1 semiconducting to metallic tube ratio in the sample. The band structure for metallic tubes close to the fermi level is similar to that of graphene with linear bands, whereas semiconducting tubes show parabolic bands close to E_F. The resulting density of states (DOS) shows a finite bandgap for semiconducting tubes, which depends on the tube diameter d_{tube}. Both metallic and

semiconducting tubes show *van Hove* singularities, leading to a characteristic absorption spectrum. A facile method of identifying tube species is photoluminescence excitation (PLE) mapping, where photons are absorbed at energy E_{22}, and re-emitted at lower energies E_{11}. Due to the low defect density in SWNT, ballistic charge transport takes place for tubes of several hundred nanometres. In networks made of SWNT the overall sheet resistance will be higher based upon bundling of tubes, insufficient tube to tube contact, and Schottky barriers between metallic and semiconducting tubes preventing high conductivity. The sheet resistance of such SWNT networks can be lowered by a factor 3 upon doping with substances like nitric acid.

To overcome the strong bundling of SWNT, tubes can be non-covalently modified by wrapping with polymers. This wrapping process not only makes tubes soluble in a wide range of solvents, depending on the polymer, but allows allows for specific selection of single chiralities of tubes, with up to 99.98 % purity.

Combined, these properties make single-walled carbon nanotubes an interesting material for flexible transparent charge transport layers.

Hybrid Metal Halide Perovskites

The structure of organic inorganic metal halide perovskites follows the ABX_3 formula, or $AB^IB^{III}X_3$ for double perovskites, where the B cation and X anion form octahedra and the A cation is situated in the remaining gaps in-between. There are many molecules and atoms that fulfil this formula and the Goldschmidt criterion, allowing for facile tuning of the bandgap of the material. This tunability is caused by the valence and conduction bands dependence on the p and s orbitals of the B and X species. As both B and X tend to be heavy atoms, strong spin orbit coupling (SOC) influences the bandgap, causing an a-typical blue shift with increasing temperatures, as the spin orbit coupling is weakened with decreasing octahedra tilt and deformation. SOC alone is insufficient to lift the Kramers degeneracy, but in the case of a non-centrosymmetric crystal it will lead to a Rashba spin splitting. Depending on the Rashba parameter this can lead to an indirect bandgap. At low temperatures absorption is dominated by the exciton, a bound hole electron pair. At higher temperatures, where excitons can thermally overcome their binding energy, absorption is dominated by free carrier band

to band transitions. In the cubic crystal structure, excitonic emission structure is threefold degenerate, a degeneracy that is lifted for the lowering of symmetry in the tetragonal and orthorhombic phase. For sufficient phonon-exciton interaction, *Fröhlich coupling* has to be considered, splitting the emission into vibrational levels, and modifying the effective mass μ. In magnetic fields, free charge carriers will be forced into a circular motion perpendicular to the magnetic field, causing *Landau levels*. For excitons, the interaction with magnetic fields has no analytical solution, but for high fields fulfilling $\hbar\omega_c < 2R_y^*$ their behaviour approaches that of free charge carriers. The transitions between these different levels can be well resolved and allows for more easy determination of exciton binding energy R_y^* and effective mass m^*.

3 Materials, Methods and Experimental Techniques

This chapter describes the experimental methods for carbon nanotube (CNT) wrapping and deposition, and growth procedures for hybrid metal halide perovskite single crystals and thin films. Additionally, important experimental techniques and setups are described to characterise the CNT thin films, and the optical properties of the studied perovskite samples.

3.1 Materials and Methods

This section details the materials used for the transparent conductive SWNT thin film deposition, and for the growth of perovskite single crystals and thin films.

3.1.1 Single-Walled Carbon Nanotubes

The single-walled carbon nanotubes used for this work where obtained commercially as dry powders and are listed in Table 3.1. For comparison, tubes grown by different methods were tested. The purity stated by all producers refers to the SWNT content, where the remaining 5 wt% is made up of both amorphous carbon and residual catalyst Fe, Mo, and or Co.

SWNT Functionalisation

The main polymer used for SWNT functionalisation in this study was highly regio-regular poly 3-hexylthiophene (P3HT), as shown in the inset of Fig.3.1. The polymer was bought from Rieke Metals and had an average $M_w = 50\,000 g\,mol^{-1}$ molecular weight. P3HT is a

Table 3.1: Overview of SWNT used for the work in this thesis and some of their properties as stated by their producers.

Producer	Method	Batch#	Purified to	ø(nm)	Length (um)
NanoIntegris	HiPCo	HP24-108	95 wt%	0.8 - 1.2	0.1 - 1
NanoIntegris	HiPCo	HP26-096	95 wt%	0.8 - 1.2	0.1 - 1
NanoArmor	CVD	AS#99685-96-8	95 wt%	0.9 - 2	5 - 30
SigmaAldrich	CoMoCAT CG300	#MKBS9938V	95 wt%	0.6 - 1.1	0.1 - 1

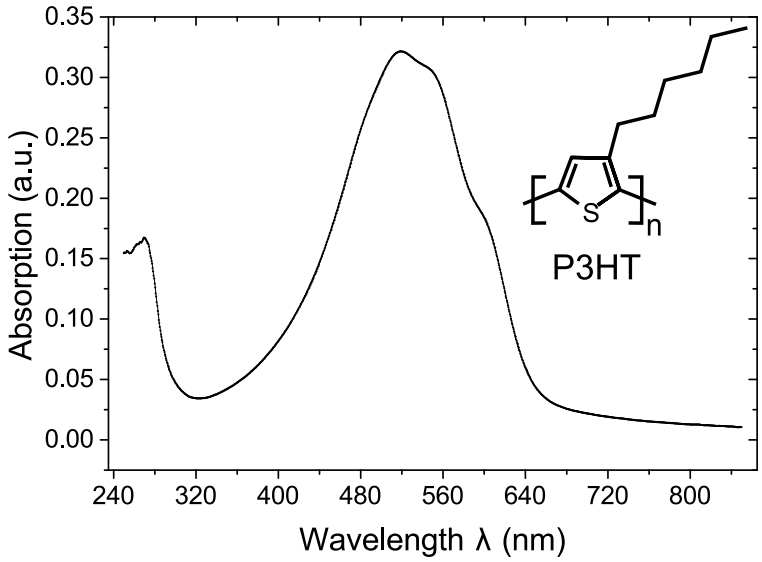


Fig. 3.1: Absorption spectrum of a P3HT thin film on glass, from the UV to the near-IR range as obtained from UV-Vis. The chemical structure of the polymer poly 3-hexylthiophene is displayed as an inset. For the regio-regular P3HT variety, the bonds between the thiophene rings are in plane. Adapted from [161].

commonly used semiconducting polymer that is well understood for both functionalisation of SWNT and use in solar cell devices.

The entire procedure of the SWNT functionalisation process is schematically displayed in Fig.3.2. First, 2.5 mg SWNT are added to 5 mL of a 0.6 g L^{-1} solution of P3HT in chlorobenzene and tip sonicated for 10 min. After the sonication, the solution is decanted into microcentrifuge tubes and centrifuged at 10 000 g for 8 min to sediment non-wrapped tubes. The supernatant is mixed with toluene in a 1:3 volume ratio. Toluene dissolves P3HT, but is a bad solvent for the P3HT functionalised tubes (fSWNT). Thus, after 60 min on a hotplate, the nanocomposites precipitate and the residual polymer solvent mixture can be decanted after another centrifugation step for 4 min at 16 000 g. For tubes with very low residual non-wrapped polymer content, the toluene precipitation/centrifugation step can be repeated

several times. Finally, the resulting fSWNT pellet is dissolved in chloroform in a pellet weight to solvent ratio dependent on the use case for the tubes.

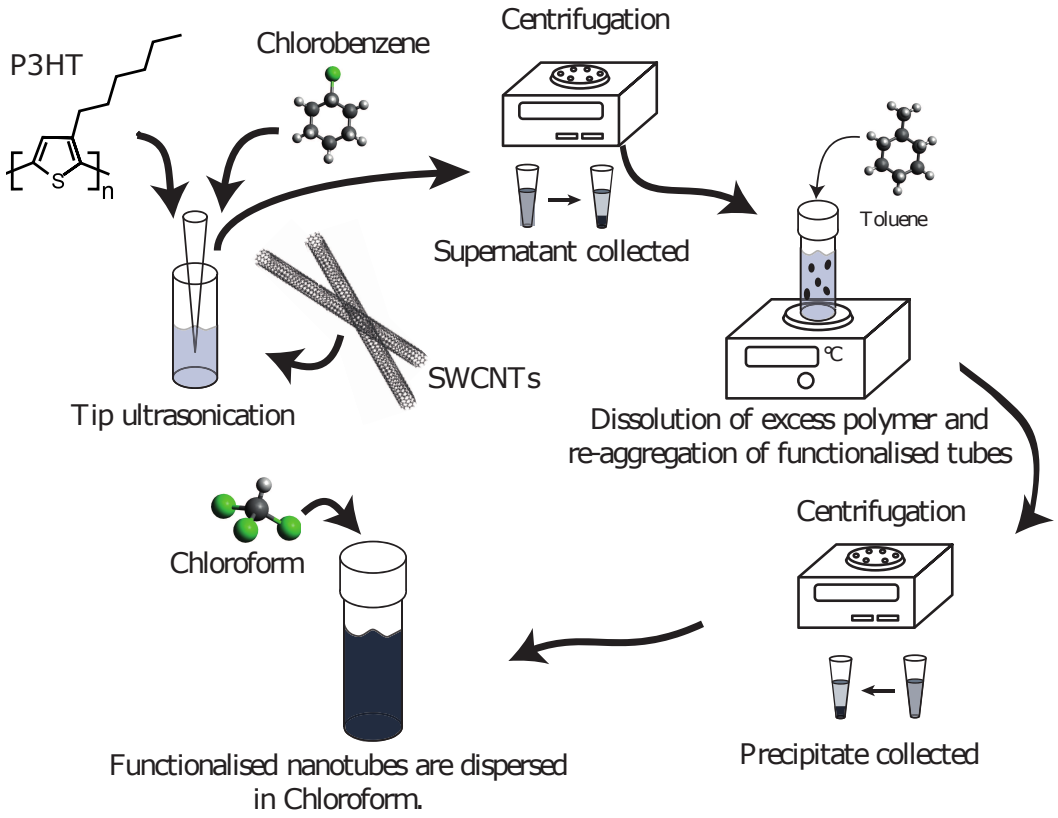


Fig. 3.2: Steps of the SWNT polymer functionalisation procedure: Polymer and tubes are added to a solvent, here chlorobenzene, and tip-sonicated. Next, the solution is filled into centrifuge tubes and centrifuged at ~12krpm for 8 min. The supernatant, which is rich in functionalised and well-dispersed SWNT, is decanted and blended with toluene, to start nano composite aggregation. After another centrifugation at ~16krpm, the precipitate is re-dissolved in chloroform, ready for use. For high purity, small polymer residue solutions, the toluene-aggregation-centrifugation step were repeated several times. Adapted with permission from G. Mazzotta [162].

Substrate Preparation

Standard microscope slides of 1 mm thickness and 25x75 mm area were used as substrates. Cut with a diamond stylus, they resulted in three 25x25 mm squares. Microscope slides usually have < 1 nm rms surface roughness, making them an ideal and cheap substrate with little batch-to-batch variation.

To remove possible dirt and glass dust from the substrates after cutting, they were in three steps first rinsed with acetone, sonicated for 5 min in acetone and then in isopropanol (IPA),

followed by blow-drying with N_2-gas. To remove any remaining organic dirt and to enhance wetting properties, the samples were exposed to an oxygen plasma at <0.4 mbar for 5 min.

Nanotube Deposition

The requirements for application in solar cells demand for a fast method yielding highly uniform, low sheet resistance transparent thin films.

One of the standard research lab techniques for organic and perovskite solar cells is spin-coating. A small substrate of <3 cm × 3 cm is fixed in place on a vacuum chuck, and spin speeds can exceed 6 krpm, with a roughly inverse relationship of resulting film thickness $t \propto \frac{1}{\omega}$ to spin-speed ω. For solutions of fSWNT, this results in non-uniform sparse films. By depositing the fSWNT solution droplet by droplet on a already spinning substrate, as shown in Fig.3.3 (b), the resulting films are improved, and can be tuned to the desired thickness by adjusting the amount of solution deposited. The best results were obtained at a spin-speed of 3 krpm with the use of a concentrated fSWNT solution.

Drop-casting was performed on substrates kept at a 45° angle with fSWNT ink droplets deposited by pipette. This angle was the best compromise between contact time of solution and achieving complete coverage of the up to 5 cm substrates. Best results were obtained for substrates heated to 45 °C, together with a dilute fSWNT ink.

Spray-coating was performed using a custom setup built by Dr M.G. Christoforo [163]. The setup included a variable x-position stage heatable with a resistive element able to output up to 100 W. The air-atomising spray nozzle of variable z/y-position was fed by a syringe pump and with a 6 bar compressed dry-air stream. For fSWNT deposition, the stage was preheated to 100°C and the nozzle brought to a height of 10 cm. For each layer 40 mL of fSWNT ink were sprayed to ensure a constant amount of passes across the sample and a uniform distribution. Layer thickness was controlled by changing the concentration of the fSWNT in the solution.

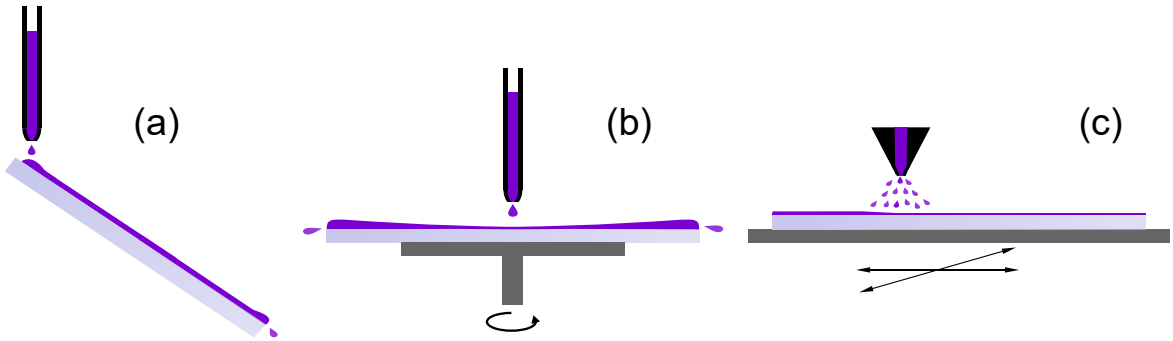


Fig. 3.3: Schematic of the three different methods used for deposition of functionalised SWNT. (a) is drop-casting, (b) spin-coating, and (c) spray-coating on a x-y-stage.

3.1.2 Perovskite Single Crystals and Thin films

As will be shown in this thesis, the growth of $MAPbI_3$ single crystals (and thin films) is temperature sensitive and yields physically distinct crystals depending on the growth temperature being smaller or larger than the cubic phase transition temperature, making growth conditions very important.

Single Crystal Growth

$MAPbI_3$, and $MAPbBr_3$ single crystals were grown using the anti-solvent vapour-assisted (ASV) crystallisation technique [105, 164], and the temperature inverse precursor solubility technique [165, 166]. A schematic detailing the process for both techniques is shown in Fig.3.4. In contrast to literature, the ASV technique was modified using chloroform as anti-solvent, with 2.5 mmol PbI_2 and 7.5 mmol MAI_2 in a vial with 5 mL of γ-butyrolactone (GBL) as solvent. After both precursors are in solution, about 200 µL of chloroform is gradually added to the solution until a stable precipitate of nanocrystals forms around the chloroform vortex. After a short low-power sonication, the solution becomes transparent and clear again, and the vial is put in a chloroform containing container on a hotplate. Crystal formation rapidity is dictated by the evaporation of chloroform and re-condensation of the chloroform vapour in the precursor solution vial. This technique allows for growth temperatures as low as 35 °C, where mm-sized crystals form after less than 3 weeks.

Growth of high temperature $MAPbI_3$ crystals started with a 0.1 molar solution of both MAI and PbI in GBL. The initial dispersion was stirred at 80 °C for ~30 min, then filtered to

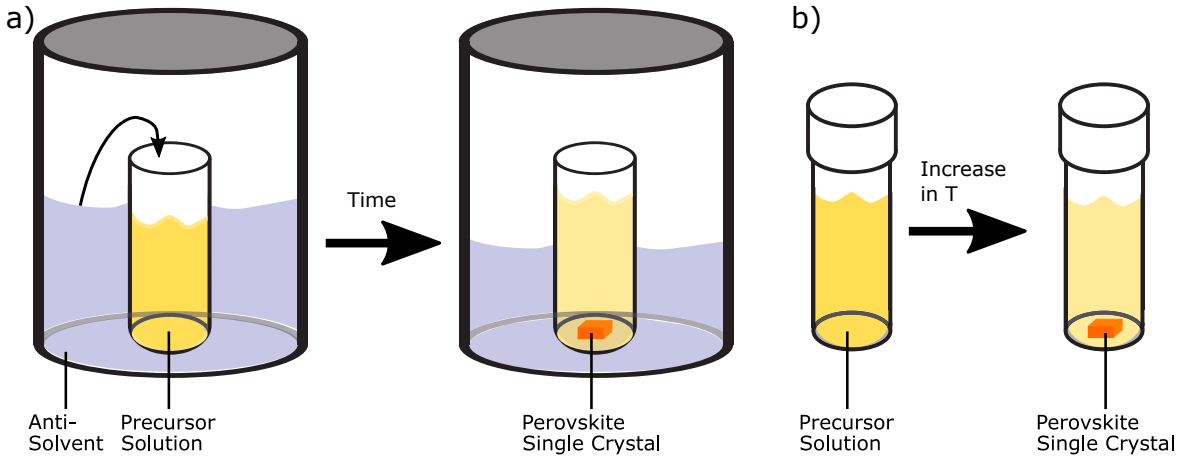


Fig. 3.4: (a) Perovskite single crystal growth following the anti-solvent vapour-assisted technique where temperatures can be kept small. (b) The inverse precursor solubility technique requires higher temperatures, and crystal growth is rapid.

remove precursors that did not go into solution, while ensuring that the precursor solution does not cool down. The solution was then closed off, as shown in Fig.3.4, and heated to 120 °C. After initial crystals formed, these were removed and used as growth seeds in a new precursor solution. These steps were repeated until the desired size of the crystals was achieved, with growth times for millimetre-scale crystals under 2 h.

It has to be noted if grown at $T > T_{cubic}$, the resulting $MAPbI_3$ crystal is not cleavable and will instead crumble, whereas for growth below T_{cubic} it is cleavable in the (001) plane orthogonal to the c-axis [167]. Moreover, only for the below T_{cubic} growth will the resulting single crystals be cuboid, for higher growth temperatures the resulting crystals have many facets as truncated dodecahedra.

$MAPbBr_3$ and $Cs_2AgBiBr_6$ used for the magneto-optical experiments in this thesis were respectively grown by collaborators Elisabeth Duijnstee and Pabitra Nayak [168], and Laura Schade [78], all of the University of Oxford. All $MAPbI_3$ crystals detailed here were grown by myself.

Thin Films

As mentioned in Ch.2.2.1, there are many techniques to create perovskite thin films, but most require high temperatures ≥55 °C to crystallise. One exception is the acetonitrile route established by Noel *et al.* [169, 170], where crystallisation happens at temperatures as low

as 25 °C. The perovskite thin films studied for this thesis were all produced following this route. For this technique, $MAPbI_3/MAPbBr_3$ precursors are added to acetonitrile, forming a dispersion. After bubbling of the dispersion with methylamine gas, a solution is formed ready for the spin-coating of highly uniform, specular films.
The films used for the magneto-optical experiments in this study where prepared by collaborators Nakita Noel at Princeton University, and Jonathan Warby at the University of Oxford.

3.2 Experimental Techniques

This section details experimental techniques employed to characterise SWNT thin films and perovskite samples.

3.2.1 Surface and Structural Characterisation

The use of transparent, highly conductive SWNT thin films as electrodes in solar cells requires layers of high homogeneity and low roughness. The methods used to characterise these properties are described here.

DekTak and Atomic Force Microscope(AFM)

To determine the thickness of an SWNT layer, DekTak and atomic force microscopy (AFM) were used. The AFM uses an oscillating cantilever to map a sample's surface in x,y and z-direction by measuring the deflection of a laser beam, as displayed in Fig.3.5. The deflection is due to the attraction and repulsion of the cantilever to the surface by van der Waals, and Coulomb forces. A DekTak profilometer has a similar operating principle, but only maps in x, and z-direction.
For an quick determination of the layer thickness, a SWNT sample on either glass or silicon was scratched with a tweezer to locally remove the nanotubes. Then, either a *Bruker DekTak* or *Oxford Instruments MFP-3D* AFM were used to test for height differences. For the DekTak, a very low stylus pressure of below 0.3 mg, was used in an effort to prevent highly ductile SWNT from moving and deforming. Similarly, AFM mapping was influenced by the

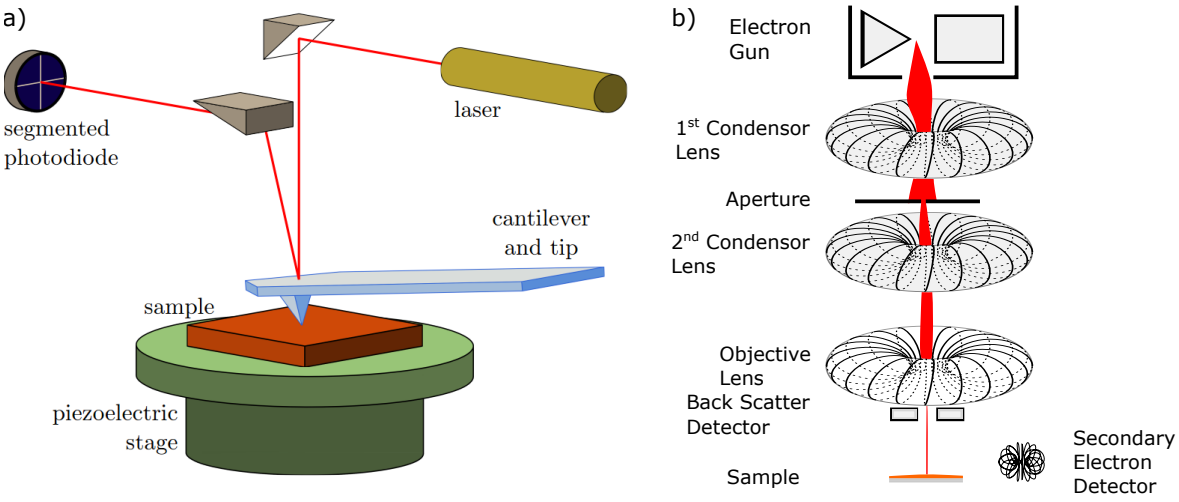


Fig. 3.5: (a) Schematic illustration of the feedback loop and the optical system of an atomic force microscope. (b) Schematic of an SEM, its different magnetic lenses and its beam pathway (red), with an overview of the position of some different detectors. (a) Adapted from [161].

SWNT ductility, rendering height and surface roughness measurements for few SWNT thick layers a difficult task.

Scanning Electron Microscope

The scanning electron microscope (SEM) uses an electron beam to probe and map samples. The general layout of a SEM is displayed in Fig.3.5. Its operational principle is similar to the light microscope's, but instead of optical lenses, it uses a set of magnetic lenses to focus and direct an electron beam in high vacuum. In theory, this allows for a resolution up to the electron's *de Broglie* wavelength $\lambda_{dB} = \frac{h}{p}$, where p is the electron momentum and h is the Planck constant. Charging of the examined samples leads to a blurring of the image and also, depending upon the sample, to sample alterations due to residual impurity molecules being burnt into the sample. Thus, a trade-off between sample burning and magnification has to be made. The burn-in, lens effects, and other negative contributions effectively limit the maximum obtainable resolution.

During the course of this thesis, a *FEI Environmental SEM* was used for the imaging of the SWNT thin films, to determine morphology and surface coverage.

X-Ray Diffraction (XRD)

To study the composition and crystal axis alignment of perovskite single crystals x-ray diffraction (XRD) was used. The structure of a crystal can be resolved, as source and detector angle dependent scattering intensity data allows for the calculation of the distance between crystal planes. This technique is based on the measurement of resonance angle ϑ, using the *Bragg equation*

$$2d \cdot sin(\vartheta) = n\lambda, \tag{3.1}$$

and a known x-ray wavelength λ, allowing for the calculation of the distance between atomic planes. For more complex crystals like $MAPbI_3$, the simple Bragg scattering condition has to be replaced with a structure factor S_{hkl}, describing the distribution of atoms in the crystal unit cell and their scattering conditions.

Lead and hydrogen have different ionic radii, resulting in different atomic structure factors which are proportional to the atomic number. For this reason, it is easy to see the influence of lead and iodine on the XRD response of a $MAPbI_3$ crystal, but difficult to see any nitrogen and hydrogen influence. Depending on the accuracy of the XRD setup, domains and their size within a crystal can be determined.

The XRD data gathered for this thesis was measured on a *Rigaku SmartLab* XRD machine using the Cu-Kα line, which allows for high precision control of detector and x-ray source angle, and for precise goniometric movements of the crystal.

3.2.2 Conductivity Measurements

To determine the sheet resistance of SWNT thin films, the *van der Pauw* technique was employed, which is shown in Fig.3.6. For this, a sample of arbitrary shape is contacted at four point-like leads on the edge of the sample. Though for the smallest possible errors, the ideal shape is that of a square. Contacted on these leads, the four possible combinations of $R_{AB,CD} = V_{CD}/I_{AB}$ are measured. As $R_{AB,CD} = R_{CD,AB}$ due to the reciprocity theorem,

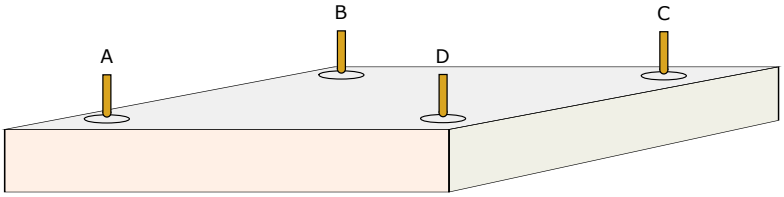


Fig. 3.6: Schematic showing the *van der Pauw* sheet resistance measurement setup, with gold-coated probe tips contacting the sample in four locations, and the letters A-D correspond to ones from Eq.3.2. In order to prevent scratching very thin fSWNT films, for these samples small conductive liquid silver dots of about twice the radius of the probes were applied to the sample.

calculating the averages of the horizontal and vertical measurements improves precision and result in $R_{vertical}$ and $R_{horizontal}$. These values are then plugged into Eq.3.2

$$e^{-\pi R_{vertical}/R_{sheet}} + e^{-\pi R_{horizontal}/R_{sheet}} = 1 \tag{3.2}$$

which can then used to calculate the sheet resistance R_{sheet}. This method is fairly insensitive to the actual size of the contacting leads, as the associated error scales with $\left(\frac{r}{D}\right)^2$, with lead diameter r and lead separation D [171]. Additionally, this method is also quite insensitive to a lead placement not perfectly on the edge of the sample, as the resulting error scales with $\left(\frac{d}{D}\right)^2$, where d is the distance of the lead to the sample edge [172]. The *van der Pauw* setup was realised in a custom setup, where four gold plated contacts were placed on the sample using four xyz-stages, and the currents and voltages where measured and supplied by a *Keithley 2450* source meter. To ensure proper calibration, a *NIST* 12 Ω/□ ITO sample was tested first before each measurement.

3.2.3 Optical Characterisation

Optical characterisation was the main tool used for perovskite characterisation, but also to measure the transmission of SWNT thin films.

Absorption Measurements

To measure the absorption spectra in the range from UV to the onset of IR, a *PerkinElmer Lambda 1050* was used. In this device, a set of different filters and lamps are used to produce

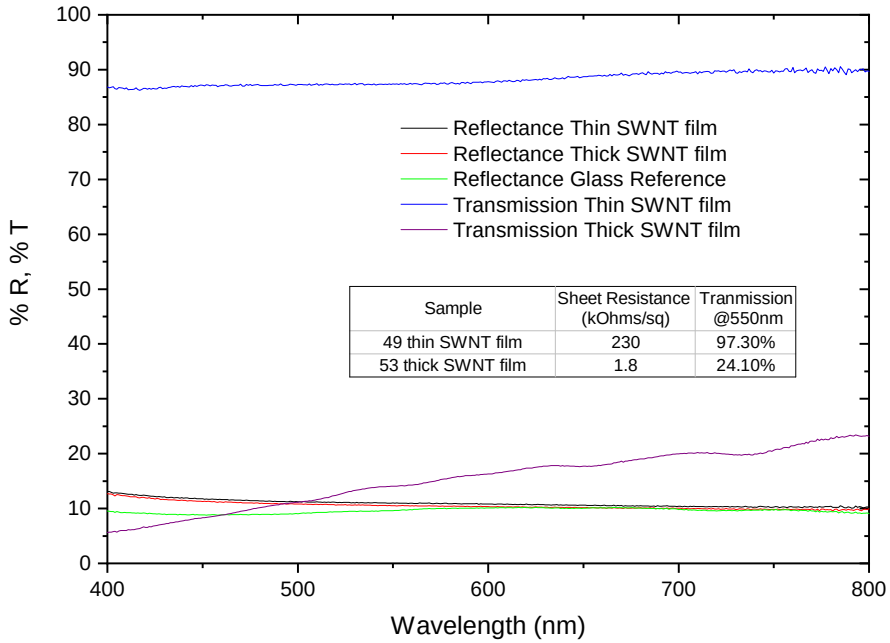


Fig. 3.7: Reflectivity and transmission of a thick and thin fSWNT sample on a glass substrate. As a comparison, the reflectivity of glass is shown also. As the reflectivity of glass is responsible for 10 % of the total loss in transmission, these can be deducted from all fSWNT film T_{550nm} measurements.

monochromatic light over a wide range for measurements between 200-1500 nm in steps of down to 1 nm.

For fSWNT thin films, an additional 10 % were added to all transmission measurements, to account for the reflectivity of glass, as shown in Fig.3.7. This treatment was performed, so the measurements are substrate independent, and comparable with values in literature.

Magneto-Optics Setup

A schematic of the *Oxford Instruments* super conducting solenoid magnet in its dewar is shown in Fig.3.8. The system can be swept from 0-19 T, and up to 21 T, when the helium reservoir surrounding the magnet is pumped. The magnetic field strength is controlled and set by an *Oxford Instruments Mercury iPS* system. The sample itself is in a variable temperature insert (VTI), which allows to set the sample temperature between 1.4 K and 300 K, using a heater and liquid helium. The liquid helium source is the main helium reservoir, which is connected to the VTI through a needle valve, and the heater is controlled with an *Oxford Instruments Mercury iTC* PID-system. The sample itself was placed in the sample

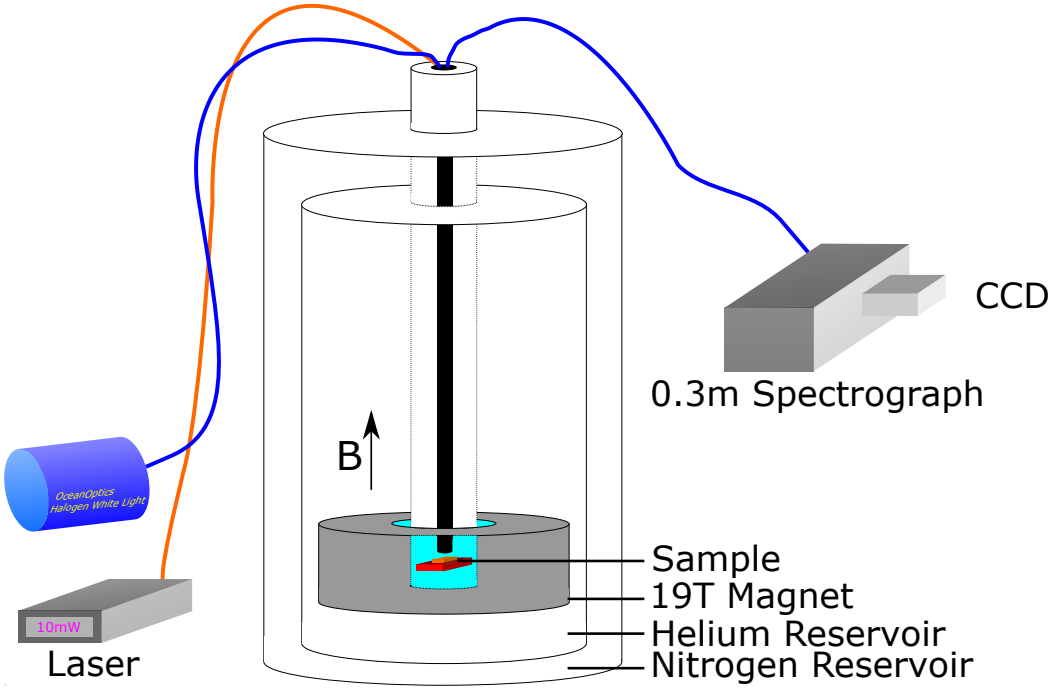


Fig. 3.8: Schematic of the magneto-optics setup, where either a halogen white light source, or a 532 nm/405 nm laser are coupled into a 500 µm UV to NIR bandwidth fibre leading into the magnet, where the light is focused by lenses on a $<1\,\mathrm{mm}^2$ spot.

holder shown in Fig.3.9, which can be modified to a thin film transmission and single crystal configuration. On the brass sample holder head a *Lake Shore Cernox CX1050SD-HT* resistance temperature sensor was attached with GE-varnish, to get an accurate temperature reading from close to the sample. The sensor was contacted by four-terminal sensing, in order to keep resistances from the contacting copper wires low. The Cernox was calibrated using an already calibrated temperature sensor with the calibration results shown in Fig.3.10. The effective temperature accuracy achieved with this sensor is only limited by the calibration, and can be assumed to be lower than 5 K over the entire experiment range from 1.4 K to 375 K.

Depending on the samples bandgaps, they were excited with either a custom-built 405 nm or *Laser Quantum ventus532* 532 nm laser for PL measurements. The lasers were passed through notch-, and short pass-filters and then coupled into a 500 µm UV-NIR fibre through a fish eye lens on an xyz-tilt-stage, to optimise coupling of the laser into the fibre. Transmission and reflectivity measurements where performed using a *Ocean Optics HL-2000-FHSA* halogen white light source which was coupled straight into the fibre per SMA connector. In

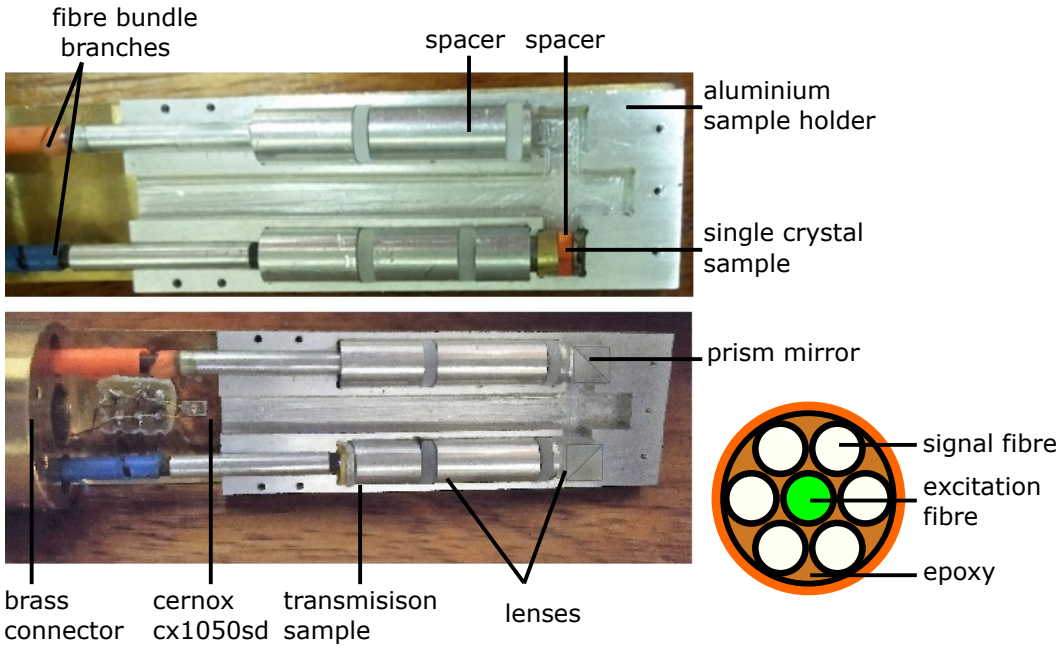


Fig. 3.9: Sample holder used for the magneto-optical experiments in both single crystal PL/reflectivity (top), and transmission/PL configuration (bottom). For the single crystal configuration, the blue fibre bundle branch alone is sufficient, for transmission both fibre bundles branches are needed. A cross-section of the fibre bundles is shown on the bottom right.

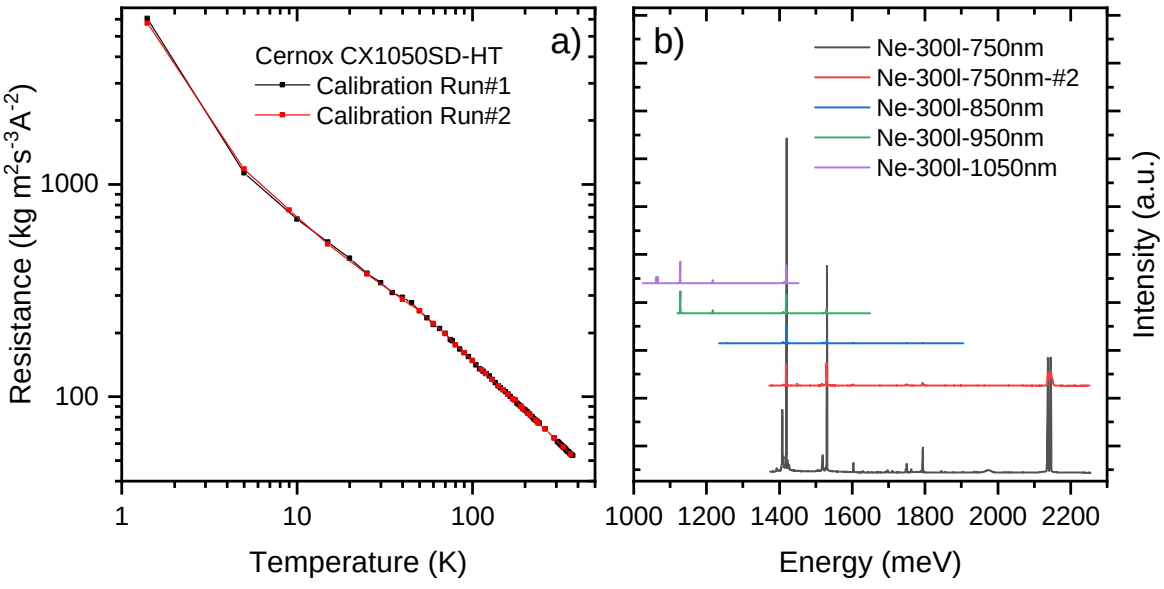


Fig. 3.10: (a) Two calibration curves of the *Cernox CX1050SD-HT* resistive thermometer. The error is estimated to be smaller than 5 K in the entire range from 1.4 K to 375 K. (b) Calibration spectra for the 300 line grating to set and calibrate the spectrograph for accurate wavelengths. The error of the wavelength calibration is estimated to be smaller than 1 meV in the range of interest,.

order to account for the excess signal due to internal reflections and others, background measurements without the sample where taken to correct transmission/reflectivity measurement data.

The signal from the sample was filtered through a long pass-filter and coupled into a 0.3 m triple grating 300, 1200, and 2400 line spectrograph. The spectrograph's central wavelength is tunable by changing the alignment of the central grating, and before each measurement the calibration was tested with a *Newport 6032* pen-style neon-calibration lamp, with spectra as shown in Fig.3.10. Additionally, an *Ocean Optics HG-1* mercury argon calibration lamp was used to test the initial calibration.

The *Andor iDus416A-LDC-DD* back-illuminated silicon CCD camera connected to the spectrograph has a high quantum efficiency (QE) for the entire UV to NIR range [173], guaranteeing good signal from all perovskite samples. The camera was cooled down to −65 K for all experiments, to ensure a good signal to noise ratio, and exposure times were set to 80 ms with 400 accumulations, to increase signal quality and limit influence of cosmic rays and other error sources.

4 Electrodes of Functionalised Single-Walled Carbon Nanotubes (fSWNT)

Flexible transparent conductive films (TCF) will become very important for use in future devices, where displays have curvature or are supposed to be transparent, as for curved car head-up displays and mobile devices. The rise of this nascent technology was shown by *Huawei*'s newly presented *Mate X*, and *Samsung's Galaxy Fold* at the MWC in February 2019, both featuring a foldable display. This is the first step in the direction of screens that cannot be broken or cracked. When flexible TCF are combined with the right high quantum efficiency emitters, they can even be highly transparent *and* emissive.

For the moment being, the gold standards for a TCF, both for touchscreen displays in smartphones and for novel solar cells, remain indium tin oxide (ITO) and fluorine doped tin oxide (FTO), both of which have excellent values for sheet resistance R_{sheet} and transmission at 550 nm T_{550nm}, but are expensive and brittle, or rough and brittle respectively. These two do not fulfil the needs for novel applications requiring flexible TCF. One contender that could fill this gap is polymer functionalised SWNT (fSWNT), which will be discussed here.

In this chapter, the properties of networks of fSWNT and the efficacy of different deposition methods are examined. This includes morphology and surface characterisation by SEM and AFM, and characterisation of the optical and electrical properties of these networks, or thin films. All of these properties are of interest and necessary for the understanding of optimisation pathways resulting in fSWNT thin films of solar cell electrode grade. In

order to be able to discern effects that are due to changes in the deposition methods, these are studied in the first section. Next, the effects of morphology on optical and electrical properties are studied, followed by the effects of doping on these films. Lastly, the stability of these transparent conductive thin films (TCF) will be discussed.

4.1 Investigation of Different Deposition Methods

As an introduction to the solution-deposited fSWNT thin films produced for this study, Fig.4.1 showcases a drop-cast fSWNT film sample with a low magnification and high magnification SEM image. In these images, different structures are visible; at low magnification an issue is visible in form of dirt, caused by the transport from clean room to SEM-lab and sample loading. Also noticable are darker patches which at higher magnification can be discerned to be due to fluctuations of fSWNT area coverage. Moreover, the average fSWNT bundle diameter can be determined from these images to be 39 ± 17 nm, implying bundles consist on average of 19 ± 8 fSWNT [174].
The following three methods introduced below were not the only deposition techniques investigated, but rather the techniques yielding the best results.

4.1.1 Drop-Casted fSWNT Films

Drop-casting of fSWNT ink onto a substrate is a facile method to obtain low sheet resistance films, at the cost of uniformity of the deposited layer. One of the driving forces behind the fSWNT distribution anisotropy is the so-called coffee ring-effect. This effect causes fSWNT in the solution to aggregate at the substrate-air-solution borders, as solvent from the centre of a droplet cannot evaporate. The resulting convection of liquid from the centre to the surface accumulates fSWNT there. This can be controlled by adding surface tension reducing additives, but the additives considered for this study did not improve the film-inhomogeneity nor improve sheet conductivity.
Instead, to counteract the coffee ring-effect, solvents with a range of different boiling solvents, chlorobenzene, dichlorobenzene, chloroform, n-methyl-2-pyrrolidone, toluene, and o-xylene, were tested with the lowest boiling point solvent chloroform performing best. In order to

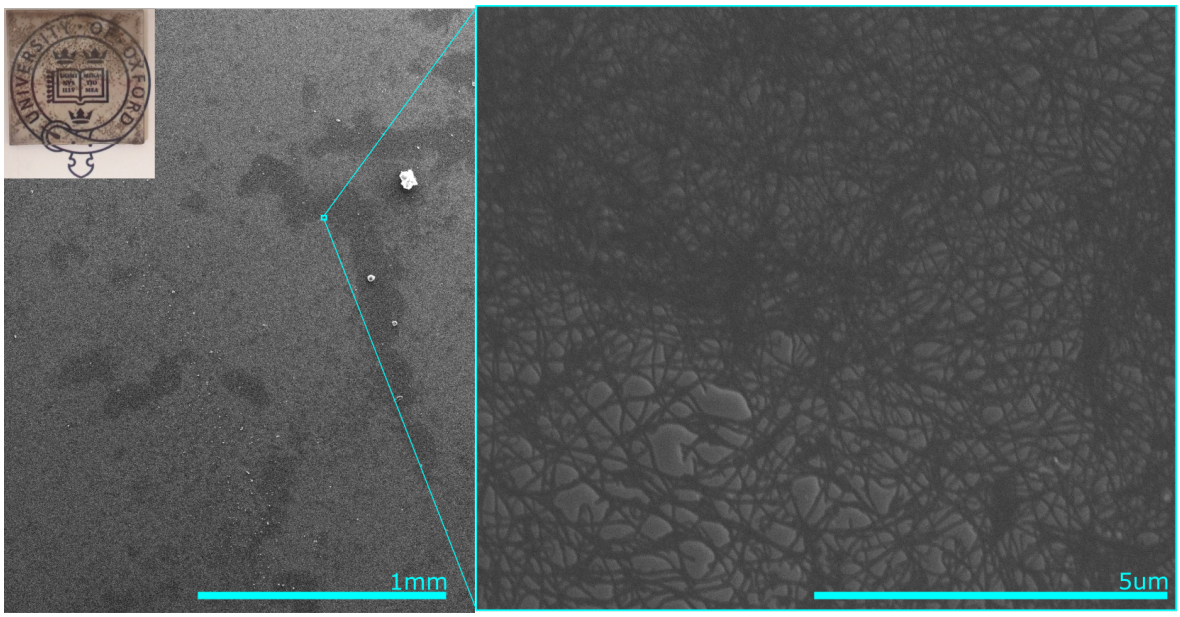


Fig. 4.1: Left: SEM image of a drop-cast SWNT film of P3HT:CG300, i.e. CG300 tubes functionalised with P3HT. An overview of the sample is given at low magnification, showing darker patches and some dirt on the sample. The inset shows the entire sample and the areas of different fSWNT density visible to the bare eye. Right: Magnification of the area highlighted by a teal box in the left image, focusing on the border between a darker/brighter patch. This shows that the dark patches are areas of higher fSWNT density. Moreover, it shows a high degree of bundling due to the drop-casting deposition method, with an average bundle diameter of 39 ± 17 nm, with diameters constant between darker/brighter areas. The scale bars correspond to 1 mm and 5 µm respectively.

decrease the coffee ring-effect even further, the fSWNT concentration was reduced to below $0.1\,\mathrm{mg\,mL^{-1}}$, one-tenth of the concentration of the standard recipe. Angling the substrate at a 45° angle for the deposition, as shown in Fig.3.3, yielded further improvements, ameliorated even more by heating the substrate to 60 °C which is the boiling point of chloroform. The optimised method led to a linear trend between film thickness and layers deposited, as shown in Fig.4.2 (b). The large variations in sheet resistance in Fig.4.2 (a) for films produced by this method are a result of the sample inhomogeneity. Correspondingly, both transmission and sheet resistance as shown in Fig.4.2 (a) have to be considered *cum grano salis*, as they are only a representation of some higher conductivity areas, and a mixture of high and low fSWNT density transmission. Another issue is visible in Fig.4.3, where an AFM map shows a uniform sample of debundled individual tubes, but also excess polymer that increases the samples roughness.

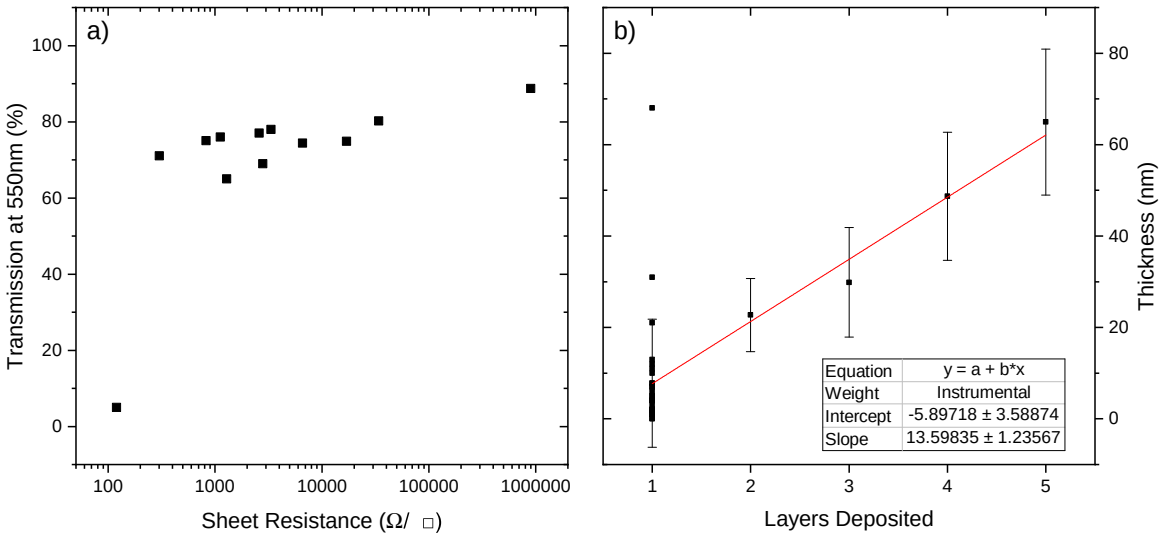


Fig. 4.2: (a) Transmission of P3HT:CG300 fSWNT drop-cast onto glass substrates. Samples show large variations, despite similar deposition. The two outliers shown here mark extreme cases of the best/worst sample obtained. (b) Linear trend of the fSWNT film thickness depending on the amount of fSWNT solution deposited. The error bars are not to be understood as the standard deviation, which would imply a normal distribution, but rather as an idea of the spread of values. To showcase this, for the first data points all measurements are shown.

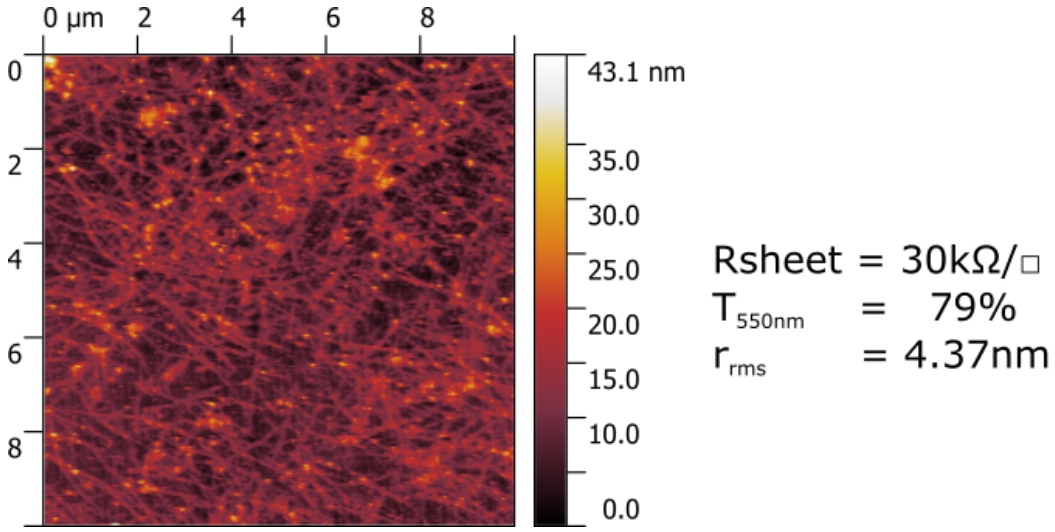


Fig. 4.3: AFM map of a drop cast sample. Locally, the sample is highly uniform and shows full coverage of the mapped 10x10 µm. The global behaviour can be seen in Fig.4.1. Transmission T_{500nm} is only 79 % due to residual P3HT clusters, which also greatly increases the rms roughness of the sample. The thickness of this sample was within 5 to 35 layers of SWNT.

4.1.2 Spin-Coated fSWNT Films

Drop by drop spin-coating enables quick deposition of fSWNT layers of variable thickness, depending on the amount of fSWNT ink deposited. An example of two P3HT:CG300 fSWNT samples, i.e. CG300 tubes functionalised with P3HT, are shown in Fig.4.4. These two films show the two extremes of a few fSWNT thick layer, and complete coverage. For the thin layer created by depositing a small amount of solution, the resulting film is sparse and non-uniform, the edge of the substrate showing a lower fSWNT concentration. The origin of this distribution is the centrifugal force $F_{cf} = m\omega^2 r$ scaling with mass m, forcing tubes and especially long tubes towards the edge of the substrate. Only after the deposition of a sufficient amount of tubes to completely cover the sample, will the layer become more uniform, as shown in the inset of Fig.4.4. In this sample, excess polymer residue is visible and only very thick bundles are visible. In fact, the layer is highly specular due to its polymer-smoothed surface.

As shown by these two limiting cases, it is necessary to compare the deposited volume with the resulting properties of the film. For each increase in the amount of deposited solution, an increase in film thickness following a roughly linear trend and increase was seen, as shown in Fig.4.5. In the same figure, the dependence on deposited volume of sheet resistance and transmission are given, showing a large spread of values. The spread of these values lies in the spin-coating method's sensitivity to height of droplet drop, impact angle and velocity for the deposition resulting in differences in homogeneity. Other solvents (dichlorobenzene, chlorobenzene, n-methyl-2-pyrrolidone, dichloroethane) resulted in worse films than chloroform, as their higher boiling point ensures that more of the fSWNT can be re-solubilised and redeposited in other areas of the substrate, increasing clustering of the tubes and film inhomogeneity.

Optimisation of this deposition method showed that the best results are yielded by very high loads of fSWNT in the deposited solution at about $0.5\,\mathrm{mg\,mL^{-1}}$ concentration. The high fSWNT concentration leads to both more uniform layers at the centre of the substrate, and thicker layers. For each additional droplet, the fSWNT can then more easily be trapped by the already deposited fSWNT.



Fig. 4.4: On the left an image of a thin fSWNT film on a glass substrate is shown, deposited by spin-coating. The sample shows the characteristic distribution of fSWNT, low at the sample edges and centre, high in the intermediate range. On the right a SEM image of a thick fSWNT layer with R_{sheet} =174 Ω/□ is displayed. The inset shows a photo of the same layer with contacting dots for conductivity measurements, and a reflection on the specular surface.

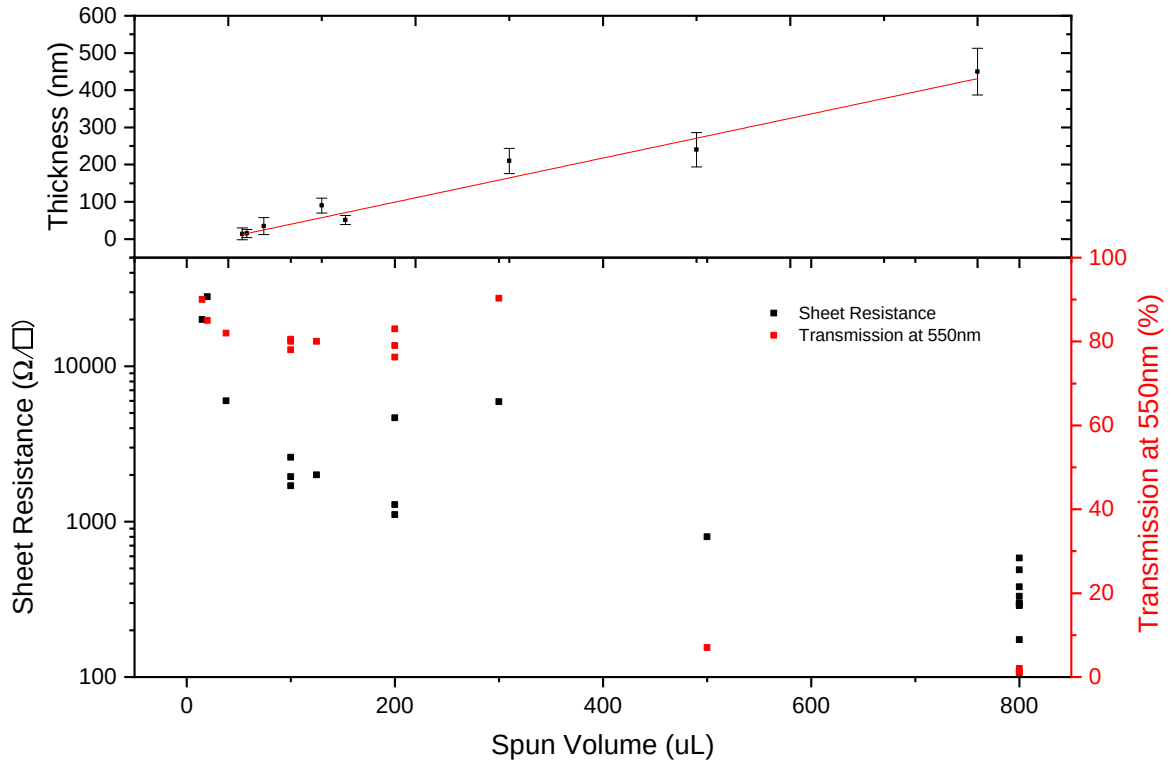


Fig. 4.5: Influence of amount of deposited solution on thickness of the resulting layer (top), and the resulting sheet resistance and transmission at 550 nm of the films (bottom). To give a better idea of the outliers and the distribution of values, R_{sheet} and T_{550nm} are displayed as scatter plots. It has to be noted, that thickness close to the centre and closer to the edge of the sample tend to be different, with more material deposited towards the sample edges.

While the films produced by this method showed good results and for thicker films good uniformity, this method does not allow for scaling up. For thin layers, scratching the substrate into a *van der Pauw* clover leaf design resulted in up to a factor 10 higher resistances due layer non-uniformity.

4.1.3 Spray-Coated fSWNT Films

The first films sprayed from the alpha version of the *LANDS* [163] spray-coating setup yielded values of 5358 $\Omega/\square$ for a thickness of about 85 nm and a transmission $T_{550nm} = 82\,\%$, for a SDBS:H_2O-solution, as the first iteration's tubing was not chloroform proof. After these promising results, the spray-coater was retrofitted with PTFE-tubing, and the parameter space of spray head height, substrate heater temperature were tested for optimal values. The ideal parameter tuple should ensure that the chloroform mist emitted by the spray head nozzle is fully evaporated before it contacts the substrate. Thus, wetting of the substrate surface is prevented and the fSWNT layer will be homogenous. The best results were obtained at 10 cm and 100 °C, a temperature that was already close to the maximum heating capacity of the 100 W substrate stage heater. This compromise of nozzle height and temperature ensured that most of the chloroform evaporated before touching the substrate, ensuring that no fSWNT were washed off, and clustering was minimised. The film shown in Fig.4.6 (a) shows an early example of a sprayed P3HT:HIPco film, where the fSWNT concentration, 0.5 mg mL^{-1}, and residual amount of P3HT was so large, that the film was almost completely opaque. The same figure also contains SEM images (b-e) of an ink concentration optimised film, which is highly uniform on a large scale, showing perfect coverage with fSWNT, but also a surplus of polymer bundling tubes together.

The resulting sheet resistance and transmission T_{550nm} values in Fig.4.7 show an even, continuous spread of the data for the sprayed tubes, without any outliers. The small variation that is visible for the T_{550nm} of the sprayed films is likely a result of a slightly higher/lower residual amount of P3HT in the sprayed fSWNT ink. The best sprayed film consisting of P3HT:CVD had a sheet resistance of 947 $\Omega/\square$ and a transmission of $T_{550nm} = 66.5\,\%$. As a comparison, results of some drop-cast and spin-coated are included, showing a much larger variation, mainly due to issues of homogeneity and issues in reproducibility.

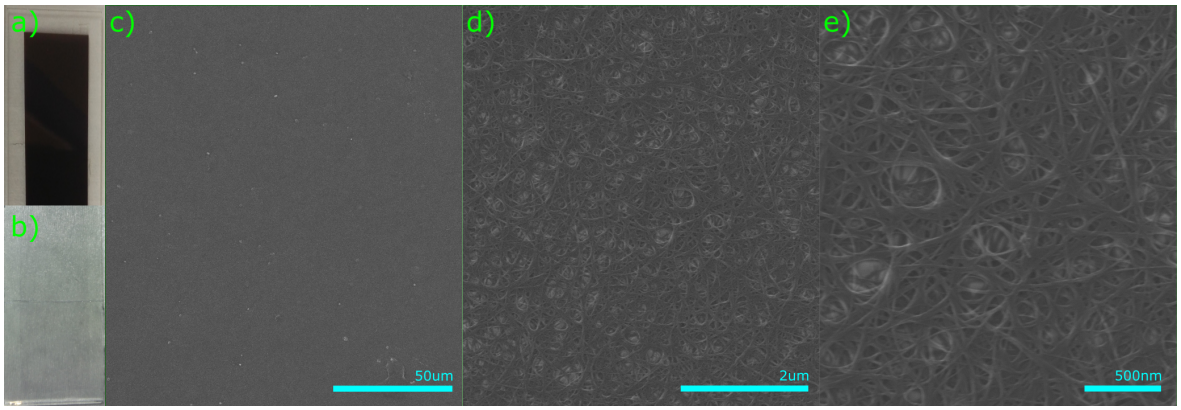


Fig. 4.6: (a) Photo of a P3HT:HIPco fSWNT solution of 0.5 mg mL^{-1} concentration sprayed on glass. (b) Photo of a P3HT:HIPco fSWNT solution of 0.075 mg mL^{-1} concentration sprayed on glass. (c) SEM image of a spray-coated sample showing large area uniformity with some dirt on top.(d-e) Magnification of (c), showing an ~three to four layer thick film, where some of the glass substrate is visible through holes in the layer. Averaging over 42 bundles yields a width of 14.5 ± 9.8 nm, implying an average bundle consists of 7 ± 5 fSWNT. The scale bars correspond to 50 µm (c), 2 µm (d), and 500 nm (e).

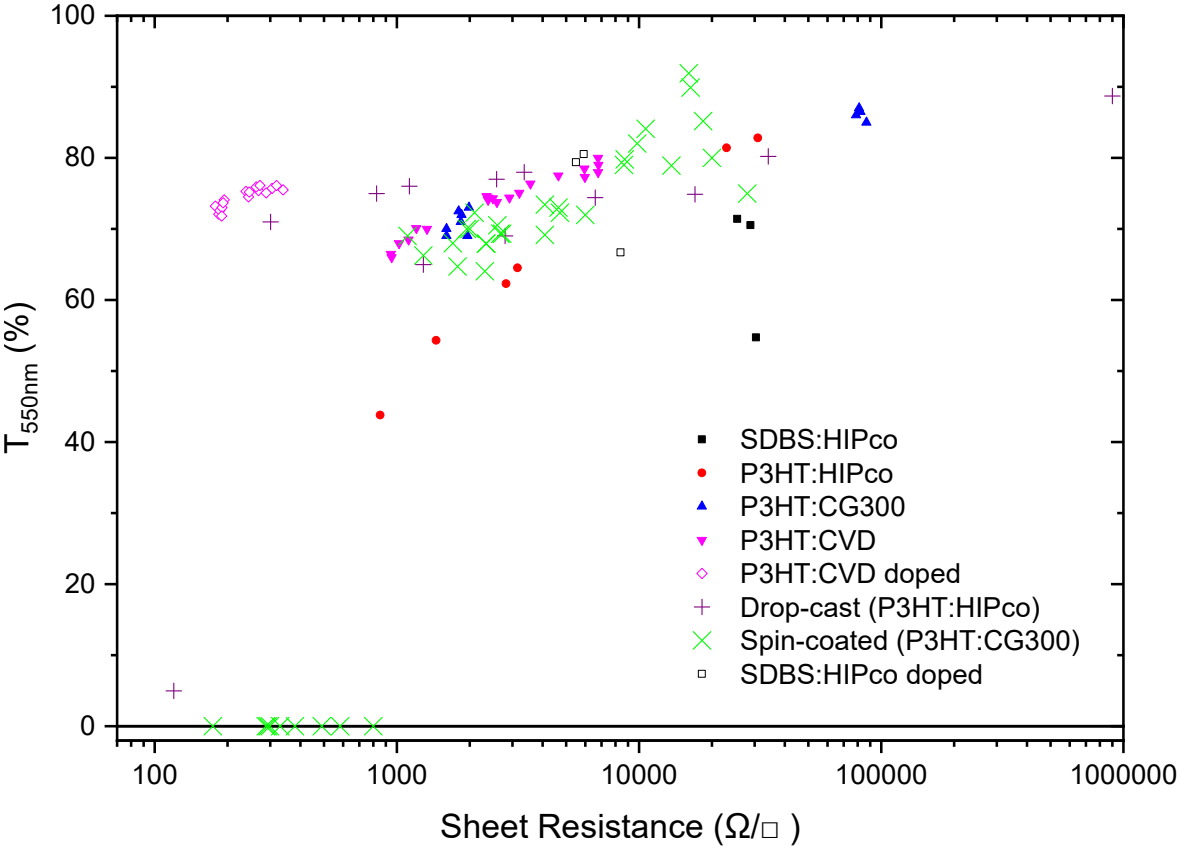


Fig. 4.7: Summary of all transmission T_{550nm} and sheet resistances for spray-coated samples. As a comparison, some spin-coated and drop-cast samples are included, as well as the values for doped P3HT:CVD and SDBS:HIPco samples.

In comparison to the other deposition techniques, spray-coated films show both high uniformity and low sheet resistance/transmission, making it the best technique tested. Correspondingly, all further tests where performed on spray-coated samples.

4.1.4 Deposition Techniques Summary

As a summary, the average and best results obtained from the different deposition techniques are given in Table 4.1. While the values for drop-cast and spin-coated samples show good

Table 4.1: Overview of different sample deposition techniques and resulting sheet resistance, with values of best samples in brackets. Average thickness and roughness r_{rms} are given for best samples. As a comparison, values for FTO/ITO are given (data from various suppliers [175–177]):

Method	R_{sheet} ($\Omega/\square$)	T_{550nm}	r_{rms} (nm)	Thickness (nm)
Drop-Casting	824* (301)	85% (82%)	4.3*	10*
Spin-Coating	2183 ± 1194 (1107)	70%(69%)	6*	96 ± 21
Spray-Coating	1095 ± 152 (951)	68%(66%)	7 ± 4	25 ± 4
ITO	4-100	78-88%	1-1.8	0.15-2
FTO	6-14	76-84%	12.5-45	200-600

*Errors omitted as underlying values are not normal distributed and misleading.

values for R_{sheet} and T_{550nm} in comparison to spray-coating, their reproducibility is poor. For example for the drop-cast samples, film thickness follows a roughly bimodal distribution. These two effectively sequential methods can wash away some of the already deposited material with each new deposition step, and re-aggregate it in other places. In contrast, spray-coating with the right settings deposits a vapour of fSWNT with only trace amount of residual chloroform, resulting in superior films, which can be scaled up to deposition on an arbitrary-sized substrate, to achieve values comparable to ITO/FTO as shown in Table 4.1. One issue all methods have in common is the too high share of residual polymer in the thin film. To counter this, different pre- and post-deposition treatments were tested. One method tested was rinsing and or submerging of samples in solvents that have a low solubility for P3HT, to try and redissolve the polymer not attached to tubes. The tested toluene, tetrahydrofuran, and dichloromethane have decreasing solubility for P3HT in that order [178], and all three did not improve transmission and sheet resistance. In contrast, a further three purification steps with toluene for the precusor fSWNT ink led to improvements of up to 6 %

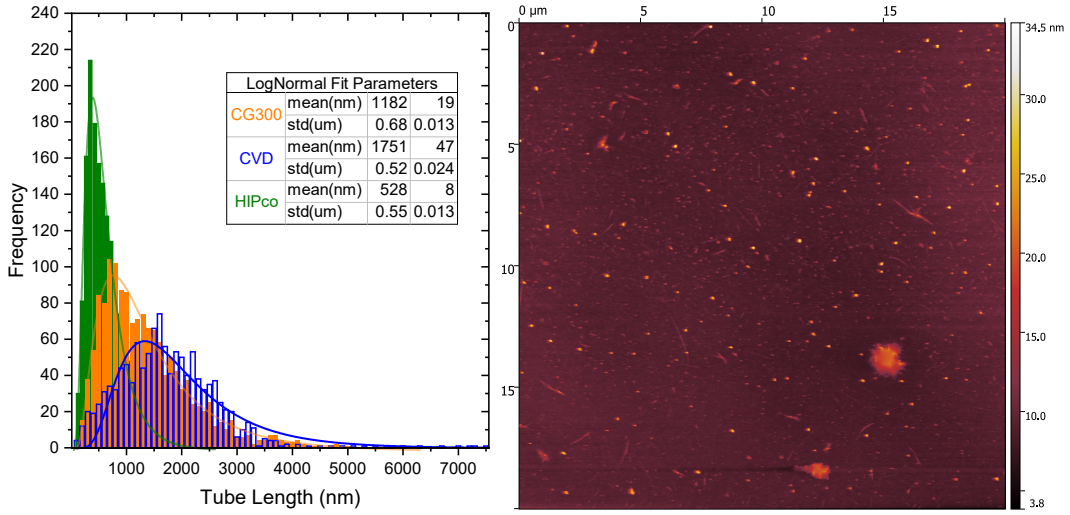


Fig. 4.8: Left: Histogram of tube lengths as determined from AFM maps for the three different species CG300, HIPco, and CVD tubes. All distributions show a good fit to a log-normal distribution with the fit parameters for mean μ and standard deviation σ. Right: Example of one of the AFM maps used to determine tube lengths. This specific sample features P3HT:HIPco fSWNT deposited on a silicon-oxide wafer.

in sheet resistances. The likely reason only a small improvement occurred is that an increased sonication time results in shorter tubes, as their length L scales with the sonication time t following $L \approx t^{-0.5}$ [179]. Baking of the fSWNT films in air or vacuum was suggested in some accounts on fSWNT FETs in literature [180, 181] suggesting that a burn-in at over 200 °C in air is sufficient to burn off polymer side-chains and improve device performance. For the films produced for this study, only small non-reproducible improvements for transmission or conductivity manifested, but the heat treatment did improve the cohesion of fSWNT film and substrate. Likely, minor improvement in some, but not all samples was due to the evaporation of residual solvents, and mild adsorbed oxygen p-type doping of the fSWNT [182]. The most effective improvement, post-deposition doping with nitric acid will be discussed in the next section.

It is of interest to note, that fSWNT films sprayed onto a flexible polyimide substrate show a 12 % lower R_{sheet} than a glass substrate sprayed in the same batch. This could be due to a higher substrate temperature, as glass is a poor heat conductor, or due to higher attraction between fSWNT/polyimide, as adhesion between SWNT and polyimide is so good that it can even be used to functionalise SWNT [183]. Moreover, polyimide is also highly transparent and flexible, making it a possible substrate for flexible fSWNT TCF.

To better understand the trends seen for the different tube species in Fig.4.7, fSWNT lengths were determined by depositing heavily diluted fSWNT ink on SiO_2, and determining fSWNT length from AFM. For CG300, HIPco and the used CVD tubes, the results are shown in Fig.4.8. After AFM mapping, the fSWNT lengths were determined by approximating with linear-order splines. The resulting histograms for HIPco, CG300, and CVD tubes can be well fit with log-normal distributions, showing an increase in length from 528 nm for HIPco to 1182 nm for CG300, to 1751 nm for the CVD tubes. This result agrees well with literature [184], which predicts lower sheet resistances for longer tubes, as described in Ch.2.1.2. It also shows that the critical parameter to optimise in order to obtain a good fSWNT TCF is the length of the used tubes, in order to achieve the necessary minimum of 500 $\Omega/\square$ with a transmission higher than 70% for device applications.

4.2 Doped fSWNT Films

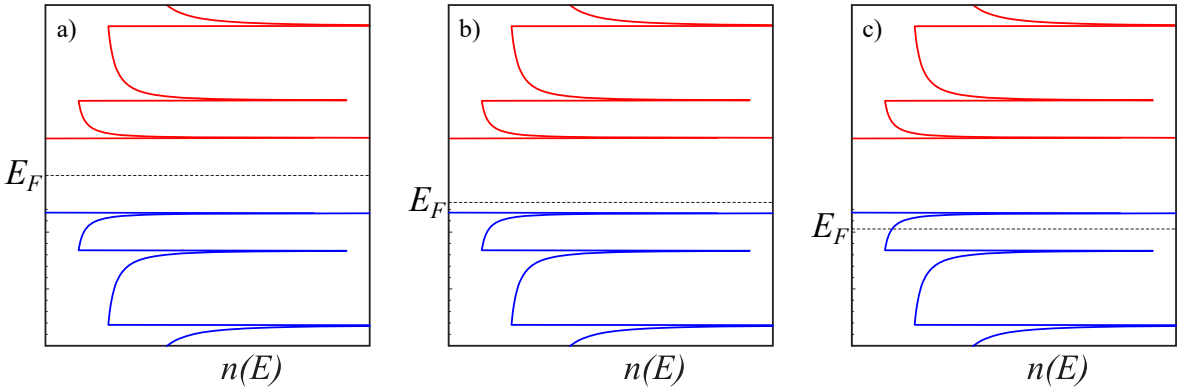


Fig. 4.9: Effect on the electronic density of states of an SWNT after doping with a very electronegative molecule, like HNO_3^+. The resulting shift of electrons from SWNT to a dopant molecule will reduce the amount of electrons in the SWNT, lowering E_F. (a) Undoped SWNT DOS. (b) For smaller diameter tubes with large bandgap, the doping will lower E_F, making the tube slightly p-type and increasing conductivity. (c) In an extreme case, the resulting drop in E_F can change a tubes type from semiconducting to metallic, reducing the resistance between tubes and increasing a SWNT-networks conductivity.

In the previous section, it was established that excess residual polymer is a problem for the fSWNT TCF, as it both decreases tube connectivity, and lowers absorption. One possibility to ameliorate these issues is doping and etching with, e.g., nitric acid (HNO_3^+). The general pathway of the effects of doping are shown in Fig.4.9. A highly electronegative ion can

attract some of the SWNT's electrons and thus dope it by inducing a shift in Fermi-energy E_F. This shift will make the tube more p-type, shifting E_F towards the valence band. For small diameter tubes with a large bandgap, or for weak dopants, this will result in a small shift of E_F as shown in Fig.4.9 (b). For strong dopants and or large diameter tubes, the doping can shift E_F into the first valence band, making the tube metallic [185], or if it is metallic it will increase the charge carrier density[1]. This shift can be shown via Raman [41, 186] and XPS measurements [187]. More directly, the shift of E_F into the valence band can be shown by the disappearance of the E_{11} and E_{22} absorption lines in UV-vis measurements as in Fig.4.10 (a). There the E_{11} lines between 1050-1600 nm are reduced greatly, and the E_{22}, lines between 400-900 nm are also greatly reduced, as shown in Fig.4.10 (b). The duration of soaking in nitric acid had a very small, if not negligible, influence on the doping efficacy. Independent of soaking duration, the majority of E_{11} and E_{22}, but also E_{33} absorption lines disappeared, making it likely that the Fermi-level of metallic tubes was also pushed into the valence band. Examples of the post-doping decreases in sheet resistance and absorption in comparison to undoped samples are shown in Fig.4.7, showing the enormous improvement of doped over undoped samples.

The combination of increased charge carrier densities in metallic tubes with the now metallic behaviour of semiconducting tubes, reduces the sheet resistance by a factor of three. Improved contacts between tubes, changing from Schottky to ohmic contact, are the likely origin of this improvement. This is the same factor as for non-polymer functionalised tubes [41, 188], showing that the polymer is not limiting the efficacy of the doping.

It is of interest to note, that the majority of the improvement for transmission occurs in the P3HT absorption range $\leq$650 nm (c.f. Fig.3.1). The reason for this decrease is the oxidation of the thiophene ring. More specifically, the sulphur in the thiophene ring is oxidised to sulphur trioxide and sulphuric acid [189], which can also be used to p-dope SWNT [188, 190]. Without the thiophene ring, the residual polymer's absorption drops strongly, greatly benefiting the T_{550nm}, which is the only transmission value given for most SWNT TCF in literature.

[1] Multi-walled nano tubes, which show an averaging of the properties of the tubes they consists of, show up to a 10% decrease in sheet resistances due to this improvement for metallic type tubes.

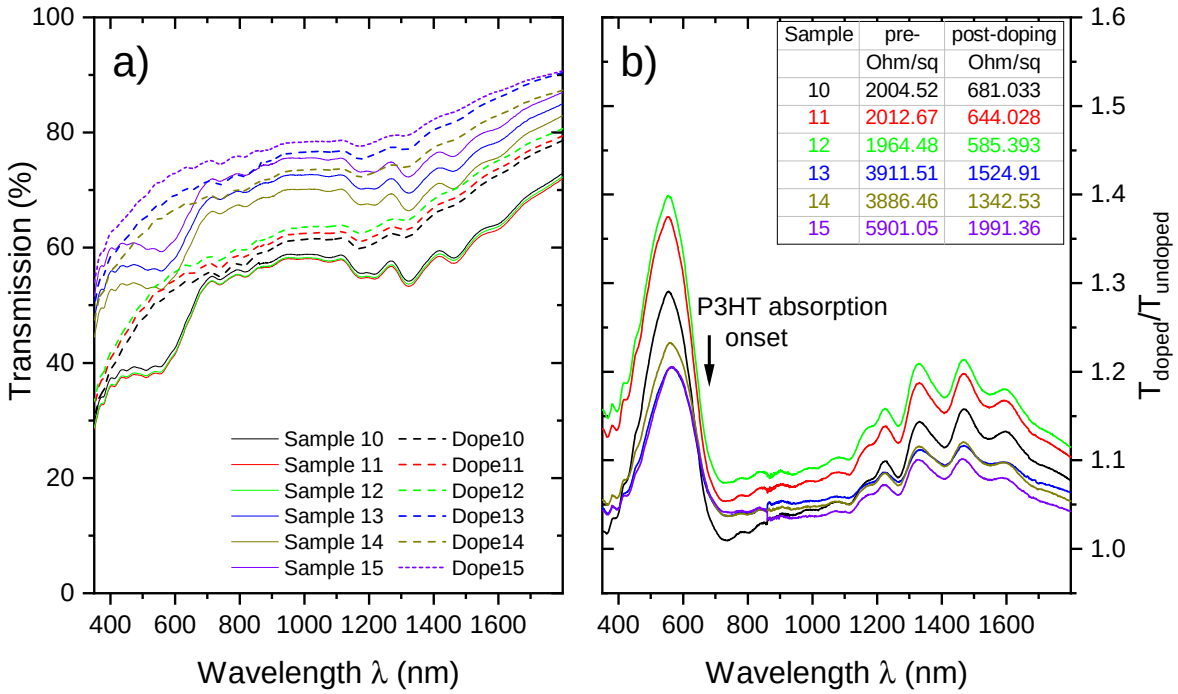


Fig. 4.10: Six different P3HT:HIPco samples with two different concentrations deposited. (a) Effect of nitric acid doping on transmission of the sprayed films. (b) Ratio of doped and undoped fSWNT film transmission, showing a large effect in the area of E_{22} lines, and the P3HT absorption band.

Most reports on SWNT networks in literature, c.f. Table 4.2 for some, are based on surfactant SDBS dispersed tubes. While these films show good transmission at T_{550nm}, their overall transmission is much lower than that of a P3HT fSWNT film. A comparison of both is shown in Fig.4.11, where the best P3HT:CVD film's and a SDBS:HIPco film's transmission are shown. While the absolute transmission cannot be compared due to differences in film thickness, comparing the general shape of the transmission curve proves the overall superiority of P3HT:SWNT based films. With the changes induced by the doping process on the thiophene ring, it became necessary to study the influence of doping on the morphology of the sample, to test if the changes to the thiophene ring influence overall sample morphology. Fortunately, as shown in Fig.4.12, doping only has a negligible influence and did not change the uniformity and or roughness r_{rms} of the sample. For some samples processed within the same batch, doping led to partial delamination of the fSWNT film from the substrate, as shown in Fig.4.13. Delamination was worse for samples that had not undergone oxygen-plasma treatment, giving an indication that residual dirt and bad contact between fSWNT

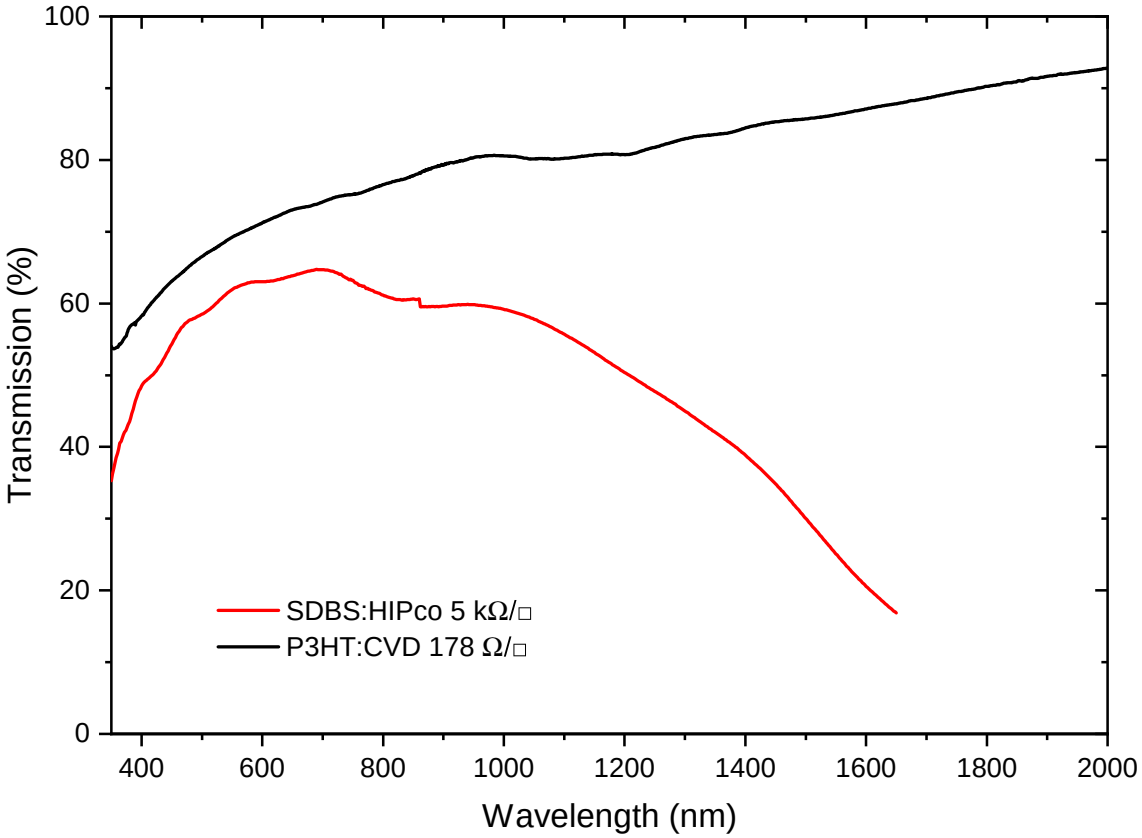
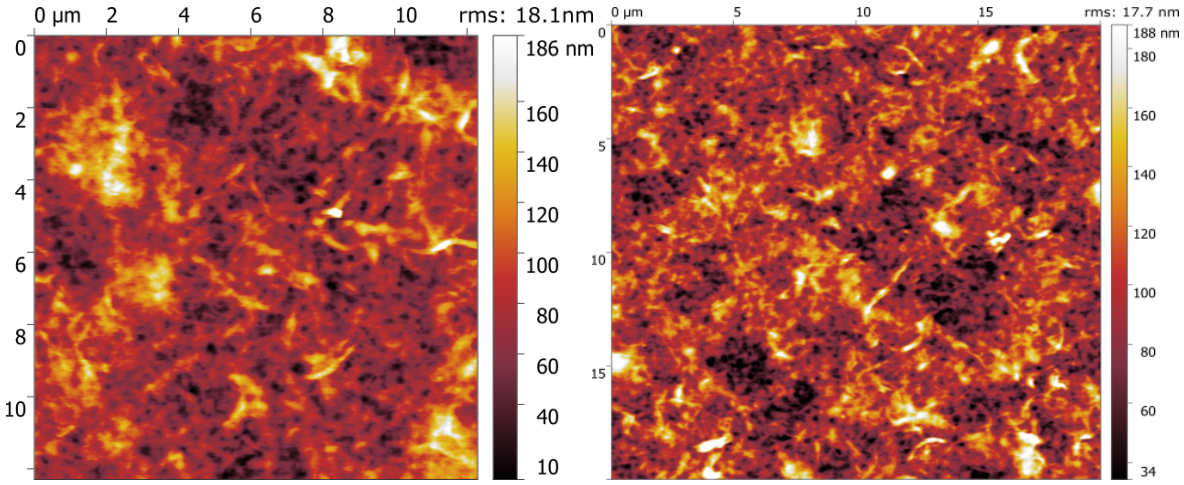


Fig. 4.11: Absorption spectrum of the best doped P3HT:CVD film produced for this study with a $T_{550nm} = 69\%$. As a comparison, the absorption spectrum of a doped SDBS:HIPco film is included also, to highlight the strengths of the polymer functionalised films with regards to transmission, especially in the near-IR region. The kink in the SDBS:HIPco data at 860 nm is due to a monochromator changeover and UV-vis instrument related.

network and substrate may be the origin of the delamination process. For some films, it was even possible to delaminate the entire film from the substrate without rupturing it, opening up the possibility to deposit on one substrate, lift the film off, and then re-depositing the fSWNT film on another substrate.

4.2.1 Stability

As the fSWNT doping is based on adsorbed or intercalated small molecules with good solubility in water, desorption under ambient conditions is a concern for these layers. To study the stability of doped fSWNT films, samples were stored under ambient English conditions (high humidity, low solar irradiance, low temperatures), to test film parameters over time.



(a) (b)

Fig. 4.12: AFM maps of (a) an undoped P3HT:CVD sample with r_{rms} of 18.4 ± 1.4 nm, and (b) of the same sample after doping showing a r_{rms} of 17.7 ± 1.5 nm, showing that doping has no influence on sample morphology. Averages and errors were obtained from measuring the sample's roughness in several different spots of the same sample before and after doping.



Fig. 4.13: P3HT:CVD TCF before (top) and after (bottom) doping with nitric acid, showing partial delamination, and an increase in T_{550nm} of about 15 %. The effective increase in T_{550nm} through doping is proportional to the amount of P3HT in the thin film.

The evolution for four samples over the course of 513 days is shown in Fig.4.14. Over the course of these 1.4 years, sheet resistance increased by 22 % on average. All four time series were well-fit by a logistic function,

$$f(x) = A_2 + \frac{A_1 - A_2}{1 + \left(\frac{x}{x_0}\right)^p} \tag{4.1}$$

implying an upper bound A_2, and a final value for the sheet resistance at about $1.31 R_{sheet,initial}$. For transmission, limited changes sub - 1 % were measured. Likely, the surface adsorbed HNO_3^+ molecules are washed away and removed by the storage in ambient conditions, with the intercalated molecules remaining in place. For the un-encapsulated

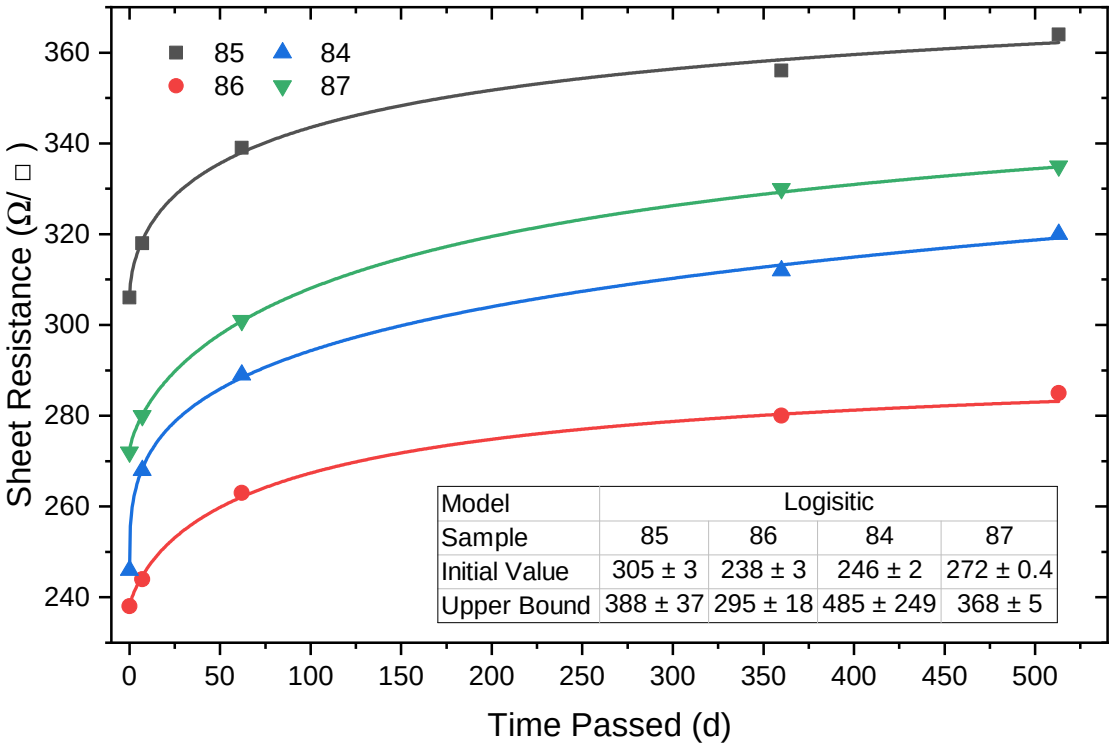


Fig. 4.14: Stability test for four HNO_3^+-doped P3HT:CVD samples over the course of 513 days of storage under typical English, ambient conditions, i.e. with high humidity, little sunlight, and low temperatures. The first measurement took place on the 3rd October 2017, the last measurement on the 28rd September 2018. The logistic fit curves serve as an guide to the eye and the fit parameters in the inset are an illustration of possible upper bounds for the sheet resistance.

usage in highly humid conditions this decrease is an issue, but when sandwiched between other layers in a device, this should not be a concern.

4.3 Summary

Single-walled carbon nanotubes show ballistic transport over great lengths, are flexible, and have a low absorption, as mentioned in Ch.2.1. These properties make them a contender for application as a transparent conductive thin film electrode in optoelectronic devices like bendable and foldable smartphones. One of the biggest issues SWNT TCF face is that the only established method for producing films of sufficient quality necessitates aqueous solutions. Unfortunately though, many technologies are water-sensitive. A possible solution is polymer functionalisation, which debundles SWNT and makes them soluble in a range of

Table 4.2: Overview of reported values for SWNT based electrodes, nitric acid (HNO_3) doped values marked with an asterisk:

Method	T_{550nm}	R_{sheet} ($\Omega/\square$)	Thickness (nm)	Tube Length
A [191]	42%	60*	130 ± 12	-
A [192]	75%	30*	50	-
A [181]	79%	120	40	-
B [193]	84% ± 2%	733 ± 26	12 ± 3	-
C [194]	80%	100*	-	-
D [195]	75%	80	80	-
E [196]	92%	1000	-	-
E [197]	81%	60*	-	-
F [37]	90.9%	60 ± 6	50	-
G [198]	68%	79.2*	-	-
H [199]	90%	128*	24	-

A: Filtration from aqueous SDBS solution; B: Drop-cast from SDS; C: Rod-coating; D: Filtered with PEDOT:PSS in H_2O; E: Sprayed from aqueous SDBS solution; F: Filtered from HSO_3Cl; G: Filtered compound with PEDOT:PSS in IPA; H: Spin-coated from dichloroethane

advantageous solvents like chloroform and toluene. To this goal, three different methods, drop-casting, spin-coating, and spray-coating, were tested for fSWNT deposition. The results from the first two methods show promise, but are challenged by their scalability and homogeneity of the produced films. Spray-coating does not share these issues, and produces films with good properties and homogeneity.

Unfortunately, these films do not show the desired high values of conductivity and transmission necessary for applications. A large part of this issue can be addressed by doping with, e.g., nitric acid. HNO_3^+ decreases the sheet resistance by about a factor of three, and at the same time improves transmission at 550 nm by up to 40%. Transmission in this region is especially important for applications, as it is around the wavelength region the human eye is the most sensitive to. Doping both greatly decreases the absorption due to excess P3HT, and at the same time also strongly reduces the SWNT E_{11} absorption lines. After 1.4 years, the doped samples stabilised at a R_{sheet} increased by 22 %.

Comparisons to other results presented in literature, c.f. Table 4.2, are difficult, as most papers omit at least one, and most commonly several out of the parameters sheet resistance, overall transmission, roughness, length of used SWNT, and distribution of these values. Cor-

respondingly it is difficult to compare the absolute results obtained here with literature, but despite this the values obtained here compare quite well.

The best sample, made with P3HT:CVD tubes, showed a sheet resistance of 178 $\Omega/\square$ with a T_{550nm} of 69 %, shown in Fig.4.11. Further improvements on this should be possible using longer tubes, allowing for higher conductivities and higher transmission due to decreased fSWNT density on the sample. These results are an excellent starting point for flexible films on polyimide substrates. Not only do fSWNT and polyimide show good cohesion, polyimide also has a very low absorption and is chemically resistant to HNO_3^+ and many solvents.

5 Magneto-Optical Properties of $Cs_2AgBiBr_6$

Organic inorganic metal halide perovskites are of great interest for application as semiconductors, with their facile synthesis and processing, combined with low defect densities. To date, thermal and environmental stability is still an issue, as the most prevalent organic formamidinium (FA) and methylammonium (MA) based hybrid perovskites are prone to decomposition under the influence of water, separating into a toxic and water soluble lead salt and an organic salt [200]. In order to both avoid using lead and at the same time increase the stability, double perovskites are an option. For these, the divalent lead is replaced by a monovalent and a trivalent species, like silver and bismuth for $Cs_2AgBiBr_6$.

Theory predicts a bandgap which depends on the degree of order and disorder of silver and bismuth octahedra. Either a direct bandgap of about 0.44 eV for a fully disordered B-site $Cs_2AgBiBr_6$ crystal, or a 1.93 eV indirect gap for a fully ordered crystal [201], with a direct gap of about 2.51 eV [202]. Experimental values in literature to date showed energies between 1.8-2 eV for an indirect gap [202–205], without clarifying the reason for the assignment of an indirect gap, and neglecting to mention the direct gap visible in their data.

In this chapter, the relation between optical properties and phase change is studied by both reflectivity (R) and photoluminescence (PL) measurements, establishing the value of the direct bandgap. The second part focusses on the magneto-optical properties at low temperatures, discussing the implications for the observed behaviour and nature of the PL emissions. Specifically, it will be detailed why the two PL emission correspond to a colour centre, and indirect bandgap emissions respectively. One of the crystals the optical experiments were

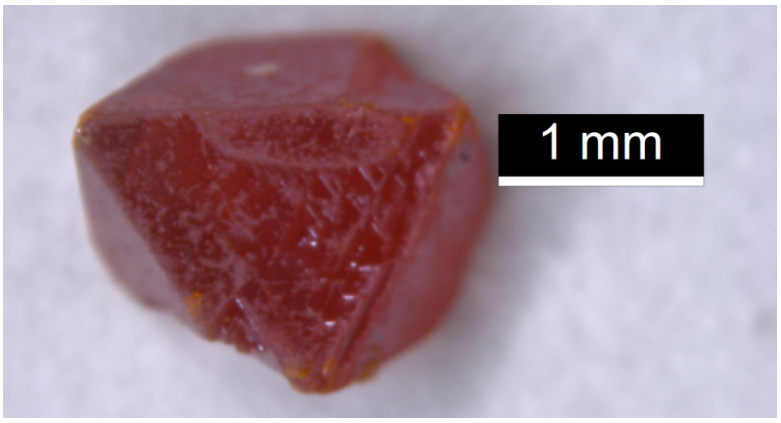


Fig. 5.1: $Cs_2AgBiBr_6$ crystal as used for the optical experiments. Single crystal grown by L.Schade, who determined crystal structure and composition by XRD and neutron diffraction experiments.

performed on is displayed in Fig.5.1.

The work in this chapter has been adapted and reproduced in part with permission from Schade *et al* [78] ACS Energy Letters 2019, 4, 299-305. Copyright 2019 American Chemical Society, and from Zelewski *et al* [206] Journal of Materials Chemistry C 2019, 7, 8350-8356. Copyright Royal Society of Chemistry. The XRD and neutron diffraction data shown here was measured by L. Schade and R.D. Johnson. PLE and high-field, and time-resolved PL measurements were performed by S.J. Zelewski and A.D. Wright respectively.

5.1 Optical Response at Room Temperature

The crystal studied for this chapter has fully ordered B-sites within the accuracy limit of the neutron diffraction experiment performed, and an has occupancy of 1.00 ± 0.05 on the B-sites. Further analysis of diffraction experiments show a phase change to a tetragonal $I4/m$ structure at about 122 K, with lattice parameters shown in Table 5.1.

Given these values, the expectation according to calculations is an indirect bandgap at about 1.93 eV [201], and a direct bandgap at about 2.51 eV [202]. These energies are close to the values seen for the higher energy PL peak, and the reflectivity signal in Fig.5.2 (a) and (b) respectively. The double PL emission structure visible in (a) has not been reported on before in literature, with the lower energy PL peak previously overlooked either due to lacking

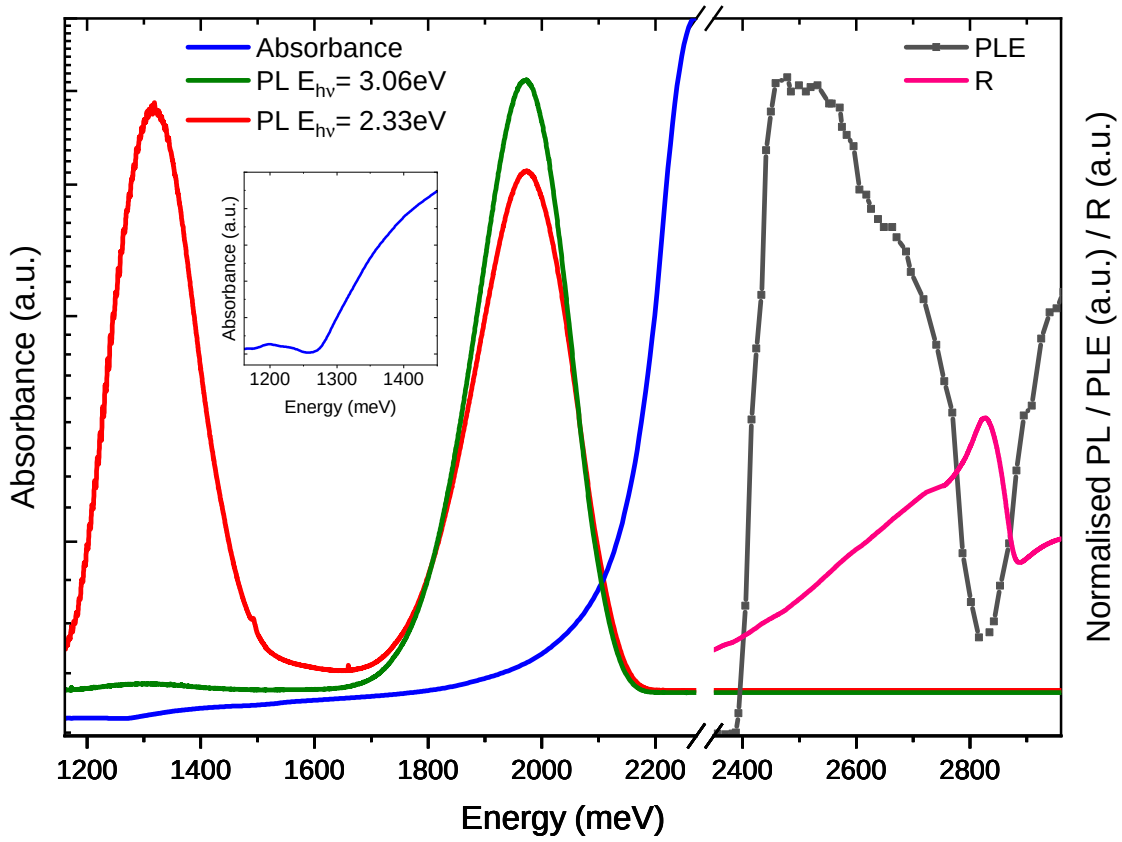


Fig. 5.2: Optical response of a $Cs_2AgBiBr_6$ single crystal under excitation with both a 405 and 532nm laser for photoluminescence (PL) and photoluminescence excitation (PLE) response, and a halogen white light source for absorption and reflectivity (R). There are two emission lines at 1.3 eV and 1.8 eV visible in the PL spectra, and one for the reflectivity measurement at 2.85 eV. The absorption measurement shows a first onset at about 1.28 eV, see inset, and another at 2.15 eV. PL, photoluminescence excitation (PLE) and reflectivity measurements displayed were done at 5 K, the absorption spectrum at room temperature.

detector sensitivity, or detector wavelength cut-off. The latter is especially likely, as both at room temperature and at 4 K, the lower 1.3 eV peak is weaker than the upper 2 eV PL peak for a 405nm excitation, as used for all reports found in literature. Henceforth, the upper energy PL peak will be referred to as PL-A, and the lower energy peak as PL-B.

The absorption measurement also shown in (a) confirms this double structure, with a weak first feature at about 1.28 eV, and a second at 2.15 eV. For the measured single crystal, after about 2.3 eV absorption saturates, but comparison with $Cs_2AgBiBr_6$ thin films [207] and nano crystals [204] show an absorption coefficient for the 3.06 eV excitation about four times

Table 5.1: Refined Crystal Structure Parameters of $Cs_2AgBiBr_6$ at room temperature (RT) and 30 K:

	NPD 30 K	NPD RT	PXRD RT
$a_{t,c}$ (Å)	7.8794(4)	11.2784(5)	11.27301(9)
$c_{t,c}$ (Å)	11.3236(7)	11.2784(5)	11.27301(9)
$V_{f.u.}$ (Å^3)	351.51(3)	358.66(3)	358.145(5)

NPD: Neutron powder diffraction; PXRD: Powder x-ray diffraction

larger than for the 2.33 eV laser excitation, which increases the sampled crystal share greatly for the 2.33 eV laser excitation.

In Fig.5.2 (b), the PLE signal is shown, which is a measure of the PL strength as a function of excitation energy. The PLE shows an onset at 2.4 eV, an energy much larger than both the PL-A and the upper absorption feature. This behaviour hints at a large Stokes shift and the importance of vibrational states. Another interesting feature of the PLE signal is that it does not grow monotonically, as normally expected due to the increasing density of states of bands above the bandgap, whereas here it shows a first peak after 2.4 eV, then a dip around 2.8 eV, and then increases again. When compared with the reflectance signal which shows the characteristic line shape of a resonance at 2.85 eV, this strongly suggests that the reflectance signal at 2.85 eV corresponds to the direct gap. The large difference between these R and PL measurements is an indicator of an indirect gap by at least 0.61 eV.

5.2 $Cs_2AgBiBr_6$ Temperature Sweep

To understand the behaviour of the crystal better, in this section the temperature dependence of the PL and reflectivity emission lines will be analysed.

5.2.1 Reflectivity (R)

The energy derivative of the reflectivity as introduced in Ch.2.1.3 is shown for the $Cs_2AgBiBr_6$ double perovskite single crystal in Fig.5.3 together with the raw reflectance data. The strength of the signal increases and becomes more narrow with lower temperatures. Moreover, after about 122 K a rapid change in peak position occurs, and at very low temperatures a secondary feature becomes visible in the spectra, which can be well fit with two reflec-

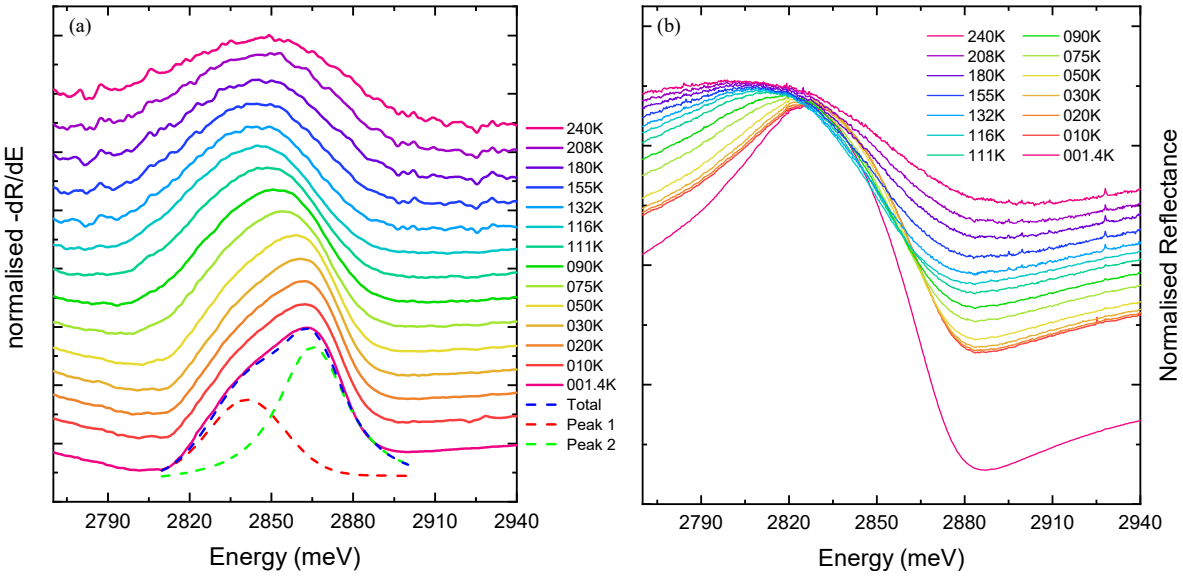


Fig. 5.3: Normalised, background reduced reflectivity (b) and $-\frac{dR}{dE}$ signal (a) for a range of temperatures between room temperature (RT) and 1.4 K. Strength of signal increases greatly at low temperatures. After about 120 K, a shift in energy is visible. For the 1.4 K $-\frac{dR}{dE}$ spectrum, the peak fit is shown which was used to determine the peak positions. For better visibility of the line shape, the spectra have been offset.

tivity peaks, as done in Fig.5.3 (a) for the 1.4 K data. The rapid change in peak energies corresponds well to the phase transition temperature known from XRD/neutron diffraction experiments, which is why a model was created to relate structural changes to the changes in bandgap that were observed. The small deviation of about 5 K between the phase change temperatures obtained by specific heat c_p, and the reflectivity data shown in Fig.5.4 is likely due to a temperature drift in the optical experiment, reinforced by the heating through the white light source. For this reason, the peak positions and the exciton energy E_X-model in Fig.5.4 were both scaled with the phase change temperature, to accurately compare model and experiment. Under the assumption of a temperature-independent exciton binding energy E_b, spontaneous tetragonal strain σ

$$\sigma = 2\,\frac{a_t - c_t}{a_t + c_t}, \tag{5.1}$$

and the volume change of the crystal were combined in the equation

$$E_g - E_b = c_0 + c_1\frac{\Delta V}{V_0} + c_2\sigma, \tag{5.2}$$

where V_0 is the 0 K unit cell volume, E_g the energy of the bandgap, where the exciton energy can be well described with the parameters $c_0 = 2683 \pm 1$ meV, $c_1 = 0.16 \pm 0.04$ eV and $c_2 = 1.01 \pm 0.02$ eV, as obtained from fitting the data in Fig.5.4. These parameters are a good description of the observed bandgap values, as both the phase change, as well as the bandgap energies are well described by Eq.5.2. Thus, the changes in energy seen above 122 K are due to crystal unit cell volume changes. As the volume decreases monotonically with decreasing temperatures, the tetragonal strain caused by octahedron rotation is the cause of the large changes in bandgap energy below 122 K, and correspondingly the ratio $c_2/c_1 > 1$. The value of 1.01 eV for the influence of increasing octahedron rotation on the bandgap is close to values observed for members of the $APbI_3$ perovskite group [208], and also similar to bandgap changes observed under variation of the Sn-I-Sn angles in tin iodide perovskites [209]. Thus the phase transition from cubic to tetragonal at about 122 K is well described by the structural changes as expressed by $a_{t,c}$ and c_t, and by the changes of the bandgap as determined by reflectance.

At 1.4 K the FWHM of the $-\frac{dR}{dE}$ peak is down to 60 meV and an almost resolved split into two peak components is visible in Fig.5.3. The splitting of about 25 meV can be well described with a double reflectivity peak fit. These two fits combined describe the entire peak at 1.4 K well, and result in a peak area ratio of 1:2. The resolution of an exciton 2s state can be excluded, as the secondary peak appears at lower energies. Instead, the origin for the split lies in the octahedral rotation $Cs_2AgBiBr_6$ undergoes in the tetragonal phase. The resulting decrease in lattice parameter a_t caused by the rotation and tetragonal strain lifts the Γ bandgap degeneracy. As two directions are equivalent and only one, c_t, out of three unit cell vectors remains the same at about 11.3 Å, see Table 5.1, the 1:2 split results.

5.2.2 Photoluminescence (PL)

Photoluminescence measurements collected between room and low temperatures with an excitation wavelength of both 405 nm, and 532 nm are displayed in Fig.5.5. Qualitatively, both excitation energies cause two PL peaks at the same energies that show small variations in peak position over the measured temperature range, albeit a larger variation for the higher energy PL-A emission line. At 1.4 K, the peak positions are 0.9 eV and 1.5 eV below

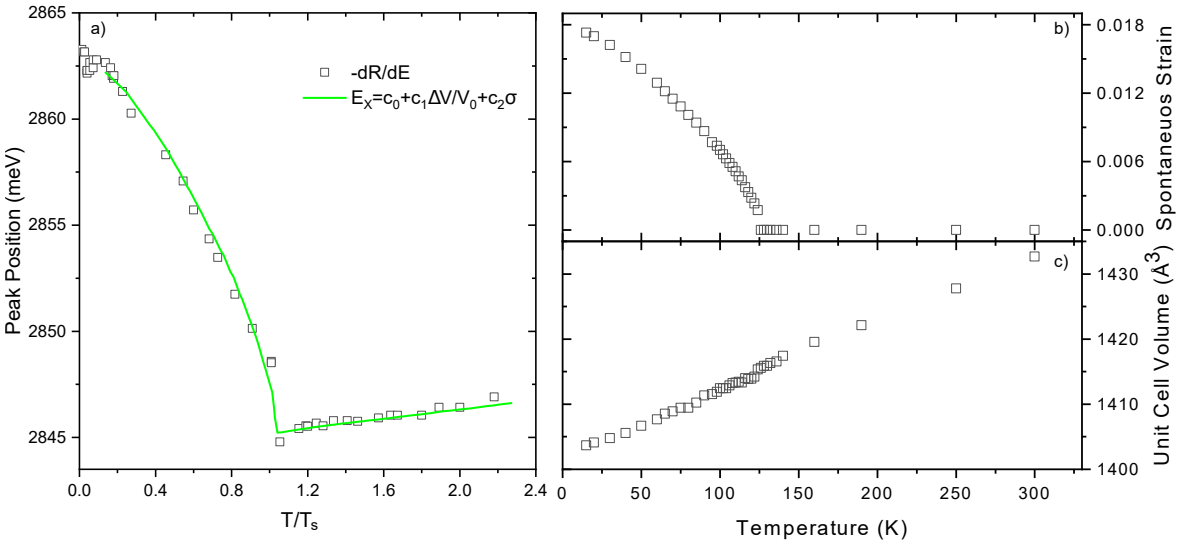


Fig. 5.4: (a) Reflectivity derivative $-\frac{dR}{dE}$ peak positions together with the modelled exciton energy obtained from Eq.5.2, showing the linear dependence between tetragonal strain and exciton energy in the tetragonal phase. To account for a temperature deviation between $-\frac{dR}{dE}$ and strain data, temperatures are scaled with the phase change temperature to obtain the reduced temperature T/T_s. (b) Spontaneous strain to the tetragonal crystal structure σ as defined in Eq.5.1, calculated from XRD measurements. The tetragonal phase transition takes place at about $T_s = 122\,\mathrm{K}$. (c) Change of $Cs_2AgBiBr_6$ single crystal unit cell volume between 15 K and room temperature.

Table 5.2: Overview of peak energies and their FWHM obtained from PL and reflectivity measurements at both 240 K and 1.4 K:

T	PL Peak 1	PL Peak 2	PL FWHM	R Peak 1	R Peak 2	R FWHM
1.4 K	2.01 eV	1.31 eV	140 meV	2.863 eV	2.838 eV	32 meV
240 K	1.78 eV	1.33 eV	610 meV	2.846 eV	-	89 meV

the bandgap, both with a FWHM of about 140 meV, as listed in Table 5.2. In comparison to $APbX_3$ perovskites, this is more than two orders of magnitude broader in FWHM. At low temperatures, peaks of such a large width can either be the result of an unusual band structure, which DFT calculations preclude [201, 202, 205, 210, 211], due to disorder and alloying [201, 212], as mostly precluded by neutron diffraction experiments, or indicative of a large phonon peak widening going beyond pure thermal phonon widening as shown in Fig.2.9. Moreover, the large FWHM of the PL peaks also indicates either an indirect process [202, 203], or possibly a defect/colour centre mediated recombination process [213–215], which will be discussed in more detail in section 5.2.2 below. There is only a weak dependence of the PL peak position on temperature for the PL-B peak, which remains within a band of

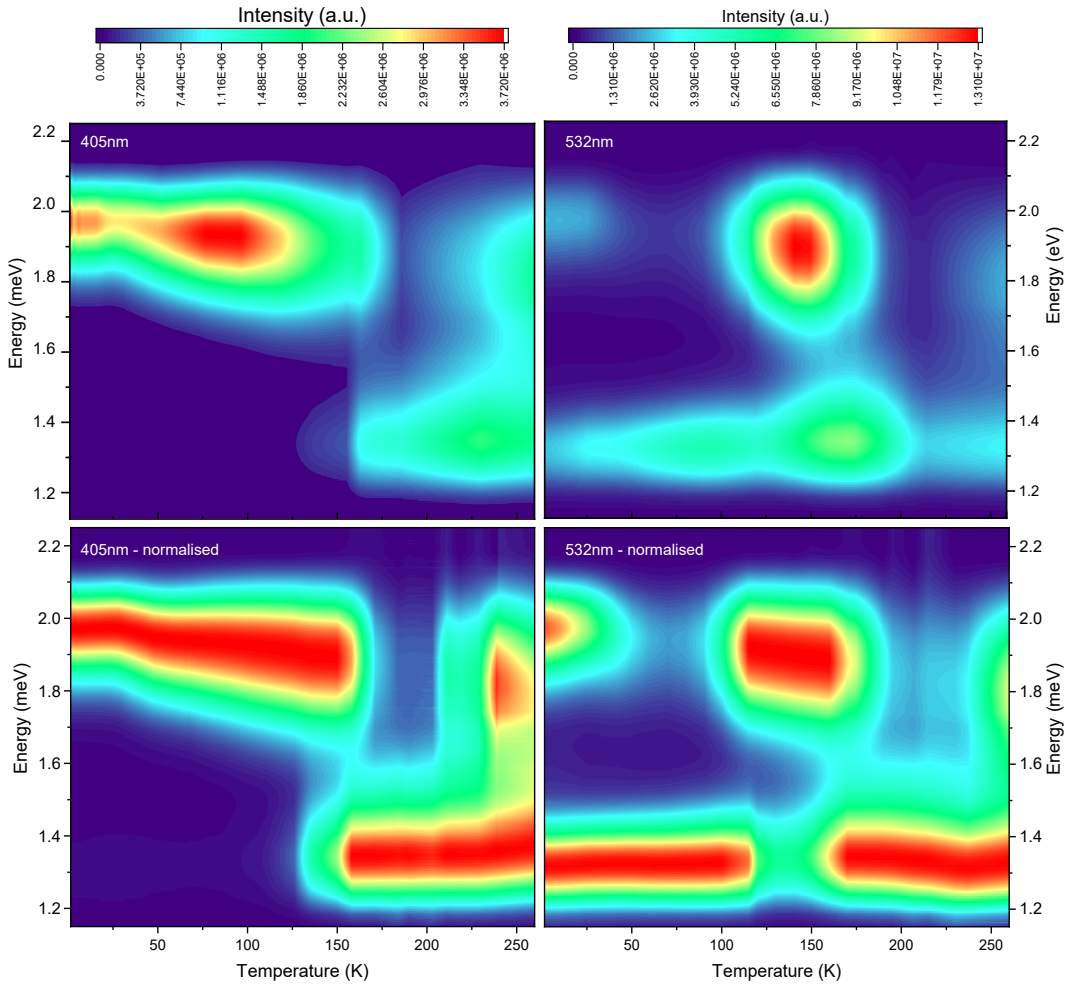


Fig. 5.5: False colour plots of temperature dependent $Cs_2AgBiBr_6$ PL spectra excited by both 405 nm (left column) and 532 nm (right column) CW laser. The bottom two PL maps are normalised to give a better overview of the evolution of the peak positions for both emission lines. Due to the *Andor iDus416A-LDC-DD* camera's ~30% higher sensitivity towards the NIR, the relative peak intensities of the PL-B peak are overestimated here in comparison to the PL-A peak.

±20 meV from the low temperature values, whereas the PL-A peak shows a steady decrease down to 1.78 eV at room temperature, as shown in Fig.5.6 (b). The energy of the PL-A at room temperature is within the range of those previously reported in literature, between 1.83 eV - 2.25 eV [204, 216–218]. In contrast to most reports on the $APbX_3$ family, the PL-A emission shows a classical *Varshni*-type [122] relation at high temperature, decreasing with rising temperature, as for conventional semiconductors such as Si and GaAs [219].

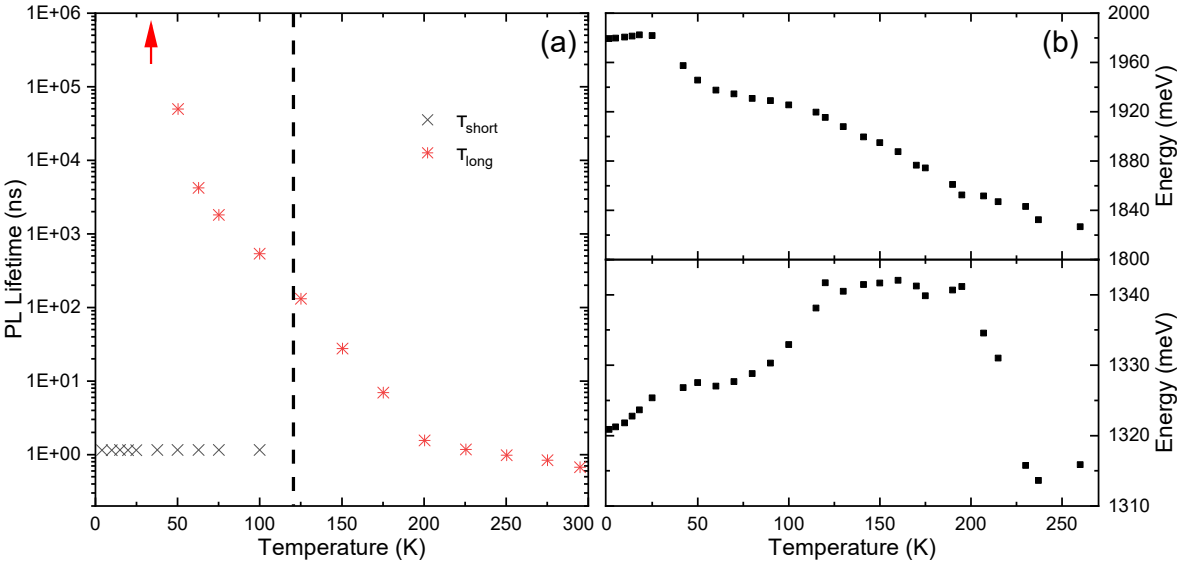


Fig. 5.6: (a) Lifetimes of the long (red) and short (grey) components, shown on both sides of the phase transition temperature 122 K. Below 50 K, the fitted long component lifetimes exceed the measurement capability of the system, as indicated by the red arrow. (b) Peak positions of both PL-A and PL-B over the range from 1.4 K to 260 K. PL-A shows a large continuous drop with increasing temperature, whereas the PL-B peak shows only a small variation in energy over the sampled temperature range.

PL Intensities and the Nature of the two PL Emissions

The influence of the $Cs_2AgBiBr_6$ phase transition on the PL behaviour is especially evident for measurements excited with a 532 nm laser, i.e., excited below its bandgap of about 2.85 eV, where a roughly four times larger volume is excited due to the larger excitation penetration depth. Under these conditions, the intensity of the higher energy PL-A is particularly sensitive to temperature, showing a very pronounced maximum just above the tetragonal-to-cubic transition, showing a strong charge carrier-phonon coupling around the phase change. As the temperature decreases from room temperature to the phase transition temperature of 122 K, the observed behaviour of increasing luminescence may be due to non-radiative trapping slowing down with reducing temperature, which would be expected to lead to an increased fraction of radiative emission, as usually observed both in semiconductors in general and in particular in lead halide perovskites [220]. The sudden drop in PL intensity upon further reducing the temperature below the cubic-to-tetragonal phase transition is consistent with a large increase in strain-induced electronic defects, as becomes evident from PL lifetimes shown in Fig.5.6 (a), and literature [211].

Nature of the PL Emission Lines

Fig.5.5 shows the temperature dependence for both the absolute and normalised PL intensities for excitation with both 532 and 405 nm. For 405 nm excitation, just above the direct bandgap, the PL-A emission is dominant for low temperatures up to the phase transition, after which the PL-B peak rapidly grows.

For the 532 nm excitation, which is below the direct bandgap, the excited volume is roughly four times greater due to the smaller absorption coefficient. For the majority of the temperature range the lower energy PL-B feature is dominant, but close to the phase transition temperature of 122 K the PL-A emission shows a strong resonant enhancement by a factor of about 20 times, in both relative and absolute terms. This suggests a significantly different origin for the two emission peaks. A competitive behaviour between the two peaks is seen very clearly in the normalised spectra where the 532 nm excitation shows an anti-correlation of the two emission intensities, in contrast to the 405 nm excitation where there is a simple exchange of intensities at the phase transition.

It has to be noted again, that in contrast to all literature published hitherto on $Cs_2AgBiBr_6$, a second PL line is visible in the data in Fig.5.2 and 5.5 at about 1.3 eV, which is physically distinct from the well-known [210, 221] and described [79, 211, 216, 222] higher energy 2 eV PL-A line.

We can gain further insight into the nature of the emissions by looking at the PLE spectrum for the upper, the PL-A peak. The PLE corresponds to the specific excitation profile associated with the particular emission process. Fig.5.7 (e) shows a direct comparison of the PL and PLE spectra, which demonstrates that there is almost no overlap of the two, suggesting a strong Stokes shift. Conventional semiconductor behaviour would show a steadily increasing density of interband transitions usually saturating above this. The steep and very sharp onset for the PLE at 2.4 eV are suggestive of a defect or colour centre with the characteristic of a strong lattice coupling, likely due to a polaronic interaction. The proper description of such a system is a Franck-Condon type of model, in which the behaviour of the ground and excited states can be represented in a configuration coordinate model as shown in Fig.5.7 (a). As a test for this theory, different couplings strengths as determined by their Huang-Rhys parameter S are plotted in Fig.5.7 (b-e), where the last of these is a good fit to the

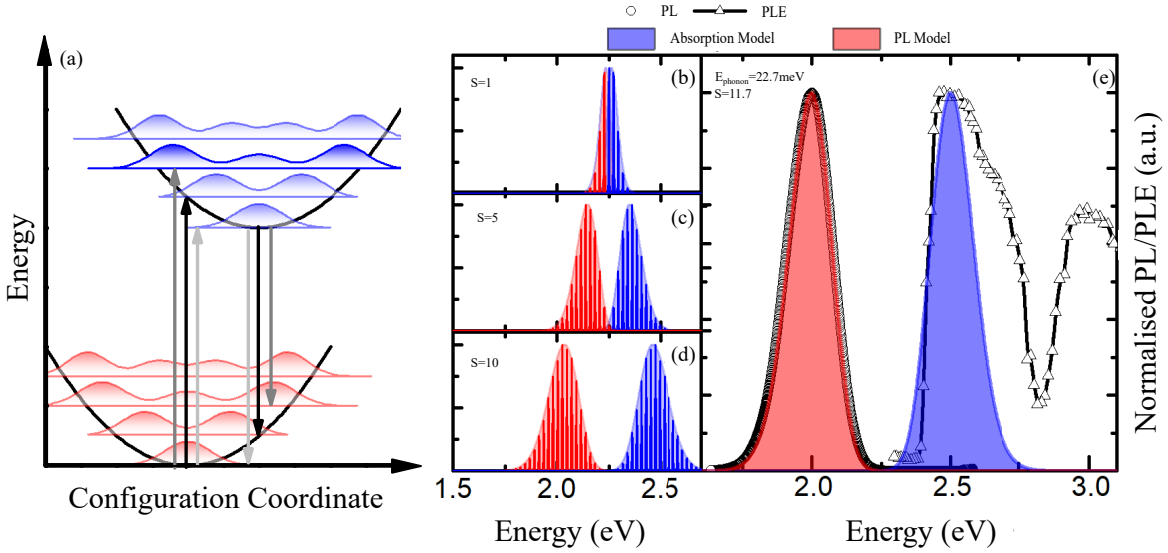


Fig. 5.7: (a) Schematic of a Frank-Condon-type Model. Excited states (blue) and ground states (red) are shown for the colour centre, including vibration sates $\nu = 0, 1, 2, 3$. The arrows show transitions with 0 (light grey), 1 (black), and 2 (dark grey) phonons involved. (b-d) Absorption (blue) and emission spectra (red) as function of the Huang-Rhys factor S. The solid lines are spectra modelled with 1 meV FWHM of each phonon assisted transition, while the lighter coloured shaded areas are calculated with 10 meV FWHM. (e) Results of the Frank-Condon model fitting (shaded areas) to the PL and PLE spectra of $Cs_2AgBiBr_6$ at 5 K. A broadening of 10 meV for each phonon transition and 22.4 meV LO-phonon energy were used in the fit, similar to literature [216].

observed data. Thus, the PL-A peak and PLE spectrum are well-described by with a Huang Rhys parameter of $S = 11.7$, resulting in fit values of 2.5 eV for the absorption peak and 2 eV for the emission peak at 5 K, corresponding to a colour centre at 2.25 eV. The same figure also includes simulations of other Huang-Rhys parameters, showing its influence on the separation between emission and absorption. This Huang-Rhys parameter corresponds well to a recent report by Steele *et al* of $S = 15.4$ [216] at room temperature, whereas other calculations of S from the FWHM of the PL emission suggest significantly larger values of order of $S_{FWHM} = 46$ [212].

The large Stokes shift in combination with the steep onset of the PLE are therefore strongly supportive of the assignment of the PL-A line as a process involving a colour centre strongly coupled to the lattice, and is not a simple indirect band-to-band process. Predictions from DFT calculations show, that a Ag_{Bi} anti-site defect is close to the energy of the colour centre observed here, at an energy offset of 0.55 eV from the valence band, and has a low formation energy ΔH [214]. It is of interest to note, that $Cs_2AgBiBr_6$ thin films reported in literature

[203, 204, 217, 218] show a higher absorption onset of about 2.2 eV, possibly indicating a weaker Stokes shift and a dependence of the colour centre's coupling strength of this colour centre to the lattice, dependent on crystal size.

When examining the assignment of PL emission peaks, the temperature dependence of the intensities gives further evidence to support this assignment. The very strong resonant enhancement at the phase transition temperature when excited at 532 nm, just in the tail of the PLE spectrum, suggests that at this temperature the lattice coupling is being strongly modified as the crystal distorts to its new structure. This reduces the Stokes shift and enhances the intensity from the direct excitation into the colour centre. Direct gap excitation at 405 nm enables both non-radiative transfer to the colour centre and excitation of any indirect bandgap emission. Therefore, an indirect gap can be assigned to the PL-B emission, which is strong when excitation is below the direct gap with 532 nm photons, but shows a significantly reduced relative emission intensity in the low temperature tetragonal phase, suggestive of an enhanced transfer into the colour centre for this phase. The PL-B assignment is consistent with the weak absorbance threshold observed around the PL-B emission, where an absorption coefficient of order $\alpha_{300K,1.3eV} = 7\,\mathrm{cm}^{-1}$ is oveserved, which is comparable to the absorption coefficient close to the indirect gap of silicon [223] giving an overall picture of weak absorption combined with strong PL, consistent with an indirect gap.

5.3 Magneto-Optical Response of $Cs_2AgBiBr_6$

Magneto-optical analysis of a material at low temperatures can be highly informative, in particular for the study of exciton binding energies and effective masses [158]. However, reflectivity studies of the direct bandgap in Fig.5.8 do not show any detectable shift of the $1s$ exciton state > 0.5 meV up to 19 T[1] nor the magnetic field activation of higher excitonic transitions such as the $2s$ up to energies of over 3.1 eV. Both of these observations suggest that the exciton binding energy is over 300 meV and are consistent with the reports of a large effective mass $m^* \approx 0.34\, m_e$ for $Cs_2AgBiBr_6$ obtained from band structure calculations [202,

[1] Measurements by collaborators at the LNCMI Toulouse show no influence on the exciton up to very high fields of up to 70 T.

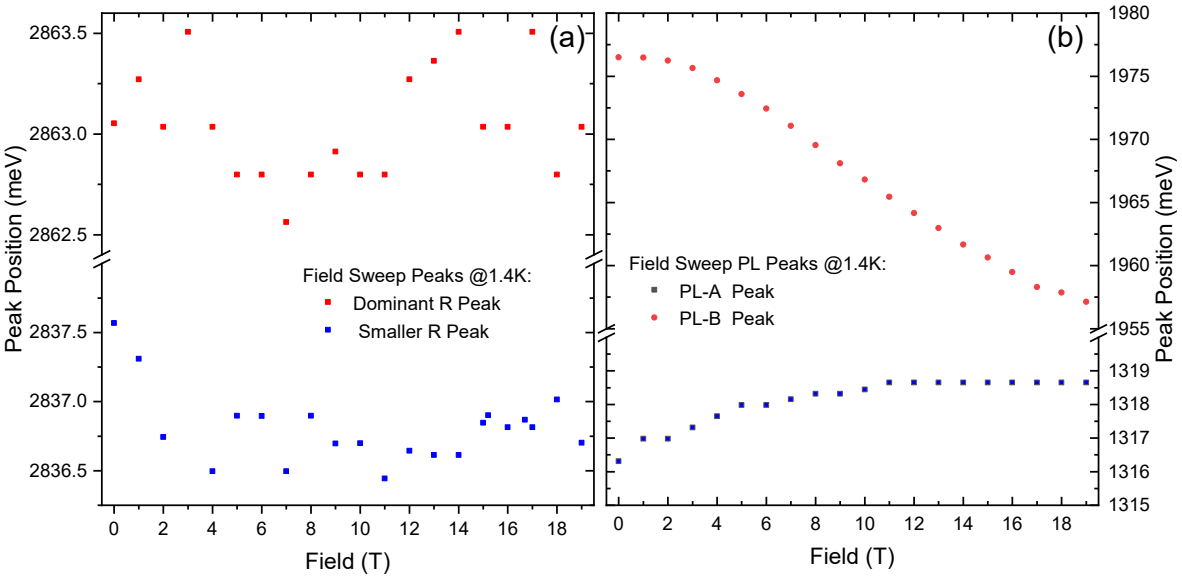


Fig. 5.8: (a) Reflectivity peak positions under magnetic field. There is no trend visible in the data, hinting at a large exciton binding energy. (b) In contrast to R, the PL-A energy shows a large field dependence, and PL-B shows a very small field dependence.

205, 214, 224]. It could also explain the low device efficiencies seen for $Cs_2AgBiBr_6$ thin film photovoltaic devices, which today are in the low 1-2% efficiency regime [207, 212, 217, 218].

5.3.1 Nature of the Higher Energy PL Emission Line Revisited

The PL-B emission in Fig.5.9 (b) does show a small blue shift of about 3 meV, but this mostly occurs at low magnetic fields and any shift saturates above 10 T. By contrast, there is a giant magneto-optical response for the PL-A emission, which provides further confirmation of its assignment as a colour centre related to the Ag_{Bi} anti-site defect. At 1.4 K the PL-A intensity is strongly supressed and red-shifted by the magnetic field as shown in Fig.5.8 and Fig.5.9. At 1.4 K, a field of 19 T already decreases intensity by 27%, and the PL-A emission energy is also strongly affected with a red-shift of 19 meV, in a correlated manner. Cooling below 60 K leads to a large blue-shift of about ~40 meV under zero magnetic field, which can be reversed by the application of a field larger than 40 T.

The likely mechanism behind this large low temperature energy shift is a formation of some magnetic interaction which can be suppressed by the application of a large magnetic field, such as the formation of some form of anti-ferromagnetically interacting regions associated

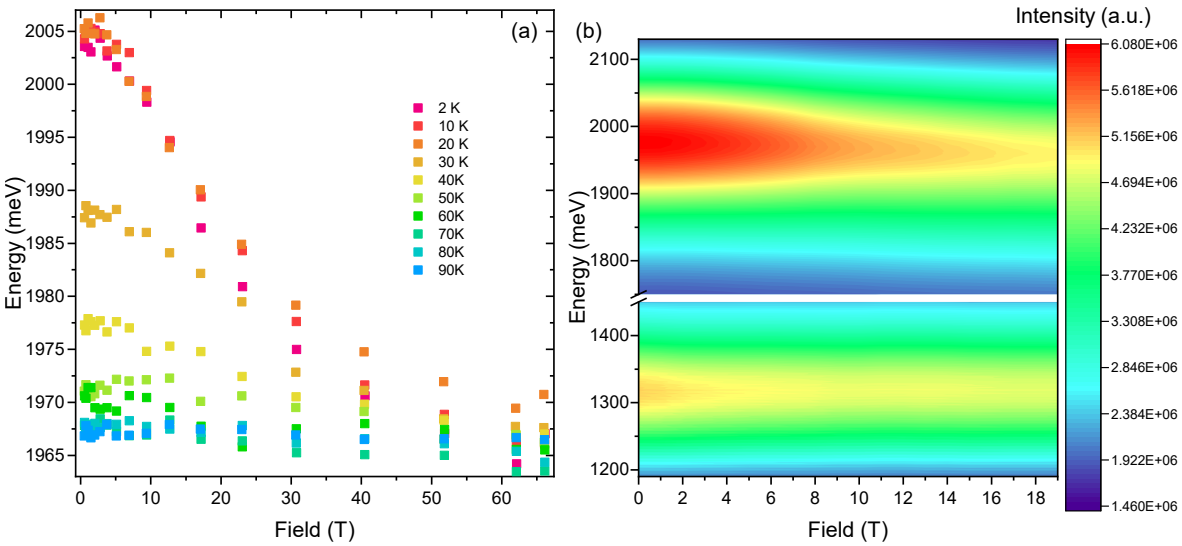


Fig. 5.9: (a) Influence of magnetic field intensity on the PL-A emission of $Cs_2AgBiBr_6$ in the temperature range from 2 K to 90 K as measured by collaborators at LNCMI Toulouse. After reaching a field of 60 T, PL-A at all measured temperatures is at a value of about 1967 meV. (b) False colour map showing the influence of magnetic field on photoluminescence peak positions. While the higher energy peak shows a redshift of 19 meV, the low energy PL peak shows small blueshift of 3 meV in peak position. The PL emission intensities decrease under strong fields, where the peak ratio of I_{19T}/I_{0T} corresponds to 0.73, and 0.93 respectively for the high, and low energy PL peak.

with the polaron formation around a self-trapped exciton [225]. In the very similar compound of silver bromide (AgBr), covalent binding of a hole from an exciton causes the silver ions to change from the Ag^+ to the Ag^{2+} configuration [226, 227]. As a result the $4d$ shell becomes partially populated and the hole is captured in the uppermost d, the $d(x^2 - y^2)$-orbital. A Jahn-Teller-type distortion results, pushing out the apical Br^--ions, and decreasing the distance to the in-plane Br^--ions [228]. Assigning the colour centre to a Ag_{Bi} anti-site defect puts the two silver ions adjacent to each other. This makes it likely that the Ag^{2+}-ions could become spin-1/2 anti-ferromagnetic with a strong superexchange, which is well known situation for a number of Ag^{2+} compounds where large values of the exchange energy **J** have been found [229–231]. Effectively, this introduces the possibility of light triggered magnetostriction, which leads to the polaron formation. This may also be enhanced by the strain associated with the distortion to the tetragonal phase described above.

Therefore, the most likely origin of the PL-A line, and the explanation for its field-dependence is the local distortion of an Ag^{2+} octahedron and a possible configuration coordinate diagram is shown in Fig.5.10, where the free exciton becomes self-trapped near a Ag_{Bi} defect with a

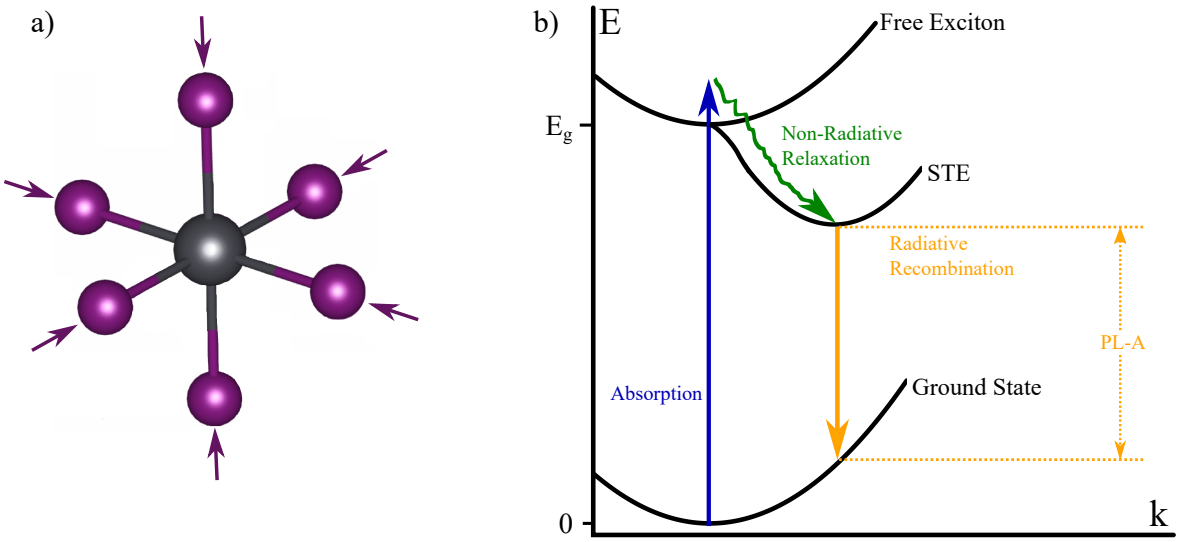


Fig. 5.10: (a) Deformation of a $AgBr_6$-octahedron upon covalent binding of an exciton. (b) Exemplary configuration coordinate diagram showing the processes and their energies involved in absorption, trapping, and radiative decay of a self-trapped exciton. The values given in the diagram correspond to the values for the direct gap, and the higher energy PL emission of $Cs_2AgBiBr_6$ at 1.4 K.

magnetically dependent trapping energy.

Self-trapped excitons in literature, e.g. in MnO [232, 233], MnS [233, 234], and in perovskite structures like $KMgF_3$ [235], show a similar behaviour under these conditions. The response of the STE shows a decrease of lifetime and intensity under magnetic fields, combined with a redshift of the emission. This is the result both of an increasing exciton radius in magnetic fields, due to detrapping of the excitons [236, 237]. Recent calculations show an even larger influence of STE on the double perovskite $Cs_2AgBiCl_6$, with experiments showing that the effect of the STE leads to an emission close to white light of 4000 K [238].

5.4 Summary

Optical experiments between 1.4 K and room temperature, and up to large magnetic fields reveal the rich internal structure of $Cs_2AgBiBr_6$ including a direct gap around 2.86 eV, a colour centre at 2.25 eV, and an indirect gap at about 1.3 eV. The changes in the bandgap energy can be well modelled following the changes in the unit cell structure between the cubic

structure at room temperature and down into the tetragonal phase below 122 K, following the two parameters of unit cell volume and octahedron rotation.

The soft crystal structure and heavy constituent atoms result in a large influence of phonons on the optical properties, inducing a Stokes shift of 0.5 eV for the defect, and phonon induced large FWHM of PL emission. The origin of the colour centre was identified to be at the site of anti-site silver atoms, based on the response to magnetic fields which is very similar to other reports on self-trapped excitons at silver atoms in silver compounds like AgBr.

The indirect gap at 1.3 eV dominates the PL response both for excitation with above, and below bandgap energy in the cubic phase as the preferred radiative recombination channel. In the tetragonal phase, the indirect gap shows a weaker emission than the colour centre, either because the density of colour centres increases below 122 K, or because the thermal energies are low enough to capture and bind excitons more efficiently at the colour centre.

6 Nature v Nurture: For $MAPbI_3$ Nurture Wins

The material class of perovskites has been known for over a century, and many prominent members of this structure have featured extensively in research. A recent development in this field are the organic-inorganic metal halides, as for example methyl ammonium lead iodide ($MAPbI_3$). Over the course of the last ten years, this material class has become the strongest contender for an efficiently mass producible clean energy source.

Although a lot of studies have been published on this type of hybrid organic-inorganic perovskites to date, many were focussed on pushing device efficiencies to higher levels, while questions as fundamental as whether $MAPbI_3$ has a direct, or indirect bandgap are still under discussion. Many theoretical and experimental studies are arguing for an indirect nature at room temperature [93, 95, 140, 146, 239–241] and others report a direct bandgap [80, 240, 242, 243]. This split of opinions and data can be better understood, after taking into consideration the difficulties of creating a perfect $MAPbI_3$ device, where minute differences in production can lead to a large divergence in solar cell efficiencies [244]. Processing, and different processing methods are of such an importance, that some perovskite films can be annealed at 185°C in air, whereas films produced from the same precursors, but under different parameters, will convert back into educts under such treatment, or will never form a perovskite film. Correspondingly, there is also large spread of reported bandgaps E_g between 1.48 eV and 1.62 eV for $MAPbI_3$ single crystals and thin films [123, 166, 242, 245–247].

Another contentious point of ongoing discussion related to the nature of the bandgap is the crystal structure of $MAPbI_3$. While it is generally agreed upon, that there are two phase transitions at about 55 °C from cubic to tetragonal, and around 160 K from tetragonal to

orthorhombic, the exact space group of the tetragonal phase is still debated. Some report an I4cm non-centrosymmetric group [93, 242, 248, 249], which in combination with the strong lead spin orbit coupling (SOC), would result in a weakly spin-split band. This effect would make the $MAPbI_3$ bandgap slightly indirect and could help explain the high efficiencies achieved in devices of this material. On the other hand, the centrosymmetric I4/mcm group [92, 159, 246] is reported on in literature, implying a direct bandgap. I4cm has a lower symmetry and is easier to fit to experimental data because of an additional parameter in comparison to I4/mcm. Correspondingly, these two cannot be discerned for very small deviations and I4/mcm should be assumed as the correct model. It is against good practice to assign the I4cm space group from a fit on XRD measurements just driven by the desire for a certain structure that could explain some of the materials properties.

This chapter's aim is to further the understanding of these differences by studying the properties of $MAPbI_3$ single crystals and thin films grown in the cubic phase, above 55 °C (HT), and in the tetragonal phase at ~40 °C (LT) by optical, and XRD structural characterisation. At the same time, this will help with the understanding of the nature of the bandgap in $MAPbI_3$ and will further the knowledge on the structure of $MAPbI_3$, by establishing the true bandgap of $MAPbI_3$.

The XRD measurements in this chapter were performed together with R.D. Johnson. The acetonitrile based 100 °C hotplated annealed, and sparse < 25 °C vacuum annealed thin films were prepared by J.H. Warby. The results in this chapter are part of a draft status manuscript being prepared for publication.

6.1 Experimental Considerations

Photoluminescence (PL) was measured by excitation with a Laser Quantum ventus532 532nm laser, exciting the sample at an above bandgap energy. The hot excitons will cool to the bandgap and can recombine there radiatively. Colour centres and sub bandgap states, even at low concentrations, can be highly effective PL emitters. Moreover, the PL will have some contribution from the surface and surface states at the energies of interest between ~1460-1700 meV. The absorption coefficient for $MAPbI_3$ gives a penetration depth of up to 200nm

in this range [250, 251] ensuring most of absorption and signal will not be dominated by the top layer of the surface. The share the bulk of the crystals contribute to the total signal is even bigger, if radiative recombination and re-emission (~0.5% for $MAPbI_3$) are taken into consideration [252]. Another possibility to determine the optical structure with a much smaller contribution from such factors are absorption measurements. For sufficiently translucent thin films, absorption measurements work well, but they are not an option for thick single crystals. Instead, by using the Kramers-Kronig relations the reflectivity (R) of a single crystal can be used to determine the corresponding absorption. A sufficient approximation of the Kramers-Kronig transformation is the negative energy derivative -dR/dE of the reflectivity, as introduced in Ch.2.1.3, and most reflectivity data is presented as this derivative here. For R data, the comparatively low power of the white light used to excite a sample only shows signal around optically strongly allowed transitions, which at low temperatures corresponds to excitons at the bandgap. Correspondingly, at a given temperature, therefore the R signal is much narrower and sharper than the PL.

6.2 $MAPbI_3$ Temperature Sweep

PL and R/transmission data for $MAPbI_3$ crystals and thin films grown above and below the cubic transition temperature in Fig.6.1 show similar behaviour up to 155 K. Two emission peaks are visible for PL and two for R, which show a continuous, roughly linear increase in energy with rising temperature. HT and LT samples only differ in which of the two emission peaks is dominant. It has to be noted, that there are no previous reliable reports of this lower emission branch that, with few exceptions, has not been discussed at all in literature to date. To facilitate the discussion of these two different emission branches visible in both PL and R/T, the upper one at higher energies will be called branch „A“, and the lower energy branch „B“.

At low temperatures, the difference between R and PL peak energies is mainly due to the exciton binding energy reduction due to Stokes shift and possibly due to shallow defects.

A distinct feature for PL in the low temperature regime is the large and broad low energy donor-acceptor (D-A) pair emission, which for low excitation intensities is the dominant

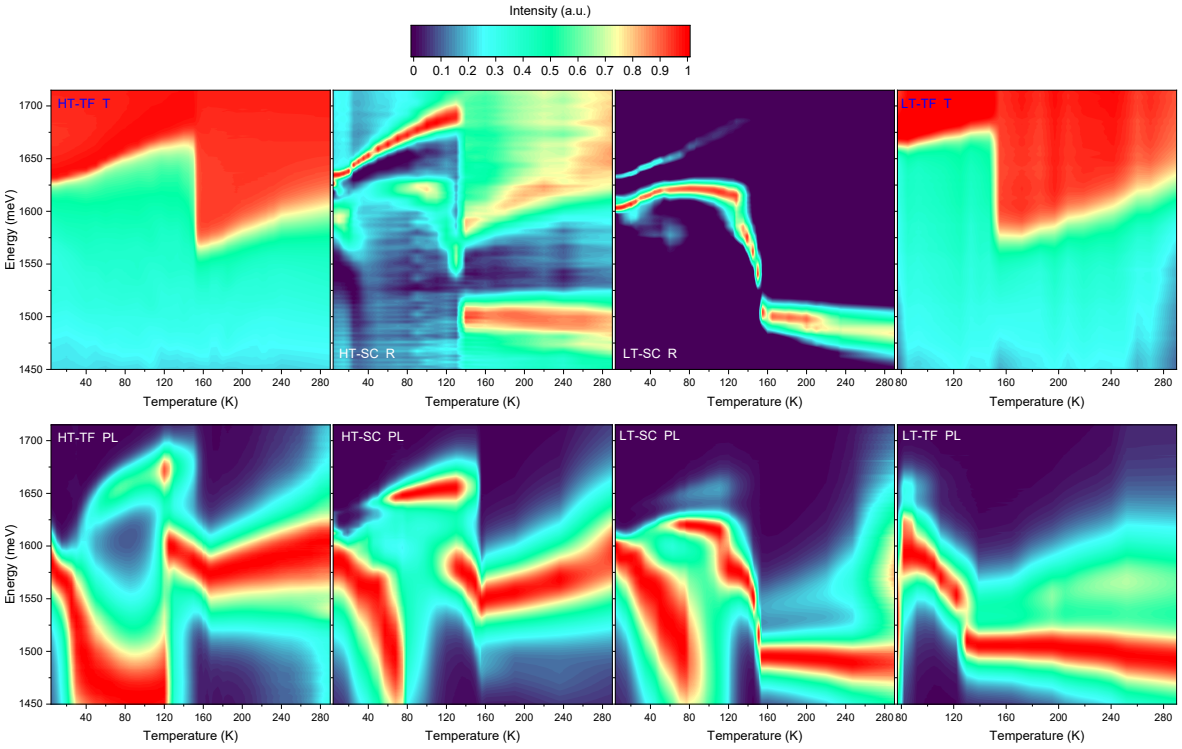


Fig. 6.1: Normalised false colour plots of photoluminescence (PL) and transmission (T) of a $MAPbI_3$ thin film (HT, first column; LT fourth column), PL and reflectivity (R) of a single crystal grown above (HT, second column) and below (LT, third column) the cubic phase transition temperature. For the HT thin film/crystal the higher energy transitions/excitons dominate, whereas for the LT crystal/thin film the lower energy transitions/excitons dominate. This domination by the lower energy transitions for LT grown samples depends on the individual sample, where some samples show a more balanced ratio of emissions. All samples show a significant contribution to PL from donor acceptor pair transitions at very low temperatures below 100 K. All false colour plots are normalised according to the intensity scale shown above.

feature of the PL signal. The relation of this emission to defects or D-A pair recombination [253, 254] is revealed by excitation intensity studies which show a shift of the centre of this emission by up to 28 meV under different intensities at 24 K, and 58 meV at 67 K as shown in Fig.6.2. Studies not showing this PL feature tend to have high excitation intensities in common, as shown, e.g., in comparison of Even et al [239] and other reports [255–257], as the emission strength grows less quickly in magnitude than the band-to-band PL.

6.2.1 Sub-10K Reflectance Splitting

At temperatures smaller than ~15 K, the lower energy R peak is split into two peaks separated by about 11 meV, as shown in Fig.6.3 (a). Despite looking very similar to an exciton/trion

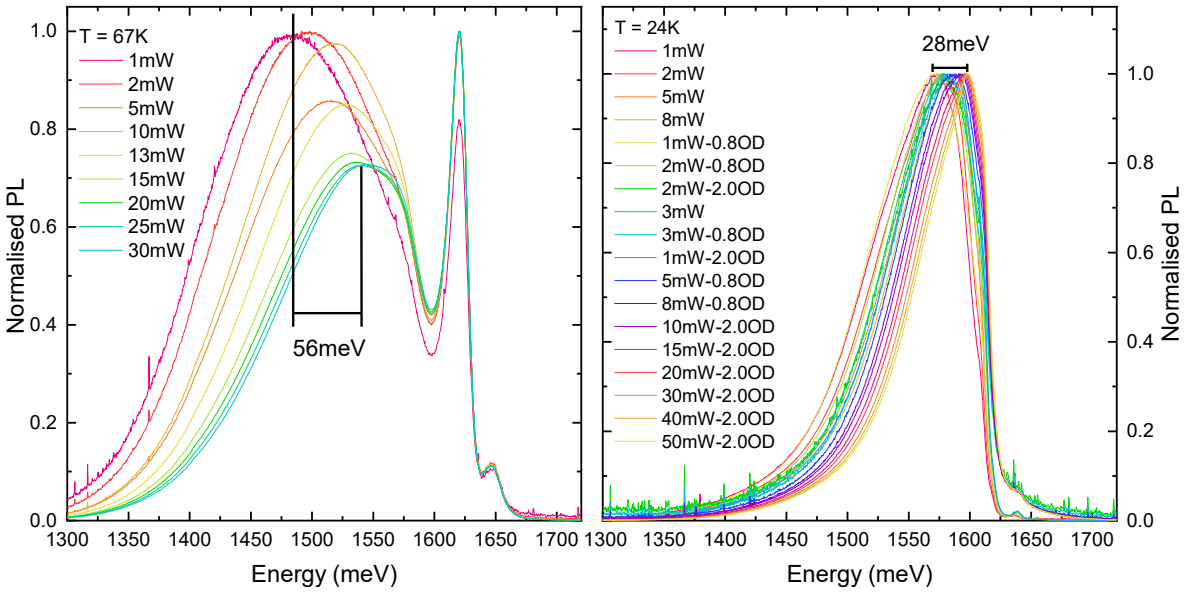


Fig. 6.2: Effect of different excitation intensities on the position of the D-A emission. The higher the temperature, the larger the effects seen, with a 58 meV shift at 67 K, and 28 meV at 24 K.

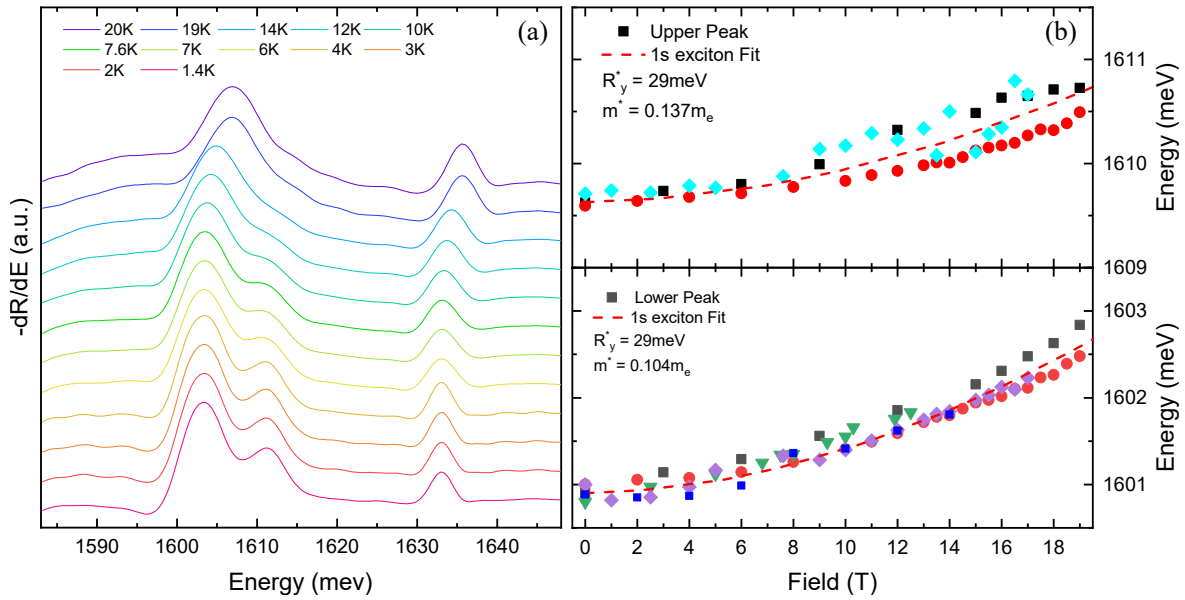


Fig. 6.3: (a) -dR/dE spectra between 1.4K and 20K showing the splitting of the 1.6 eV B-peak into two clearly separate peaks at very low temperatures. (b) The field response of the two 9 meV-split R peaks shows a roughly diamagnetic response, where the higher energy transition shows a lower field dependence. As an guide of eye, theoretically calculated transition energies for a 1*s* exciton state after Makado *et al* [160] are included as an guide of eye.

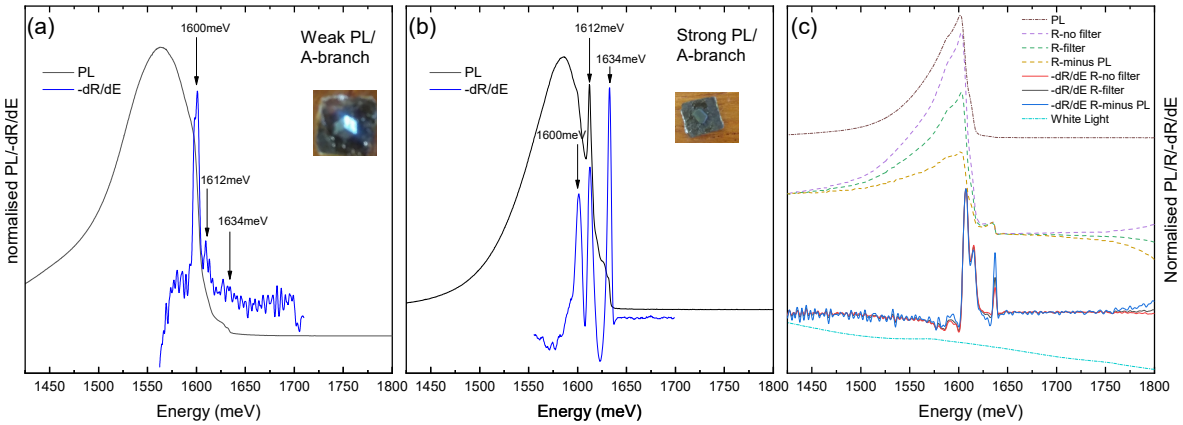


Fig. 6.4: PL and R measurements of $MAPbI_3$ single crystals at 1.4 K. (a) Measurements in off-normal geometry showing almost no PL contribution to the R signal, and only small 1612 meV R signal. (b) Measurements with the ideal geometry for coupling into the fibre showing a much larger 1612 meV peak. (c) Filtering out some of the excitation white light shows a reduction to the 1612 meV peak, but no change for the 1600 meV R B-peak and a slight increase in intensity for the 1634 meV A-peak. The shown difference between filtered and unfiltered R stresses this even more. All spectra shown here are offset by some intensity, to allow for the better comparison of the individual spectra.

split in e.g. CdTe, with a small energy splitting between the two peaks, and a higher intensity for the lower energy peak, a trion can be excluded. Under the influence of magnetic fields, both exciton and trion should show a similar field response[1], whereas the two peaks here show a dissimilar response to magnetic fields. Both peaks are well described by exciton $1s$ states, as shown in Fig.6.3 (b),

For a sample with off-normal incidence, the amount of PL emitted in the direction of the collecting lenses can be minimised, as implemented with the sample shown in Fig.6.4 (a). In comparison to a sample with a surface normal to the excitation laser as in (b), a much larger amount of PL is collected, and the intensity ratio of the two split peaks is reversed. This shows, that the 1612 meV peak is due to PL noise in the signal, and should be disregarded. As a confirmation of this, Fig.6.4 (c) shows the influence of a decreased white light excitation. As an approximation, the emitted PL intensity is proportional to the (square of the) density of excited charges, and thus to the excitation intensity. In contrast, reflectance is independent of the excitation power, and shows no decrease.

[1] In contrast to the exciton, a trion will be spin-1/2, but this only results in a singlet/triplet split, not in a different field response.

Consequently, the splitting observed for R spectra at low temperatures is a not part of the dielectric function, but noise due to PL.
In comparison to the field response of the A-branch, which is detailed in Ch.7, the approximate values for the exciton binding energy R_y^* are considerably larger, even considering the large error of ± 5 meV on this energy, as no $2s$ state is visible to get a better estimate of R_y^*.

6.2.2 Tetragonal Phase

The phase transition shows a different behaviour for A- and B-branches, where A undergoes a sharp, first order phase transition that includes a 120 meV jump around the 155 K phase transition temperature. The B-branch, in contrast to this, shows a smooth and slow second order phase change that can be perfectly tracked through the phase transition temperature both in PL and R. The difference of these two behaviours shows that there is different physics involved for the two emission branches, and moreover, that they are distinct from each other. Above the orthorhombic to tetragonal phase transition temperature, the behaviour seen for the HT/LT samples diverges. The HT samples only show the A-peak in PL, but both B and A in R, where the latter is much weaker and is not observed at all for most samples. The LT samples shows a strong B-peak in R, and both peaks for the PL signal, similar to reports of PL combined with photoconductivity, diffuse reflectance, and circular photogalvanic effect (CGE) measurements [105, 123, 146, 258], which point at a spin-sensitive nature of the B-branch. The origin of only a small trace of an A-peak in reflectance for most LT samples in the tetragonal phase will be detailed later in section 6.3.

6.2.3 Heating to 100°C

Since LT and HT crystals mainly differ in their growth temperature, it is necessary to test if a LT crystal can be converted into a HT crystal by bringing it to the HT growth temperature of 100 °C. For this, LT samples were slowly heated up, and then kept at 100 °C for hours at a time, and then slowly cooled down to RT. The crystals studied at temperatures higher than RT and up to 100 °C were heated up under low pressures $<10^{-5}$ bar of a residual helium atmosphere. To prevent outgassing of methylammonium at high temperatures and

low pressures, the crystals were covered in a thin layer of PMMA. Due to the low pressure, the temperature of the sample head and sample could be easily stabilised and controlled.
After slowly ramping temperature from RT at ~16 °C/hour to about 100 °C, the temperature at which the HT samples were grown or crystallised, a LT sample from the same batch as used to obtain the data in Fig.6.1, shows a gradual decline in intensity of both the B/A-peak, until both peaks have decreased in intensity so much, that they are close the noise/background level. Both peaks continue to coexist in PL up to 100 °C, and follow the same increase/decrease in energy as observed between 155-300K. After keeping the crystal at 370K for >12h to allow the crystal to settle at this temperature, the two PL emission lines still coexist. Also, no change in the $-\frac{dR}{dE}$ signal occurs after slowly cooling down to room temperature with ~20 °C/hour as shown in Fig.6.5. This behaviour shows the big influence different growth conditions have on the $MAPbI_3$ crystal, producing physically distinct crystals, that cannot be converted into the other crystal state by bringing them to the same original parameters. Moreover, it shows that the LT crystal is not in a non-relaxed state which through relaxation and annealing at high temperatures will reach the stable final state.
If the crystal is stressed though by partial outgassing of methylammonium[2], the observed behaviour of the crystal changes. This is shown in Fig.6.6, where a crystal without a covering PMMA layer was kept under vacuum at 370K for several hours. After cooling the sample down again, only the A peak reappears. Upon optical inspection of the crystal, a covering layer of pure, yellow lead iodide is revealed on top of the $MAPbI_3$ crystal, showing that the „destruction“of a LT crystal can convert it to a type of HT crystal. In order to better understand this tenuous link between HT and LT thus established, XRD studies were performed.

6.3 XRD Structure Analysis

In a first XRD comparison between HT/LT $MAPbI_3$ single crystals, Fig.6.7 shows that the LT crystal has one dominant domain, one dominant peak, whereas the HT crystal shows

[2] As reported in literature [259, 260], only the methylammonium is outgassed and the Pb and I moieties form leadiodide PbI_2.

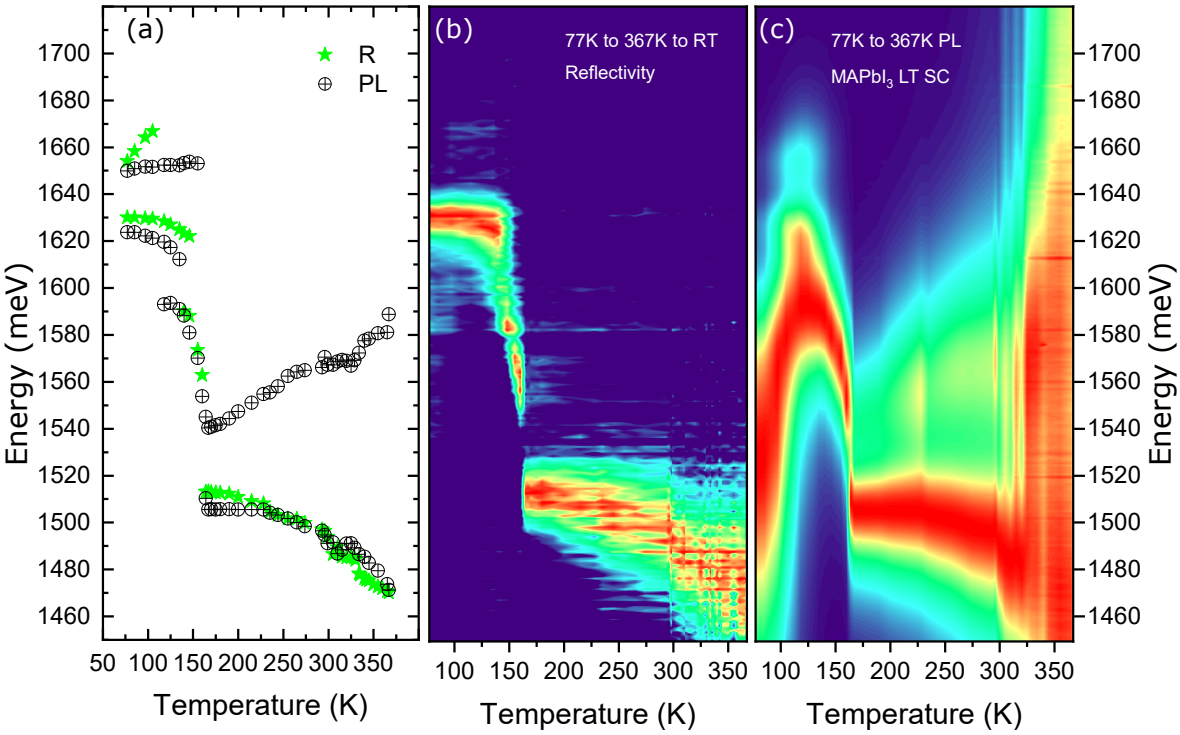


Fig. 6.5: (a) Energies of the peaks observed between 77K and 370K for a PMMA covered single crystal. (b) False colour plot of the $-\frac{dR}{dE}$ spectra observed on warming a sample from 77K to 370K, and cooling back down to RT. (c) Normalised false colour plots of PL (left) and R (right) of a LT $MAPbI_3$ crystal heated from 77 K up to 370 K. Above 300 K, the crystals PL emission intensity decreases markedly, whereas the R signal remains consistently strong. On cooling down, the emission lines are at the same energies as during the temperature ramp up. The $-\frac{dR}{dE}$ spectra shown in (b) are displayed individually in Fig.6.6 (b)

several different domains/peaks. So within the sampling depth of about 6 µm of the highly sensitive, high resolution XRD setup, the HT crystals shows several different lattice plane (d-) spacings.

As the intensity of the scattered x-rays scales with the volume involved in the scattering process, a fit to the obtained data allows us to roughly quantify volume fractions. For the LT grown crystals, one dominant domain makes up 88% of the sampled crystal volume as determined from the area of the peak fit, whereas for the HT crystal the intensities are more equally distributed among four peaks.

As the penetration depth of the Cu-Kα x-rays for the measurements in Fig.6.7 is about 6 µm, it is an interesting question, whether the large variation in peak angles for the HT crystal originates from the surface, or the bulk. A grazing incidence geometry measurement with x-rays impinging on the sample at an angle close to 90° from the surface normal can

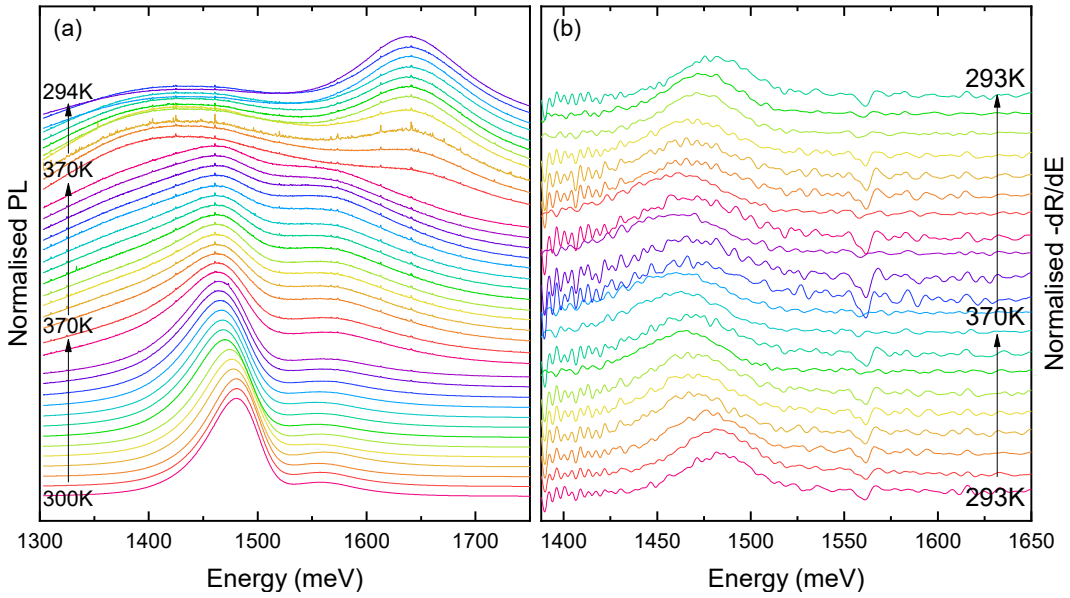


Fig. 6.6: (a) Influence on PL of partial destruction of a $MAPbI_3$ LT single crystal by outgassing of methylammonium, by heating it up to 373K under vacuum without a covering PMMA layer. While heating up to 373K, both A and B peak are visible. After about three hours at 370K, both PL peaks have almost disappeared, and are dominated by background. Upon cooling down, only the A PL peak reappears, and is shifted to higher energies. (b) In contrast, a PMMA covered $MAPbI_3$ single crystal shows the same behaviour before and after the heating to 370 K.

help to discern the influence of the surface and bulk of the sample. Fig.6.8 (a) shows the grazing incidence response of the (0012) crystal plane of a $MAPbI_3$ HT crystal, sampling to a crystal depth of about 200 nm. Qualitatively, the surface of the crystal shows several different peaks/d-spacings, and a total peak width of about 0.4°. In contrast, testing of the inside of a HT crystal after cleaving[3] shows a single peak that is much narrower at about 0.15° width. Moreover, the position of the (0012) peak after cleaving is a good match to the lattice parameters of $a_{t,LT} = 8.867$ Å and $c_{t,LT} = 12.667$ Å as determined for the LT crystal. The difference in behaviour between these grazing incidence measurements, and the conformity of the single HT core/bulk peak with the LT lattice parameters indicates a large and deep sample surface with a strong effect on crystal structure.

The penetration depth in the wavelength range of interest is of roughly the same size as the the surface depth determined here. In an absorption measurement, as in Fig.6.8 (b), the

[3]Read: careful fracturing of a crystal and selection of a splinter from the crystal core. $MAPbI_3$ HT single crystals are almost impossible to cleave, they normally prefer to just crumble and fracture. In contrast, it is more facile for LT $MAPbI_3$ crystals to be cleft perpendicular to the crystal $[00\ell]$-axis.

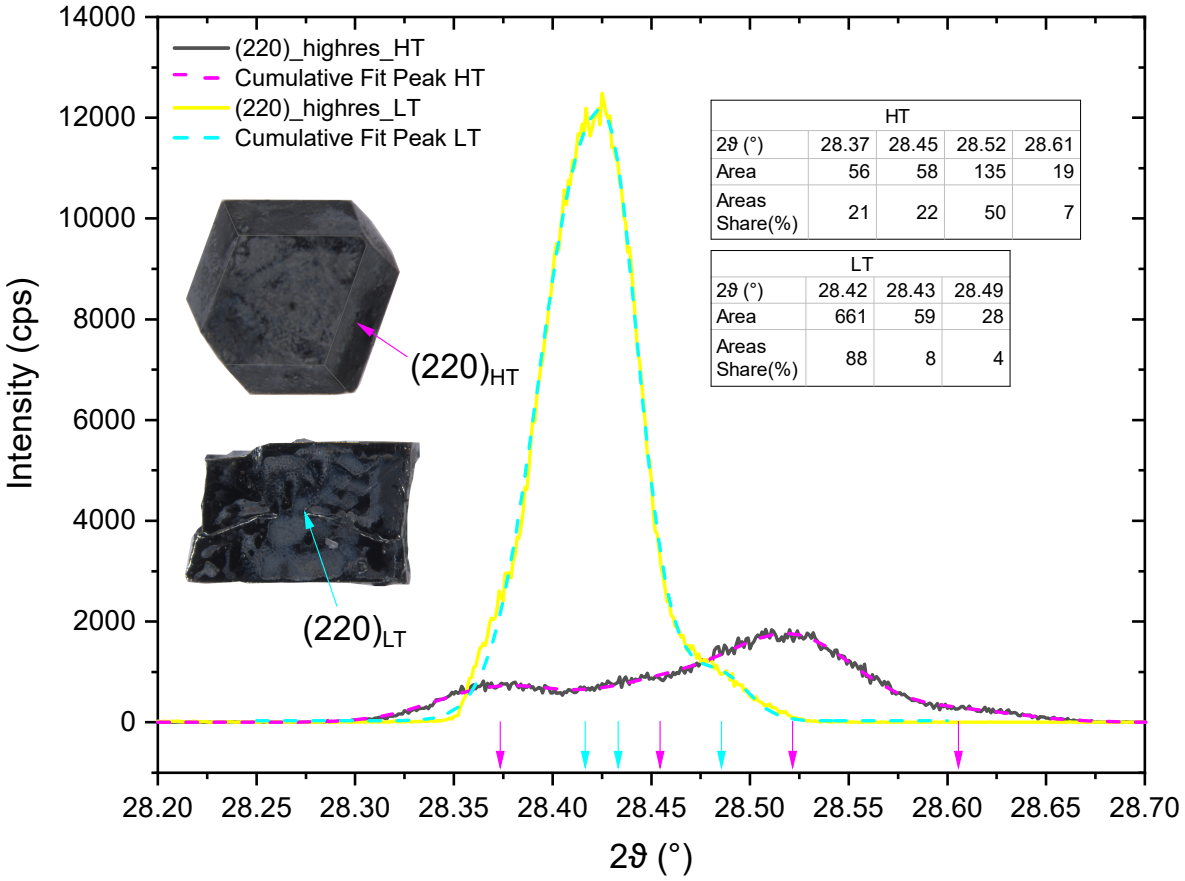


Fig. 6.7: XRD scans of the (220) peak of two $MAPbI_3$ single crystals. The crystal surface corresponding to the (220) plane is indicated by arrows on the crystals. The LT grown cuboid crystal shows three different lattice plane spacings, where the two dominant ones make up 8% and 88% of the volume respectively. The HT grown truncated dodecahedron crystal shows a larger number of lattice plane spacings, with a volume share more equally distributed, as shown in the inset table. Both XRD spectra are well described by the cumulative Gaussian peak fit, and their resulting peak angles are indicated by arrows at the abscissa.

entirety of the the crystals is sampled, and shows the same behaviour, the same absorption onset for LT and HT crystal. To test the implication of these absorption measurements, the PL from a freshly cleft HT crystal was compared to an as-grown HT crystal, and the double PL structure is revealed. Fig.6.8 (b) shows the two different PL curves, which are at the same energy for the PL-A peak, but the freshly cleft crystal shows the additional PL-B peak. Recently Chen et al [261], realised a 20 µm thick $MAPbI_3$ single crystal device. The external quantum efficiency (EQE) of the solar cell shows a current generation onset around the energy observed for the PL-B peak, as shown in Fig.6.8 (c). In comparison, a regular polycrystalline $MAPbI_3$ thin film device only showing the PL-A peak has a similar first EQE onset, as measured by J.M. Ball at the University of Oxford. One might argue that the early, high

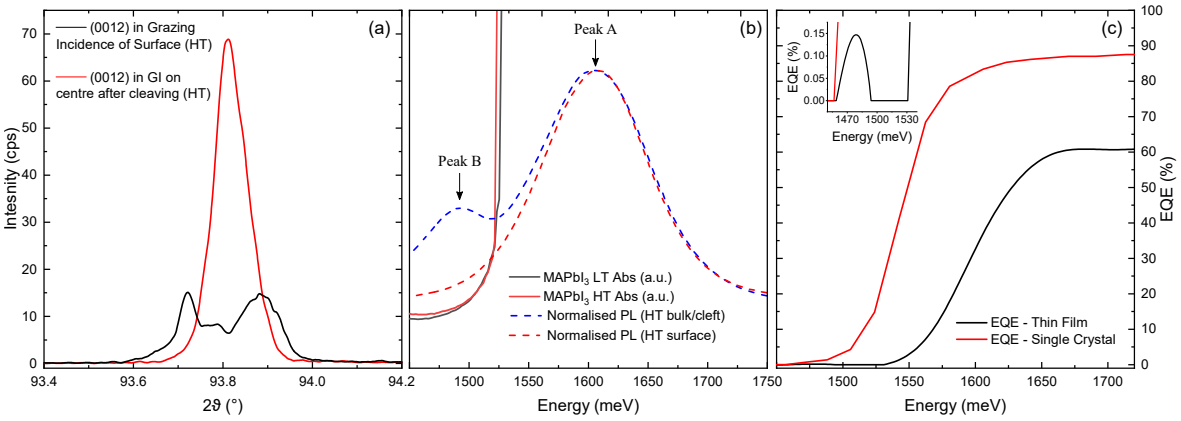


Fig. 6.8: (a) Grazing incidence XRD scans of the (0012) peak of a HT $MAPbI_3$ single crystal. The first scan of the top most ~200 nm shows at least three peaks, whereas the large shard from the core of the same single crystal shows only one strong peak. The existence of several (0012) peaks points to areas in the crystal with different lattice plane d-spacings. (b) PL emission from the freshly cleft surface within a HT crystal, and a HT crystal. Additionally, the absorption for one HT and one LT crystal are shown. (c) External quantum efficiency (EQE) measurements on a $MAPbI_3$ single crystal and thin film device. Single crystal EQE data in (c) reprinted with permission from Chen *et al* ACS Energy Lett. (2019), pp. 1258–1259, [261]. Copyright 2019 American Chemical Society under the CC BY-SA 4.0. $MAPbI_3$ thin film EQE data obtained from J.M. Ball at Oxford.

wavelength EQE onset for the SC device is based on sub-bandgap Urbach-states, but it does not serve to explain that the same first onset is visible for $MAPbI_3$ thin film devices at the same wavelengths, corresponding precisely to the PL-B peak positions. So although further, higher precision EQE measurements are required for the polycrystalline thin films, this shows that both A- and B- state contribute to device current.

From these four different measurements in Fig.6.8, it can be inferred that the part of the crystal responsible for the majority of the A emissions must be the surface of the crystals, but that the bulk contributes to the A emissions also. In this case the „depth“of the surface can be quite large, in case of thin film devices probably encompassing the entire device thickness.

As the A phase has a strong PL emission despite coming from only a small share of the LT crystal and sitting at a higher energy, it is a sign that the A-peak corresponds to a more emissive direct gap, whereas the B-peak is related to an indirect gap. A colour centre can be excluded as the origin of the B peak, as the low density of possible defects would not yield a significant contribution to the R signal. This assignment is similar to a report in literature by Chen *et al*, who performed TRPL measurements at <100 K, where the B-PL peaks shows for

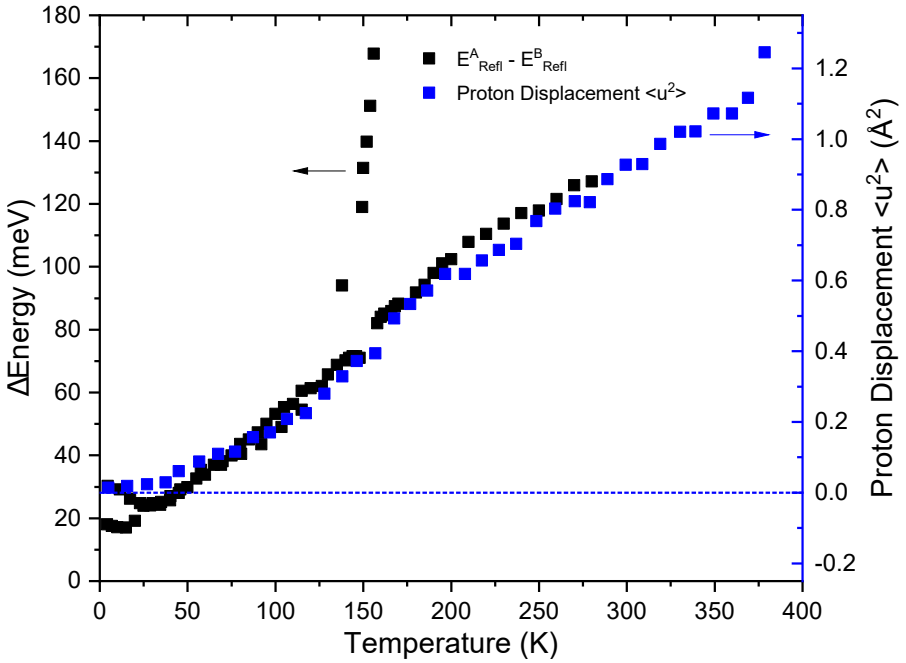


Fig. 6.9: The difference in energy between the higher energy (A-state) and lower energy (B-state) peaks shows a linear trend above ~45 K that continues up to room temperature. This energy difference shows the same trend as reported by Leguy *et al* for the mean squared displacement of protons as determined by quasi-elastic neutron scattering (QENS) on a $MAPbI_3$ thin film. The residual energy offset difference at low temperatures is likely due to part of the $CH_3NH_3^+$-ions freezing in a certain non-equilibrated position. QENS data adapted with permission from Leguy et al [117] Nat. Commun. 2015, 6, 1764-1769, under the CC BY-SA 4.0.

both HT/LT thin films and single crystals. At these low temperatures, they showed feeding of carriers from the A state into the B state, which is shown to have longer life times than the A state [262].

6.4 Nature of the A and B Peaks

Taking the difference of the A/B-peak energies as in Fig.6.9 shows a linear trend after ~40 K and up to 300 K. A similar behaviour has been reported in literature obtained by both CGE [146], and photoconductivity measurements [123], albeit these reports only gave a tentative explanation for the origin of the B signal they reported.

It is of interest to note that the onset of linear behaviour seen in the data presented here, and in literature, corresponds well with some theoretically predicted and experimentally shown methyl ammonium $CH_3NH_3^+$ -ion activation energies [263, 264], and the experimentally

determined mean (methyl ammonium-) proton displacement [117] shown in Fig.6.9. The correlation between the ΔE and average hydrogen displacement suggests the origin of the A/B-peak is related to the fluctuations of the MA-ion orientations leading to a temporary internal field and a direct/indirect gap of the same magnitude as seen here [136, 143, 265, 266], leading to a dynamic Rashba effect. As shown in section 6.3, there are many domains with different crystal lattice d-spacing in the surface of the (HT) sample, making the ferroelectric domains shown by Rakita *et al* [93] weaker or prevent them completely, due to the lack of possibility for the MA^+ to randomly, spontaneously align. This is also supported by the CGE measurements of Niesner *et al* [146], which showed a large dependence on experiment geometry, and saw a difference in signal strength between different samples.
This behaviour also explains the direct contradictions in literature stating the absence of inversion symmetry [167] or the existence thereof [94], as determined by second harmonic generation (SHG). The crystal showing SHG for parts of the crystal was grown following a LT recipe, whereas the crystal showing no SHG was grown at HT, implying that any SHG that occurred was well below the detection limit or couldn't be detected at all as the relevant states were covered by the sample surface.

6.4.1 Estimate of the Rashba Parameter

Assuming equal masses for hole and electron $m_e = m_h$, in a simple Rashba model

$$E_i(k) = E_i(0) + (-1)^i \frac{\hbar^2 k^2}{2m_i^*} + (-1)^i \alpha_R k \tag{6.1}$$

with Rashba coeffiecient α_R, the transition energy minimum will be at $k = \frac{m^*}{2\hbar}\alpha_R$, and the separation of states will be $\Delta E = \frac{m^*}{4\hbar^2}\alpha_R^2$. Combining the two allows for calculation of α_R with the formula of

$$\alpha_R = 2\hbar\sqrt{\frac{\Delta E}{m^*}}, \tag{6.2}$$

where ΔE is the energy difference between the observed A/B emission peaks, a measure of the spin-splitting [142, 146]. Using the values from Fig.6.9 (b) for ΔE, and the effective mass as determined in Ch.7, yields Rashba-parameters between 1.7 eV Å at 1.4 K, and 3.8 eV Å at room temperature, although the latter value is much less accurate due to the increase in

damping of the R signal. Nonetheless, both values are well within the range of values of energy splitting between 5 meV-120 meV as calculated in literature [95, 118, 139, 140, 142, 143, 265, 267–269].

6.5 Conclusions

The differences in $MAPbI_3$ behaviour based upon growth temperature is of great interest for device fabrication, as the lower energy B-peak is a feature also seen in thin films. This result reinforces the importance to fabricate devices under stable, reproducible conditions to enhance reproducibility of experiments. The origin of this secondary emission line lies in the difference between bulk and surface of the sample, where the surface in this case must be assumed to be up to 200 nm thick, as becomes obvious from the difference in behaviour in XRD experiments between bulk and surface scattering response. The former shows a single lattice d-spacing, whereas the latter shows many domains with different lattice d-spacings, belonging to different crystal domains. The influence of the surface also matters for PL measurements on different areas of the same crystal, changing the A/B-peak area ratio, as locally the surface changes.

From the differences in behaviour seen for the A- and B-peaks, the A-emission line was determined to be due to the direct gap, whereas B was assigned to an indirect gap. The origin of the two peaks lies in a dynamical Rashba splitting, which is the natural state of the bulk, but strongly depends on the surfaces composition for its strength there. To obviate A emission only behaviour, the surface of the sample should be as homogenous as possible, to result in a strong B signal.

The higher efficiency and stability seen for mixed cation perovskites $(A^a_{1-x}A^b_x)BX_3$ is highly likely to be influenced by this. A first indication of this was shown for thin films recently [270], where no phase change was visible for $(Cs,Ma)Pb(I,Br)_3$ thin films. This also agrees with recent calculations showing variations in cation size create local octahedral tilting, preventing internal fields by blocking large scale MA alignment [271, 272] increasing the strength of the direct nature of these materials.

The room temperature dynamic Rashba coefficient of about 3.8 eV Å measured here compares well to literature [95, 118, 139, 140, 142, 146, 265, 267–269]. This spin splitting and corresponding indirectness of $MAPbI_3$ offers a further explanation for the great performance of $MAPbI_3$ devices and their long carrier lifetimes. But while the indirect B state may effectively serve as a charge transport pathway with very low recombination rates [138], it is likely that a large polaronic charge screening effect contributes to this also [137].

7 Polarons in $MAPbI_3$ and $MAPbBr_3$

Defect densities in standard semiconductors like silicon and gallium arsenide have to be very small to achieve properties that allow for efficient solar cell devices close to their physical limits set by the *Shockley-Queisser* limit [273]. In contrast, the facile solvent-based production for metal halide perovskites produces small grains on the order of several hundred nanometres which have a defect density on the order of $10^{10}\,\mathrm{cm}^{-3}$ [105]. Following the behaviour of classical semiconductors, the expectations would be devices limited by their defects, yet perovskites far exceed these expectations.

In contrast to classical semiconductors, perovskites like $MAPbI_3$ and $MAPbBr_3$ tend to have a low LO-phonon energy[257, 274, 275] of around 4-21 meV, causing an early onset and strong contribution of the Fröhlich coupling between excitons and crystal to the energy scape of the transitions in these materials [257].

Magneto-optical measurements allow for the study of the influence of polarons on optical transitions, and correspondingly on R_y^* and m^*, by comparing the two regimes $\hbar\omega_c < 2R_y^*$ and $\hbar\omega_c > 2R_y^*$, where polaron-exciton and (free) Landau-level transitions dominate respectively. The Landau regime has been studied in detail for $MAPbI_3$ and $MAPbBr_3$ single crystals [159] and thin films [158, 276–279] as listed in Table 7.1. All the data shown there is dominated by fits to the $\hbar\omega_c > 2R_y^*$ regime, where the fit for the effective mass estimate is dominated by the high energy, high field transitions of free charge carriers.

In this chapter, magneto-optical results of $MAPbI_3$ and $MAPbBr_3$ measured in reflectivity (R) and transmission (T) on single crystals (SC) and thin films (TF) samples at 1.4 K are presented. In comparison to previous studies in the literature, here the focus is on high

Table 7.1: Overview of values for effective mass m^*, g_{exc}, and the exciton binding energy R_y^* obtained from high field transmission and reflectivity measurements on $MAPbI_3$ and $MAPbBr_3$ thin films and single crystals given in literature:

	m^*/m_e	R_y^* (meV)	g_{exc}
$MAPbBr_3$ thin film[279]	0.13	76	2.03
$MAPbBr_3$ thin film[278]	0.12	37	1.2
$MAPbBr_3$ thin film[276]	$0.117 \pm 10\%$	$25 \pm 20\%$	
$MAPbI_3$ thin film[279]	0.15	50	1.72
$MAPbI_3$ thin film[276]	0.104	16	
$MAPbI_3$ thin film[158]	$0.1 \pm 5\%$	16 ± 2	
$MAPbI_3$ thin film[277]	0.102 ± 0.002	16 ± 1	
$MAPbI_3$ single crystal[159]	0.104 ± 0.005	16 ± 2	2.66 ± 0.1

quality non-pulsed measurements, allowing to determine the device relevant polaron-screened exciton effective mass and binding energy with a much higher precision in the low field regime $\hbar\omega_c < 2R_y^*$.

The results show an increase in both binding energy and effective mass going from $MAPbI_3$ to $MAPbBr_3$, following the more „ionic“ nature of the bond of Pb-Br in comparison to Pb-I, and the larger bandgap. These results are comparable to previous data in the literature obtained from thin film high field data for a variety of (MA,FA)Pb(Br,I)$_3$ combinations [158, 159, 276–279], albeit the determined masses are higher and binding energies lower. Part of this chapter is based on a manuscript currently in preparation.

7.1 Samples

Different $MAPbI_3$ and $MAPbBr_3$ thin films and single crystals were studied for the work in this chapter, as shown in Fig.7.1. These included both low temperature (LT) and high temperature (HT) grown $MAPbI_3$ films and single crystals, as detailed in the previous chapter Ch.6. Both HT and LT crystals and films yielded comparable results. As the higher energy signal corresponding to the direct gap and exciton was much more pronounced for the HT samples, consequently the HT $MAPbI_3$ samples showed stronger excitonic features, and $2s/3d$ excited states that were not visible or not as strong for the LT grown $MAPbI_3$ single crystals.

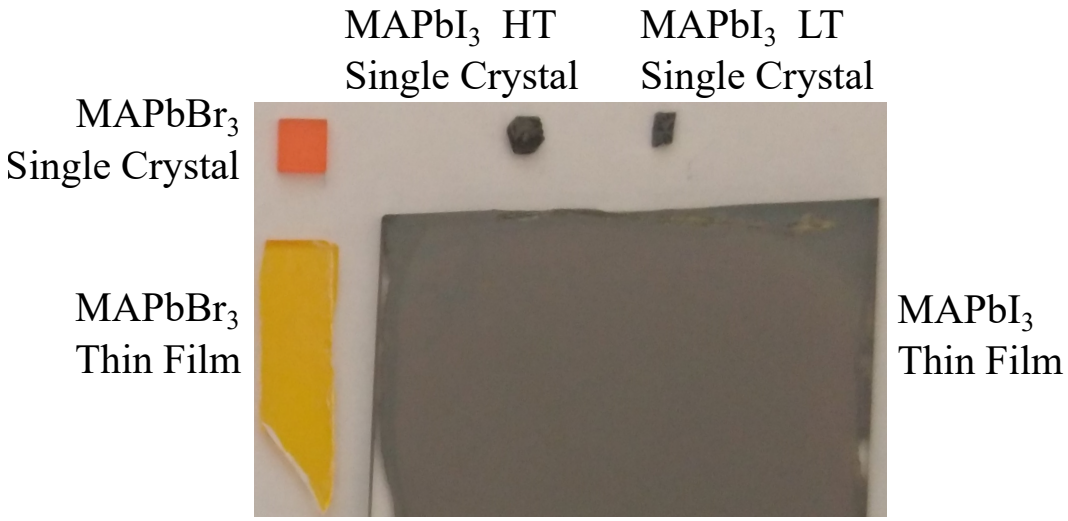


Fig. 7.1: $MAPbBr_3$ and $MAPbI_3$ thin films (TF) and single crystals (SC) as used for the measurement of transmission and reflectivity under magnetic fields. The HT $MAPbI_3$ crystal has a dodecahedral shape, the LT crystal a cuboid shape.

7.2 Field-Dependence of Transition Energies for $MAPbBr_3$

Single crystals and thin films of $MAPbBr_3$ show a dominant feature at about 2.25 eV and 2.27 eV as visible in Fig.7.2. This energy shift is quite common in the comparison of nanometre-scale films and millimetre bulk perovskite crystals. While the SC shows a sharp transition width of around 4.3 meV, the TF peak is much broader at more than 15.5 meV as visible in Fig.7.2 (c,d). In order to improve the weak signal and bring out the smaller field-dependent transitions for the TF, the transmission data was divided by the zero-field measurement to improve resolution as shown in (c). Narrower peaks in $MAPbBr_3$ SC are a result of lower defect densities [105] and a lower number of crystal domains in comparison to the small surface-to-volume ratio crystallites in a TF. Correspondingly, SC data allows for more accurate determination of transition energies, owing to the narrower peaks. The peak data does not follow a linear trend with increasing magnetic field as expected for Landau level transitions, allowing the interpretation of the diamagnetic, i.e. roughly quadratic-field dependency, response of the sample to magnetic fields as transitions to free exciton $1s$ and excited exciton $2s/3d$ states.

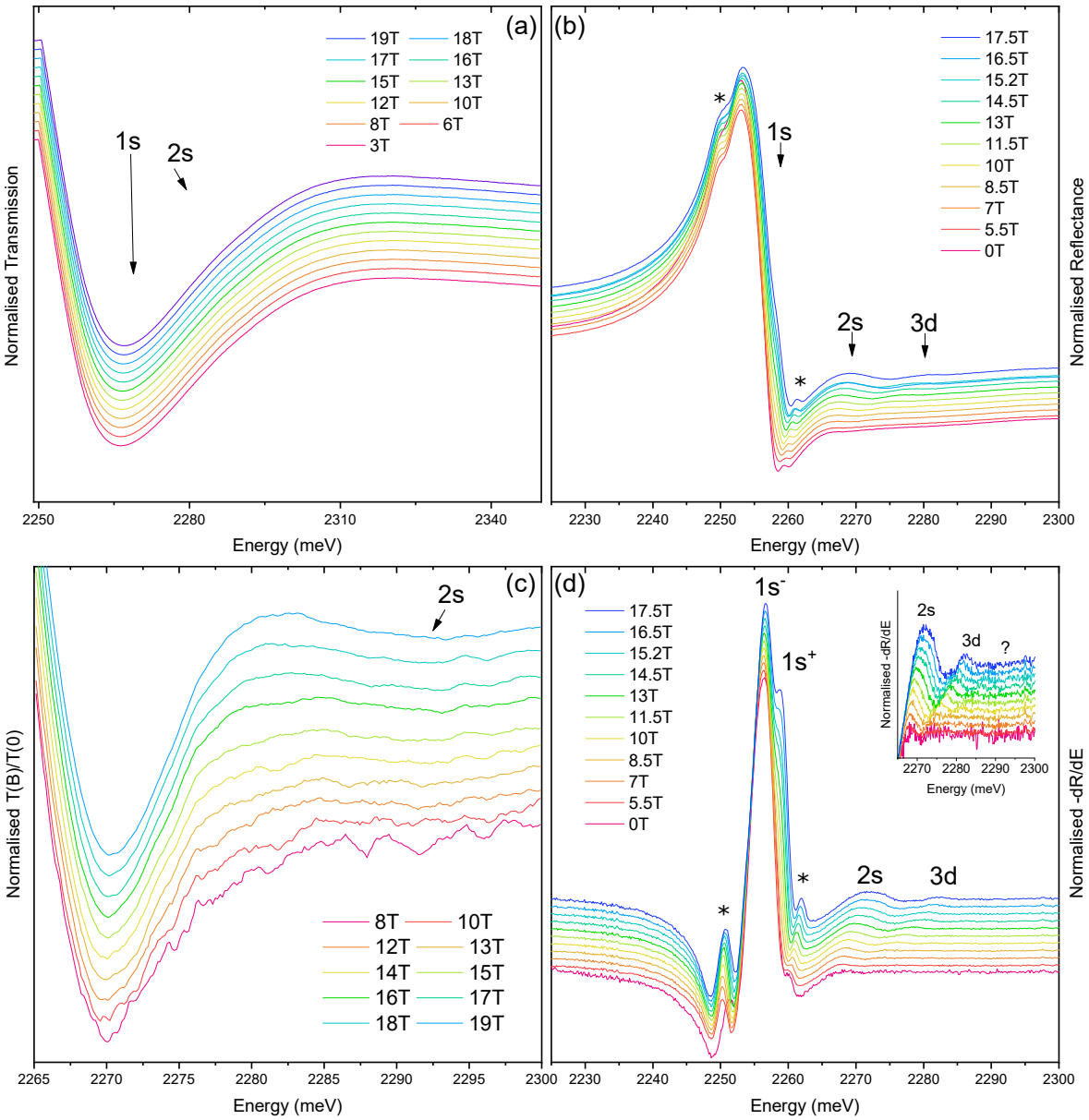


Fig. 7.2: Magnetic field response of TF transmission (a,c) and SC reflectivity (b,d) of $MAPbBr_3$ at 1.4 K. $-\frac{dR}{dE}$ shows sharp transitions, whereas the TF response is less sharp in energy, and higher order transitions are not visible without dividing the data by the zero-field spectrum. The spectra have been offset for the ease of readability. For the same reason, (d) includes an inset featuring the weaker $2s$, and $3d$ signal. On the higher energy side of the $3d$ transitions in $-\frac{dR}{dE}$, there may be another transition visible, marked "?", but the signal is too small to be fit at these low fields. The extra peaks below/above $1s$ in $-\frac{dR}{dE}$ marked with an asterisk are discussed in the text.

At higher fields, the $1s$-state's Zeeman splitting into spin $|\pm\frac{1}{2}\rangle$ states $1s^+$ and $1s^-$ is resolved for the SC, allowing to determine the effective g-factor g_{exc} to about 2.6 for $MAPbBr_3$. For the higher order transitions, a Zeeman splitting is not yet resolved at 19 T. In general, the response of the exciton transisitons follow a diamagnetic behaviour up to 19 T, similar to transitions in a hydrogen atom in a magnetic field.

Fitting The Transition Energies

As the magnetic field dependence of the transitions of an exciton cannot be solved analytically, a numerical solution by Makado *et al* [160] was employed to compare the experimental data with a theoretical model. The numerical solutions of Makado *et al* were derived from adding the Coulomb term $\frac{e^2}{\epsilon_r \mathbf{r}}$ to the general free charge Hamiltonian given in Eq.2.47 to yield

$$\mathcal{H} = -\Delta^2 - \frac{2}{r} - \imath\gamma\frac{\partial}{\partial\phi} + \frac{1}{4}\gamma^2\rho^2 \tag{7.1}$$

in polar cylindrical coordinates. After the transformation to cylindrical coordinates, the dimensionless magnetic field strength is given by $\gamma = \hbar\omega_c/2R_y^*$, where the field dependence arises from $\omega_c = eB/m^*$. The numerical approximation to this equation yielded Rydberg normalised energies $E(\gamma)/R_y^*$ dependent on γ. Since both γ and energies are dependent on the Rydberg energy, fitting of the experimental data was involved, as no $2s$ transition was visible at zero field, which could have been used to calculate the Rydberg energy via $R_y^* = \frac{4}{3}(E_{2s} - E_{1s})$.

For this procedure first the sparse, discrete numerical Makado dataset was interpolated with Beziér-splines. Next, a likely range for R_y^* was determined by eye. Within this energy interval the magnetic fields were calculated and the distance between experimental energies of $1s^{\pm}$, $2s$ and $3d$, and the Makado energies was minimised using the *Nelder-Mead*-algorithm.

As the excitation light source was unpolarised and higher order peaks are weak at low fields, only the $1s$ Zeeman splitting was consistently resolved in the experiments and used for the fit. From this array of fit parameters, the set of parameters with the lowest mean square error was chosen as the likeliest fit to the data.

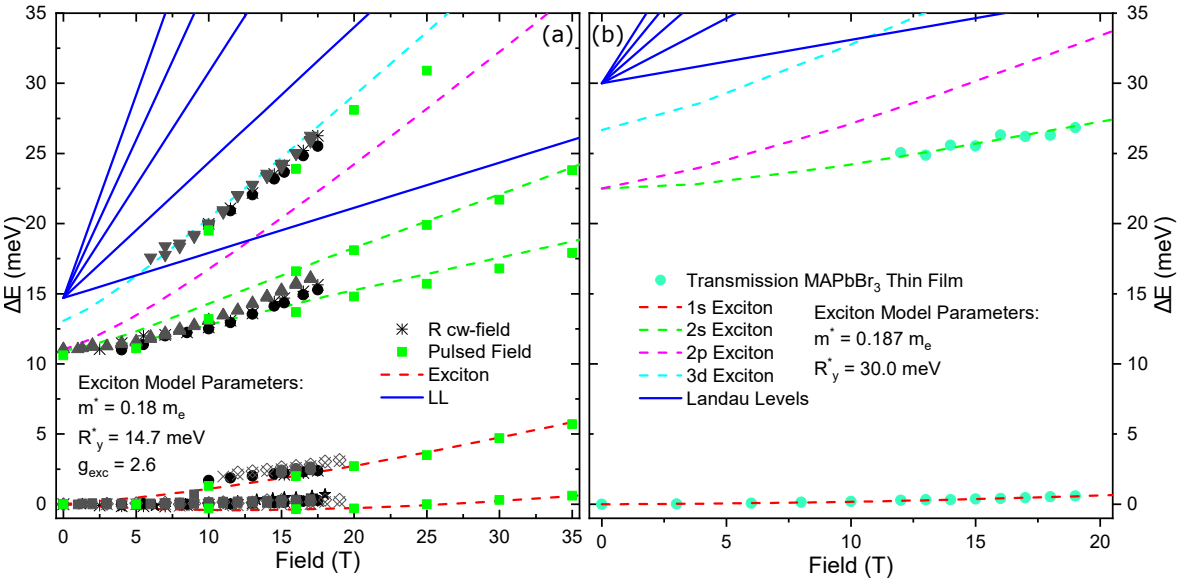


Fig. 7.3: Energies of the different transitions visible in $MAPbBr_3$ TF transmission data (b), and SC (a). Included are some Landau level transition energies (blue, solid), and the excitonic field response as calculated by Makado *et al.* [160] (dashed). For the SC, pulsed high field data from collaborators at LNCMI Toulouse is included to give a comparison to higher fields and energies. Each measurement series corresponds to one group of symbols. Both m^* and R_y^* differ for SC and TF, and are larger for the latter.

Table 7.2: Overview of fit results obtained from magneto-optical data up to 19 T for $MAPbBr_3$ thin films (TF) and single crystals (SC) including polaron mass m^*/m, Rydberg energy R_y^*, and g-factor g_{exc}:

	m^*/m	R_y^* (meV)	g_{exc}	r_p(Å)
TF	$0.187\,m_e \pm 0.005$	$30\,\mathrm{meV} \pm 0.5$		
SC	$0.18\,m_e \pm 0.001$	$14.7\,\mathrm{meV} \pm 0.2$	2.6 ± 0.05	45 ± 1

7.2.1 Transition Energies for $MAPbBr_3$

The peak energies determined from the field dependent transmission and reflectivity spectra for $MAPbBr_3$ obtained from Fig.7.2 and other measurements series are shown in Fig.7.3, for SC (a) and TF (b), together with the modelled excitonic transition energies (dashed lines) and Landau levels (solid lines). While a $2s$ Zeeman split is not resolved in the steady-state, low field, high accuracy SC data, these transition lines are shown as Zeeman split, as they explain some of the spread of data visible for the $2s$ energies, and mirror the high field pulsed data from collaborators at LNCMI Toulouse. Exciton transition lines are obtained from fitting the experimental data with the method outlined above, achieving a good fit, albeit an good description of the $2s$ is difficult.

There is a large difference in fit values for both m^* and R_y^* in comparison of SC and TF as shown in Table 7.2. Both are larger for the TF sample, same as for $MAPbI_3$ TF/SC, which is why this difference will be discussed together with those results in section 7.4 below.
For the dataset of thin films (TF) and single crystals (SC), this method yielded exciton effective masses that are larger than all $MAPbBr_3$ data in Table 7.1, and at the same time also show a lower binding energy. As the data shown here was measured at low fields $\hbar\omega_c < 2R_y^*$ where excitonic transitions dominate, and it diverges from the high field literature data in this specific way, these values are indicative of a large polaron-exciton. As a polaron-exciton, the exciton is slowed down by its interaction with the lattice, increasing its mass. Its energy is decreased at the same time as the Coulomb forces acting on the exciton are lowered by the lattice-exciton interaction.
The radius of the polaron can be estimated by the equation

$$r_p = \sqrt{\frac{2\hbar}{m^*\omega_{LO}}}, \tag{7.2}$$

which depends on the effective mass of the polaron and the LO-phonon frequency ω_{LO}. Using the value of 20.7 meV [274], a size of 45 Å can be calculated for $MAPbBr_3$, considerably larger than the unit cell. As a large polaron, a changeover from polaron-exciton transitions to free carrier transitions dominated behaviour should be visible at $\hbar\omega_{LO}$, but this is at an energy higher than most transitions resolved here. In fact, such a change of behaviour was recently observed at about $2\hbar\omega_{LO}$ by collaborators at the LNCMI Toulouse in pulsed measurements up to 70 T. As the regime change happens at $2\hbar\omega_{LO}$, this implies one LO-phonon contributes for both electron and hole in this process.

The Mystery of the Asterisks

The additional data visible just below and above the $1s$ state of the single crystal visible in both Fig.7.2 (b,d) is visible both at all fields, and before/after the $-\frac{dR}{dE}$- data processing, showing that it is an actual feature of the data, not an artefact. In comparison to field-dependent refletivity data measured at lower white light excitation powers as in Fig.7.4 (d),

it is noticeable that these extra peaks have become almost imperceptible. At higher fields the lower peak has almost become visible again, as it's further from the $1s$ exciton state.
For the lower energy peak at an offset of $-5.8\,\text{meV}$ from the R $1s$ signal, the likely origin is a PL influence on the measurement. This behaviour can be seen in Fig.7.4 (c). In this plot the comparison of both zero-field PL and R, and at 17.5 T shows that the additional peak perfectly coincides with the position of the PL peak. While undesired in a R spectrum, it does not alter or influence the observed peaks, as $1s$ Zeeman splitting as well as $2s$ peak position are not influenced by this feature. Moreover, in comparison of Fig.7.2 (d) and Fig.7.4 (d), measured at high and low excitation power respectively, the intensity of this peak decreases greatly. From the combination of excitation power dependence of the strength of this peak, and its field dependence, it can be identified as a PL influence on the R measurement.
In Fig.7.4, these two extra peaks' positions are plotted together with the calculated exciton $1s^{\pm}$ transitions shifted by $3\,\text{meV}$ for $1s^{+}$ and $-5.8\,\text{meV}$ for $1s^{-}$. Apart from the 0-4 T data for the lower energy peak, this diamagnetic-type description of the observed peaks is surprisingly good.

As the excitons studied here are not just excitons, but polaron-excitons, it is worth the consideration looking at excited states of these to compare with the observed shifts. Theorists predict two of these, namely the relaxed excited state (RES) and the low absorption Franck-Condon states [156, 280–282]. Their respective energies are given by

$$E_{RES} = 0.042\alpha_{FC}^2\hbar\omega_{LO}, \tag{7.3}$$

and

$$E_{FCK} = 0.1414\alpha_{FC}^2\hbar\omega_{LO}, \tag{7.4}$$

where α_{FC} is the Fröhlich coupling constant given by

$$\alpha_{FC} = \frac{e^2}{\hbar}\frac{1}{4\pi\epsilon_0}\left(\frac{1}{\epsilon_\infty} - \frac{1}{\epsilon_{static}}\right)\sqrt{\frac{m^*}{2\hbar\omega_{LO}}}. \tag{7.5}$$

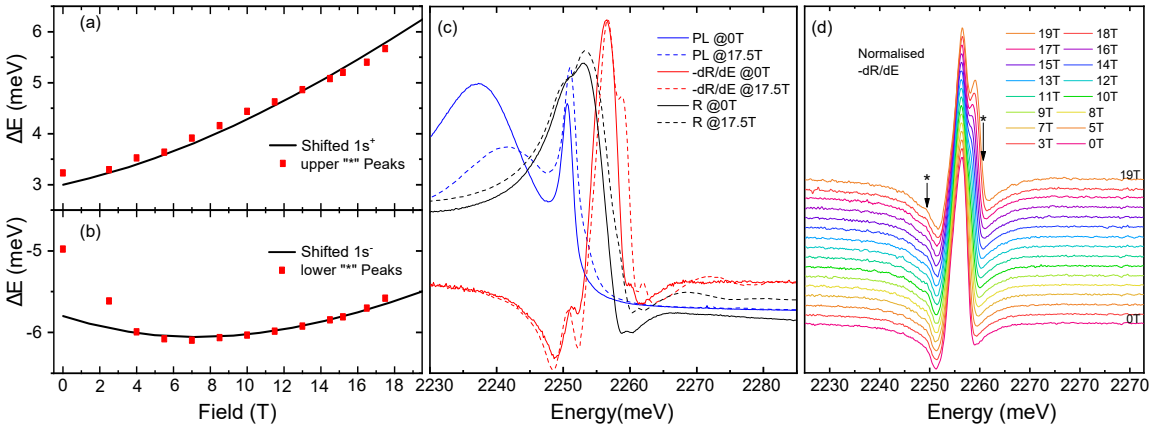


Fig. 7.4: (a,b) Modelled exciton $1s^{\pm}$-states (black lines) shifted to match the additional asterisked peaks seen in Fig.7.2 (b,d). The $1s^{+}$ is offset by 3 meV, the $1s^{-}$-state by -5.8 meV. The good description of the dataset hints at an origin related to the exciton $1s$. (c) Comparison of PL with R response of a $MAPbBr_3$ single crystal at 1.4 K, showing the extraneous sub-$1s$ peak in R and $-\frac{dR}{dE}$ is due to PL influence. (d) Reflectance of a $MAPbBr_3$ single crystal under illumination with a weak intensity white light. The asterisks mark the positions of the extra peaks visible in Fig.7.2. Higher order transitions are not visible for this crystal, likely due to the averaging of the more coarse 300line grating, in comparison to the 1200line grating used for the measurements in Fig.7.2.

Using the $MAPbBr_3$ LO-phonon energy of 20.7 meV [274], values of $E_{FCK} = 10.3$ meV and $E_{RES} = 3$ meV result.

Surprisingly, a shift of the modelled $MAPbBr_3$ $1s^{+}$ transition line by the amount of 3 meV, i.e. E_{RES}, yields a good description of the higher energy peaks shown in Fig.7.4, likely making this peak a polaronic signal. As the expected $2s$ transition almost coincides with the E_{FCK}, it may be that there is some influence of this state on the $2s$ signal, and in fact fitting the $2s$ state accurately proved challenging.

7.3 Field-Dependence of Transition Energies for $MAPbI_3$

In Fig.7.5 the low excitation intensity field $R/-\frac{dR}{dE}$ response of a LT $MAPbI_3$ single crystal is shown in (a,b), and the high excitation intensity response of a HT crystal in (d). (c) shows the transmission for a HT-type $MAPbI_3$ thin film. All feature a strong $1s$ and $2s$ signal, and the higher resolution measurement at higher intensities in (d) also resolves the $2s^{\pm}$ Zeeman splitting and a $3d$-transition. Similar as discussed for $MAPbBr_3$, the higher

excitation intensity also brings out an additional feature marked with an asterisk in the $R/-\frac{dR}{dE}$ spectra, which can be attributed to a PL influence. The main difference between (b) and (d) is the usage of a 300/1200line grating. Accordingly, the $1s$ and $2s$ splitting resolved are not extra data, but are averaged over through the larger binning size of the 300 line grating in (b).

The transition energies as obtained by fit are shown in Fig.7.6, which includes data of four low temperature (LT), and two high temperature (HT) grown single crystals in (a) and one HT/LT thin film each in (b). Due to minute variations in the crystal structure, some variation in transition energies can be expected, and this explains the spread of values visible for the $1s/2s$ state. Despite this variation, all SC data is well described with the parameters of 8.9 meV, and $0.104\,m_e$, with a g-factor of 2.6, as obtained from fitting both $1s^{\pm}$, $2s^{\pm}$, and the $3d$-state. For the TF, again, both binding energy and effective mass are larger than for the SC with 10.1 meV and $0.125\,m_e$.

It has to be noted that, again as with $MAPbBr_3$, the $2s$ state cannot be perfectly described by the model employed here. The exact origin of the difference to the model remains unknown and should be investigated in future work and calculations.

Although in the last chapter, Ch.6, the behaviour seen for HT/LT samples differed, it is not surprising that there is no difference to be seen for the binding energies, g-factors, and effective masses. As shown by the difference in behaviour between PL and R, the former is dominated by the top ~250 nm of the crystal/thin film, whereas the latter penetrates deeper and can resolve both states, rendering the difference between HT/LT void, which is good to know for researchers interested in devices.

In comparison to previously published values, the obtained value for the exciton binding energy are 50% and 20% smaller for SC and TF, but the effective mass is roughly the same. Reading out the Yang *et al* [159] data by using a plot digitiser [283], obtaining the previous best data set on $MAPbI_3$, the picture becomes clearer. In Fig.7.7, their low and high field data and fit are shown, together with the low field fit obtained in this work. There are large discrepancies between their high and low field data, and the effective mass value is a result of their trying to harmonise their dataset, as especially evident from the $2p$ or $3d$ data. Thus,

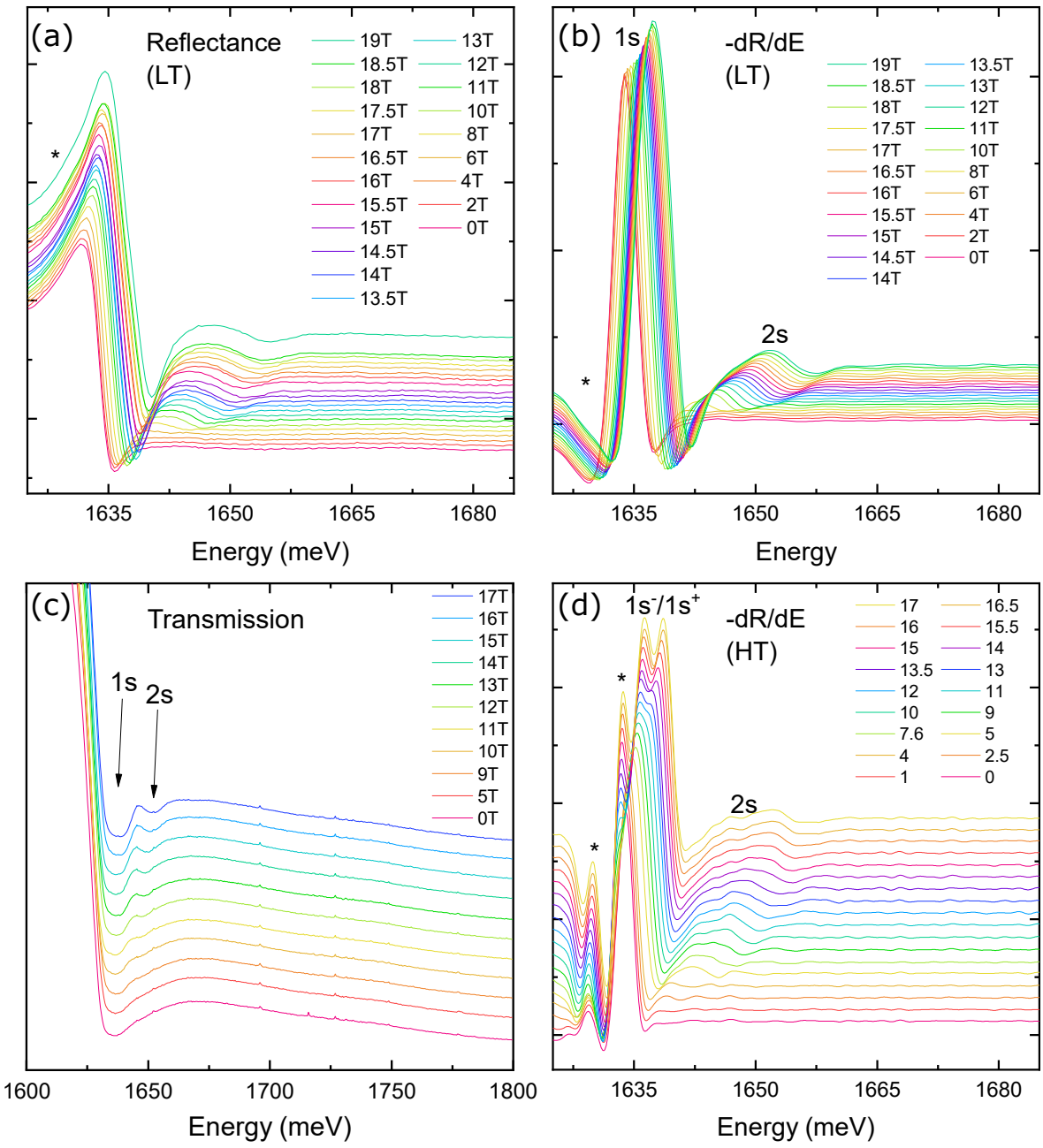


Fig. 7.5: Normalised field response of $MAPbI_3$ single crystals R (a), $-\frac{dR}{dE}$ (b,d) and thin film transmission (c) at 1.4 K. The untreated raw transmission shows the $1s$ and $2s$ state for the thin film. The single crystal additionally shows a feature corresponding to PL marked with an asterisk, that increases in strength with increased excitation intensity. Another difference between (a,b) and (d) is that the former were measured using a 300line grating on a LT crystal, the latter on a HT crystal using a higher resolution 1200line grating, allowing for higher resolution.

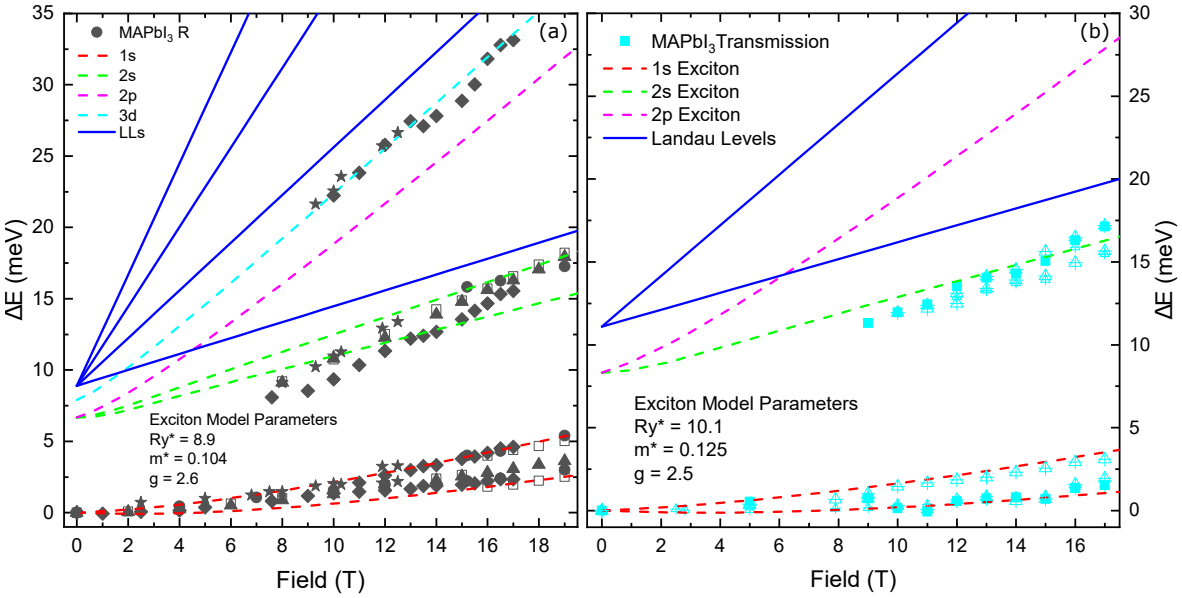


Fig. 7.6: Energies of the different transitions visible in the $MAPbI_3$ transmission data of two thin films, and six HT/LT single crystals (a). Included are the Landau level transition energies (blue, solid), and the excitonic field response (dashed) as calculated by Makado *et al.* [160]. Fitting $1s^{\pm}$, $2s^{\pm}$ and $3d$ data with the exciton model, values of R_y^* =8.9 meV, g_{exc} = 2.6 and an effective mass of $0.104\,m_{\mathrm{e}}$ for the single crystal, and 10.1 meV and $0.125\,m_{\mathrm{e}}$ for the thin films.

the effective masses determined for this thesis are of comparable size, but have a much higher accuracy then the previously published values.

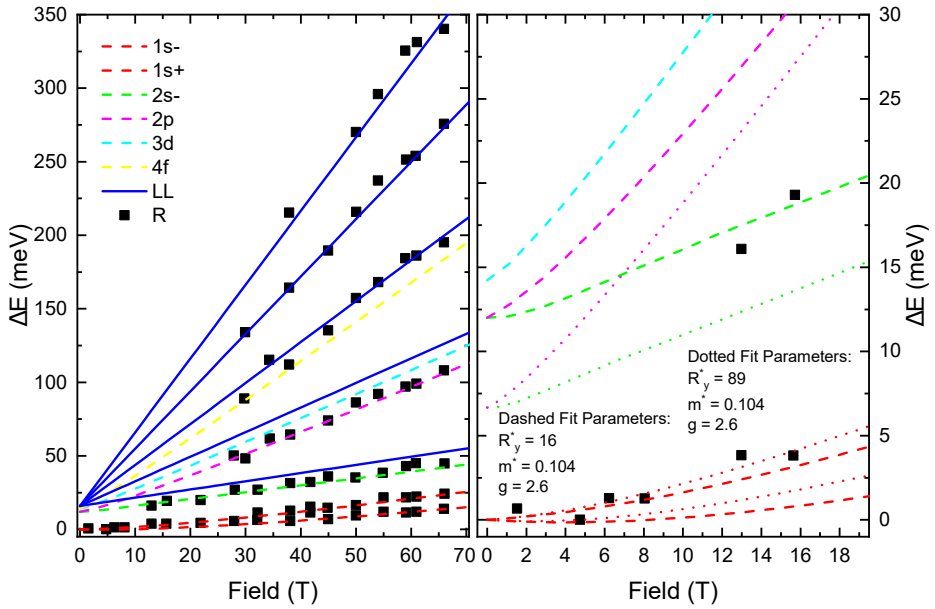


Fig. 7.7: Transition energies for a $MAPbI_3$ single crystal as reported by Yang *et al* [159]. The left shows the entire dataset, which shows a good fit to the theoretical model of 16 meV binding energy and $0.104\,m_{\mathrm{e}}$. On the right, the focus is on the low field regime, where the fit is less accurate.

7.4 Differences Thin Film/Single Crystal

For both $MAPbBr_3$ and $MAPbI_3$, a large difference of almost a factor of two can be observed for the exciton binding energy R_y^*, of thin films and single crystals. This is very interesting, as Mahboubi-Soufiani *et al* compared the effects of perovskite thin film crystallite size on exciton binding energy and effective mass [277] and reported no influence. They studied thin films with average grain sizes between 200-780 nm, and compared their high field response to that of a $MAPbI_3$ single crystal, in work they had published a month earlier of the same year [159], and all these measurements arrived at a binding energy of 16 meV. For the effective mass, they reported values between 0.102-0.109 m_e, with no clear trend discernible. As the new data presented in this chapter is both more detailed, and also more precise, there does seem to be an influence of the crystal structure, i.e. crystallite size, on the observed properties, with large crystals having more advantageous values for devices both in R_y^* and m^*.

7.5 Summary

Modelling and calculations show, that the observed effective masses should be between ~20-40% higher for the low field, low energy regime, than for free carriers in Landau levels if polarons are influencing the excitons [128, 255, 279, 284], which is what was observed here for both $MAPbBr_3$ and $MAPbI_3$ thin films and single crystals.

Fitting of the observed transitions also yielded smaller exciton binding energies as listed in Table 7.3, showing that thin films for both $MAPbBr_3$ and $MAPbI_3$ have about twice as large an exciton binding energy, and more than 30% larger effective mass, where the origin is likely to be the smaller TF crystallite size.

Table 7.3: Overview of results obtained from magneto-optical data up to 19 T. An estimate of polaron mass m_p is given also:

Anion/Modification	m^*/m	R_y^* (meV)	g_{exc}
Br TF	$0.187\,m_e \pm 0.005$	$30\,\text{meV} \pm 0.5$	
Br SC	$0.18\,m_e \pm 0.001$	$14.7\,\text{meV} \pm 0.2$	2.6 ± 0.05
I TF	$0.125\,m_e \pm 0.005$	$10.1\,\text{meV} \pm 0.3$	
I SC	$0.104\,m_e \pm 0.001$	$8.9\,\text{meV} \pm 0.2$	2.6 ± 0.05

Correspondingly, reports on the mobility in literature [274, 286–289] based on previous estimates of the effective mass m^* for $MAPbBr_3$ and $MAPbI_3$ are likely to overestimate mobility, as the Feynman large polaron approach of $\mu \propto \frac{1}{m^*}$ [290, 291] they employed depends on the effective mass. Accordingly, anyone building devices based on these two perovskites should focus on preparing devices consisting of a single piece of single crystal, to gain the benefits of the lower exciton binding energy and effective mass.

Additional research on the temperature dependence of the exciton binding energy are highly likely to provide further insights into $MAPbI_3$ and $MAPbBr_3$, as preliminary high field studies [270, 292], have shown a decrease in exciton binding energy upon crossing into the tetragonal phase, indicating further interesting material properties can be discovered there.

8 Summary and Outlook

In this last chapter, a quick summary and outlook is presented here for the chapters concerning themselves with fSWNT electrodes, $Cs_2AgBiBr_6$ double perovskites, optical/structural properties of $MAPbI_3$, and the magneto-optical properties of $MAPbBr_3$ and $MAPbI_3$.

8.1 Electrodes of Functionalised Single-Walled Carbon Nanotubes (fSWNT)

Several different deposition techniques were tested for polymer-functionalised single-walled carbon nanotubes, where spray-coating resulted in the best films with regards to uniformity and reproducibility.

Longer tubes result in films that have lower sheet resistances, but this is not the only method of improving fSWNT films. Doping with highly electronegative small molecules, for example with HNO_3^+, results in a decrease in sheet resistance of up to a factor of three, which is very likely due to a change in nature from semiconducting to metallic-type after doping, caused by a shift in Fermi-energy.

The sprayed, doped fSWNT films resulted in values of down to $178\,\Omega/\square$ at 69% transmission, close to those necessary for application in devices. This shows the efficacy of this novel SWNT deposition technique, and opens up many possible applications. For example, there is a recent report on a triple junction all perovskite solar cell [293], which required the use of orthogonal solvents, and the deposition of ITO nano particles as electrodes. fSWNT are soluble in solvents orthogonal to perovskites, and already now they show better values for R_{sheet} than

ITO nano particle films [294]. Thus, tandem cells are an interesting playing field for these novel electrodes.

In order to get to this point, other polymers may have to be tested, and the surface roughness of the resulting films optimised. Moreover, a study of the functionalisation process itself would be of interest, as tubes are cut shorter and shorter with increasing sonication time [179], opening a facile path to better sheet resistance values.

8.2 Outlook on Magneto-Optical Properties of $Cs_2AgBiBr_6$

$Cs_2AgBiBr_6$ is a rather recent addition to the perovskite family. Accordingly, there are a few theoretical studies on its band structure, but experimental data was still incomplete. The direct bandgap was identified at 2.85 eV and can be described well by a model based on the crystal unit cell volume and the spontaneous tetragonal strain. Thus, the correlation between optical and structural properties of $Cs_2AgBiBr_6$ can be described from room temperature, through the phase transition at 122 K, down to 1.4 K. For the PL response of this material, for the first time a second PL peak at 1.3 eV was described, which can be identified as belonging to the indirect gap of this material, visible both in absorption and PL. The 2 eV emission, which commonly was held to be the indirect gap in literature, was identified to be due to a colour centre, more specifically due to a Ag_{Bi} anti-site defect, which shows a considerable Stokes shift between emission and absorption.

The free exciton at the direct gap showed negligible response to magnetic fields, pointing to a large binding energy >300 meV. Together with a direct bandgap that is too large for harvesting light from the solar spectrum, a tailoring of the bandgap is called for. Slavney *et al* [295] report such a tuning by doping with tellurium, changing the observed absorption onset. If tuned to the right values, this may even lead to white light emission capable materials, as reported for a doped $Cs_2Na_xAg_{1-x}BiCl_6$ [238], with tunable emission properties. Moreover, a change from direct to indirect nature has been predicted for an order parameter based on the Ag/Bi ordering in the crystal [201], opening another pathway for optimisation of this material. By putting these methods to the test, it is likely that the efficiencies seen for

$Cs_2AgBiBr_6$ based solar cell devices can be pushed well beyond the reported best value of 2.2% efficiency [217].

8.3 Nature v Nurture: For $MAPbI_3$ Nurture Wins

Photoluminescence and reflectance analysis of $MAPbI_3$ crystals shows an interesting incongruity at room temperature, where most reported $MAPbI_3$ thin films and single crystals show a PL emission at about 1.6 eV, whereas our reflectance measurements show only the weakest traces of a signal at 1.6 eV, but a strong signal at 1.48 eV. Moreover, for thin films and single crystals grown in the tetragonal phase <55 °C, a second PL line exists at precisely 1.48 eV. The intensity ratio of the two observed PL peaks depends on the spot of the crystal measured. This behaviour makes sense after an XRD study on cubic phase and tetragonal phase grown crystals, where the former shows a crystal consisting of many domains, whereas the lower temperature grown crystal consists almost exclusively of one dominant domain. Focusing on the surface of an as grown high temperature (HT) crystal, and a freshly cleft face of a HT growth crystal, the origin of the A/B-behaviour is revealed to be the sample's surface. For the freshly cleaved surface a single peak in the XRD response shows, while the surface of the as-grown crystals shows an array of different peaks. Moreover, the freshly cleaved high temperature crystal also shows the double PL emission. With a strong PL emission coming from a small share of the surface of the crystal, the 1.6 eV emission is identified as coming from a direct band-to-band transition, whereas the 1.48 eV is based on an indirect gap. By studying the evolution of the energy difference of the two emission lines, the origin of the lower energy peak is assigned to be due to the dynamical Rashba effect caused by the methylammonium, which requires spontaneous long range alignment of the MA-ions. Thus, the varying intensity of the lower energy peak can be explained by stronger or weaker alignment of the MA-ions. These new discoveries and understanding of their origin may well be of large benefit for the device community. Not only could it serve to better understand the improved performance of mixed cation perovskites, but can also lead the way to higher efficiency and better reproducibility. To give a recent example, Ramadan *et al* published a report on $MAPbI_3$ deposited from acetonitrile, where the <25 °C vacuum annealed samples showed a performance about

1% lower than the samples annealed at 100 °C in air [296], showcasing a possible impact of the lower energy, indirect gap.

Lastly, initial experiments on $MAPbBr_3$ single crystals have started showing the same behaviour as low temperature $MAPbI_3$, with two emission lines visible in reflectance, offering ample opportunity for further studies.

8.4 Polarons in $MAPbI_3$ and $MAPbBr_3$

In the last chapter, the influence of exciton lattice interactions, of polarons, was investigated indirectly by comparing high precision low field low energy magneto-optical transition energies with high energy, high field data reported in literature. Both for the studied $MAPbBr_3$ and $MAPbI_3$ thin films and single crystals, the fitted exciton binding energies were lower than reported for the high field data, and at the same time the observed effective masses were higher, confirming a polaronic influence on the exciton properties. Moreover, higher field data from collaborators at LNCMI Toulouse also shows clearly that the transition between the polaronic-dressed, and undressed free carrier regime takes place at about $2\hbar\omega_{LO}$, confirming the phonon influence.

The most interesting observation has to be the difference manifest for single crystals and thin films. For both $MAPbI_3$ and $MAPbBr_3$ the thin films showed exciton binding energies about twice as large as for single crystals, while also having larger effective masses. This is an important result for the optimisation of devices in trying to obtain the highest possible device efficiencies, portending the path to the highest efficiencies will require less polycrystalline perovskite layers.

Bibliography

[1] Joel Jean et al. "Pathways for solar photovoltaics". In: *Energy Environ. Sci.* 8.4 (2015), pp. 1200–1219. DOI: 10.1039/C4EE04073B (Cited on p. 1).

[2] NREL. *Best Research-Cell Efficiencies Chart [status 2019-04-11]*. 2019 (Cited on pp. 1, 22).

[3] Richard H. Friend et al. "Perovskite LEDs". In: *Sci. Video Protoc.* 1.1 (2019), pp. 1–5. DOI: 10.32386/scivpro.000008 (Cited on p. 1).

[4] Wired. *Wired MWC Statement (Accessed 24/02/2019) https://bit.ly/2SgkOm6* (Cited on p. 2).

[5] P. R. Wallace. "The Band Theory of Graphite". In: *Phys. Rev.* 71.9 (1947), pp. 622–634. DOI: 10.1103/PhysRev.71.622 (Cited on p. 4).

[6] D H Robertson, D W Brenner, and J. W. Mintmire. "Energetics of nanoscale graphitic tubules". In: *Phys. Rev. B* 45.21 (1992), pp. 12592–12595. DOI: 10.1103/PhysRevB.45.12592 (Cited on p. 4).

[7] Charles M. Lieber et al. "Atomic structure and electronic properties of single-walled carbon nanotubes". In: *Nature* 391.6662 (1998), pp. 62–64. DOI: 10.1038/34145 (Cited on p. 5).

[8] S. Reich, C. Thomsen, and J. Maultzsch. *Carbon Nanotubes*. Ed. by C. Thomsen, S. Reich, and J. Maultzsch. Weinheim, Germany: Wiley-VCH Verlag GmbH, 2004, pp. 1–215. DOI: 10.1002/9783527618040 (Cited on pp. 5, 11, 20, 21).

[9] Rudolf Gross and Achim Marx. *Festkörperphysik*. München: Oldenbourg Wissenschaftsverlag, 2012, p. 982 (Cited on pp. 9, 19, 25, 33).

[10] S. Reich et al. "Tight-binding description of graphene". In: *Phys. Rev. B* 66.3 (2002), p. 035412. DOI: 10.1103/PhysRevB.66.035412 (Cited on p. 11).

[11] Siegfried Hunklinger. *Festkörperphysik*. Ed. by 3. 3rd. De Gruyter Oldenbourg, 2012, p. 627 (Cited on pp. 12, 14, 29, 30, 34).

[12] Noriaki Hamada, Shinichi Sawada, and Atsushi Oshiyama. "New one-dimensional conductors: Graphitic microtubules". In: *Phys. Rev. Lett.* 68.10 (1992), pp. 1579–1581. DOI: 10.1103/PhysRevLett.68.1579 (Cited on p. 12).

[13] Riichiro Saito et al. "Electronic structure of graphene tubules based on C60". In: *Phys. Rev. B* 46.3 (1992), pp. 1804–1811. DOI: 10.1103/PhysRevB.46.1804 (Cited on p. 12).

[14] C.T. White and J. W. Mintmire. "Density of states reflects diameter in nanotubes". In: *Nature* 394.6688 (1998), pp. 29–30. DOI: 10.1038/27801 (Cited on p. 14).

[15] R Saito, G. Dresselhaus, and M S Dresselhaus. "Trigonal warping effect of carbon nanotubes". In: *Phys. Rev. B* 61.4 (2000), pp. 2981–2990. DOI: 10.1103/PhysRevB.62.4273 (Cited on p. 14).

[16] X. Blase et al. "Hybridization effects and metallicity in small radius carbon nanotubes". In: *Phys. Rev. Lett.* 72.12 (1994), pp. 1878–1881. DOI: 10.1103/PhysRevLett.72.1878 (Cited on p. 14).

[17] S. Reich and C. Thomsen. "Chirality dependence of the density-of-states singularities in carbon nanotubes". In: *Phys. Rev. B* 62.7 (2000), pp. 4273–4276. DOI: 10.1103/PhysRevB.62.4273 (Cited on p. 14).

[18] M Ouyang. "Energy Gaps in Metallic Single-Walled Carbon Nanotubes". In: *Science (80).* 292.5517 (2001), pp. 702–705. DOI: 10.1126/science.1058853 (Cited on p. 14).

[19] J.-C Charlier. "Defects in Carbon Nanotubes". In: *Acc. Chem. Res.* 35.12 (2002), pp. 1063–1069. DOI: 10.1021/ar010166k (Cited on p. 14).

[20] Ali Javey et al. "Ballistic carbon nanotube field-effect transistors". In: *Nature* 424.6949 (2003), pp. 654–657. DOI: 10.1038/nature01797 (Cited on pp. 14, 15).

[21] David Mann et al. “Ballistic Transport in Metallic Nanotubes with Reliable Pd Ohmic Contacts”. In: *Nano Lett.* 3.11 (2003), pp. 1541–1544. DOI: 10.1021/nl034700o (Cited on p. 15).

[22] Paul L. McEuen et al. “Disorder, Pseudospins, and Backscattering in Carbon Nanotubes”. In: *Phys. Rev. Lett.* 83.24 (1999), pp. 5098–5101. DOI: 10.1103/PhysRevLett.83.5098 (Cited on p. 15).

[23] W. et al Liang. “Fabry - Perot interference in a nanotube electron waveguide”. In: *Nature* 411.6838 (2001), pp. 665–669 (Cited on p. 15).

[24] T. W. Ebbesen et al. “Electrical conductivity of individual carbon nanotubes”. In: *Nature* 382.July (1996), pp. 54–56. DOI: 10.1038/382054a0 (Cited on p. 15).

[25] T. Dürkop et al. “Extraordinary Mobility in Semiconducting Carbon Nanotubes”. In: *Nano Lett.* 4.1 (2004), pp. 35–39. DOI: 10.1021/nl034841q (Cited on p. 15).

[26] Giulio Mazzotta et al. “Solubilization of Carbon Nanotubes with Ethylene-Vinyl Acetate for Solution-Processed Conductive Films and Charge Extraction Layers in Perovskite Solar Cells”. In: *ACS Appl. Mater. Interfaces* (2018). DOI: 10.1021/acsami.8b15396 (Cited on p. 15).

[27] Zhuangchun Wu. “Transparent, Conductive Carbon Nanotube Films”. In: *Science (80-.).* 305.5688 (2004), pp. 1273–1276. DOI: 10.1126/science.1101243 (Cited on p. 15).

[28] E. S. Snow et al. “Random networks of carbon nanotubes as an electronic material”. In: *Appl. Phys. Lett.* 82.13 (2003), pp. 2145–2147. DOI: 10.1063/1.1564291 (Cited on p. 15).

[29] L. Hu, D. S. Hecht, and G. Grüner. “Percolation in Transparent and Conducting Carbon Nanotube Networks”. In: *Nano Lett.* 4.12 (2004), pp. 2513–2517. DOI: 10.1021/nl048435y (Cited on p. 16).

[30] Andriy V. Kyrylyuk et al. “Controlling electrical percolation in multicomponent carbon nanotube dispersions”. In: *Nat. Nanotechnol.* 6.6 (2011), pp. 364–369. DOI: 10.1038/nnano.2011.40 (Cited on p. 16).

[31] I. Balberg and N. Binenbaum. “Computer study of the percolation threshold in a two-dimensional anisotropic system of conducting sticks”. In: *Phys. Rev. B* 28.7 (1983), pp. 3799–3812. DOI: 10.1103/PhysRevB.28.3799 (Cited on p. 16).

[32] M A Alam et al. “T heory of Nanocomposite for Macroelectronics Applications”. In: *MRS Bull.* 31.June (2006), pp. 28–30 (Cited on p. 16).

[33] Sebastien Nanot et al. “Single-Walled Carbon Nanotubes”. In: *Springer Handb. Nanomater.* Vol. 14. 1-3. Berlin, Heidelberg: Springer Berlin Heidelberg, 2013, pp. 105–146. DOI: 10.1007/978-3-642-20595-8_4 (Cited on pp. 16, 21).

[34] Y. Yosida and I. Oguro. “Variable range hopping conduction in bulk samples composed of single-walled carbon nanotubes”. In: *J. Appl. Phys.* 86.2 (1999), pp. 999–1003. DOI: 10.1063/1.370838 (Cited on p. 16).

[35] Andrej Znidarsic et al. “Spatially resolved transport properties of pristine and doped single-walled carbon nanotube networks”. In: *J. Phys. Chem. C* 117.25 (2013), pp. 13324–13330. DOI: 10.1021/jp403983y (Cited on p. 16).

[36] David Hecht, Liangbing Hu, and George Gruener. “Conductivity scaling with bundle length and diameter in single walled carbon nanotube networks”. In: *Appl. Phys. Lett.* 89.13 (2006), p. 133112. DOI: 10.1063/1.2356999 (Cited on pp. 16, 22).

[37] David S Hecht et al. “High conductivity transparent carbon nanotube films deposited from superacid”. In: *Nanotechnology* 22.7 (2011), p. 075201. DOI: 10.1088/0957-4484/22/7/075201 (Cited on pp. 16, 69).

[38] Zhongrui Li et al. “Does the wall number of carbon nanotubes matter as conductive transparent material?” In: *Appl. Phys. Lett.* 91.5 (2007), p. 053115. DOI: 10.1063/1.2767215 (Cited on p. 16).

[39] Adrian Bachtold et al. “Aharonov–Bohm oscillations in carbon nanotubes”. In: *Nature* 397.6721 (1999), pp. 673–675. DOI: 10.1038/17755 (Cited on p. 16).

[40] C. Schönenberger et al. “Interference and interaction in multi-wall carbon nanotubes”. In: *Appl. Phys. A Mater. Sci. Process.* 69.3 (1999), pp. 283–295. DOI: 10.1007/s003390051003 (Cited on p. 16).

[41] Peter N. Nirmalraj et al. “Electrical Connectivity in Single-Walled Carbon Nanotube Networks”. In: *Nano Lett.* 9.11 (2009), pp. 3890–3895. DOI: 10.1021/nl9020914 (Cited on pp. 16, 64).

[42] M. Stadermann et al. “Nanoscale study of conduction through carbon nanotube networks”. In: *Phys. Rev. B* 69.20 (2004), p. 201402. DOI: 10.1103/PhysRevB.69.201402 (Cited on p. 16).

[43] Daeseob Shim et al. “Improvement of SWCNT transparent conductive films via transition metal doping”. In: *Chem. Commun.* 47.18 (2011), p. 5202. DOI: 10.1039/c1cc10190k (Cited on p. 16).

[44] Peter Y. Yu and Manuel Cardona. *Fundamentals of Semiconductors*. Ed. by H. Eugene Stanley; and William T. Rhodes. Fourth Edi. Graduate Texts in Physics. Berlin, Heidelberg: Springer Berlin Heidelberg, 2010, p. 788. DOI: 10.1007/978-3-642-00710-1 (Cited on pp. 18, 19, 32, 34).

[45] Jason W. Christopher, Bennett B. Goldberg, and Anna K. Swan. "Long tailed trions in monolayer MoS2: Temperature dependent asymmetry and resulting red-shift of trion photoluminescence spectra". In: *Sci. Rep.* 7.1 (2017). DOI: 10.1038/s41598-017-14378-w (Cited on pp. 18, 19).

[46] Yuhei Miyauchi, Mototeru Oba, and Shigeo Maruyama. "Cross-polarized optical absorption of single-walled nanotubes by polarized photoluminescence excitation spectroscopy". In: *Phys. Rev. B* 74.20 (2006), p. 205440. DOI: 10.1103/PhysRevB.74.205440 (Cited on p. 19).

[47] J. S. Lauret et al. "Ultrafast Carrier Dynamics in Single-Wall Carbon Nanotubes". In: *Phys. Rev. Lett.* 90.5 (2003), p. 4. DOI: 10.1103/PhysRevLett.90.057404 (Cited on p. 19).

[48] P. H. Tan et al. "Photoluminescence Spectroscopy of Carbon Nanotube Bundles: Evidence for Exciton Energy Transfer". In: *Phys. Rev. Lett.* 99.13 (2007), p. 137402. DOI: 10.1103/PhysRevLett.99.137402 (Cited on p. 19).

[49] R Bruce Weisman and Sergei M Bachilo. "Dependence of Optical Transition Energies on Structure for Single-Walled Carbon Nanotubes in Aqueous Suspension: An Empirical Kataura Plot". In: *Nano Lett.* 3.9 (2003), pp. 1235–1238. DOI: 10.1021/nl034428i (Cited on p. 20).

[50] R R Nair et al. "Fine Structure Constant Defines Visual Transparency of Graphene". In: *Science (80-.).* 320.5881 (2008), pp. 1308–1308. DOI: 10.1126/science.1156965 (Cited on p. 20).

[51] Tsuneya Ando, Yisong Zheng, and Hidekatsu Suzuura. "Dynamical Conductivity and Zero-Mode Anomaly in Honeycomb Lattices". In: *J. Phys. Soc. Japan* 71.5 (2002), pp. 1318–1324. DOI: 10.1143/JPSJ.71.1318 (Cited on p. 20).

[52] Virginia a Davis et al. "True solutions of single-walled carbon nanotubes for assembly into macroscopic materials". In: *Nat. Nanotechnol.* 4.12 (2009), pp. 830–834. DOI: 10.1038/nnano.2009.302 (Cited on p. 20).

[53] Michael J O'Connell et al. "Band gap fluorescence from individual single-walled carbon nanotubes." In: *Science (80-.).* 297.5581 (2002), pp. 593–596. DOI: 10.1126/science.1072631 (Cited on p. 21).

[54] Chris Dwyer et al. "DNA-functionalized single-walled carbon nanotubes". In: *Nanotechnology* 13.5 (2002), pp. 601–604. DOI: 10.1088/0957-4484/13/5/311 (Cited on p. 21).

[55] Adrian Nish et al. "Highly selective dispersion of single-walled carbon nanotubes using aromatic polymers." In: *Nat. Nanotechnol.* 2.10 (2007), pp. 640–646. DOI: 10.1038/nnano.2007.290 (Cited on p. 21).

[56] Suman Kalyan Samanta et al. "Conjugated polymer-Assisted dispersion of single-wall carbon nanotubes: The power of polymer wrapping". In: *Acc. Chem. Res.* 47.8 (2014), pp. 2446–2456. DOI: 10.1021/ar500141j (Cited on p. 21).

[57] Kevin S. Mistry, Brian A. Larsen, and Jeffrey L. Blackburn. "High-yield dispersions of large-diameter semiconducting single-walled carbon nanotubes with tunable narrow chirality distributions". In: *ACS Nano* 7.3 (2013), pp. 2231–2239. DOI: 10.1021/nn305336x (Cited on p. 21).

[58] Gerald J. Brady et al. "Polyfluorene-Sorted, Carbon Nanotube Array Field-Effect Transistors with Increased Current Density and High On/Off Ratio". In: *ACS Nano* 8.11 (2014), pp. 11614–11621. DOI: 10.1021/nn5048734 (Cited on p. 21).

[59] Samuel D Stranks et al. "Electronic and Mechanical Modification of Single-Walled Carbon Nanotubes by Binding to Porphyrin Oligomers". In: *ACS Nano* 5.3 (2011), pp. 2307–2315. DOI: 10.1021/nn103588h (Cited on p. 21).

[60] Jan-Kai Chang et al. "Graphene Anodes and Cathodes: Tuning the Work Function of Graphene by Nearly 2 eV with an Aqueous Intercalation Process". In: *ACS Appl. Mater. Interfaces* 7.31 (2015), pp. 17155–17161. DOI: 10.1021/acsami.5b03934 (Cited on p. 21).

[61] Severin N Habisreutinger et al. "Carbon Nanotube/Polymer Composites as a Highly Stable Hole Collection Layer in Perovskite Solar Cells". In: *Nano Lett.* 14.10 (2014), pp. 5561–5568. DOI: 10.1021/nl501982b (Cited on p. 21).

[62] Sumio Iijima and Toshinari Ichihashi. "Single-shell carbon nanotubes of 1-nm diameter". In: *Nature* 363.6430 (1993), pp. 603–605. DOI: 10.1038/363603a0 (Cited on p. 21).

[63] Sumio Iijima. "Helical microtubules of graphitic carbon". In: *Nature* 354.6348 (1991), pp. 56–58. DOI: 10.1038/354056a0 (Cited on p. 21).

[64] Mildred S Dresselhaus, G. Dresselhaus, and Ph. Avouris. "Carbon nanotubes: Advanced topics in the synthesis, structure, properties and applications". In: *Mater. Today* 11.3 (2008), p. 57. DOI: 10.1016/S1369-7021(08)70021-X (Cited on pp. 21, 22).

[65] Pavel Nikolaev et al. “Gas-phase catalytic growth of single-walled carbon nanotubes from carbon monoxide”. In: *Chem. Phys. Lett.* 313.1-2 (1999), pp. 91–97. DOI: 10.1016/S0009-2614(99)01029-5 (Cited on p. 21).

[66] Jose E. Herrera et al. “Relationship between the Structure/Composition of Co–Mo Catalysts and Their Ability to Produce Single-Walled Carbon Nanotubes by CO Disproportionation”. In: *J. Catal.* 204.1 (2001), pp. 129–145. DOI: 10.1006/jcat.2001.3383 (Cited on p. 22).

[67] B. Kitiyanan et al. “Controlled production of single-wall carbon nanotubes by catalytic decomposition of CO on bimetallic Co–Mo catalysts”. In: *Chem. Phys. Lett.* 317.3-5 (2000), pp. 497–503. DOI: 10.1016/S0009-2614(99)01379-2 (Cited on p. 22).

[68] Sergei M. Bachilo et al. “Narrow (n,m)-Distribution of Single-Walled Carbon Nanotubes Grown Using a Solid Supported Catalyst”. In: *J. Am. Chem. Soc.* 125.37 (2003), pp. 11186–11187. DOI: 10.1021/ja036622c (Cited on p. 22).

[69] Neha Arora and N. N. Sharma. “Arc discharge synthesis of carbon nanotubes: Comprehensive review”. In: *Diam. Relat. Mater.* 50 (2014), pp. 135–150. DOI: 10.1016/j.diamond.2014.10.001 (Cited on p. 22).

[70] Juan Ramon Sanchez-Valencia et al. “Controlled synthesis of single-chirality carbon nanotubes”. In: *Nature* 512.7512 (2014), pp. 61–64. DOI: 10.1038/nature13607 (Cited on p. 22).

[71] Tae-Jin Park et al. “Purification strategies and purity visualization techniques for single-walled carbon nanotubes”. In: *J. Mater. Chem.* 16.2 (2006), pp. 141–154. DOI: 10.1039/B510858F (Cited on p. 22).

[72] Gustav Rose. “Beschreibung einiger neuen Mineralien des Urals”. In: *Ann. der Phys. und Chemie* 124.12 (1839), pp. 551–573. DOI: 10.1002/andp.18391241205 (Cited on p. 22).

[73] J. M. Tarascon et al. “Oxygen and rare-earth doping of the 90-K superconducting perovskite YBa2Cu3O7”. In: *Phys. Rev. B* 36.1 (1987), pp. 226–234. DOI: 10.1103/PhysRevB.36.226 (Cited on p. 22).

[74] Francis Galasso and Wilda Darby. “Preparation of Single Crystals of Complex Perovskite Ferroelectric and Semiconducting Compounds”. In: *Inorg. Chem.* 4.1 (1965), pp. 71–73. DOI: 10.1021/ic50023a015 (Cited on p. 22).

[75] M. DiDomenico and S. H. Wemple. “Oxygen-Octahedra Ferroelectrics. I. Theory of Electro-optical and Nonlinear optical Effects”. In: *J. Appl. Phys.* 40.2 (1969), pp. 720–734. DOI: 10.1063/1.1657458 (Cited on p. 22).

[76] David B. Mitzi. “Synthesis, Structure, and Properties of Organic-Inorganic Perovskites and Related Materials”. In: *Prog. Inorg. Chem.* Ed. by Kenneth D. Karlin. 48th ed. Wiley, 1999, pp. 1–121. DOI: 10.1002/9780470166499.ch1 (Cited on pp. 22, 23).

[77] M. M. Lee et al. “Efficient Hybrid Solar Cells Based on Meso-Superstructured Organometal Halide Perovskites”. In: *Science (80-.).* 338.6107 (2012), pp. 643–647. DOI: 10.1126/science.1228604 (Cited on pp. 22, 23).

[78] Laura Schade et al. “Structural and Optical Properties of Cs2AgBiBr6 Double Perovskite”. In: *ACS Energy Lett.* 4.1 (2019), pp. 299–305. DOI: 10.1021/acsenergylett.8b02090 (Cited on pp. 23, 24, 25, 26, 44, 72).

[79] George Volonakis et al. “Lead-Free Halide Double Perovskites via Heterovalent Substitution of Noble Metals”. In: *J. Phys. Chem. Lett.* 7.7 (2016), pp. 1254–1259. DOI: 10.1021/acs.jpclett.6b00376 (Cited on pp. 23, 80).

[80] Constantinos C. Stoumpos, Christos D. Malliakas, and Mercouri G. Kanatzidis. “Semiconducting tin and lead iodide perovskites with organic cations: Phase transitions, high mobilities, and near-infrared photoluminescent properties”. In: *Inorg. Chem.* 52.15 (2013), pp. 9019–9038. DOI: 10.1021/ic401215x (Cited on pp. 23, 87).

[81] Akihiro Kojima et al. “Organometal Halide Perovskites as Visible-Light Sensitizers for Photovoltaic Cells”. In: *J. Am. Chem. Soc.* 131.17 (2009), pp. 6050–6051. DOI: 10.1021/ja809598r (Cited on p. 23).

[82] C R Kagan. “Organic-Inorganic Hybrid Materials as Semiconducting Channels in Thin-Film Field-Effect Transistors”. In: *Science (80-.).* 286.5441 (1999), pp. 945–947. DOI: 10.1126/science.286.5441.945 (Cited on p. 23).

[83] Giles E. Eperon et al. “Formamidinium lead trihalide: A broadly tunable perovskite for efficient planar heterojunction solar cells”. In: *Energy Environ. Sci.* 7.3 (2014), pp. 982–988. DOI: 10.1039/c3ee43822h (Cited on p. 23).

[84] Pablo P. Boix et al. “Perovskite Solar Cells: Beyond Methylammonium Lead Iodide”. In: *J. Phys. Chem. Lett.* 6.5 (2015), pp. 898–907. DOI: 10.1021/jz502547f (Cited on p. 23).

[85] A. S. Verma and V. K. Jindal. “Lattice constant of cubic perovskites”. In: *J. Alloys Compd.* 485.1-2 (2009), pp. 514–518. DOI: 10.1016/j.jallcom.2009.06.001 (Cited on p. 23).

[86] Jia Yue Yang and Ming Hu. “Temperature-Induced Large Broadening and Blue Shift in the Electronic Band Structure and Optical Absorption of Methylammonium Lead Iodide Perovskite”. In: *J. Phys. Chem. Lett.* 8.16 (2017), pp. 3720–3725. DOI: 10.1021/acs.jpclett.7b01719 (Cited on pp. 23, 26).

[87] Zhen Li et al. “Stabilizing Perovskite Structures by Tuning Tolerance Factor: Formation of Formamidinium and Cesium Lead Iodide Solid-State Alloys”. In: *Chem. Mater.* 28.1 (2016), pp. 284–292. DOI: 10.1021/acs.chemmater.5b04107 (Cited on p. 23).

[88] Mats Johnsson and Peter Lemmens. "Crystallography and Chemistry of Perovskites". In: *Handb. Magn. Adv. Magn. Mater.* Chichester, UK: John Wiley & Sons, Ltd, 2007. DOI: 10.1002/9780470022184.hmm411 (Cited on p. 24).

[89] Gregor Kieslich, Shijing Sun, and Anthony K. Cheetham. "Solid-state principles applied to organic–inorganic perovskites: New tricks for an old dog". In: *Chem. Sci.* 5.12 (2014), pp. 4712–4715. DOI: 10.1039/c4sc02211d (Cited on p. 24).

[90] Severin N. Habisreutinger et al. "Dopant-Free Planar n–i–p Perovskite Solar Cells with Steady-State Efficiencies Exceeding 18%". In: *ACS Energy Lett.* 2.3 (2017), pp. 622–628. DOI: 10.1021/acsenergylett.7b00028 (Cited on p. 24).

[91] Eric T. McClure et al. "Cs2AgBiX6 (X = Br, Cl): New Visible Light Absorbing, Lead-Free Halide Perovskite Semiconductors". In: *Chem. Mater.* 28.5 (2016), pp. 1348–1354. DOI: 10.1021/acs.chemmater.5b04231 (Cited on p. 24).

[92] Anna Osherov et al. "The Impact of Phase Retention on the Structural and Optoelectronic Properties of Metal Halide Perovskites". In: *Adv. Mater.* 28.48 (2016), pp. 10757–10763. DOI: 10.1002/adma.201604019 (Cited on pp. 24, 26, 88).

[93] Yevgeny Rakita et al. "Tetragonal CH3NH3PbI3 is ferroelectric". In: *Proc. Natl. Acad. Sci.* 114.28 (2017), E5504–E5512. DOI: 10.1073/pnas.1702429114 (Cited on pp. 24, 87, 88, 100).

[94] Kyle Frohna et al. "Inversion symmetry and bulk Rashba effect in methylammonium lead iodide perovskite single crystals". In: *Nat. Commun.* 9.1 (2018), p. 1829. DOI: 10.1038/s41467-018-04212-w (Cited on pp. 24, 100).

[95] Eline M. Hutter et al. "Direct–indirect character of the bandgap in methylammonium lead iodide perovskite". In: *Nat. Mater.* 16 (2017), pp. 115–120. DOI: 10.1038/nmat4765 (Cited on pp. 24, 29, 87, 101, 102).

[96] Shaojie Jiang et al. "Pressure-Dependent Polymorphism and Band-Gap Tuning of Methylammonium Lead Iodide Perovskite". In: *Angew. Chemie Int. Ed.* 55.22 (2016), pp. 6540–6544. DOI: 10.1002/anie.201601788 (Cited on p. 24).

[97] P. S. Whitfield et al. "Structures, Phase Transitions and Tricritical Behavior of the Hybrid Perovskite Methyl Ammonium Lead Iodide". In: *Sci. Rep.* 6.June (2016), pp. 1–16. DOI: 10.1038/srep35685 (Cited on p. 24).

[98] Takeo Oku. "Crystal Structures of CH3NH3PbI3 and Related Perovskite Compounds Used for Solar Cells". In: *Sol. Cells - New Approaches Rev.* Vol. 2. InTech, 2015, p. 64. DOI: 10.5772/59284 (Cited on p. 24).

[99] Federico Brivio, Alison B. Walker, and Aron Walsh. "Structural and electronic properties of hybrid perovskites for high-efficiency thin-film photovoltaics from first-principles". In: *APL Mater.* 1.4 (2013). DOI: 10.1063/1.4824147 (Cited on p. 24).

[100] H Mashiyama, Y Kawamura, and Y. Kubota. "The Anti-Polar Structure of CH3NH3PbBr3". In: *J. Korean Phys. Soc.* 51.92 (2007), p. 850. DOI: 10.3938/jkps.51.850 (Cited on p. 24).

[101] Andrea Bernasconi and Lorenzo Malavasi. "Direct evidence of permanent octahedra distortion in MAPbBr3 hybrid perovskite". In: *ACS Energy Lett.* 2.4 (2017), pp. 863–868. DOI: 10.1021/acsenergylett.7b00139 (Cited on pp. 24, 26).

[102] Christian Wehrenfennig et al. "High Charge Carrier Mobilities and Lifetimes in Organolead Trihalide Perovskites". In: *Adv. Mater.* 26.10 (2014), pp. 1584–1589. DOI: 10.1002/adma.201305172 (Cited on p. 24).

[103] Valerio D'Innocenzo et al. "Tuning the light emission properties by band gap engineering in hybrid lead halide perovskite". In: *J. Am. Chem. Soc.* 136.51 (2014), pp. 17730–17733. DOI: 10.1021/ja511198f (Cited on p. 24).

[104] Ilya A. Shkrob and Timothy W. Marin. "Charge trapping in photovoltaically active perovskites and related halogenoplumbate compounds". In: *J. Phys. Chem. Lett.* 5.7 (2014), pp. 1066–1071. DOI: 10.1021/jz5004022 (Cited on p. 24).

[105] D. Shi et al. "Low trap-state density and long carrier diffusion in organolead trihalide perovskite single crystals". In: *Science (80-.).* 347.6221 (2015), pp. 519–522. DOI: 10.1126/science.aaa2725 (Cited on pp. 25, 43, 93, 103, 105).

[106] Jun Hong Noh et al. "Chemical management for colorful, efficient, and stable inorganic-organic hybrid nanostructured solar cells". In: *Nano Lett.* 13.4 (2013), pp. 1764–1769. DOI: 10.1021/nl400349b (Cited on p. 25).

[107] Sven Rühle. "Tabulated values of the Shockley-Queisser limit for single junction solar cells". In: *Sol. Energy* 130 (2016), pp. 139–147. DOI: 10.1016/j.solener.2016.02.015 (Cited on p. 25).

[108] T Smith and J Guild. "The C.I.E. colorimetric standards and their use". In: *Trans. Opt. Soc.* 33.3 (1931), pp. 73–134. DOI: 10.1088/1475-4878/33/3/301 (Cited on p. 25).

[109] Belen Suarez et al. "Recombination Study of Combined Halides (Cl, Br, I) Perovskite Solar Cells". In: *J. Phys. Chem. Lett.* 5.10 (2014), pp. 1628–1635. DOI: 10.1021/jz5006797 (Cited on p. 25).

[110] Paul Gratia et al. "Intrinsic Halide Segregation at Nanometer Scale Determines the High Efficiency of Mixed Cation/Mixed Halide Perovskite Solar Cells". In: *J. Am. Chem. Soc.* 138.49 (2016), pp. 15821–15824. DOI: 10.1021/jacs.6b10049 (Cited on p. 25).

[111] Giulia Longo et al. “Fully Vacuum-Processed Wide Band Gap Mixed-Halide Perovskite Solar Cells”. In: *ACS Energy Lett.* 3.1 (2018), pp. 214–219. DOI: 10.1021/acsenergylett.7b01217 (Cited on p. 25).

[112] Jacky Even et al. “Solid-State Physics Perspective on Hybrid Perovskite Semiconductors”. In: *J. Phys. Chem. C* 119.19 (2015), pp. 10161–10177. DOI: 10.1021/acs.jpcc.5b00695 (Cited on pp. 25, 27, 28, 29).

[113] Marina R. Filip et al. “Steric engineering of metal-halide perovskites with tunable optical band gaps”. In: *Nat. Commun.* 5 (2014), pp. 1–9. DOI: 10.1038/ncomms6757 (Cited on p. 26).

[114] Ivo Borriello, Giovanni Cantele, and Domenico Ninno. “Ab initio investigation of hybrid organic-inorganic perovskites based on tin halides”. In: *Phys. Rev. B* 77.23 (2008), p. 235214. DOI: 10.1103/PhysRevB.77.235214 (Cited on p. 26).

[115] Rebecca J. Sutton et al. “Bandgap-Tunable Cesium Lead Halide Perovskites with High Thermal Stability for Efficient Solar Cells”. In: *Adv. Energy Mater.* (2016). DOI: 10.1002/aenm.201502458 (Cited on p. 26).

[116] Jarvist M. Frost et al. “Atomistic origins of high-performance in hybrid halide perovskite solar cells”. In: *Nano Lett.* 14.5 (2014), pp. 2584–2590. DOI: 10.1021/nl500390f (Cited on p. 26).

[117] Aurelien M.A. Leguy et al. “The dynamics of methylammonium ions in hybrid organic-inorganic perovskite solar cells”. In: *Nat. Commun.* 6.May (2015). DOI: 10.1038/ncomms8124 (Cited on pp. 26, 99, 100).

[118] Anna Amat et al. “Cation-induced band-gap tuning in organohalide perovskites: Interplay of spin-orbit coupling and octahedra tilting”. In: *Nano Lett.* 14.6 (2014), pp. 3608–3616. DOI: 10.1021/nl5012992 (Cited on pp. 26, 101, 102).

[119] Constantinos C. Stoumpos and Mercouri G. Kanatzidis. “The Renaissance of Halide Perovskites and Their Evolution as Emerging Semiconductors”. In: *Acc. Chem. Res.* 48.10 (2015), pp. 2791–2802. DOI: 10.1021/acs.accounts.5b00229 (Cited on p. 26).

[120] Carlo Motta et al. “Revealing the role of organic cations in hybrid halide perovskite CH3NH3PbI3”. en. In: *Nat. Commun.* 6.1 (2015), p. 7026. DOI: 10.1038/ncomms8026 (Cited on pp. 26, 29).

[121] Osvald Knop et al. “Alkylammonium lead halides. Part 2. CH3NH3PbX3 (X = Cl, Br, I) perovskites: cuboctahedral halide cages with isotropic cation reorientation”. In: *Can. J. Chem.* 68.3 (1990), pp. 412–422. DOI: 10.1139/v90-063 (Cited on p. 26).

[122] Y P Varshni. “Band-to-Band Radiative Recombination in Groups IV, VI, and III-V Semiconductors (I)”. In: *Phys. status solidi* 19.2 (1967), pp. 459–514. DOI: 10.1002/pssb.19670190202 (Cited on pp. 26, 78).

[123] Wei Huang et al. “Observation of Unusual Optical Band Structure of CH3NH3PbI3 Perovskite Single Crystal”. In: *ACS Photonics* 5.4 (2018), pp. 1583–1590. DOI: 10.1021/acsphotonics.8b00033 (Cited on pp. 26, 87, 93, 99).

[124] Selina Olthof. “Research Update: The electronic structure of hybrid perovskite layers and their energetic alignment in devices”. In: *APL Mater.* 4.9 (2016), p. 091502. DOI: 10.1063/1.4960112 (Cited on p. 27).

[125] T. Umebayashi et al. “Electronic structures of lead iodide based low-dimensional crystals”. In: *Phys. Rev. B* 67.15 (2003), p. 155405. DOI: 10.1103/PhysRevB.67.155405 (Cited on pp. 27, 28).

[126] Michael A. Becker et al. “Bright triplet excitons in caesium lead halide perovskites”. In: *Nature* 553.7687 (2018), pp. 189–193. DOI: 10.1038/nature25147 (Cited on pp. 27, 32).

[127] Jacky Even et al. “Importance of Spin–Orbit Coupling in Hybrid Organic/Inorganic Perovskites for Photovoltaic Applications”. In: *J. Phys. Chem. Lett.* 4.17 (2013), pp. 2999–3005. DOI: 10.1021/jz401532q (Cited on p. 27).

[128] Federico Brivio et al. “Relativistic quasiparticle self-consistent electronic structure of hybrid halide perovskite photovoltaic absorbers”. In: *Phys. Rev. B - Condens. Matter Mater. Phys.* 89.15 (2014), pp. 1–6. DOI: 10.1103/PhysRevB.89.155204 (Cited on pp. 27, 115).

[129] James Endres et al. “Valence and Conduction Band Densities of States of Metal Halide Perovskites: A Combined Experimental-Theoretical Study”. In: *J. Phys. Chem. Lett.* 7.14 (2016), pp. 2722–2729. DOI: 10.1021/acs.jpclett.6b00946 (Cited on p. 27).

[130] Z. G. Yu. “Effective-mass model and magneto-optical properties in hybrid perovskites”. In: *Sci. Rep.* 6.1 (2016), p. 28576. DOI: 10.1038/srep28576 (Cited on p. 28).

[131] Al. L. Efros and M. Rosen. “The Electronic Structure of Semiconductor Nanocrystals”. In: *Annu. Rev. Mater. Sci.* 30.1 (2000), pp. 475–521. DOI: 10.1146/annurev.matsci.30.1.475 (Cited on p. 28).

[132] Jacky Even, Laurent Pedesseau, and Claudine Katan. “Analysis of Multivalley and Multibandgap Absorption and Enhancement of Free Carriers Related to Exciton Screening in Hybrid Perovskites”. In: *J. Phys. Chem. C* 118.22 (2014), pp. 11566–11572. DOI: 10.1021/jp503337a (Cited on p. 28).

[133] H A Kramers. “Théorie générale de la rotation paramagnétique dans les cristaux”. In: *Proc. Acad. Sci. Amsterdam.* Vol. 33. 1930, p. 959 (Cited on p. 29).

[134] Yu A Bychkov and E I Rashba. "Oscillatory effects and the magnetic susceptibility of carriers in inversion layers". In: *J. Phys. C Solid State Phys.* 17.33 (1984), pp. 6039–6045. DOI: 10.1088/0022-3719/17/33/015 (Cited on p. 29).

[135] Samuel D. Stranks et al. "The Physics of Light Emission in Halide Perovskite Devices". In: *Adv. Mater.* 1803336 (2018), p. 1803336. DOI: 10.1002/adma.201803336 (Cited on p. 29).

[136] Pooya Azarhoosh et al. "Research Update: Relativistic origin of slow electron-hole recombination in hybrid halide perovskite solar cells". In: *APL Mater.* 4.9 (2016). DOI: 10.1063/1.4955028 (Cited on pp. 29, 100).

[137] Laura M Herz. "Charge-Carrier Mobilities in Metal Halide Perovskites: Fundamental Mechanisms and Limits". In: *ACS Energy Lett.* 2 (2017), ASAP. DOI: 10.1021/acsenergylett.7b00276 (Cited on pp. 29, 102).

[138] Fan Zheng et al. "Rashba spin-orbit coupling enhanced carrier lifetime in CH3NH3PbI3". In: *Nano Lett.* 15.12 (2015), pp. 7794–7800. DOI: 10.1021/acs.nanolett.5b01854 (Cited on pp. 29, 102).

[139] Thibaud Etienne, Edoardo Mosconi, and Filippo De Angelis. "Dynamical Origin of the Rashba Effect in Organohalide Lead Perovskites: A Key to Suppressed Carrier Recombination in Perovskite Solar Cells?" In: *J. Phys. Chem. Lett.* 7.9 (2016), pp. 1638–1645. DOI: 10.1021/acs.jpclett.6b00564 (Cited on pp. 29, 101, 102).

[140] Mikaël Kepenekian et al. "Rashba and Dresselhaus Effects in Hybrid Organic-Inorganic Perovskites: From Basics to Devices". In: *ACS Nano* 9.12 (2015), pp. 11557–11567. DOI: 10.1021/acsnano.5b04409 (Cited on pp. 29, 87, 101, 102).

[141] S. Sarikurt et al. "Spin texturing in a parabolically confined quantum wire with Rashba and Dresselhaus spin - Orbit interactions". In: *Chinese Phys. B* 23.1 (2014). DOI: 10.1088/1674-1056/23/1/017102 (Cited on p. 29).

[142] M. Kim et al. "Switchable S = 1/2 and J = 1/2 Rashba bands in ferroelectric halide perovskites". In: *Proc. Natl. Acad. Sci.* 111.19 (2014), pp. 6900–6904. DOI: 10.1073/pnas.1405780111 (Cited on pp. 29, 100, 101, 102).

[143] Chao Zheng, Shidong Yu, and Oleg Rubel. "Structural dynamics in hybrid halide perovskites: Bulk Rashba splitting, spin texture, and carrier localization". In: *Phys. Rev. Mater.* 2.11 (2018), p. 114604. DOI: 10.1103/PhysRevMaterials.2.114604 (Cited on pp. 29, 100, 101).

[144] Omer Yaffe et al. "Local Polar Fluctuations in Lead Halide Perovskite Crystals". In: *Phys. Rev. Lett.* 118.13 (2017), p. 136001. DOI: 10.1103/PhysRevLett.118.136001 (Cited on p. 29).

[145] Daniel Niesner et al. "Giant Rashba Splitting in CH3NH3PbBr3 Organic-Inorganic Perovskite". In: *Phys. Rev. Lett.* 117.12 (2016), p. 126401. DOI: 10.1103/PhysRevLett.117.126401 (Cited on p. 29).

[146] Daniel Niesner et al. "Structural fluctuations cause spin-split states in tetragonal (CH3NH3)PbI3 as evidenced by the circular photogalvanic effect". In: *Proc. Natl. Acad. Sci.* (2018), p. 201805422. DOI: 10.1073/pnas.1805422115 (Cited on pp. 29, 87, 93, 99, 100, 102).

[147] Maya Isarov et al. "Rashba Effect in a Single Colloidal CsPbBr 3 Perovskite Nanocrystal Detected by Magneto-Optical Measurements". In: *Nano Lett.* 17.8 (2017), pp. 5020–5026. DOI: 10.1021/acs.nanolett.7b02248 (Cited on p. 29).

[148] Edoardo Mosconi, Thibaud Etienne, and Filippo De Angelis. "Rashba Band Splitting in Organohalide Lead Perovskites: Bulk and Surface Effects". In: *J. Phys. Chem. Lett.* 8.10 (2017), pp. 2247–2252. DOI: 10.1021/acs.jpclett.7b00328 (Cited on p. 29).

[149] Ming Fu et al. "Neutral and Charged Exciton Fine Structure in Single Lead Halide Perovskite Nanocrystals Revealed by Magneto-optical Spectroscopy". In: *Nano Lett.* 17.5 (2017), pp. 2895–2901. DOI: 10.1021/acs.nanolett.7b00064 (Cited on p. 29).

[150] R. J. Elliott. "Intensity of Optical Absorption by Excitons". In: *Phys. Rev.* 108.6 (1957), pp. 1384–1389. DOI: 10.1103/PhysRev.108.1384 (Cited on p. 31).

[151] Shivam Singh et al. "Effect of Thermal and Structural Disorder on the Electronic Structure of Hybrid Perovskite Semiconductor CH3NH3PbI3". In: *J. Phys. Chem. Lett.* 7.15 (2016), pp. 3014–3021. DOI: 10.1021/acs.jpclett.6b01207 (Cited on p. 31).

[152] Volkhard May and Oliver Kühn. *Charge and Energy Transfer Dynamics in Molecular Systems*. 3rd. Wiley-VCH Verlag GmbH, 2011, p. 577 (Cited on p. 32).

[153] Ivan Pelant and Jan Valenta. *Luminescence Spectroscopy of Semiconductors*. Vol. 21. 4. Oxford University Press, 2012, pp. 359–379. DOI: 10.1093/acprof:oso/9780199588336.001.0001 (Cited on p. 32).

[154] Jing Feng. "Mechanical properties of hybrid organic-inorganic CH3NH 3BX3 (B = Sn, Pb; X = Br, I) perovskites for solar cell absorbers". In: *APL Mater.* 2.8 (2014). DOI: 10.1063/1.4885256 (Cited on p. 32).

[155] Y. Chen et al. "Extended carrier lifetimes and diffusion in hybrid perovskites revealed by Hall effect and photoconductivity measurements". In: *Nat. Commun.* 7 (2016), p. 12253. DOI: 10.1038/ncomms12253 (Cited on p. 32).

[156] J. T. Devreese. "Fröhlich Polarons. Lecture course including detailed theoretical derivations". In: 5 (2015), p. 264. DOI: http://arxiv.org/abs/1611.06122 (Cited on pp. 32, 110).

[157] Samoza. *Franck Condon Diagram* (Cited on p. 33).

[158] Atsuhiko Miyata et al. "Direct measurement of the exciton binding energy and effective masses for charge carriers in organic–inorganic tri-halide perovskites". In: *Nat. Phys.* 11 (2015), pp. 582–587. DOI: 10.1038/nphys3357 (Cited on pp. 35, 82, 103, 104).

[159] Zhuo Yang et al. "Unraveling the Exciton Binding Energy and the Dielectric Constant in Single-Crystal Methylammonium Lead Triiodide Perovskite". In: *J. Phys. Chem. Lett.* 8.8 (2017), pp. 1851–1855. DOI: 10.1021/acs.jpclett.7b00524 (Cited on pp. 35, 88, 103, 104, 112, 114, 115).

[160] P C Makado and N C McGill. "Energy levels of a neutral hydrogen-like system in a constant magnetic field of arbitrary strength". In: *J. Phys. C Solid State Phys.* 19.6 (1986), pp. 873–885. DOI: 10.1088/0022-3719/19/6/008 (Cited on pp. 34, 91, 107, 108, 114).

[161] Markus Dollmann. "Zinc Oxide Nanowires and P3HT in Bulk Heterojunction Hybrid Solar Cells". Master Thesis. University of Heidelberg, 2015 (Cited on pp. 40, 46).

[162] Giulio Mazzotta. "Solubilisation of carbon nanotubes with a non-conjugated polymer for device applications". DPhil Thesis. University of Oxford, 2018, p. 188 (Cited on p. 41).

[163] M. G. Christoforo. *LANDS - Large Area Nanoparticle Deposition System (Accessed 22/02/2019).* DOI: http://afmd.github.io/LANDS/ (Cited on pp. 42, 59).

[164] Yevgeny Rakita et al. "Low-Temperature Solution-Grown CsPbBr3 Single Crystals and Their Characterization". In: *Cryst. Growth Des.* 16.10 (2016), pp. 5717–5725. DOI: 10.1021/acs.cgd.6b00764 (Cited on p. 43).

[165] Makhsud I. Saidaminov et al. "Retrograde solubility of formamidinium and methylammonium lead halide perovskites enabling rapid single crystal growth". In: *Chem. Commun.* 51.100 (2015), pp. 17658–17661. DOI: 10.1039/C5CC06916E (Cited on p. 43).

[166] Makhsud I. Saidaminov et al. "High-quality bulk hybrid perovskite single crystals within minutes by inverse temperature crystallization". In: *Nat. Commun.* 6.1 (2015), p. 7586. DOI: 10.1038/ncomms8586 (Cited on pp. 43, 87).

[167] Yevgeny Rakita et al. "Tetragonal CH3NH3PbI3 is ferroelectric". In: *Proc. Natl. Acad. Sci.* 114.28 (2017), E5504–E5512. DOI: 10.1073/pnas.1702429114 (Cited on pp. 44, 100).

[168] Pabitra K. Nayak et al. "Mechanism for rapid growth of organic–inorganic halide perovskite crystals". In: *Nat. Commun.* 7.1 (2016), p. 13303. DOI: 10.1038/ncomms13303 (Cited on p. 44).

[169] Nakita K. Noel et al. "A low viscosity, low boiling point, clean solvent system for the rapid crystallisation of highly specular perovskite films". In: *Energy Environ. Sci.* 10.1 (2017), pp. 145–152. DOI: 10.1039/C6EE02373H (Cited on p. 44).

[170] Nakita K. Noel et al. "Highly Crystalline Methylammonium Lead Tribromide Perovskite Films for Efficient Photovoltaic Devices". In: *ACS Energy Lett.* 3 (2018), pp. 1233–1240. DOI: 10.1021/acsenergylett.8b00509 (Cited on p. 44).

[171] L. J. van der Pauw. "A Method of Measuring the Resisitivy and Hall Coefficient of Lamellae of Arbitrary Shape". In: *Philips Tech. Rev.* 20.8/9 (1958), pp. 220–224 (Cited on p. 48).

[172] Daniel W. Koon, Arshad A. Bahl, and Edward O. Duncan. "Measurement of contact placement errors in the van der Pauw technique". In: *Rev. Sci. Instrum.* 60.2 (1989), pp. 275–276. DOI: 10.1063/1.1140423 (Cited on p. 48).

[173] *Andor iDUS416 specifications (Accessed: 23/02/2019) https://bit.ly/2EuJsvo* (Cited on p. 52).

[174] T Schuettfort et al. "Synthesis and spectroscopic characterization of solution processable highly ordered polythiophene–carbon nanotube nanohybrid structures". In: *Nanotechnology* 21.2 (2010), p. 025201. DOI: 10.1088/0957-4484/21/2/025201 (Cited on p. 54).

[175] *Ossila.* 2019 (Cited on p. 61).

[176] *Delta Technologies.* 2019 (Cited on p. 61).

[177] *SigmaAldrich.* 2019 (Cited on p. 61).

[178] Miranda Roesing, Jason Howell, and David Boucher. "Solubility characteristics of poly(3-hexylthiophene)". In: *J. Polym. Sci. Part B Polym. Phys.* 55.14 (2017), pp. 1075–1087. DOI: 10.1002/polb.24364 (Cited on p. 61).

[179] Frank Hennrich et al. "The Mechanism of Cavitation-Induced Scission of Single-Walled Carbon Nanotubes". In: *J. Phys. Chem. B* 111.8 (2007), pp. 1932–1937. DOI: 10.1021/jp065262n (Cited on pp. 62, 118).

[180] G. J. Brady et al. "Quasi-ballistic carbon nanotube array transistors with current density exceeding Si and GaAs". In: *Sci. Adv.* 2.9 (2016), pp. 1–9. DOI: 10.1126/sciadv.1601240 (Cited on p. 62).

[181] Yangxin Zhou, Liangbing Hu, and George Gruener. "A method of printing carbon nanotube thin films". In: *Appl. Phys. Lett.* 88.12 (2006), p. 123109. DOI: 10.1063/1.2187945 (Cited on pp. 62, 69).

[182] Carla M. Aguirre et al. "The Role of the Oxygen/Water Redox Couple in Suppressing Electron Conduction in Field-Effect Transistors". In: *Adv. Mater.* 21.30 (2009), pp. 3087–3091. DOI: 10.1002/adma.200900550 (Cited on p. 62).

[183] Masahiro Shigeta, Masaharu Komatsu, and Naotoshi Nakashima. "Individual solubilization of single-walled carbon nanotubes using totally aromatic polyimide". In: *Chem. Phys. Lett.* 418.1-3 (2006), pp. 115–118. DOI: 10.1016/j.cplett.2005.10.088 (Cited on p. 62).

[184] Michael W. Rowell and Michael D. McGehee. "Transparent electrode requirements for thin film solar cell modules". In: *Energy Environ. Sci.* 4.1 (2011), pp. 131–134. DOI: 10.1039/C0EE00373E (Cited on p. 63).

[185] D. H. Kim et al. "Effect of SOCl2 doping on electronic properties of single-walled carbon nanotube thin film transistors". In: *Phys. Status Solidi* 248.11 (2011), pp. 2668–2671. DOI: 10.1002/pssb.201100106 (Cited on p. 64).

[186] Antti Kaskela et al. "Aerosol-synthesized SWCNT networks with tunable conductivity and transparency by a dry transfer technique". In: *Nano Lett.* 10.11 (2010), pp. 4349–4355. DOI: 10.1021/nl101680s (Cited on p. 64).

[187] Ralf Graupner et al. "Doping of single-walled carbon nanotube bundles by Brønsted acids". In: *Phys. Chem. Chem. Phys.* 5.24 (2003), p. 5472. DOI: 10.1039/b311016h (Cited on p. 64).

[188] Urszula Dettlaff-Weglikowska et al. "Effect of SOCl 2 Treatment on Electrical and Mechanical Properties of Single-Wall Carbon Nanotube Networks". In: *J. Am. Chem. Soc.* 127.14 (2005), pp. 5125–5131. DOI: 10.1021/ja046685a (Cited on p. 64).

[189] Leonard S. Levitt and Edgar Howard. "Determination of Thiophene by Oxidative Decomposition with Nitric Acid". In: *Anal. Chem.* 25.1 (1953), pp. 196–197. DOI: 10.1021/ac60073a048 (Cited on p. 64).

[190] J. Vavro et al. "Thermoelectric Power of p-Doped Single-Wall Carbon Nanotubes and the Role of Phonon Drag". In: *Phys. Rev. Lett.* 90.6 (2003), p. 065503. DOI: 10.1103/PhysRevLett.90.065503 (Cited on p. 64).

[191] C. M. Aguirre et al. "Carbon nanotube sheets as electrodes in organic light-emitting diodes". In: *Appl. Phys. Lett.* 88.18 (2006), p. 183104. DOI: 10.1063/1.2199461 (Cited on p. 69).

[192] Zhuangchun Wu. "Transparent, Conductive Carbon Nanotube Films". In: *Science (80-.).* 305.5688 (2004), pp. 1273–1276. DOI: 10.1126/science.1101243 (Cited on p. 69).

[193] G. Dinesha M. R. Dabera et al. "Does Electronic Type Matter when Single-Walled Carbon Nanotubes are Used for Electrode Applications?" In: *Adv. Funct. Mater.* 25.28 (2015), pp. 4520–4530. DOI: 10.1002/adfm.201501394 (Cited on p. 69).

[194] Budhadipta Dan, Glen C. Irvin, and Matteo Pasquali. "Continuous and scalable fabrication of transparent conducting carbon nanotube films". In: *ACS Nano* 3.4 (2009), pp. 835–843. DOI: 10.1021/nn8008307 (Cited on p. 69).

[195] Sukanta De et al. "Transparent, Flexible, and Highly Conductive Thin Films Based on Polymer - Nanotube Composites". In: *ACS Nano* 3.3 (2009), pp. 714–720. DOI: 10.1021/nn800858w (Cited on p. 69).

[196] Núria Ferrer Anglada et al. "Synthesis and characterization of carbon nanotube-conducting polymer thin films". In: *Diam. Relat. Mater.* 13.2 (2004), pp. 256–260. DOI: 10.1016/j.diamond.2003.10.026 (Cited on p. 69).

[197] Robert C. Tenent et al. "Ultrasmooth, Large-Area, High-Uniformity, Conductive Transparent Single-Walled-Carbon-Nanotube Films for Photovoltaics Produced by Ultrasonic Spraying". In: *Adv. Mater.* 21.31 (2009), pp. 3210–3216. DOI: 10.1002/adma.200803551 (Cited on p. 69).

[198] Il Jeon et al. "Single-Walled Carbon Nanotube Film as Electrode in Indium-Free Planar Heterojunction Perovskite Solar Cells: Investigation of Electron-Blocking Layers and Dopants". In: *Nano Lett.* 15.10 (2015), pp. 6665–6671. DOI: 10.1021/acs.nanolett.5b02490 (Cited on p. 69).

[199] Sungsoo Kim et al. "Spin-and spray-deposited single-walled carbon-nanotube electrodes for organic solar cells". In: *Adv. Funct. Mater.* 20.14 (2010), pp. 2310–2316. DOI: 10.1002/adfm.200902369 (Cited on p. 69).

[200] Severin N Habisreutinger. "Single-Walled Carbon Nanotubes as Charge Extraction Layer for Perovskite Solar Cells Single-Walled Carbon Nanotubes as Charge Extraction Layer for Perovskite Solar Cells". DPhil Thesis. University of Oxford, 2016, p. 191 (Cited on p. 71).

[201] Jingxiu Yang, Peng Zhang, and Su-Huai Wei. "Band Structure Engineering of Cs2AgBiBr6 Perovskite through Order–Disordered Transition: A First-Principle Study". In: *J. Phys. Chem. Lett.* 9.1 (2018), pp. 31–35. DOI: 10.1021/acs.jpclett.7b02992 (Cited on pp. 71, 72, 77, 118).

[202] Marina R. Filip et al. "Band Gaps of the Lead-Free Halide Double Perovskites Cs2BiAgCl6 and Cs2BiAgBr6 from Theory and Experiment". In: *J. Phys. Chem. Lett.* 7.13 (2016), pp. 2579–2585. DOI: 10.1021/acs.jpclett.6b01041 (Cited on pp. 71, 72, 77, 82).

[203] Davide Bartesaghi et al. “Charge Carrier Dynamics in Cs2AgBiBr6 Double Perovskite”. In: *J. Phys. Chem. C* 122.9 (2018), pp. 4809–4816. DOI: 10.1021/acs.jpcc.8b00572 (Cited on pp. 71, 77, 82).

[204] Sidney E. Creutz et al. “Colloidal Nanocrystals of Lead-Free Double-Perovskite (Elpasolite) Semiconductors: Synthesis and Anion Exchange to Access New Materials”. In: *Nano Lett.* 18.2 (2018), pp. 1118–1123. DOI: 10.1021/acs.nanolett.7b04659 (Cited on pp. 71, 73, 78, 82).

[205] Eric T. McClure et al. “Cs2AgBiX6 (X = Br, Cl): New Visible Light Absorbing, Lead-Free Halide Perovskite Semiconductors”. In: *Chem. Mater.* 28.5 (2016), pp. 1348–1354. DOI: 10.1021/acs.chemmater.5b04231 (Cited on pp. 71, 77, 82).

[206] S. J. Zelewski et al. “Revealing the nature of photoluminescence emission in the metal-halide double perovskite Cs2AgBiBr6”. In: *J. Mater. Chem. C* 7.27 (2019), pp. 8350–8356. DOI: 10.1039/c9tc02402f (Cited on p. 72).

[207] Cuncun Wu et al. “The Dawn of Lead-Free Perovskite Solar Cell: Highly Stable Double Perovskite Cs2AgBiBr6 Film”. In: *Adv. Sci.* 5.3 (2018), p. 1700759. DOI: 10.1002/advs.201700759 (Cited on pp. 73, 83).

[208] Constantinos C. Stoumpos and Mercouri G. Kanatzidis. “The Renaissance of Halide Perovskites and Their Evolution as Emerging Semiconductors”. In: *Acc. Chem. Res.* 48.10 (2015), pp. 2791–2802. DOI: 10.1021/acs.accounts.5b00229 (Cited on p. 76).

[209] Jeremy L. Knutson, James D. Martin, and David B. Mitzi. “Tuning the Band Gap in Hybrid Tin Iodide Perovskite Semiconductors Using Structural Templating”. In: *Inorg. Chem.* 44.13 (2005), pp. 4699–4705. DOI: 10.1021/ic050244q (Cited on p. 76).

[210] Ke Zhao Du et al. “Bandgap Engineering of Lead-Free Double Perovskite Cs2AgBiBr6through Trivalent Metal Alloying”. In: *Angew. Chemie - Int. Ed.* 56.28 (2017), pp. 8158–8162. DOI: 10.1002/anie.201703970 (Cited on pp. 77, 80).

[211] Weiwei Meng et al. “Parity-Forbidden Transitions and Their Impact on the Optical Absorption Properties of Lead-Free Metal Halide Perovskites and Double Perovskites”. In: *J. Phys. Chem. Lett.* 8.13 (2017), pp. 2999–3007. DOI: 10.1021/acs.jpclett.7b01042 (Cited on pp. 77, 79, 80).

[212] Weinan Yuan et al. “In Situ Regulating the Order–Disorder Phase Transition in Cs2AgBiBr6 Single Crystal toward the Application in an X-Ray Detector”. In: *Adv. Funct. Mater.* 1900234 (2019), p. 1900234. DOI: 10.1002/adfm.201900234 (Cited on pp. 77, 81, 83).

[213] Robert L. Z. Hoye et al. “Fundamental Carrier Lifetime Exceeding 1 µs in Cs 2 AgBiBr 6 Double Perovskite”. In: *Adv. Mater. Interfaces* 5.15 (2018), p. 1800464. DOI: 10.1002/admi.201800464 (Cited on p. 77).

[214] Zewen Xiao et al. “Thermodynamic Stability and Defect Chemistry of Bismuth-Based Lead-Free Double Perovskites”. In: *ChemSusChem* 9.18 (2016), pp. 2628–2633. DOI: 10.1002/cssc.201600771 (Cited on pp. 77, 81, 83).

[215] Robin Kentsch et al. “Exciton Dynamics and Electron–Phonon Coupling Affect the Photovoltaic Performance of the Cs 2 AgBiBr 6 Double Perovskite”. In: *J. Phys. Chem. C* 122.45 (2018), pp. 25940–25947. DOI: 10.1021/acs.jpcc.8b09911 (Cited on p. 77).

[216] Julian A Steele et al. “Giant Electron-Phonon Coupling and Deep Conduction Band Resonance in Metal Halide Double Perovskite”. In: *ACS Nano* (2018). DOI: 10.1021/acsnano.8b02936 (Cited on pp. 78, 80, 81).

[217] Enrico Greul et al. “Highly stable, phase pure Cs2AgBiBr6 double perovskite thin films for optoelectronic applications”. In: *J. Mater. Chem. A* 5.37 (2017), pp. 19972–19981. DOI: 10.1039/C7TA06816F (Cited on pp. 78, 82, 83, 119).

[218] Weiyin Gao et al. “High-Quality Cs2AgBiBr6 Double Perovskite Film for Lead-Free Inverted Planar Heterojunction Solar Cells with 2.2 % Efficiency”. In: *ChemPhysChem* 19.14 (2018), pp. 1696–1700. DOI: 10.1002/cphc.201800346 (Cited on pp. 78, 82, 83).

[219] Valerio D’Innocenzo et al. “Excitons versus free charges in organo-lead tri-halide perovskites”. In: *Nat. Commun.* 5.1 (2014), p. 3586. DOI: 10.1038/ncomms4586 (Cited on p. 78).

[220] Samuel D. Stranks et al. “Recombination Kinetics in Organic-Inorganic Perovskites: Excitons, Free Charge, and Subgap States”. In: *Phys. Rev. Appl.* 2.3 (2014), pp. 1–8. DOI: 10.1103/PhysRevApplied.2.034007 (Cited on p. 79).

[221] Adam H. Slavney et al. “A Bismuth-Halide Double Perovskite with Long Carrier Recombination Lifetime for Photovoltaic Applications”. In: *J. Am. Chem. Soc.* 138.7 (2016), pp. 2138–2141. DOI: 10.1021/jacs.5b13294 (Cited on p. 80).

[222] Hong Jian Feng et al. “Double Perovskite Cs2BBiX6(B = Ag, Cu; X = Br, Cl)/TiO2Heterojunction: An Efficient Pb-Free Perovskite Interface for Charge Extraction”. In: *J. Phys. Chem. C* 121.8 (2017), pp. 4471–4480. DOI: 10.1021/acs.jpcc.7b00138 (Cited on p. 80).

[223] Martin A Green and Mark J Keevers. “Optical properties of intrinsic silicon at 300 K”. In: *Prog. Photovoltaics Res. Appl.* 3.3 (1995), pp. 189–192. DOI: 10.1002/pip.4670030303 (Cited on p. 82).

[224] Christopher N. Savory, Aron Walsh, and David O. Scanlon. "Can Pb-Free Halide Double Perovskites Support High-Efficiency Solar Cells?" In: *ACS Energy Lett.* 1.5 (2016), pp. 949–955. DOI: 10.1021/acsenergylett.6b00471 (Cited on p. 83).

[225] R.T. Williams and K.S. Song. "The Self-Trapped Exciton". In: *J. Phys. Chem. Solids* 51.7 (1990), pp. 679–716. DOI: 10.1016/0022-3697(90)90144-5 (Cited on p. 84).

[226] W. Hayes and I. B. Owen. "EPR of the self-trapped exciton in AgCl". In: *J. Phys. C Solid State Phys.* 9.3 (1976), pp. L69–L71. DOI: 10.1088/0022-3719/9/3/004 (Cited on p. 84).

[227] W. Hayes, I. B. Owen, and P. J. Walker. "Optically-detected EPR of excitons in AgCl, AgCl:Br and AgBr". In: *J. Phys. C Solid State Phys.* 10.10 (1977), pp. 1751–1759. DOI: 10.1088/0022-3719/10/10/017 (Cited on p. 84).

[228] P. G. Baranov et al. "Self-Trapped Excitons in Ionic-Covalent Silver Halide Crystals and Nanostructures: High-Frequency EPR, ESE, ENDOR and ODMR Studies". In: *Appl. Magn. Reson.* 39.4 (2010), pp. 453–486. DOI: 10.1007/s00723-010-0180-6 (Cited on p. 84).

[229] T. Lancaster et al. "Intrinsic magnetic order in Cs2AgF4 detected by muon-spin relaxation". In: *Phys. Rev. B* 75.22 (2007), p. 220408. DOI: 10.1103/PhysRevB.75.220408 (Cited on p. 84).

[230] Jamie L. Manson et al. "Characterization of the Antiferromagnetism in Ag(pyz) 2 (S 2 O 8) (pyz = Pyrazine) with a Two-Dimensional Square Lattice of Ag 2+ Ions". In: *J. Am. Chem. Soc.* 131.13 (2009), pp. 4590–4591. DOI: 10.1021/ja9005223 (Cited on p. 84).

[231] D. Kurzydłowski and W. Grochala. "Large exchange anisotropy in quasi-one-dimensional spin- 1/2 fluoride antiferromagnets with a d(z2)1 ground state". In: *Phys. Rev. B* 96.15 (2017), p. 155140. DOI: 10.1103/PhysRevB.96.155140 (Cited on p. 84).

[232] Junichi Nishitani, Takeshi Nagashima, and Tohru Suemoto. "Magnetic-excitation-assisted photoluminescence from self-trapped exciton states in MnO". In: *J. Phys. Condens. Matter* 28.1 (2016), p. 016004. DOI: 10.1088/0953-8984/28/1/016004 (Cited on p. 85).

[233] S. Mochizuki. "Spin-wave-assisted photoluminescence in MnS". In: *J. Phys. Condens. Matter* 2.34 (1990), pp. 7225–7231. DOI: 10.1088/0953-8984/2/34/015 (Cited on p. 85).

[234] S Mochizuki et al. "Spin-wave-assisted photoluminescence in MnO at low temperatures". In: *J. Phys. Condens. Matter* 4.30 (1992), pp. 6501–6508. DOI: 10.1088/0953-8984/4/30/018 (Cited on p. 85).

[235] W. Beall Fowler, M. J. Marrone, and M. N. Kabler. "Theory of Self-Trapped Exciton Luminescence in Halide Crystals". In: *Phys. Rev. B* 8.12 (1973), pp. 5909–5919. DOI: 10.1103/PhysRevB.8.5909 (Cited on p. 85).

[236] H. Kanzaki, S. Sakuragi, and K. Sakamoto. "Excitons in AgBr1-æClæ - transition of relaxed state between free and self-traffed exciton". In: *Solid State Commun.* 9.13 (1971), pp. 999–1002. DOI: 10.1016/0038-1098(71)90448-0 (Cited on p. 85).

[237] K Imanaka et al. "Self-Trapped Exciton Luminescence after Tunnelling of Vk and Na0 Centers in CsI:Na Crystals". In: *Phys. status solidi* 108.2 (1981), pp. 449–458. DOI: 10.1002/pssb.2221080220 (Cited on p. 85).

[238] Jiajun Luo et al. "Efficient and stable emission of warm-white light from lead-free halide double perovskites". In: *Nature* 563.7732 (2018), pp. 541–545. DOI: 10.1038/s41586-018-0691-0 (Cited on pp. 85, 118).

[239] Jacky Even et al. "Solid-state physics perspective on hybrid perovskite semiconductors". In: *J. Phys. Chem. C* 119.19 (2015), pp. 10161–10177. DOI: 10.1021/acs.jpcc.5b00695 (Cited on pp. 87, 90).

[240] Tianyi Wang et al. "Indirect to direct bandgap transition in methylammonium lead halide perovskite". In: *Energy Environ. Sci.* 10.2 (2017), pp. 509–515. DOI: 10.1039/C6EE03474H (Cited on p. 87).

[241] Scott McKechnie et al. "Dynamic symmetry breaking and spin splitting in metal halide perovskites". In: *Phys. Rev. B* 98.8 (2018), p. 085108. DOI: 10.1103/PhysRevB.98.085108 (Cited on p. 87).

[242] Yangyang Dang et al. "Bulk crystal growth of hybrid perovskite material CH3NH3PbI3". In: *CrystEngComm* 17.3 (2015), pp. 665–670. DOI: 10.1039/c4ce02106a (Cited on pp. 87, 88).

[243] Valerio Sarritzu et al. "Direct or Indirect Bandgap in Hybrid Lead Halide Perovskites?" In: *Adv. Opt. Mater.* 6.10 (2018), p. 1701254. DOI: 10.1002/adom.201701254 (Cited on p. 87).

[244] Wei Zhang et al. "Enhanced optoelectronic quality of perovskite thin films with hypophosphorous acid for planar heterojunction solar cells". en. In: *Nat. Commun.* 6 (2015), p. 9. DOI: 10.1038/ncomms10030 (Cited on p. 87).

[245] Duyen H. Cao et al. "Remnant PbI2, an unforeseen necessity in high-efficiency hybrid perovskite-based solar cells?" In: *APL Mater.* 2.9 (2014), pp. 1–8. DOI: 10.1063/1.4895038 (Cited on p. 87).

[246] Yasuhiro Yamada et al. “Photoelectronic responses in solution-processed perovskite CH3NH3PbI3 solar cells studied by photoluminescence and photoabsorption spectroscopy”. In: *IEEE J. Photovoltaics* 5.1 (2015), pp. 401–405. DOI: 10.1109/JPHOTOV.2014.2364115 (Cited on pp. 87, 88).

[247] Wei Huang et al. “Optical bandgap energy of CH3NH3PbI3 perovskite studied by photoconductivity and reflectance spectroscopy”. In: *Sci. China Technol. Sci.* 61.6 (2018), pp. 886–892. DOI: 10.1007/s11431-017-9211-6 (Cited on p. 87).

[248] Feng Hao et al. “Anomalous band gap behavior in mixed Sn and Pb perovskites enables broadening of absorption spectrum in solar cells”. In: *J. Am. Chem. Soc.* 136.22 (2014), pp. 8094–8099. DOI: 10.1021/ja5033259 (Cited on p. 88).

[249] Yasuhiro Yamada et al. “Dynamic Optical Properties of CH3NH3PbI3 Single Crystals as Revealed by One- and Two-photon Excited Photolumines-cence Measurements”. In: *J. Am. Chem. Soc.* 137.33 (2015), pp. 10456–10459 (Cited on p. 88).

[250] Guichuan Xing et al. “Long-range balanced electron-and hole-transport lengths in organic-inorganic CH3NH3PbI3”. In: *Science (80-.).* 342.6156 (2013), pp. 344–347. DOI: 10.1126/science.1243167 (Cited on p. 89).

[251] Stefaan De Wolf et al. “Organometallic Halide Perovskites: Sharp Optical Absorption Edge and Its Relation to Photovoltaic Performance”. In: *J. Phys. Chem. Lett.* 5.6 (2014), pp. 1035–1039. DOI: 10.1021/jz500279b (Cited on p. 89).

[252] Yanjun Fang et al. “Quantification of re-Absorption and re-emission processes to determine photon recycling efficiency in perovskite single crystals”. In: *Nat. Commun.* 8 (2017), pp. 1–9. DOI: 10.1038/ncomms14417 (Cited on p. 89).

[253] Jenya Tilchin et al. “Hydrogen-like Wannier–Mott Excitons in Single Crystal of Methylammonium Lead Bromide Perovskite”. In: *ACS Nano* 10.6 (2016), pp. 6363–6371. DOI: 10.1021/acsnano.6b02734 (Cited on p. 90).

[254] Weiguang Kong et al. “Characterization of an abnormal photoluminescence behavior upon crystal-phase transition of perovskite CH3NH3PbI3”. In: *Phys. Chem. Chem. Phys.* 17.25 (2015), pp. 16405–16411. DOI: 10.1039/c5cp02605a (Cited on p. 90).

[255] K. Galkowski et al. “Spatially resolved studies of the phases and morphology of methylammonium and formamidinium lead tri-halide perovskites”. In: *Nanoscale* 9.9 (2017), pp. 3222–3230. DOI: 10.1039/c7nr00355b (Cited on pp. 90, 115).

[256] M. Ibrahim Dar et al. “Origin of unusual bandgap shift and dual emission in organic-inorganic lead halide perovskites”. In: *Sci. Adv.* 2.10 (2016). DOI: 10.1126/sciadv.1601156 (Cited on p. 90).

[257] Adam D Wright et al. “Electron–phonon coupling in hybrid lead halide perovskites”. In: *Nat. Commun.* 7.May (2016). DOI: 10.1038/ncomms11755 (Cited on pp. 90, 103).

[258] Huawei Zhou et al. “Antisolvent diffusion-induced growth, equilibrium behaviours in aqueous solution and optical properties of CH3NH3PbI3 single crystals for photovoltaic applications”. In: *RSC Adv.* 5.104 (2015), pp. 85344–85349. DOI: 10.1039/c5ra17579h (Cited on p. 93).

[259] Jack Chun-Ren Ke et al. “In situ investigation of degradation at organometal halide perovskite surfaces by X-ray photoelectron spectroscopy at realistic water vapour pressure”. In: *Chem. Commun.* 53.37 (2017), pp. 5231–5234. DOI: 10.1039/c7cc01538k (Cited on p. 94).

[260] Yu Han et al. “Degradation observations of encapsulated planar CH3NH3PbI3 perovskite solar cells at high temperatures and humidity”. In: *J. Mater. Chem. A* 3.15 (2015), pp. 8139–8147. DOI: 10.1039/C5TA00358J (Cited on p. 94).

[261] Zhaolai Chen et al. “Single-Crystal MAPbI3 Perovskite Solar Cells Exceeding 21% Power Conversion Efficiency”. In: *ACS Energy Lett.* (2019), pp. 1258–1259. DOI: 10.1021/acsenergylett.9b00847 (Cited on pp. 97, 98).

[262] Yanwen Chen et al. “Communicating Two States in Perovskite Revealed by Time-Resolved Photoluminescence Spectroscopy”. In: *Sci. Rep.* 8.1 (2018), p. 16482. DOI: 10.1038/s41598-018-34645-8 (Cited on p. 99).

[263] Yue-yu Zhang et al. “Intrinsic Instability of the Hybrid Halide Perovskite Semiconductor CH3NH3PbI3”. In: *Chinese Phys. Lett.* 35.3 (2018), p. 036104. DOI: 10.1088/0256-307X/35/3/036104 (Cited on p. 99).

[264] Simone Meloni et al. “Ionic polarization-induced current-voltage hysteresis in CH3NH3PbX3 perovskite solar cells”. In: *Nat. Commun.* 7.May 2015 (2016). DOI: 10.1038/ncomms10334 (Cited on p. 99).

[265] Thibaud Etienne, Edoardo Mosconi, and Filippo De Angelis. “Dynamical Rashba Band Splitting in Hybrid Perovskites Modeled by Local Electric Fields”. In: *J. Phys. Chem. C* 122.1 (2018), pp. 124–132. DOI: 10.1021/acs.jpcc.7b09791 (Cited on pp. 100, 101, 102).

[266] Shi Liu et al. “Ferroelectric Domain Wall Induced Band-Gap Reduction and Charge Separation in Organometal Halide Perovskites”. In: *J. Phys. Chem. Lett.* 6.4 (2015), pp. 693–699. DOI: 10.1021/jz502666j (Cited on p. 100).

[267] Samuel D. Stranks and Paulina Plochocka. “The influence of the Rashba effect”. In: *Nat. Mater.* 17.5 (2018), pp. 381–382. DOI: 10.1038/s41563-018-0067-8 (Cited on pp. 101, 102).

[268] Fan Zheng et al. “Rashba Spin–Orbit Coupling Enhanced Carrier Lifetime in CH3NH3PbI3”. In: *Nano Lett.* 15.12 (2015), pp. 7794–7800. DOI: 10.1021/acs.nanolett.5b01854 (Cited on pp. 101, 102).

[269] Claudio Quarti et al. “Structural and optical properties of methylammonium lead iodide across the tetragonal to cubic phase transition: implications for perovskite solar cells”. In: *Energy Environ. Sci.* 9.1 (2016), pp. 155–163. DOI: 10.1039/C5EE02925B (Cited on pp. 101, 102).

[270] Fabian Ruf et al. “Temperature-dependent studies of exciton binding energy and phase-transition suppression in (Cs,FA,MA)Pb(I,Br) 3 perovskites”. In: *APL Mater.* 7.3 (2019), p. 031113. DOI: 10.1063/1.5083792 (Cited on pp. 101, 116).

[271] Dibyajyoti Ghosh et al. “Good Vibrations: Locking of Octahedral Tilting in Mixed-Cation Iodide Perovskites for Solar Cells”. In: *ACS Energy Lett.* 2.10 (2017), pp. 2424–2429. DOI: 10.1021/acsenergylett.7b00729 (Cited on p. 101).

[272] Dibyajyoti Ghosh et al. “Mixed A-Cation Perovskites for Solar Cells: Atomic-Scale Insights Into Structural Distortion, Hydrogen Bonding, and Electronic Properties”. In: *Chem. Mater.* 30.15 (2018), pp. 5194–5204. DOI: 10.1021/acs.chemmater.8b01851 (Cited on p. 101).

[273] William Shockley and Hans J. Queisser. “Detailed balance limit of efficiency of p-n junction solar cells”. In: *J. Appl. Phys.* 32.3 (1961), pp. 510–519. DOI: 10.1063/1.1736034 (Cited on p. 103).

[274] Michael Sendner et al. “Optical phonons in methylammonium lead halide perovskites and implications for charge transport”. In: *Mater. Horizons* 3.6 (2016), pp. 613–620. DOI: 10.1039/C6MH00275G (Cited on pp. 103, 109, 111, 116).

[275] Miguel A. Pérez-Osorio et al. “Vibrational Properties of the Organic–Inorganic Halide Perovskite CH3NH3PbI3 from Theory and Experiment: Factor Group Analysis, First-Principles Calculations, and Low-Temperature Infrared Spectra”. In: *J. Phys. Chem. C* 119.46 (2015), pp. 25703–25718. DOI: 10.1021/acs.jpcc.5b07432 (Cited on p. 103).

[276] Krzysztof Galkowski et al. “Determination of the exciton binding energy and effective masses for methylammonium and formamidinium lead tri-halide perovskite semiconductors”. In: *Energy Environ. Sci.* 9.3 (2016), pp. 962–970. DOI: 10.1039/C5EE03435C (Cited on pp. 103, 104).

[277] Arman Mahboubi Soufiani et al. “Impact of microstructure on the electron–hole interaction in lead halide perovskites”. In: *Energy Environ. Sci.* 10.6 (2017), pp. 1358–1366. DOI: 10.1039/C7EE00685C (Cited on pp. 103, 104, 115).

[278] M. Hirasawa et al. “Magnetoabsorption of the lowest exciton in perovskite-type compound (CH3NH3)PbI3”. In: *Phys. B Condens. Matter* 201.C (1994), pp. 427–430. DOI: 10.1016/0921-4526(94)91130-4 (Cited on pp. 103, 104).

[279] Kenichiro Tanaka et al. “Comparative study on the excitons in lead-halide-based perovskite-type crystals CH3NH3PbBr3 CH3NH3PbI3”. In: *Solid State Commun.* 127.9-10 (2003), pp. 619–623. DOI: 10.1016/S0038-1098(03)00566-0 (Cited on pp. 103, 104, 115).

[280] Satoru J. Miyake. “Strong-Coupling Limit of the Polaron Ground State”. In: *J. Phys. Soc. Japan* 38.1 (1975), pp. 181–182. DOI: 10.1143/JPSJ.38.181 (Cited on p. 110).

[281] H. Löwen. “Spectral properties of an optical polaron in a magnetic field”. In: *J. Math. Phys.* 29.6 (1988), pp. 1498–1504. DOI: 10.1063/1.527893 (Cited on p. 110).

[282] J. Devreese and R. Evrard. “On the excited states of a symmetrical polaron model”. In: *Phys. Lett.* 11.4 (1964), pp. 278–279. DOI: 10.1016/0031-9163(64)90324-5 (Cited on p. 110).

[283] Ankit Rohatgi. *WebPlotDigitizer v4.2*. DOI: https://automeris.io/WebPlotDigitizer (Cited on p. 112).

[284] Giacomo Giorgi et al. “Small photocarrier effective masses featuring ambipolar transport in methylammonium lead iodide perovskite: A density functional analysis”. In: *J. Phys. Chem. Lett.* 4.24 (2013), pp. 4213–4216. DOI: 10.1021/jz4023865 (Cited on p. 115).

[286] Kiyoshi Miyata et al. “Large polarons in lead halide perovskites”. In: *Sci. Adv.* 3.8 (2017), e1701217. DOI: 10.1126/sciadv.1701217 (Cited on p. 116).

[287] Jarvist Moore Frost. “Calculating polaron mobility in halide perovskites”. In: *Phys. Rev. B* 96.19 (2017), p. 195202. DOI: 10.1103/PhysRevB.96.195202 (Cited on p. 116).

[288] Zhi-Gang Yu. “Rashba Effect and Carrier Mobility in Hybrid Organic–Inorganic Perovskites”. In: *J. Phys. Chem. Lett.* 7.16 (2016), pp. 3078–3083. DOI: 10.1021/acs.jpclett.6b01404 (Cited on p. 116).

[289] E. Menéndez-Proupin et al. “Self-consistent relativistic band structure of the CH3NH3PbI3 perovskite”. In: *Phys. Rev. B* 90.4 (2014), p. 045207. DOI: 10.1103/PhysRevB.90.045207 (Cited on p. 116).

[290] R. P. Feynman. “Slow Electrons in a Polar Crystal”. In: *Phys. Rev.* 97.3 (1955), pp. 660–665. DOI: 10.1103/PhysRev.97.660 (Cited on p. 116).

[291] R. P. Feynman et al. “Mobility of Slow Electrons in a Polar Crystal”. In: *Phys. Rev.* 127.4 (1962), pp. 1004–1017. DOI: 10.1103/PhysRev.127.1004 (Cited on p. 116).

[292] Arman Mahboubi Soufiani et al. “Polaronic exciton binding energy in iodide and bromide organic-inorganic lead halide perovskites”. In: *Appl. Phys. Lett.* 107.23 (2015), p. 231902. DOI: 10.1063/1.4936418 (Cited on p. 116).

[293] David P. McMeekin et al. “Solution-Processed All-Perovskite Multi-junction Solar Cells”. In: *Joule* 3.2 (2019), pp. 387–401. DOI: 10.1016/j.joule.2019.01.007 (Cited on p. 117).

[294] Tobias Koeniger and Helmut Muenstedt. “Coatings of indium tin oxide nanoparticles on various flexible polymer substrates: Influence of surface topography and oscillatory bending on electrical properties”. In: *J. Soc. Inf. Disp.* 16.4 (2008), p. 559. DOI: 10.1889/1.2905043 (Cited on p. 118).

[295] Adam H. Slavney et al. “Defect-Induced Band-Edge Reconstruction of a Bismuth-Halide Double Perovskite for Visible-Light Absorption”. In: *J. Am. Chem. Soc.* 139.14 (2017), pp. 5015–5018. DOI: 10.1021/jacs.7b01629 (Cited on p. 118).

[296] Alexandra J. Ramadan et al. “Unravelling the Improved Electronic and Structural Properties of Methylammonium Lead Iodide Deposited from Acetonitrile”. In: *Chem. Mater.* 30.21 (2018), pp. 7737–7743. DOI: 10.1021/acs.chemmater.8b03084 (Cited on p. 120).